# Study and Optimisation of the nonlinear and 6D dynamics of an electron beam in an ultra-low emittance storage ring

Thesis submitted in accordance with the requirements of
the University of Liverpool for the degree of Doctor in Philosophy by

**Lina HOUMMI**

May 2021

*Je te frapperai sans colère*
*Et sans haine, comme un boucher,*
*Comme Moïse le rocher !*
*Et je ferai de ta paupière,*

*Pour abreuver mon Sahara,*
*Jailler les eaux de la souffrance.*
*Mon désir gonflé d'espérance*
*Sur tes pleurs salés nagera*

*Comme un vaisseau qui prend le large,*
*Et dans mon coeur qu'ils soûleront*
*Tes chers sanglots retentiront*
*Comme un tambour qui bat la charge !*

*Ne suis-je pas un faux accord*
*Dans la divine symphonie,*
*Grâce à la vorace Ironie*
*Qui me secoue et qui me mord ?*

*Elle est dans ma voix, la criarde !*
*C'est tout mon sang, ce poison noir !*
*Je suis le sinistre miroir*
*Où la mégère se regarde !*

*Je suis la plaie et le couteau !*
*Je suis le soufflet et la joue !*
*Je suis les membres et la roue,*
*Et la victime et le bourreau !*

*Je suis de mon coeur le vampire,*
*- Un de ces grands abandonnés,*
*Au rire éternel condamnés,*
*Et qui ne peuvent plus sourire !*

*L'Héautontimorouménos, Charles Baudelaire*

# Contents

# Preface

*This thesis is primarily my own work. The sources of other materials are identified. It is the result of four years of PhD, shared both in terms of years and funding, between the University of Liverpool/Cockcroft Institute, U.K., and the synchrotron SOLEIL, France.*

The present thesis is composed of seven chapters, which are largely independent. The first chapter offers a general introduction on synchrotrons, the second on lattice design for fourth generation storage rings. Expert readers may begin at the third chapter, which applies the hybrid scheme developed for the ESRF-Extremely Brilliant Source (ESRF-EBS)and the so-called High-Order Achromat (HOA) scheme to the SOLEIL storage ring upgrade and compares their transverse performances. Both schemes are nonlinearly optimised using the code Multi-Objective Genetic Algorithm (MOGA) in Bmad in the fourth chapter, which also discusses their injection schemes. As ultra-low emittance lattices drastically reduce the dispersion thus the momentum compaction factor, the fifth chapter introduces the longitudinal motion and an extension of the code MOGA-Bmad which allows both the transverse optimisation and the minimisation of the destructive parts of the momentum compaction factor. The last chapter describes the reduction of the on-momentum transverse dynamics of the hybrid lattice in the presence of synchro-betatron oscillations.

## Conventions

The complex number is noted $i$. Vectors are written $\mathbf{U}$, their norm $U$ or $\|U\|$.

**Derivatives** The derivative with regard to the longitudinal position $s$ is noted:

$$u' = \frac{du}{ds} \tag{1}$$

The derivative with time $t$ is noted:

$$\dot{u} = \frac{du}{dt} \tag{2}$$

**Sextupole strength** Two conventions exist in the accelerator community regarding the strength of the sextupoles. Unless stated otherwise, the convention used in this document is:

$$k_2 = \frac{1}{2}\left(\frac{1}{B\rho}\frac{\partial^2 B}{\partial x^2}\right) \tag{3}$$

A second convention can nonetheless be found in the description of MOGA-Bmad results. Indeed, the Bmad convention removes the factor $\frac{1}{2}$ in the second-order derivative, and is therefore twice the equation above. The use of this convention will be stated in the relevant tables.

## Language abbreviations

To ease the reading, the following abbreviations are used in the text of the present thesis.

TABLE 1: Language abbreviations used in the present document

| Name | Abbreviation |
|---|---|
| *Confer* | *cf* |
| Constant | cst |
| Equation | Eq. |
| Figure | Fig. |
| *Id est* | *i.e.* |
| No dimension | n.d. |
| Section | Sec. |

# Abstract

Since the discovery of synchrotron radiation in 1947 and the first dedicated facilities, storage-ring-based light sources led to numerous discoveries and participated in the further advancement of sciences. To match the needs of researchers, they evolved drastically, increasing both their energies and their brilliance. The first chapter introduces synchrotron radiation and the main characteristics of synchrotrons. Today, the new challenge is the extremely brilliant sources, which aims at increasing the photon brilliance by at least a factor 100; various challenges arise in different disciplines, such as magnet designs and vacuum. To achieve such a high brilliance, fourth-generation storage-ring based light sources are designed to approach the diffraction limit of the photon source, by reducing their transverse emittances. As part of a global transition from third- to fourth- generation storage-ring-based light sources, the present thesis introduces, compares and analyses the effect of ultra-low emittance on the transverse and longitudinal dynamics of ultra-low emittance lattices, applied to the SOLEIL upgrade.

Such a reduction of the natural horizontal emittance is achieved with the use of Multi-Bend Achromats (MBA) and strong focusing. Both are introduced in the second chapter, along with basic notions of accelerator physics. As strong focusing increases the natural chromaticities, ultra-low emittance lattices require strong sextupoles to correct them. Yet, they affect the stability and beam lifetime. The presence of strong sextupoles was integrated in the linear design, to minimise their effect on the lattice performances. Two specific MBA lattices are studied and compared in the present thesis. The first lattice is the ESRF-EBS-type MBA lattice, introducing a minus identity transformation to compensate the nonlinear impact of sextupoles thanks to the lattice symmetry and to a tight control of the betatron phase advance between sextupoles. The presence of two dispersion bumps maximises the efficiency of the sextupoles, further reducing their required strengths. The second scheme is the so-called High-Order Achromat (HOA) lattice.

Ultra-low emittance lattices are being studied for the future upgrade of the SOLEIL 2.75 GeV storage ring. The targeted horizontal emittance of the new lattice is below 100 pm.rad, corresponding to a reduction of a factor 40 compared to the current lattice. Two 7BA lattices were designed, using either the hybrid or the HOA scheme, and a natural horizontal emittance of $\simeq 75\,\mathrm{pm.rad}$ was achieved with the inclusion of reverse bending

magnets. Both schemes are compared in terms of magnets, strengths and number, and their bare transverse dynamics before any nonlinear optimisation. The effect of ultra-low emittance on the Touschek lifetime and Intra-Beam Scattering is finally studied on the hybrid lattice.

Nonlinear optimisation of both schemes is achieved using the code MOGA-Bmad, which optimises the transverse dynamic apertures at three set energy deviations while maintaining constant chromaticities. Results are discussed in the fourth chapter, which also follows the evolution of lattice studies for the SOLEIL upgrade project: the lattices under study evolved from a 24- and 20-fold symmetry towards the maintenance of the beamlines' positions, which dropped the symmetry down to 4. The use of the HOA lattice proved more efficient and flexible to answer to the new implementation constraints. In terms of injection, since the strong focusing and the low $\beta$-functions cause the transverse dynamic apertures to be merely a few millimetres wide instead of 10-30 mm in the case of the current SOLEIL lattice, the current transverse off-axis injection scheme requires the inclusion of a high-$\beta_x$ section in the ultra-low emittance lattices under study to locally increase the transverse acceptance. Another scheme injects the beam directly on-axis, but onto an off-momentum closed orbit thanks to a Multipole-Injector Kicker (MIK). To distinguish the closed orbits at the MIK, this scheme requires the insertion of a dispersion bump.

In ultra-low emittance lattices, the increased number of dipoles and the use of reverse bending magnets ensure a low dispersion along the ring, which yields to a low zeroth-order momentum compaction factor. Some ultra-low emittance lattices, such as a 5BA lattice of 80 pm.rad natural horizontal emittance, have their first-order momentum compaction factor overtake the zeroth, which results in a perturbed longitudinal stability and an atrophied RF bucket. This yields to a reduced beam stability and lifetime. Analytical calculations of the three lowest orders in momentum compaction factor are conducted to describe the requirements of a minimisation of the first-order. Three methods developed to minimise this effect and restore the RF bucket are discussed in the fifth chapter. Among them, extension of MOGA-Bmad includes the minimisation of the first-order momentum compaction factor, while optimising the transverse on- and off-momentum dynamics.

Although the hybrid scheme provides a large on-momentum transverse dynamic aperture in 4D thanks to the application of the non-interleaved principle on its sextupoles, its off-momentum performance is limited. Further studies in 6D reveal intrinsic off-momentum transverse oscillations, which are considered to result from of a nonlinear increase of the path length. The effect of the inhomogeneous sextupole distribution in the hybrid scheme is presented and compared with the HOA lattice under study, in the last chapter. The path length is described in terms of higher-order elements depending on the nonlinear magnets, using the first-order canonical perturbation theory.

# Acknowledgements

My first thoughts are to my SOLEIL supervisor, Dr. Ryutaro Nagaoka, who dedicated his time on directing my studies and helping me grow as a researcher. Acknowledgements are not enough to express my gratitude for your guidance and wisdom, and for your continuous support. Thank you.

Thank you to my academic supervisors, Pr. Carsten P. Welsch, for your support and understanding, and to Dr. Javier Restá Lopez, for our bimonthly meetings and your help on beam dynamics studies.

Mes plus chaleureux remerciements à l'équipe Physique des Accélérateurs du synchrotron SOLEIL, au sein de laquelle j'ai passé deux belles années. Merci pour votre accompagnement bienveillant, votre savoir, et vos encouragements. Merci à Pascale Brunelle, pour toujours s'être rendue disponible, pour les questions et les visites. Merci à Marie-Agnès Tordeux d'avoir éclairé mes lanternes sur les chemins de l'injection. Merci à Alexandre Loulergue d'avoir dégagé du temps pour me montrer quelques rouages en optique linéaire. Merci à Laurent Nadolski pour ses explications claires et efficaces. Merci à Amor Nadji, pour son aide et sa patience. Enfin, merci à Alexis Gamelin, David Amorim et Randy Ollier, derniers arrivants, mais avec qui j'ai pu beaucoup échanger.

Many thanks to Hung-Chun Chao for the intensive training on MOGA-Bmad at the beginning of my PhD. A warm thank you to Maher Attal for the discussions during the month October 2017 he spent in SOLEIL, and for allowing me to drown you of questions. Thank you to Michael Ehrlichman, who found the time to answer some questions on his MOGA-Bmad development, which helped finalise the extension I wrote.

Over the two years I spent at the Cockcroft Institute, I had the amazing luck to start my PhD with many incredible people. Among them: the R.S. group! Thank you for the laughs, the talks and continu(ing)ous support. Growing together was the highlight of those last years! The warmest thank you to my friends: Pavel Juarez Lopez, Edward Martin, Ewa Oponowicz, Volodymyr Rodin, Amir Salehilashkajani, Roland Schnurer, Ruta Sirvinskaite, Bianca Veglia, Milena Vujanovic, Jacinta Yap. Thank you to Alex Herrod and Andrew Vint for the early evening laughs in the empty corridor. Thank you to the Quasar group and its current and past members: Alexandra Alexandrova, Samantha Colosimo, Thomas Primidis, Maxine Sharples, Ricardo Torres, Vasilis Tzoganis, Alexandra Welsch, Joe Wolfenden and Hao Zhang, to cite but a few. Thank you Louis Bizet, Alisa Healy, Tom Pacey, Taaj Sian. Thank you to those I must have forgotten.

Merci à mes amis, Nour Cherkaoui, Sára Horváthy, Rémi Lucas, Ode Mekki, Ismaïl Mourtada, Léo Wojszvzyk et le groupe HX2: après les dures années, j'espère vous avoir dans les plus belles! Merci à mes professeurs de prépa, pour avoir cru en nous quand on n'y croyait pas nous-mêmes: Julien Cubizolles, Alain Lumediluna, Jean-Pierre Roudneff, Nicolas Tozel, pour n'en citer quelques-uns. Mes remerciements à Catherine Nguyen, Joséphine Morizet, Claire Li, pour le soutien post-ingénierie. Merci à Inès Ghorbel et la Team SiPho. Un merci tout en musique pour Pierre-Alexis Touzeau et Julien Hanck, qui m'ont accueillie dans leurs explorations orchestrales. Merci à Natacha Broye, Pierrick Fromentin pour leur présence indéfectible à travers les décennies.

Mes derniers remerciements iront à ma famille. Merci à ma douce maman, pour son épaule et son amour sans faille. Merci à mon frère, à ma grand-mère, à mes tantes et tonton et cousin-e-s, pour leurs messages et leurs pensées. Merci à tout mon entourage, présent ou non. Enfin, merci à mon amour, d'avoir supporté les pluies anglaises, essuyé quelques larmes et amplifié les rires, jusqu'à cette ligne d'arrivée.

# Chapter 1

# Introduction to fourth-generation storage ring light sources

This chapter gives a brief introduction to some basic notions of accelerators, and outlines some of the advancements that led to nowadays synchrotron light sources. Since the discovery of synchrotron radiation in 1947 and the first dedicated facilities, storage-ring-based light sources led to numerous discoveries and participated in the further advancement of sciences. To match the needs of their researches, they evolved drastically, increasing both their energies and their brilliance. Today, the new challenge is the extremely brilliant sources, increasing the photon brilliance by at least a factor 100. To achieve such a high photon quality, improvements are to be made at each level of the synchrotron accelerator technology.

The scope of this thesis is the study, characterisation and optimisation of ultra-low emittance lattices. Such designs will be discussed in Chapter 2. Practical examples are conducted on the SOLEIL storage ring within the parameters of its upgrade project. A presentation of the synchrotron SOLEIL and its current characteristics is conducted at the end of the present chapter.

## 1.1 Towards ring-based light sources

To design electron light sources, one should understand the different means to control the trajectory of a charged particle. This section introduces the main elements required to understand the scope of this thesis. First, the motion of a charged particle in an electromagnetic field is described. This allows the introduction of the different types of electromagnetic elements which constitute the building blocks of a storage ring.

### 1.1.1 Motion of charged particles

The trajectory of electrically charged particles can be modified and controlled with electromagnetic (EM) fields. Their motion is entirely defined by the effect of the Lorentz force:

$$\mathbf{F}_L = q\left(\mathbf{E} + \mathbf{v} \times \mathbf{B}\right) = \frac{d\mathbf{p}}{dt} \tag{1.1}$$

where $\mathbf{p}$[eV/c]= $\gamma_L m \mathbf{v}$ is the particle momentum, $q$[C] the charge of the particle, $\mathbf{B}$[T] and $\mathbf{E}$[V.m$^{-1}$] the magnetic and electric fields respectively, and $\mathbf{v}$ [m.s$^{-1}$] the velocity of the particle. In high-energy machines, $v = \beta_L c \lesssim c$, where $\gamma_L$[n.d.]= $\frac{E}{E_0} = \frac{1}{\sqrt{1-\beta_L^2}}$ is the relativistic Lorentz factor, $E = E_0 + E_k$ the total energy of the particles with $E_0$ the rest mass energy and $E_k$ the kinetic energy. The factor $\beta_L$ is the ratio between the relative velocity $v$ of a particle and $c$[m.s$^{-1}$] the speed of light.

In synchrotron light sources, the kinetic energy of particles is much higher than their rest energy: the particles can therefore be considered highly relativistic. For instance, the SOLEIL storage ring has a working energy of 2.75 GeV, corresponding to a Lorentz factor $\gamma_L = 5382$, thus $\beta_L = 0.9999999825$. The total energy of the highly-relativistic particle is expressed as:

$$E = \gamma_L m_0 c^2 \tag{1.2}$$

with $E$[eV] the energy of the particle, $\gamma_L$[n.d.] the Lorentz factor, $m_0$[kg] the particle rest mass, and $c$[m.s$^{-1}$] the speed of light.

**Beam deflection** The magnetic force $\mathbf{F}_B = q\mathbf{v} \times \mathbf{B}$ is perpendicular to both the velocity and the magnetic field: a charged particle under a constant magnetic field moves along a circular arc. The resulting bending radius depends on the magnetic field, the momentum of the particle and its charge, according to:

$$B_0\rho = \frac{p}{q} \tag{1.3}$$

where $\rho$[m] is the bending radius, $\mathbf{p}$[eV/c] the particle momentum and $q$[C] its charge. The product $B_0\rho$[T.m] is referred to as the beam rigidity. For electrons, this equation practically becomes $B\rho$ [T.m] $= 3.3356\, p$ [GeV.c$^{-1}$]. The beam rigidity is a constant of the motion, provided no energy loss is taken into considerations. In high-energy storage rings, synchrotron radiation (*cf* 1.2.3) is the cause of energy losses, which are compensated each turn: the beam rigidity can therefore be considered constant.

**Acceleration of a charged particle** In the event of an electric field, the charged particle experiences an electric force $\mathbf{F} = q\mathbf{E}$. Depending on the direction of the electric field, the force will either accelerate (if $\mathbf{E} \times \mathbf{v} = \|vE\|\,\mathbf{z}$) or decelerate the particle (if $\mathbf{E} \times \mathbf{v} = -\|vE\|\,\mathbf{z}$). Third generation storage ring lattices use Radio-Frequency (RF) cavities which provide a time-varying accelerating field to restore the energy of the electrons. Further details on this type of acceleration, among others, can be found in Appendix A.

### 1.1.2 Towards synchrotron accelerators

This section describes two main principle which led to the development of first synchrotrons: phase stability and weak focusing.

#### 1.1.2.1 Phase stability

The principle of phase stability, first described independently by E. Mc Millan [1] and V. Veksler [2] in 1944, synchronises the RF frequency with the cyclotron frequency in circular accelerator. In one period of RF oscillation, the accelerating field passes twice through the value of appropriate acceleration: at the synchronous phase $\phi_s$ and at its symmetric phase $\pi - \phi_s$. They are the fixed points of the acceleration.

**Around the synchronous phase $\phi_s$** If a particle arrives at a phase $\phi < \phi_s$ displayed in red in Fig. 1.1, the corresponding accelerating field will be lower than that of the reference particle: the corresponding particle will be less accelerated and will eventually arrive later at a following acceleration period, with a higher phase $\phi > \phi_s$, in green in Fig. 1.1. There, it will experience a higher acceleration than the synchronous particle, and will eventually arrive in advance in the following acceleration span, with a phase $\phi < \phi_s$. The phase of non-synchronous particles oscillates around the synchronous phase during the acceleration process. Furthermore, the particles regroup in bunches around the synchronous particle. This principle is the phase stability, illustrated in Fig. 1.1.

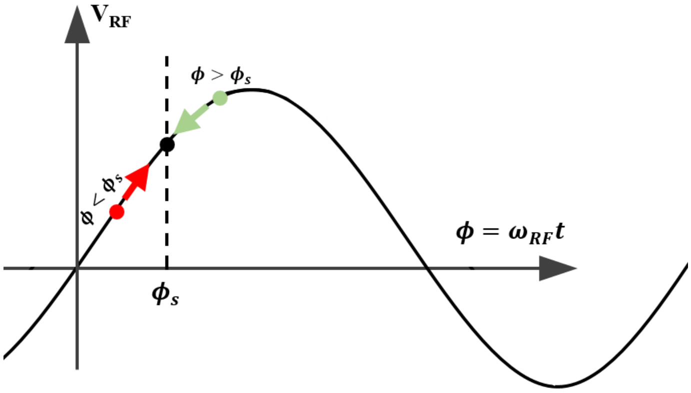

Figure 1.1: Illustration of the phase stability principle.

This principle was described independently by E. Mc Millan [1] and V. Veksler [2] in 1944: it can be applied to maintain stable orbits by phase-focusing the particles in a periodic accelerator. Proof of principle was conducted on synchrocyclotrons, described in Appendix A.

**Around the unstable point ($\pi - \phi_s$)** The negative slope, on the contrary, pushes away the particles from the fixed point $\pi - \phi_s$. Indeed, a particle of phase $\frac{\pi}{2} < \phi_1 < \pi - \phi_s$ receives a higher energy gain than the particle at $\pi - \phi_s$. It will arrive even earlier at the next acceleration period, with a lower phase $\phi_2 < \phi_1$. Symmetrically, a particle of phase $\pi - \phi_s < \phi_3 < \pi$ receives a lower energy gain than the synchronous particle. It will arrive later at the next acceleration period, with a higher phase $\phi_4 > \phi_3$. The motion is unstable around the phase $\pi - \phi_s$. Further explanations and illustrations are available in Chapter 5.

#### 1.1.2.2 Weak-focusing synchrotrons

In cyclotrons and synchrocyclotrons described in the Appendix A, particles are enclosed in a bulk accelerator, and reach a maximum accelerated energy. To reach higher energies, particles are enclosed in larger defined paths: the bending forces are distributed in a circular trajectory, creating a synchrotron. The defined path is a closed trajectory for the particle around the ring: it is called the design closed orbit, or design orbit. The position of a particle along its orbit is denoted by the longitudinal coordinate $s$[m], as depicted in Fig. 1.3. The length of the design closed orbit is noted $C_0$.

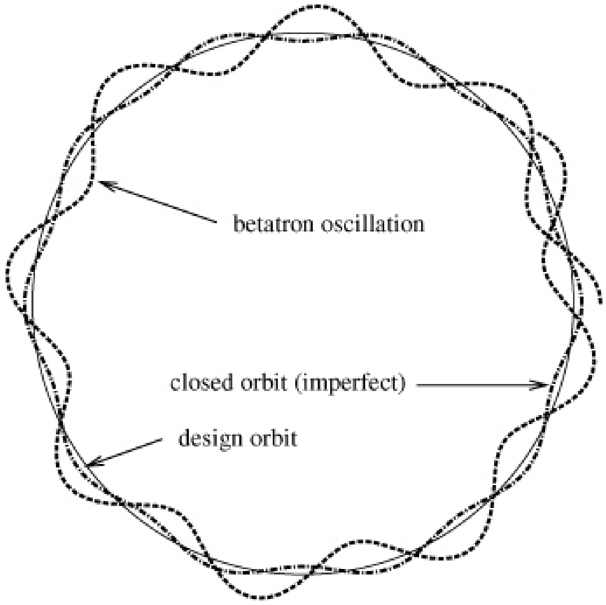

FIGURE 1.2: Illustration of betatron oscillations around the design orbit. From [3].

The transverse motion of the particles is described by $\frac{d\mathbf{v}}{dt} = q\mathbf{v} \times \mathbf{B}$. The motion remains stable if small variations around the design orbit are compensated by focusing forces, resulting in oscillations: those are called the betatron oscillations. The orbit followed by the oscillating particles is called the closed orbit. Figure 1.2 illustrates such an oscillatory motion. The constant magnetic field which defines the particles design orbit is provided by dipoles, or bending magnets. Their force and gradient are derived in the Appendix B.

**Transverse coordinates** To describe the motion of the particles around their orbit, a curvilinear coordinate system is used and represented in Fig. 1.3. The closed orbit is located by the bending radius $\rho(s)$, at the longitudinal position $s$. At each position $s$[m], the particle's position is defined by a 4D cartesian frame $(x, x' = \frac{dx}{ds}, y, y')$, with

$(x, x')$ the horizontal amplitude and divergence, $(y, y')$ the vertical coordinates. The divergences also corresponds to the variation of the particles momentum with regard to the reference particle : $u' = \frac{\Delta p_u}{p_0}$, with $u \in \{x, y\}$. This 4D vector defines the transverse plane.

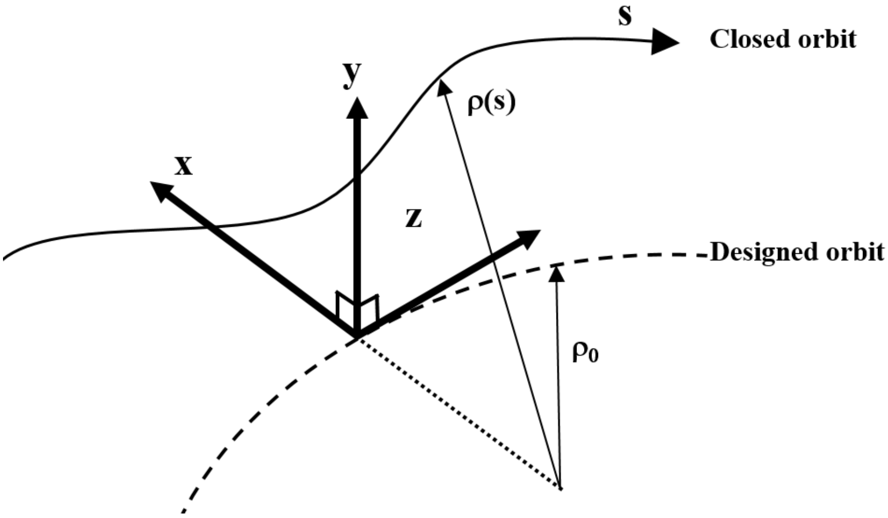

Figure 1.3: Representation of the 6D coordinate system.

**Weak focusing** The betatron oscillations are described by the following transverse equations of motion [4]:

$$\begin{cases} \ddot{x} + (1-n)\omega_0^2 x = 0 \\ \ddot{y} + n\omega_0^2 y = 0 \end{cases} \tag{1.4}$$

with $\omega_0 = \frac{eB_0}{m}$, and $f_0 = \frac{\omega_0}{2\pi}$ the revolution frequency or cyclotron frequency, and $n = \frac{-\rho}{B_0}(\frac{\partial B_z}{\partial r})_{r=\rho}$ is the field index. The motion therefore is stable in the horizontal and vertical planes if and only if the field index verifies: $0 < n < 1$. This is the principle of weak focusing. The transverse motion of the particles is weakly focused by the bending forces, of strength $\frac{1}{\rho^2}$ (*cf* 2.1.1). The first weak focusing synchrotron was the 3 GeV Cosmotron in 1952 at Brookhaven National Laboratory (BNL). A 6 GeV proton synchrotron built at Lawrence Berkeley National Laboratory (LBNL) in 1954, the Bevatron, led to the discovery of antiprotons in 1955 [5].

#### 1.1.2.3 Strong-focusing or alternating gradient principle

Analogically to focused photon beams, a beam of charged particles experiences inherent divergence. In addition, slight differences in momenta induce variations in the perceived bending angles, increasing the diverging effect. Under this effect, the particles move away from the ideal trajectory: if left unattended, particles would be lost turn after turn, as the beam size keeps growing. To keep the particles in the vicinity of the ideal orbit, focusing forces in the transverse plane are required. While weak focusing can be sufficient for small rings, a larger circumference imposes the use of stronger focusing forces.

The alternating-gradient (or strong-focusing) principle was discovered and described by E.D. Courant, H.S. Snyder and M.S. Livingston in 1956. The particles are kept in the vicinity of the design orbit by alternating a focusing force decreasing with radius ( $n \gg 1$) and increasing with radius ($n \ll -1$). This leads to an overall focusing in both planes [6]. Focusing forces require an affine magnetic field, which is achieved by quadrupoles. Their forces and specificities are introduced in the Appendix B. The first strong-focusing 1.2 GeV electron accelerator was built in 1954 at Cornell, USA [7]. In 1959, Centre Européen pour la Recherche Nucléaire (CERN) builds the Proton Synchrotron (PS) at 2.8 GeV nominal energy, and had 6.2 betatron oscillations per revolution. Completed in 1960 in Brookhaven, the Alternating Gradient Synchrotron (AGS) became the highest-energy proton accelerator with a 3.3 GeV nominal energy [8], until 1968.

## 1.2 Properties of synchrotron radiation

A bending force applied on charged relativistic particles yields to the spontaneous emission of photons: this is referred to as ”synchrotron radiation”. It was first observed in 1947 in the General Electric 80 MeV electron synchrotron built in 1946, in Schenectady, New York [9] and was announced in May 1947 [10] as a parasitic effect that damped the beam and induced losses. Following this discovery, electron synchrotrons kept working under this parasitic condition. The first electron synchrotron built for the study of the emitted radiation was built in 1956: it was the Cornell 320 MeV synchrotron. D. Tomboulian and P. Hartman studied the emission, which occurred in the soft X-ray range [11]. Further developments of storage ring were made, to provide the highest quality of photon source in synchrotron light sources and higher energies for colliders. The typical lattice used a FODO cell and achieved emittances of a few hundred nm.rad. The first second-generation radiation source, the 2.5 GeV Synchrotron Radiation Source (SRS); was built in Daresbury and operated from 1981 to 2008 [12].

### 1.2.1 Main properties of synchrotron radiation

When electrons are bent, they radially lose energy in the form of radiation. This phenomenon was first observed on dipoles in 1947, in a 70 MeV synchrotron [10]. In current synchrotron light sources, the particles are highly relativistic. This section gathers the main properties of synchrotron radiation for highly relativistic particles, considering $\beta_L \sim 1$, to highlight its applications. The main parameters of synchrotron radiation, achieved with the use of insertion devices in third generation synchrotrons, are:

- broad spectrum: from the infrared to the hard X-rays, with a tunability of the frequency by the manipulation of the insertion device’s gap.
- high flux: a high intensity photon beam for rapid experiments.

- high brilliance: highly collimated photon beam generated by a small divergence and small size source (spatial coherence);
- high stability: a stable photon source in terms of flux and spectrum, for a high quality experiments.
- polarised photon beam: plane on the electron's orbit and elliptical otherwise;
- pulsed-time structure: the duration of the radiation emission is short, creating a pulse, of length down to tens of picoseconds, ensuring a high time resolution of the experiments.

A detailed explanation of the frequency and energy distribution of the synchrotron radiation is available in Appendix C.

### 1.2.2 Brilliance

The brilliance of the photon beam represents the number of photons per second emitted in a given spatial section $d\Omega dS$ and in a given bandwidth $(d\lambda/\lambda)$. It is an indicator of the beam optical quality. The brilliance is expressed as:

$$B = \frac{d^4N[\text{photons}]}{dt[\text{s}]d\Omega[\text{mrad}^2]dS[\text{mm}^2](d\lambda/\lambda)[0.1\ \%\ \text{bandwidth}]} \tag{1.5}$$

with $N$ the photon flux, $\Omega$ the solid angle, $S$ the cross section, $(d\lambda/\lambda)$ the wavelength bandwidth. A high brilliance is therefore achieved with a photon beam of high density, with both a high number of photons $N$ and small sizes to minimise $d\Omega dS$. Neglecting diffraction, the product of the solid angle and the spot size $d\Omega dS$ is proportional to the product of the electron beam emittances $\epsilon_x\epsilon_y$. Achieving a highly brilliant source by reducing the electron emittances is the goal of the fourth generation storage ring light sources.

### 1.2.3 Radiated power

For highly relativistic particles, the power is emitted radially [13]. Therefore, the total power emitted by a highly relativistic electron beam is, according to the generalisation of Larmor's theorem obtained by Liénard in 1898 [14]:

$$P = \frac{e^2\gamma_L^4}{6\pi\epsilon_0 c}\|(\dot{\beta})^2\| = \frac{e^4}{6\pi\epsilon_0 m_0^4 c^5}E^2B^2 \tag{1.6}$$

with $\dot{\beta} = \frac{\dot{\mathbf{p}}}{\gamma_L m_0 c}$, $e$ the electron charge, $\epsilon_0$ the vacuum permittivity, $m_0$ the electron rest mass, $c$ the speed of light, $\gamma_L$ the Lorentz factor, $E$ the beam energy and $B$ the magnetic field of the bending magnet.

#### 1.2.3.1 Energy loss

The emission of radiation reduces the total energy of the electrons, resulting in an overall loss of energy that has to be compensated for beam storage. Compensation is achieved with the use of RF cavities, re-accelerating the particles. The amount of lost energy depends on the time the electrons spend under the influence of a dipolar magnetic field, i.e. the length of the dipole and the velocity of the electrons: $U_0 = \int_{dipoles} P\,dt = P\frac{2\pi\rho}{c}$. The total energy loss $U_0$ is referred to per turn and per electron, and is expressed as:

$$U_0[\text{keV}] = \frac{e^2\gamma_L^4}{3\epsilon_0\rho} =_{e^-} 8.846\times 10^4\frac{E^4[\text{GeV}]}{\rho[\text{m}]} \tag{1.7}$$

The total energy loss is the sum of Eq. (1.7) over the beam. The number of electrons per beam is defined by the beam current. Therefore, the power radiated by a beam is $P = \frac{e\gamma^4}{3\epsilon_0\rho}I$. The total power radiated by a beam of average current $I$, in a dipole of length $L_{dip}$ is:

$$P[\text{kW}] = \frac{e\gamma^4}{6\pi\epsilon_0\rho^2}L_{dip}I =_{e^-} 14.08\frac{L_{dip}[\text{m}]I[\text{A}]E^4[\text{GeV}]}{\rho^2[\text{m}]} \tag{1.8}$$

#### 1.2.3.2 Radiation damping of the synchrotron motion

Radiation loss has a damping effect on the synchrotron motion, and affects the transverse motion of the electrons. This section introduces the damping process. In a storage ring, where the energy of the particles is kept constant, the energy loss through radiation is exactly compensated by RF cavities. The radiation loss around the synchronous particle is described as: $U = U_0 + \frac{dU}{dE}|_{E=E_0}\Delta E$, where $E_0$ is the synchronous energy. A particle of energy variation $\Delta E$ will complete its revolution before the synchronous particle if $\Delta E < 0$ or after if $\Delta E > 0$, according to the phase stability principle. The relative change in the path length $C$ with energy is:

$$\frac{\Delta C}{C_0} = \alpha_C\frac{\Delta E}{E_0} \tag{1.9}$$

where $C_0$ is the circumference, and $\alpha_C$ the momentum compaction factor (*cf* 2.1.2.4). The difference in arrival time becomes: $\Delta\tau = \alpha_C T_0\frac{\Delta E}{E_0}$. Including the RF compensation, the arrival time $\tau$ verifies the damped harmonic oscillations below:

$$\frac{d^2\tau}{dt^2} + 2\alpha_E\frac{d\tau}{dt} + \omega_s^2\tau = 0 \tag{1.10}$$

with $\alpha_E = \frac{\frac{dU}{dE}|_{E=E_0}}{2T_0}$ is the damping coefficient, $T_0$[s] the revolution period and $\omega_s$ the synchrotron frequency. The damping coefficient depends on the variation of the radiated energy with the energy of the particle, $\frac{dU}{dE}|_{E=E_0} = U_0(2+\mathcal{D})$, where $\mathcal{D}$ is the damping partition, and depends entirely on the dipoles (*cf* Eq. (2.24)).

## 1.3 Third-generation synchrotron light sources

Third-generation synchrotron light sources were optimised for higher brilliance (*cf* 1.2.2). The use of Chasman-Green lattices and Triple Bend Achromats (*cf* 2.2.2) reduced the emittance down to a few nm.rad, and the inclusion of insertion devices (*cf* 1.3.1) optimised the brilliance of the photon source. Among them, the European Synchrotron Radiation Facility (ESRF) in France, operating at 6 GeV was built in 1992, the 7 GeV Advanced Photon Source (APS) at Argonne National Laboratory in 1996, the Swiss Light Source (SLS) at 2.4 GeV in 2000. Third-generation synchrotrons are still in operation, and are developing methods to improve the brilliance of their future machines, creating a fourth generation of storage-ring-based light sources (*cf* 1.4).

Third-generation synchrotron light sources, currently in operation worldwide, provide a high-brilliant photon beam to $\simeq$ 4800 users per year in Europe alone [15]. The high brilliance is ensured by a reduction of the electron emittances with the use of Chasman-Green or Triple Bend Achromat lattices (*cf* 2.2.2), with horizontal emittances reduced to a few nm.rad. The use of insertion devices, described in the following section, optimises the brilliance of the photon source, by reducing the photon bandwidth and forcing the generation of a greater number of photons. This section describes the characteristics of the radiation emitted by insertion devices. The typical layout of a third-generation will be described, and the current storage ring light sources worldwide will be shortly introduced.

### 1.3.1 Insertion devices for high brilliance

Current synchrotron light sources are highly-brilliant photon sources thanks to the use of undulators and wigglers: they are generally defined as insertion devices, and are used to provoke and enhance the synchrotron radiation phenomenon. The principle of the undulator was applied in 1952, and produced coherent infrared radiation [16, 17]. Undulators and wigglers are inserted in the middle of dedicated straight sections in a storage ring, where the waist of the electron beam is the smallest.

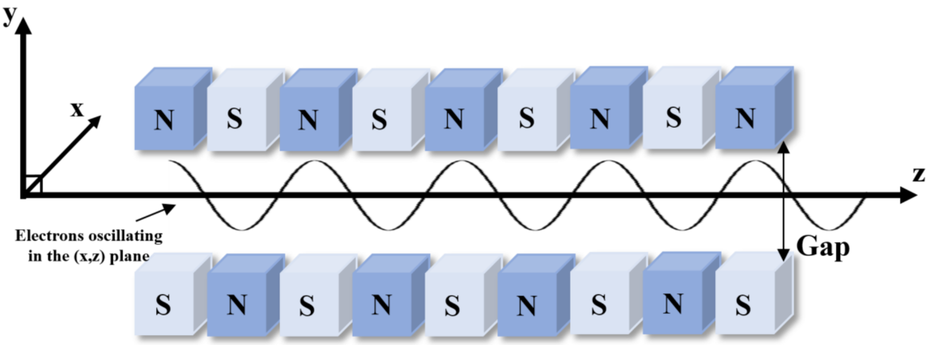

Figure 1.4: Undulator principle and scheme. The polarities of the magnets are noted N and S, for the North and South poles respectively.

Undulators and wigglers are electromagnetic elements, composed of a periodic arrangement of small constant-field dipoles. Figure 1.4 illustrates the magnetic arrangement of such a device. The polarity of the dipoles are alternating, to ensure the creation of a sinusoidal magnetic field in the vertical plane:

$$B_{y,undulator} = B_0 \sin(k_u z) \tag{1.11}$$

with $B_0$ [T] the magnetic amplitude, $k_u\,[\mathrm{m}^{-1}] = \frac{2\pi}{\lambda_u}$ and $\lambda_u$ [m] the period of the undulator. Such an oscillating magnetic field acts upon the electrons through the Lorentz force (*cf* Eq. (1.1)).

An insertion device is characterised by four main parameters: its period $\lambda_u$, which defines the wavelength spectrum of the emitted photons, its gap $2g$, its factor $K_u$ and its length $L_u$. These parameters govern the shape of the emitted radiation, which is detailed in the Appendix D. Different types of insertion devices are implemented in third generation storage rings, to comply with the different requirements of synchrotron radiation users. A brief overview of some insertion devices is given in Appendix E.

**Brilliance of an undulator** The brilliance reached by the radiation from an undulator and a wiggler is of order $10^{18-20}$ photons.s$^{-1}$.mrad$^{-1}$.mA$^{-1}$.(10% bandwidth)$^{-1}$. To compare, the radiation from a dipole is of the order up to $\simeq 10^{15}$. Figure 1.5 illustrates the brilliance of the photon sources of the SOLEIL storage ring, at maximum beam current $I = 500$ mA. For one undulator, the radiation is composed of harmonics of the main wavelength $\lambda_n$, and are therefore displayed in the brilliance graph: the number of harmonics depends on the type of undulator and its $K$ factor. In the higher energies, $K \gtrsim 1$ and more harmonics are emitted.

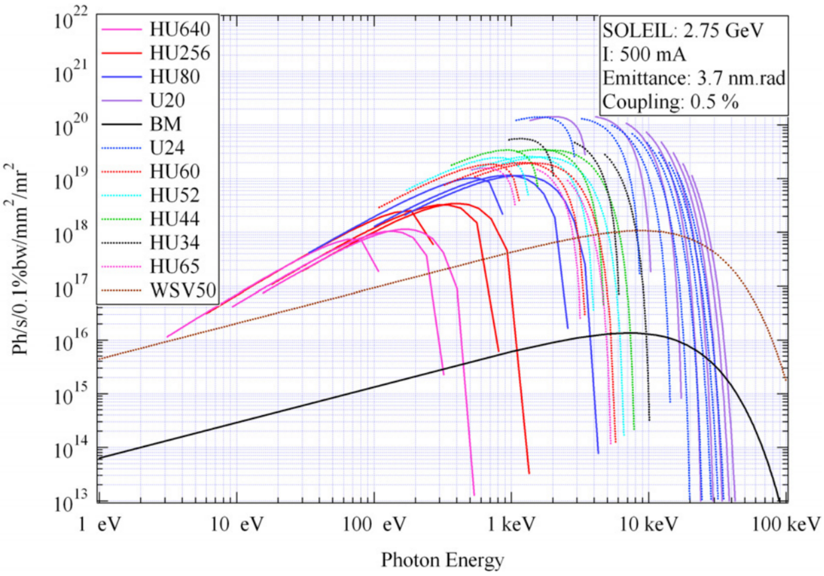

Figure 1.5: Brilliance achieved by the undulators of the SOLEIL storage ring, at the maximum beam current $I = 500$ mA, from [18].

### 1.3.2 Layout of a third-generation synchrotron light source

From the rest energy of charged particles to the working energy of the machine, the particles have to undergo different stages of acceleration. To benefit from the synchrotron radiation and its properties, electrons are stored in a circular accelerator, called a storage ring, at energies of the GeV order. To reach such a high energy range, electrons are accelerated from creation to storage.

A first acceleration occurs in a LINear ACcelerator (linac) where the electrons are accelerated to energies of up to 100 MeV. Acceleration in a linear trajectory is rapidly limited by the length of the accelerator and its electric field. To further accelerate the electrons after the linac, the particles are injected a circular accelerator, a booster. Using RF quadrupoles first developed in 1970 by Kapchinskii and Teplyakov [19], boosters accelerate turn by turn the electrons, up to the nominal storage energy when the particles are then transferred in the storage ring.

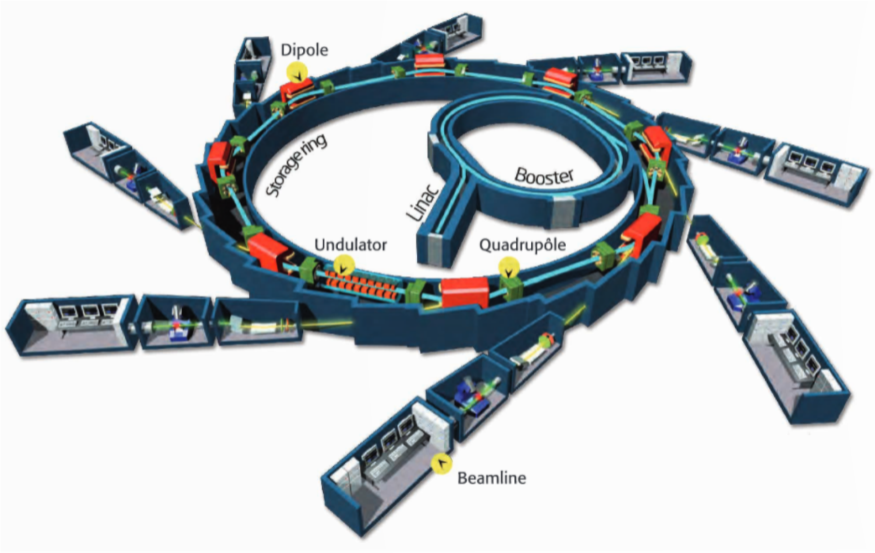

FIGURE 1.6: Overview of a synchrotron light source. From [20].

When the electrons reach the required energy, after a couple of turns in the booster, the electrons are injected in the storage ring where they will radiate synchrotron radiation in undulators and wigglers: the radiated photon beam is sent into dedicated beamlines, where scientists -or users, set their experiments. In a storage ring, the energy loss due to synchrotron radiation (*cf* Eq. (1.7)) is compensated by RF cavities, which accelerate the particles using a time-varying electric field (A.2). Further discussion will be conducted in the chapter 5. Figure 1.6 illustrates the overall layout of a synchrotron light source, along with some elementary magnetic elements: dipoles are represented in red, quadrupoles in green and an undulator is displayed with its corresponding beamline. An optic station collects and shapes the photon beam by collimating, focusing even selecting a required wavelength, using monochromators for instance. The photons then attain the experiment booth, where the samples are. After the experiment booth, the control cabin, where the beamline scientists and their users control the good process of their experiment.

### 1.3.3 Third-generation synchrotron light sources worldwide

Third-generation storage ring light sources are built worldwide. Table 1.1 gathers some parameters of several synchrotrons: their energy, circumference, localisation and date of construction. Their optical lattices configurations are described in Chapter 2.

TABLE 1.1: Third generation synchrotron light sources based on a storage ring, classified by date of construction.

| Name | Energy | Circumference | Date | Localisation |
|---|---|---|---|---|
| ESRF | 6 GeV | 844 m | 1992 | France |
| ALS | 1.5-1.9 GeV | 196.8 m | 1992 | USA |
| TLS | 1.5 GeV | 120 m | 1993 | Taiwan |
| ELETTRA | 2.4 GeV | 259 m | 1994 | Italy |
| PLS | 2 GeV | 281 m | 1994 | South Korea |
| MAX II | 1.5 GeV | 90 m | 1994 | Sweden |
| APS | 7 GeV | 1104 m | 1996 | USA |
| LNLS | 1.35 GeV | 93 m | 1996 | Brazil |
| SPring-8 | 8 GeV | 1434 m | 1997 | Japan |
| BESSY II | 1.9 GeV | 240 m | 1998 | Germany |
| ANKA | 2.5 GeV | 110 m | 2000 | Germany |
| SLS | 2.4 GeV | 288 m | 2000 | Switzerland |
| SPEAR3 | 3 GeV | 234 m | 2004 | USA |
| CLS | 2.9 GeV | 171 m | 2004 | Canada |
| SOLEIL | 2.75 GeV | 354 m | 2006 | France |
| DIAMOND | 3 GeV | 560 m | 2006 | UK |
| AS | 3 GeV | 216 m | 2006 | Australia |
| MAX III | 700 MeV | 36 m | 2006 | Sweden |
| Indus-II | 2.5 GeV | 173 m | 2006 | India |
| SSRF | 3 GeV | 432 m | 2008 | China |
| PETRA-III | 6 GeV | 2300 m | 2009 | Germany |
| ALBA | 3 GeV | 268.8 m | 2011 | Spain |
| SOLARIS | 1.5 GeV | 96 m | 2016 | Poland |
| SESAME | 2.5 GeV | 133 m | 2018 | Jordan |

## 1.4 Future challenges and fourth-generation X-ray sources

To follow the general progress made in sciences, the equipment for dedicated experiment has to improve as well. Therefore, photon sources should improve and provide innovative characteristics to their users: Free Electron Laser (FEL), new undulators, etc. Storage ring light sources still offer a dedicated source of X-ray photons. To match the requirements of future sciences, the brilliance of photon sources should be drastically increased in the X-ray range. Such an ultra-brilliant source requires a complete redesign of its storage ring lattice, to provide an ultra-low emittance electron beam.

This section introduces two X-ray light sources, the X-FEL and the ultimate storage ring light source: the Diffraction Limited Storage Ring (DLSR) and its specifications. While worldwide light sources aim at reaching that ultimate limit, different strategies to approach this goal are briefly discussed here, and will be explained in the next chapter.

### 1.4.1 Diffraction Limited Storage Rings

The minimisation of any photon beam size is limited by its natural diffraction: the minimum size detectable is the Airy disk. For optical detectors, the Airy disk is the best image of a source point a detector can get: therefore, any photon beam below the Airy disk in size can be considered a source point for the detector. The radius of the Airy disk depends on the focal length $f$ of the detector's objective, the diameter $d$ of the entrance pupil, and is proportional to the wavelength according to:

$$R_{Airy} = 1.22\lambda\frac{f}{d} \tag{1.12}$$

In a storage ring, the equivalent can be defined when the photon beam size is limited by its natural diffraction. Such a storage ring is called a Diffraction Limited Storage Ring (DLSR) [21]. The photon beam size is expressed as:

$$\begin{cases} \sigma_{ph} = \sqrt{\sigma_x^2 + \sigma_{ph,e}^2} \\ \sigma'_{ph} = \sqrt{\sigma_{x'}^2 + \sigma'^2_{ph,e}} \end{cases} \tag{1.13}$$

where $\sigma_x = \sqrt{\epsilon_x\beta_x + (D_x\sigma_e)^2)}$ and $\sigma'_x = \sqrt{\frac{\epsilon_x}{\beta_x} + (D'_x\sigma_e)^2)}$ are the electron beam size and divergence respectively, $\sigma_{ph,e}$ and $\sigma'_{ph,e}$ the natural photon beam size and divergence. The impact of the energy spread $\sigma_e$ of the electron beam can be set to zero at the interesting point by creating a dispersion-free zone: $D_x = 0$ m and $D'_x = 0$ rad. The electron beam size is then only defined by the $\beta$-function at the insertion device and its emittances. A detailed introduction to the Twiss functions is conducted in Chapter 2.

The radiation extracted from an undulator can be fitted with a Gaussian mode. The photon beam size and divergence limited by the diffraction are then extracted and given by the product:

$$\sigma_{ph}\sigma'_{ph} \simeq \frac{\lambda}{4\pi} \tag{1.14}$$

#### 1.4.1.1 Emittance of a DLSR

The diffraction-limited photon emittance $\epsilon_{ph}$ therefore is $\epsilon_{ph} = \frac{\lambda}{4\pi}$, i.e. no further reduction of the photon beam size can be achieved. This condition translates in the electron emittances:

$$\epsilon_{x,y} \ll \epsilon_{ph}(\lambda) = \frac{1}{2}\sigma_{ph}\sigma'_{ph} = \frac{\lambda}{4\pi} \tag{1.15}$$

where $\epsilon_{x,y}$ are the emittances of the transverse plane, $\epsilon_{ph}$ the emittance of the photon beam and $\lambda$[m] the main wavelength of the emitted radiation. The condition is wavelength-dependent, and is achieved for high wavelength in current third generation storage rings. For a valid condition in the whole emission spectrum, especially in the X-ray range, it should be valid in high energies: hard X-rays, around 1 nm. For such a wavelength, the required photon emittance is 0.16 pm.rad. The related brilliance now reads $B = \frac{\text{flux}}{\frac{\lambda^2}{4}}$.

#### 1.4.1.2 Beam matching

To benefit from the ideal brightness, the electron transverse emittances have to be reduced. Nonetheless, the resulting photon beam could, in the case of poor matching, have greater dimensions than the diffraction limit. This condition is illustrated in Fig. 1.7. If an electron beam has a large horizontal amplitude, but a small divergence (left on the figure), the combination of the electron sizes with the diffraction limit will create a large photon beam. On the contrary, if the amplitude and divergence of the electron beam match the diffraction limit dimensions (right on the figure), the photon beam will be closer to the diffraction limit [22].

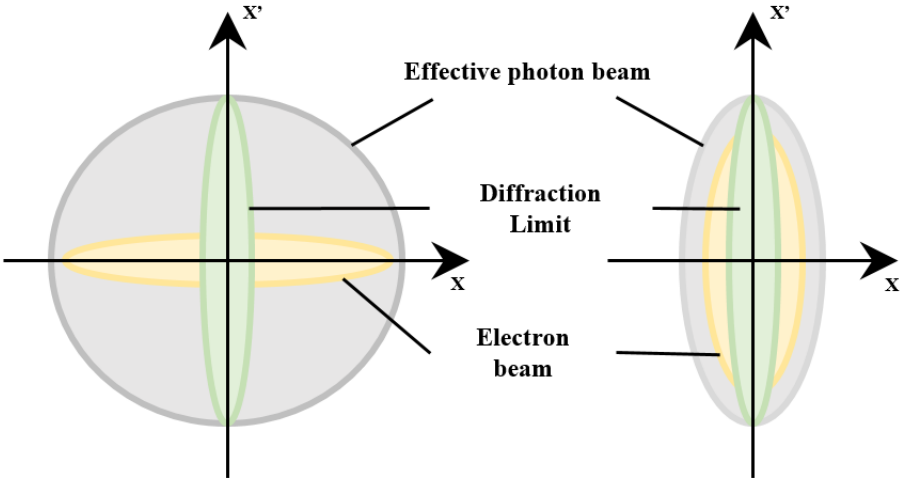

FIGURE 1.7: Matching of the electron and photon beams for optimised brilliance.

Further focusing of the beam may be necessary to reduce the amplitudes. Nonetheless, too strong a focusing will yield to the opposite situation: a large divergence and a small amplitude, with the same consequences on the photon beam dimensions. The optimum focusing is reached when the area $\sigma_{ph}\sigma'_{ph}$ is minimum, i.e. for:

$$\frac{\sigma_{ph}(\lambda)}{\sigma'_{ph}(\lambda)} = \frac{\sigma_{x,y}(e-)}{\sigma'_{x,y}(e-)} \Rightarrow \beta_{x,y} = \frac{L}{\pi} \tag{1.16}$$

where $L$ is the length of the insertion device. For an undulator of 4 m, the required $\beta$-functions are as low as 1.27 m. This equation can be found as equal to $\frac{L}{2\pi}$, like in [23] where is plotted the variation of the relative brilliance with the horizontal $\beta$-function, in the case of a local ultra-low emittance. Their result is displayed in Fig. 1.8.

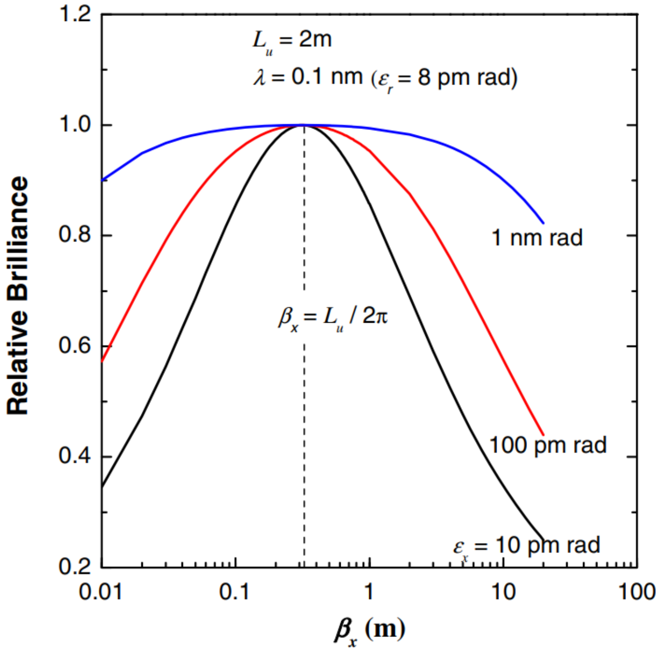

FIGURE 1.8: Variation of the relative brilliance with the horizontal $\beta$-function, in the case of ultra-low emittance, from [23].

In the ultra-low emittance case, the dependence of the brilliance with the $\beta$-function is more pronounced, as it is the limiting factor of the photon beam size: in the case of fourth generation storage rings, where emittances are of the order of 100 pm.rad, the dependence of the brilliance with the $\beta$-function is smoother around the extrema $\frac{L}{2\pi}$: to achieve at least 90% of the maximum brilliance, the required values are in the range $\beta \in \simeq [0.1; 3]$ m for a 3 m long undulator. This range is reduced to $\simeq [0.2; 2]$ m for 95% of the maximum brilliance, which is still large enough to provide some freedom in the lattice design. Fourth generation storage ring ought to include the optimum $\beta$-functions in the middle of their straight sections to benefit from the highest brilliance achievable.

#### 1.4.1.3 Spatial and temporal coherences

The photons emitted by a laser, using the stimulated emission principle, are 100% correlated: their phase difference is constant, and they hold the same information. This property is called coherence: it describes the correlation between the different characteristics of a photon beam. In the case of synchrotron radiation, two types of coherence are distinguished: temporal coherence and spatial coherence.

Temporal coherence occurs when the radiation of an electron bunch is emitted at about the same phase: it requires small bunches, of typical length of the order of the radiation wavelength. Spatial coherence naturally occurs in spontaneous and stimulated emission modes. For larger bunches, the spatial coherence depends on the electron beam sizes and the wavelength:

$$f_{coh}(\lambda) = \frac{\frac{\lambda}{4\pi}}{(\epsilon_x(e-) \oplus \epsilon_r(\lambda))} \times \frac{\frac{\lambda}{4\pi}}{(\epsilon_y(e-) \oplus \epsilon_r(\lambda))} \tag{1.17}$$

Ultra-low emittance lattices will highly increase the spatial and temporal coherences of the emitted synchrotron radiation. For instance, with a reduced level of dispersion and momentum compaction factor, the natural electron bunch length of the studied ultra-emittance lattices for the upgrade of SOLEIL is around 0.5 mm, instead of 2 mm for the current lattice. Similarly, the reduction of the natural horizontal emittance from 4 nm.rad down to 100 pm.rad increases the spatial coherence by at least a factor 40 × 40 in both transverse emittances, assuming an identical coupling factor between the horizontal and the vertical plane. Discussions occur among the French beamline community on whether they need a larger spatial or temporal coherence, or both for their upgraded studies [24].

### 1.4.2 X-ray Free Electron Lasers

Another type of light sources emerges: the Free Electron Lasers, dedicated to the generation of hard X-rays. They are three worldwide: the SACLA XFEL (250 MeV) [25] which was a proof of principle and is not currently in operation, the Linear Coherent Light Source (LCLS) in the USA, which prepares an upgrade including a 4 GeV linac [26], and the European XFEL of 17.5 GeV electron beam [27].

In the case of the European XFEL, the electrons are accelerated linearly using supraconductive cavities over a couple of kilometres, to reach 17.5 GeV. The photon beam is then generated by undulators, which gaps and periodicity allow a tunability of the photon beam wavelength within, with the example fo the European XFEL, [0.05:0.4] and [0.4 to 4.7] nm, of the order of an Ångström, complementing the photon range of synchrotron-based light sources which reach a X-ray wavelength of 0.1 nm for a 8 GeV storage ring.

The FELs create a highly collimated electron beam, with 100% coherence and very short pulses, of femtosecond duration, compared to about 10 ps in the case of SOLEIL. FELs provide a high number of pulses to their users: 120 pulses per second in the case of the LCLS, which upgrade will provide a repetition rate of a million pulses per second. Furthermore, with the high energy of the electrons, the photon flux generated by the undulator exceeds the flux obtained with a synchrotron source, resulting in an averaged brilliance as high as $10^{25}$ photons.$\text{s}^{-1}$.$\text{mrad}^{-1}$.$\text{mA}^{-1}$.$(10\%\ \text{bandwidth})^{-1}$, thus $10^5$ times higher than third-generation storage ring light sources.

### 1.4.3 Ultra-low emittance lattices

From FODO lattices to Chasman-Green lattices and even Triple Bend Achromats, third-generation storage ring light sources improved their emittance by a factor 100. Pursuing the increase in dipole magnets for reduction of creation of emittance, upgrade designs use Multi-Bend Achromat lattices. Discussion and details are provided in 2.2.3. Figure 1.9 compares the natural horizontal emittance normalised with energy for the third-generation storage rings and their first upgrade considerations. First developments decreased the electron beam emittance by at least a factor 50.

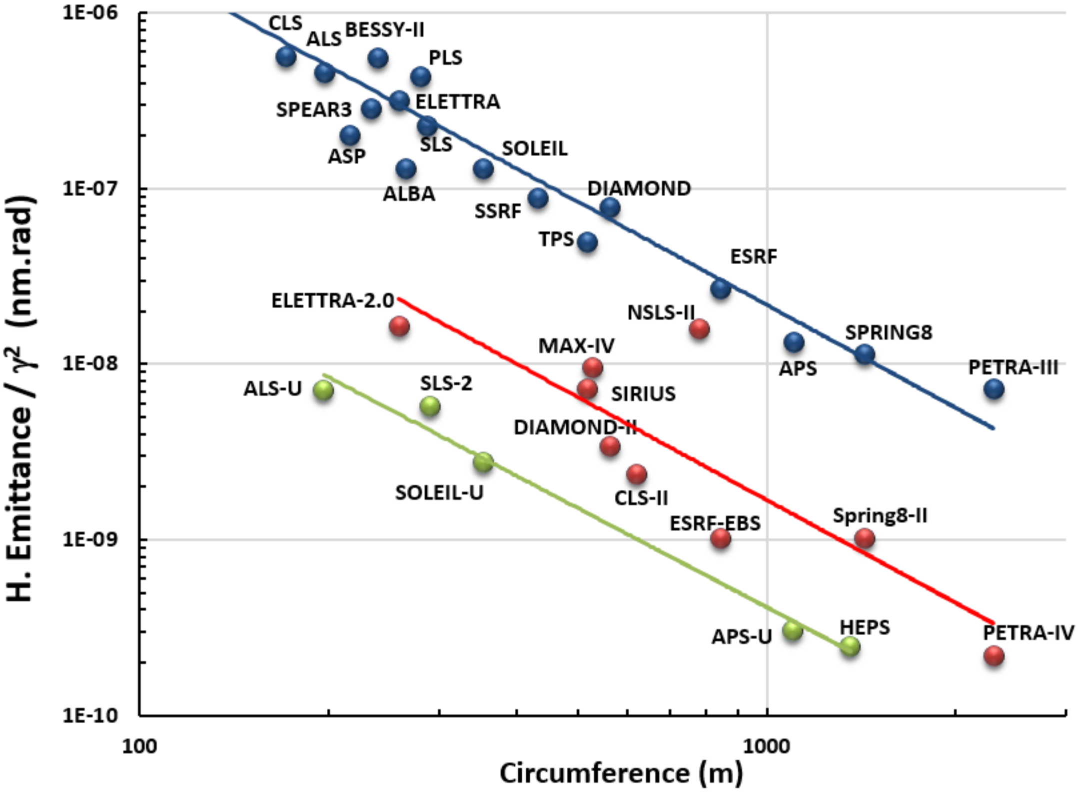

Figure 1.9: Evolution of the normalised emittance with the circumference for third-generation storage rings (blue fit) and fourth-generation storage rings (red and green fits), adapted from R. Bartolini [28].

### 1.4.4 Challenges

Achieving ultra-low emittance in a storage ring presents certain challenges for their operation [29] and the maintenance of their performances. Indeed, the ultra-low emittance requires a strong control of the electron beam sizes, *i.e.* the low dispersion and strong focusing, resulting in high-gradient magnets. This will be discussed in the next chapter, in 2.2. Since the majority of upgrade projects conserves the circumference of their current machine, the magnet occupation of the lattice increases, and the tight optics limit the lengths of corrective magnets; the lattice becomes very sensitive to magnetic and alignment errors [30].

#### 1.4.4.1 Magnets

The strong-focusing and tight MBA lattices require the design of strong-gradient and small magnets [31], with a high field quality to reduce their errors [32]. The magnetic gradients are on the verge of the magnetic saturation of quadrupole and sextupole electromagnets, reaching 100 T.m$^{-1}$ and around 10.000 T.m$^{-2}$ respectively, in some cases [33]. To achieve such high gradients, the reduction of the inner gap of such magnets is inevitable. Yet, this reduction enters in disagreement with vacuum requirements, where the chamber cross section should be large enough to provide a high vacuum conductance. Indeed, smaller gap increases impedance effects and particle loss increases in smaller gaps.

The use of permanent magnets is considered for higher gradients, especially for sextupoles [34]: yet, the problem of achieving the first turn of the rings with the presence of high-gradient permanent sextupoles remains under discussion. Furthermore, the increased number of magnets per period in ultra-low emittance lattices reduces the allocated space for additional corrective magnets. Ultra-low emittance designs generally include combined-function magnets, as well as novel magnets, to release those constraints. Further discussion is conducted in the next chapter 2.2.4.

#### 1.4.4.2 Vacuum

A minimum inner gap for high gradient magnets is only achievable with small-radius vacuum chamber. A compromise has to be found between the vacuum properties, for which larger chambers ensure a higher quality, and the gap reduction for strong gradients.

Coating the chambers allows the reduction of the photon-stimulated desorption effect and increase the pumping efficiency. Non-evaporable getter (NEG) coating is already extensively used in low-gap insertion devices in third-generation storage rings, and more than fifty percent of SOLEIL chambers are NEG-coated [35]. As a result, a large majority of MAX-IV vacuum chambers are NEG-coated, but not on the RF cavities and other magnets [36, 37]. Also, since the electron beam will be reduced in size and is much more sensitive to any interaction, the coating of the vacuum is in discussion to limit the interaction of the beam with its environment [38].

#### 1.4.4.3 Injection

Low emittance and strong focusing lead to low $\beta$-functions in the straight sections, and a considerably reduced transverse dynamic aperture: nevertheless, current transverse off-axis injection needs a larger dynamic aperture, which can be provided by local high $\beta$-functions. Yet, the reduction of symmetry shall affect the overall performances of the lattice 2.1.3. Transverse on-axis injection as well as longitudinal on-axis injection are being studied[39]. A swap-out method using an intermediate accumulator ring is also developed [40]. They will be detailed in Chapter 4.

#### 1.4.4.4 Insertion devices and beamlines

With a reduction of an averaged factor 50 of the electron beam emittances, the optics of the beamlines, as well as their insertion devices, will have to be improved to maximise the benefits of such a brilliant photon beam. Indeed, the smaller photon beam will be, the more sensitive shall be the beamlines to optical errors, and more subject to defocalisation and diffraction. Beamlines organise their own workshops to prepare for the upgrade light sources.

#### 1.4.4.5 Alignment and magnet errors

The fourth-generation storage ring lattices are more sensitive to magnets errors and alignment errors. The new storage rings will require faster and more precise systems, to align the lattice. For instance, the ESRF had alignment tolerances of the order of 50 $\mu$m for their magnets. The use of girders, where several magnetic elements are placed onto, drastically reduces the risk of alignment errors [41]. Novel techniques are being developed to compute with the tight tolerances of the $4^{\text{th}}$ generation storage ring lattices [30]. Correction of errors and feedback, such as beam-based alignment and fast-orbit correction, need to be more precise and more effective.

#### 1.4.4.6 Numerical tools for lattice optimisation

The foreseen ultra-low emittance lattices have a considerably reduced transverse and energy acceptance because of the strong nonlinearities excited by quadrupoles and sextupoles. Optimising such lattices for improved performances will demand managing dozens of variables and objectives at the same time. To do so, genetic algorithm and machine learning techniques are used [42–44].

## 1.5 Case of the upgrade of the synchrotron SOLEIL's storage ring

### 1.5.1 The SOLEIL synchrotron

SOLEIL, an acronym for ”Source Optimisée de Lumiére à Énergie Intermédiaire de Lure” (Optimised Light Source of Intermediate Energy to LURE), is the French national third-generation storage-ring-based synchrotron light source. Located on the Plateau de Saclay (Essonne), SOLEIL is a private company created on October $16^{\text{th}}$ 2001 by both Commissariat à l'Énergie atomique et aux Énergies Alternatives (CEA) and the Centre National de la Recherche Scientifique (CNRS), and is based on public fundings. It delivers synchrotron radiation from the infrared to the hard X-rays to a various span of users since January 2008. SOLEIL is composed of three distinct accelerators: a 16 m-linac, which accelerates the electrons from the electron gun to 100 MeV. The electron beam is then transferred in the booster, to be accelerated to the nominal energy 2.75 GeV, when they are injected in the 354 m storage ring.

### 1.5.2 The current storage ring

The SOLEIL 2.75 GeV storage ring is composed of 16 cells, arranged into 4 superperiods. Figure 1.10 displays the $\beta$-functions and the dispersion of a superperiod. On the figure is also displayed the magnetic lattice: in blue are the dipoles, red the quadrupoles. Sextupoles are simulated as thin lenses, and are displayed as black bars.

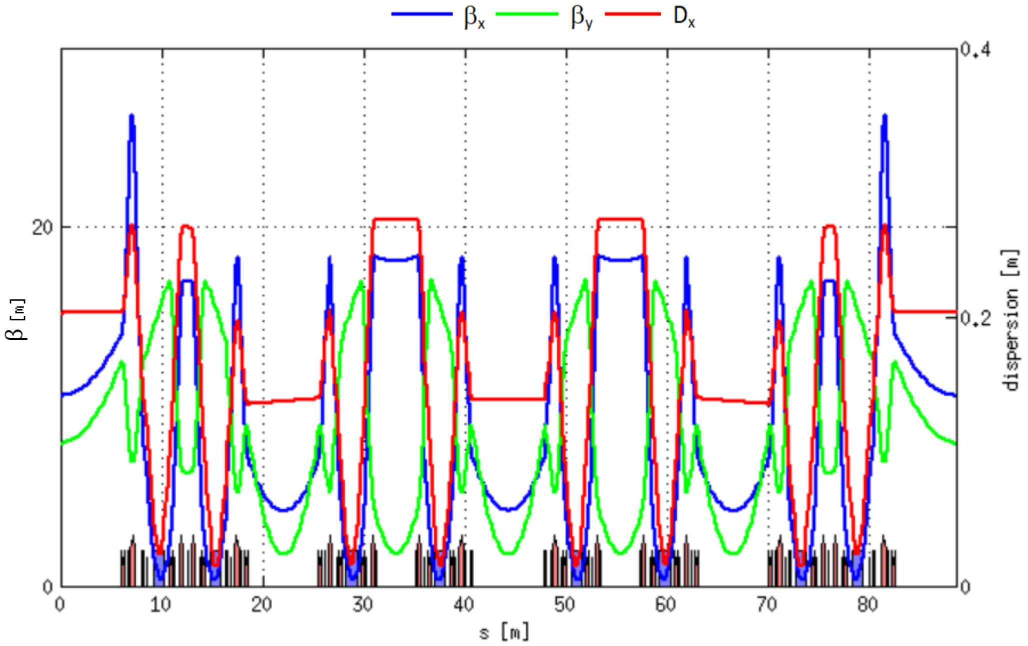

FIGURE 1.10: Twiss parameters and magnet layout of one superperiod of the SOLEIL 2.75 GeV storage ring.

Each cell is based on a Modified Double Bend Achromat (m-DBA) or a modified Chasman-Green lattice (*cf* 2.2.2): the dispersion is non zero in the straight sections. Accommodating for the different needs of the beamlines, SOLEIL has three types of straight sections: four of 12 m, twelve of 7 m and eight of 3.6 m. A total of 24 straight sections corresponds to 46% of the ring circumference: 21 of them are dedicated to insertion devices, 2 for RF cavities and one for the injection. Table 1.2 gathers general parameters of the current storage ring [45].

The natural horizontal emittance of the storage ring is 4 nm.rad, decreased to 3.9 nm.rad including the damping effect of wigglers. The vertical emittance is set to 1% of the horizontal emittance, to increase the beam stability.

The energy loss due to the dipoles in the linear lattice amounts to 944 keV. This value increases up to 1149 keV when the gap of the insertion devices are closed, which includes the stimulated synchrotron radiation. Those losses are compensated with four RF cavities, of fixed frequency 352.2 MHz, defined by the revolution frequency according to the synchronism condition defined in Eq. (A.3).

Table 1.2: SOLEIL current 2.75 GeV 4-superperiod storage ring general parameters.

| | |
|---|---|
| Energy | 2.75 GeV |
| Circumference | 354 m |
| Number of cells | 16 |
| Number of superperiods | 4 |
| Number of straight sections | $4 \times 12$ m, $12 \times 7$ m, $8 \times 3.8$ m |
| Straight sections available for insertion | 46% of the total length |
| Horizontal emittance $\epsilon_x$ | 3.9 nm.rad |
| Emittance coupling $\frac{\epsilon_y}{\epsilon_x}$ | 1% |
| Betatron tunes $(\nu_x, \nu_y)$ | (18.17, 10.23) |
| Natural chromaticities $(\xi_{nat_x}, \xi_{nat_y})$ | (-52.55, -21.24) |
| Chromaticities $(\xi_x, \xi_y)$ | (1.4, 2.3) |
| Momentum compaction factor $\alpha_0$ | $4.16 \times 10^{-4}$ |
| Momentum compaction factor $\alpha_1$ | $4.50 \times 10^{-3}$ |
| Energy spread $\sigma_E$ | $1.016 \times 10^{-3}$ |
| Energy loss per turn | 944 keV from the dipoles |
| | 205 keV from the insertions |
| Average pressure | $5 \times 10^{-10}$ mbar |
| Beam lifetime | 12 h |
| Revolution time $T_0$ | 1.18 $\mu$s |
| Revolution frequency $\omega_{syn}$ | 847.2 kHz |
| Harmonic number $h$ | 416 |
| RF voltage | 2.9 MV |
| RF frequency | 352.2 MHz |
| Number of RF cavities | 4 |

### 1.5.3 Beamlines and undulators

The stored electron beam provides synchrotron radiation from the infrared to hard X-rays range, to 29 beamlines, both dipole-based and ID-based. Figure 1.11 locates the beamlines around the storage ring. The beamlines are based on 9 dipoles, 2 wigglers and 18 undulators.

Since January 2012, the straight section SDL13 was modified to insert two insertion devices, for the use of the two 180 m beamlines, ANATOMIX and NANOSCOPIUM. The optics are locally modified to ensure a low beam waist in the middle of each in-vacuum undulator by the inclusion of quadrupoles in the middle of the dedicated straight section. To distinguish the two photon beams, and to allow space for both beamlines, an angle is created between the two undulators. The $\beta$-function of the canted section SDL13 are displayed in Fig. 1.12.

### 1.5.4 Upgrade of the storage ring

The upgrade of the storage ring aims at decreasing the horizontal emittance of the electron beam below < 100 pm.rad, corresponding to a factor 40 to 50, while conserving

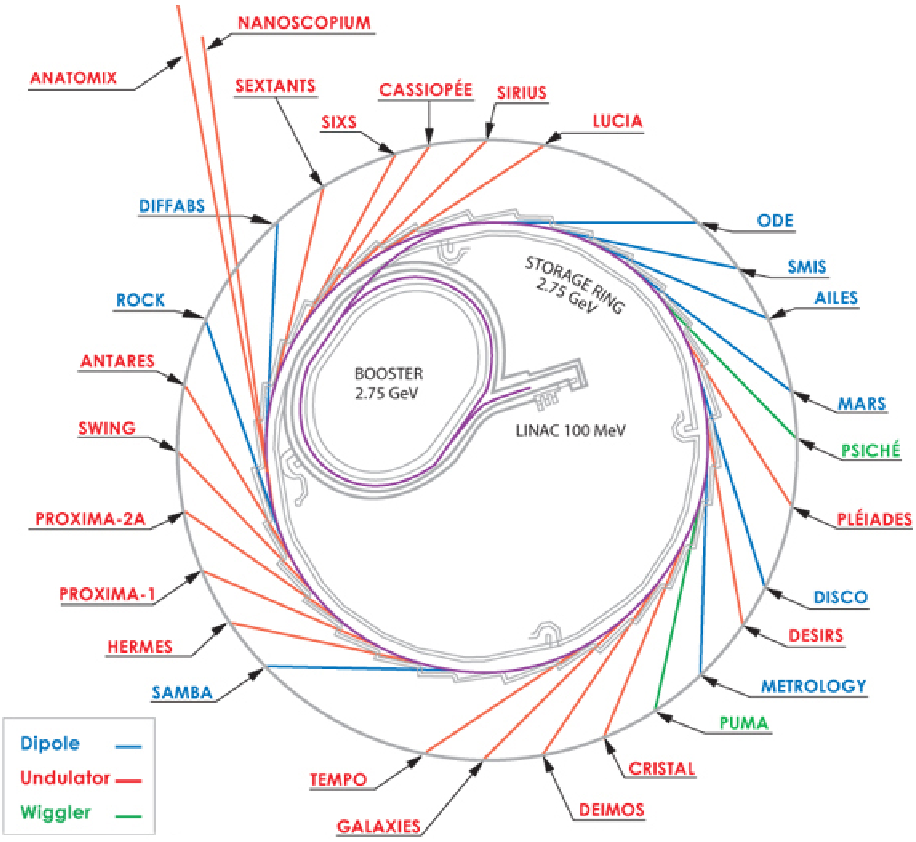

FIGURE 1.11: Map of the 29 beamlines around the SOLEIL 2.75 GeV storage ring. From [46].

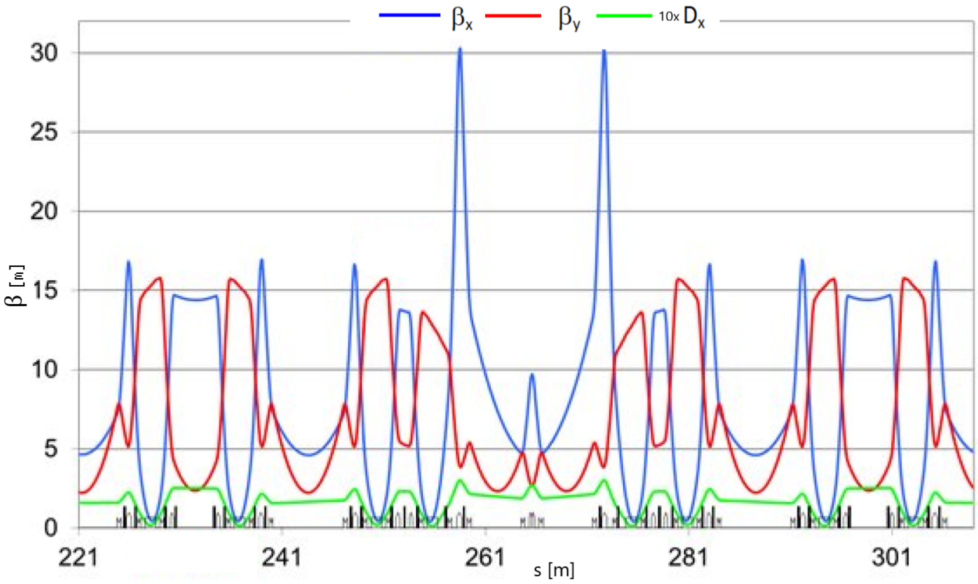

FIGURE 1.12: Canted optics for the two long beamlines, Anatomix and Nanoscopium. Edited from [47].

its main characteristics: its nominal energy should be conserved, to maintain the current energy range of the synchrotron radiation for the beamlines. Furthermore, the new lattice should fit in the current tunnel of the storage ring, fixing its circumference. The upgraded lattice shall provide photon beams of a broad energy range: from the infrared to 30 keV on undulators and 80 keV on wigglers.

TABLE 1.3: General constraints applied to the ultra-low emittance lattice design for the upgrade of the SOLEIL storage ring.

| | |
|---|---|
| Storage ring energy | 2.75 GeV |
| Circumference | 354 m |
| Emittance | $< 100$ pm.rad |
| Straight section length | $> 4.4$ m |
| $(\beta_x, \beta_y)$ @ID | (1-3, 1-3) m |

Further constraints are imposed by the necessary RF cavities and insertion devices in the straight sections. To better fit the electron beam in the insertion devices, the $\beta$-functions should remain low in the middle of the straight sections. Table 1.3 gathers the first constraints of the SOLEIL upgrade project. The storage ring is currently composed of four arcs, of 22.5 degrees deflection angle each. To keep the beamlines parallel and keep their position, the same angle should be implemented in each arc of the upgraded lattice.

## 1.6 Conclusion

This chapter introduced the main historical line of accelerator developments and breakthroughs which permitted the discovery of synchrotron radiation and its exploitation. Synchrotron light sources provide synchrotron radiation worldwide, and are primary photon sources in the hard X-ray range.

To provide a photon beam of higher quality to their users, synchrotrons worldwide are developing their fourth generation storage rings: aiming at a factor of 100 increase in the brilliance, the upgrade projects investigate both lattices and magnet designs to achieve an ultra-low emittance, and approach the diffraction limit. Such designs are introduced in the next chapter, applied to the SOLEIL storage ring and compared.

# Chapter 2

# Lattice design for diffraction-limited storage rings

An extremely brilliant source is achieved with an electron beam of small emittance (1.2.2), which is an intrinsic parameter of the linear lattice. This chapter presents the necessary accelerator physics fundamentals and concepts for the understanding of the subsequent chapters. To go from emittances of the order of 1 nm.rad to less than 100 pm.rad, the linear optics designs have increased the number of dipole magnets. Minimisation of the emittance creation in each magnet can be achieved following the Theoretical Minimum Emittance principle.

Concretely, the following ultra-low emittance lattice schemes are presented: the so-called hybrid lattice, first developed for the ESRF-EBS by P. Raimondi [41] and widely used worldwide, and a High-Order Achromat (HOA) lattice based on the first- and second-order achromat lattices already put in place in several machines, and explored by S. Leeman, A. Streun and J. Bengtsson for ALS-U and SLS-II [48, 49]. Their principles and general characteristics are reviewed, before application on the SOLEIL storage ring. This chapter analyses the advantages and drawbacks of both lattices, in terms of feasibility, robustness and transverse dynamics.

## 2.1 Accelerator physics for electron-based light sources

This section introduces the main elements required to understand the scope of this thesis. The motion of a charged particle in an electromagnetic field has been described in the previous chapter 1.1.1, introducing the different types of electromagnetic elements which constitute the building blocks of a storage ring: the dipoles and the quadrupoles. In this section, the transverse motion of the particles will be described. From the equations of motion, we shall derive and define different specific accelerator notions and characteristics of electron storage rings, that are to be looked for, for the upgraded machines. Unless stated otherwise, the following sections will consider the energy of the particles constant. Expert readers can skip this section and begin at the ultra-low emittance lattices properties in Sec. 2.2, go to the ultra-low emittance schemes studied in this chapter, in Sec. 2.3, or start directly with the designs of such schemes for the SOLEIL storage ring upgrade in Sec. 3.

### 2.1.1 Transverse motion of a charged particle

In an accelerator built solely with dipoles and quadrupoles, the trajectory of the transverse particles is defined by the bending and the focusing forces. This motion of the particles is linear in terms of transverse displacement. It is described by the closed orbit fixed by the dipoles, and the betatron oscillations around that closed orbit (1.1.2.3). The Hill's equations below describe the betatron motion in the transverse plane. Derivation of these equations are largely available in the literature [50].

$$\begin{cases} x'' + K_x(s)x = 0 \\ y'' + K_y(s)y = 0 \end{cases} \tag{2.1}$$

where $K_x = \left(\frac{1}{\rho(s)^2} \pm k_1(s)\right)$, $K_y = \mp k_1(s)$, with an upper sign in the case of a focusing quadrupole, and a lower sign for a defocusing quadrupole, $\rho$[m] the bending radius, $k_1$[m$^{-2}$] the normalised focusing strength, and $s$[m] the longitudinal coordinate. The functions $K_{u\in\{x,y\}}$ are periodic of period $C_0$, the total length of the ideal trajectory. Considering perfect magnetic fields along the ring, the periodic functions $K_{u\in\{x,y\}}$ are piece-wise constant. The solutions of those oscillatory second-order differential equations depend only on the sign of the periodic functions $K_{u\in\{x,y\}}$. The solutions of the Hill's equations for a constant $K_{u\in\{x,y\}}$ are :

$$u(s) = \begin{cases} a\cos(\sqrt{K_u}s + b) & K_u > 0 \\ as + b & K = 0 \\ a\cosh(\sqrt{-K_u}s + b) & K_u < 0 \end{cases} \tag{2.2}$$

with $u \in \{x, y\}$ and $(a, b)$ constants determined by the initial conditions $(u_0, u_0')$. This linear system can be simplified using a matrix description. Since $K_{u\in\{x,y\}}$ remains constant for each element of the lattice, the position $u(s)$ within an element can be entirely determined by its value at the entrance of the element:

$$\begin{pmatrix} u(s) \\ u'(s) \end{pmatrix} = M_{s_0\to s} \begin{pmatrix} u(s_0) \\ u'(s_0) \end{pmatrix} \tag{2.3}$$

$M_{s_0 \to s}$ is called the transfer matrix between the longitudinal positions $s$ and $s_0$. Following are the transfer matrices of linear magnetic elements:

$$M_{s_0\to s} = \begin{cases} \begin{pmatrix} \cos(\sqrt{K}l) & \frac{1}{\sqrt{K}}\sin(\sqrt{K}l) \\ -\sqrt{K}sin(\sqrt{K}l) & \cos(\sqrt{K}l) \end{pmatrix} & K > 0, \text{ foc. quadrupole} \\ \begin{pmatrix} 1 & l \\ 0 & 1 \end{pmatrix} & K = 0, \text{ drift space} \\ \begin{pmatrix} \cosh(\sqrt{|K|}l) & \frac{1}{\sqrt{|K|}}\sinh(\sqrt{|K|}l) \\ -\sqrt{|K|}\sinh(\sqrt{|K|}l) & \cosh(\sqrt{|K|}l) \end{pmatrix} & K < 0, \text{ defoc. quadrupole} \\ \begin{pmatrix} \cos(\frac{l}{\rho}) & \rho\sin(\frac{l}{\rho}) \\ -\frac{1}{\rho}sin(\frac{l}{\rho}) & \cos(\frac{l}{\rho}) \end{pmatrix} & K = \frac{1}{\rho^2}, \text{ sector dipole} \end{cases} \tag{2.4}$$

with $l = s - s_0$.

Now, let us introduce an intermediate position $s_1 \setminus s_0 < s_1 < s$. The position at $s_1$ can be determined from $s_0$, the position at $s$ from $s_1$: $M_{s_0\to s} = M_{s_1\to s} \times M_{s_0\to s_1}$. The transfer matrices can be subdivided into smaller intervals. An entire ring can therefore be defined by the product of the transfer matrices of its elements: the particle can be tracked down along the ring, with just its initial coordinates at a single position of the ring.

**Stability condition** Let us define $M_{period}$ the transfer matrix of the smallest period of the ring. After one complete turn, the transfer matrix is $(M_{period})^{periodicity}$; after $N$ turns, $(M_{period})^{N\times periodicity}$. A necessary and sufficient condition on the stability of the motion is that the transfer matrices remain bounded: otherwise, an amplification will occur turn after turn, and particles will be lost. The sequence $(M^n)_{n\in\mathbb{N}}$ of $2 \times 2$ matrices is bounded if and only if their eigenvalues are. The eigenvalues verify $\lambda^2 - \text{trace}(M_{period})\lambda + \det(M) = 0$. As no amplification is expected from the linear elements, $\det(M) = 1$. Let us write the eigenvalue $\lambda = ae^{\pm i\phi}$, $a \in \mathbb{R}$ and $\phi$ the phase advance. The eigenvalues remain bounded if and only if $\phi \in \mathbb{R} \iff |\text{trace}(M)| \leqslant 2$.

### 2.1.1.1 Twiss parameters

Using the betatron phase advance over one turn $\nu \equiv \phi(C_0)$, the one-turn transfer matrix is generally expressed as the following, combining rotational and focusing matrices:

$$M = \begin{pmatrix} \cos(\nu) + \alpha\sin(\nu) & \beta\sin(\nu) \\ -\gamma\sin(\nu) & \cos(\nu) - \alpha\sin(\nu) \end{pmatrix} \tag{2.5}$$

where $(\alpha, \beta, \gamma)$ are the Twiss parameters. The sign of the matrix elements should be entirely dependent on the phase advance, to avoid any conflict. To do so, $\beta$ and $\gamma$ are fixed as positive. The elements of $M$ can be defined as *cosinus*-like and *sinus*-like functions, noted $C$ and $S$ respectively. The matrix M can be written $M = \begin{pmatrix} C & S \\ C' & S' \end{pmatrix}$. The value of the $(\alpha, \beta, \gamma)$ parameters can be known at any point of the ring using the following transformation:

$$\begin{pmatrix} \beta \\ \alpha \\ \gamma \end{pmatrix} = \begin{pmatrix} C^2 & -2CS & S^2 \\ -CC' & CS' + SC' & -SS' \\ C'^2 & -2C'S' & S'^2 \end{pmatrix} \tag{2.6}$$

which derivation can be found in [51]. The determinant of the transfer matrix is 1, as there is no amplification. This criterion imposes the following link between the Twiss parameters:

$$\beta\gamma = 1 + \alpha^2 \tag{2.7}$$

The transfer matrix of any linear portion from an arbitrary position $s_0$ of the lattice can be expressed with the Twiss parameters. The knowledge of the Twiss functions $(\beta, \alpha)$ and the phase advance $\phi$ is enough to fully describe the particles trajectory along the ring:

$$M_{s \longrightarrow s_0} = \begin{pmatrix} \sqrt{\frac{\beta_s}{\beta_{s_0}}}(\cos(\phi) + \alpha_{s_0}\sin(\phi)) & \sqrt{\beta_s\beta_{s_0}}\sin(\phi) \\ \frac{\alpha_{s_0} - \alpha_s}{\sqrt{\beta_s\beta_{s_0}}}\cos(\phi) - \frac{1 + \alpha_s\alpha_{s_0}}{\sqrt{\beta_s\beta_{s_0}}}\sin(\phi) & \sqrt{\frac{\beta_{s_0}}{\beta_s}}(\cos(\phi) - \alpha\sin(\phi)) \end{pmatrix} \tag{2.8}$$

### 2.1.1.2 General solution of the equations of motion

Using the Twiss formalism from the transfer matrices, the general solution of the equation of motion becomes:

$$u(s) = \sqrt{\epsilon\beta_u(s)}\cos(\phi_u(s) + \phi_0) \tag{2.9}$$

where $\epsilon$ and $\phi_0$ are constants defined by initial conditions. The Twiss function $\sqrt{\beta}$ refers to the beam envelope. The oscillatory form of the motion describes the "betatron motion" or "betatron oscillations". From Eq. (2.9) and its derivative, one finds $\alpha = -\frac{\beta'}{2}$. Primary analysis of any lattice includes the variation of the Twiss functions $\beta$ and $\alpha$ along the lattice, as they reflect the variations of the transverse beam sizes.

### 2.1.1.3 Betatron tune

By inserting the general solution of Eq. (2.9) in the equation of motion (2.1), one restores Floquet's theorem which defines the phase advance $\phi$ between two longitudinal points along the lattice:

$$\phi(s) = \int_0^s \frac{dl}{\beta(l)}, \tag{2.10}$$

arbitrarily starting the ring at a point $s_0 = 0$. The phase advance relies entirely on the amplitude component $\beta$, which is controlled by the quadrupole magnets. After one complete turn of the ring, the phase advance $\nu$ numbers the total betatron oscillations the particle had around its closed orbit. This total is called the betatron tune $Q$:

$$Q \equiv \frac{\nu}{2\pi} = \frac{1}{2\pi} \oint \frac{ds}{\beta(s)} \tag{2.11}$$

**Working point** The tunes $(Q_x, Q_y)$ of the ideal particle define the working point of the ring. It can be modified using the quadrupoles: they act directly on the $\beta$-functions. A pair of quadrupoles is required to uniquely change the betatron tunes:

$$\begin{pmatrix} \Delta Q_x \\ \Delta Q_y \end{pmatrix} = \begin{pmatrix} a & b \\ c & d \end{pmatrix} \begin{pmatrix} \Delta k_x \\ \Delta k_y \end{pmatrix} \tag{2.12}$$

The elements of the above matrix are practically computed by alternatively shutting off one quadrupole at once. Changing the working points is generally used to avoid resonances (see 2.1.3).

#### 2.1.1.4 Hamiltonian formalism

The Hill's equations can be derived from the following Hamiltonian:

$$H = \frac{x'^2 + y'^2}{2} + \frac{1}{2}K_x x^2 + \frac{1}{2}K_y y^2 \tag{2.13}$$

where $K_{u\in\{x,y\}}$ is the frequency component of the Hill's equation in the plane $u \in \{x, y\}$, and $(u, u')$ the phase-space coordinates. The Hamiltonian here above can be simplified by finding a plane where at least one coordinate is a constant of the motion. To do so, the transverse coordinates $(u, p_u)$ are switched with a canonical transformation to $(\phi_u, J_u)_{u\in\{x,y\}}$, using the following generating function:

$$G_1(u, \phi_u, s) = -\frac{u^2}{2\beta_u(s)} \left( \tan(\phi_u) - \frac{\beta_u'(s)}{2} \right) \tag{2.14}$$

The derivation of the generating function can be found in the literature [52]. The coordinates $(\phi_u, J_u) = \frac{\partial G_1}{\partial \phi}(u, \phi_u, s)$ are called the angle-action variables. In that plane, the Hamiltonian is:

$$H(\phi_u, J_u)_{u\in\{x,y\}} = H(u, u') + \frac{\partial G_1}{\partial s} = \frac{J_u}{\beta_u(s)} \equiv H_0 \tag{2.15}$$

The Hamiltonian gives $\frac{d\phi_u}{ds} = \frac{\partial H_0}{\partial \phi_u} = \frac{1}{\beta_u(s)}$, recovering equation (2.10).Furthermore, $\frac{dJ_u}{ds} = -\frac{\partial H_0}{\partial \phi_u} = 0$ : the action variable $J$ is an invariant of the motion. The phase space motion in this plane is purely circular.

The transverse coordinates are expressed in $(\phi_u, J_u)_{u\in\{x,y\}}$ with the following:

$$\begin{cases} u = \sqrt{2J_u\beta_u(s)}\cos(\phi_u) \\ p_u = -\sqrt{\dfrac{2J_u}{\beta_u(s)}} \left( \sin(\phi_u) - \dfrac{\beta_u'(s)}{2}\cos(\phi_u) \right) \end{cases} \tag{2.16}$$

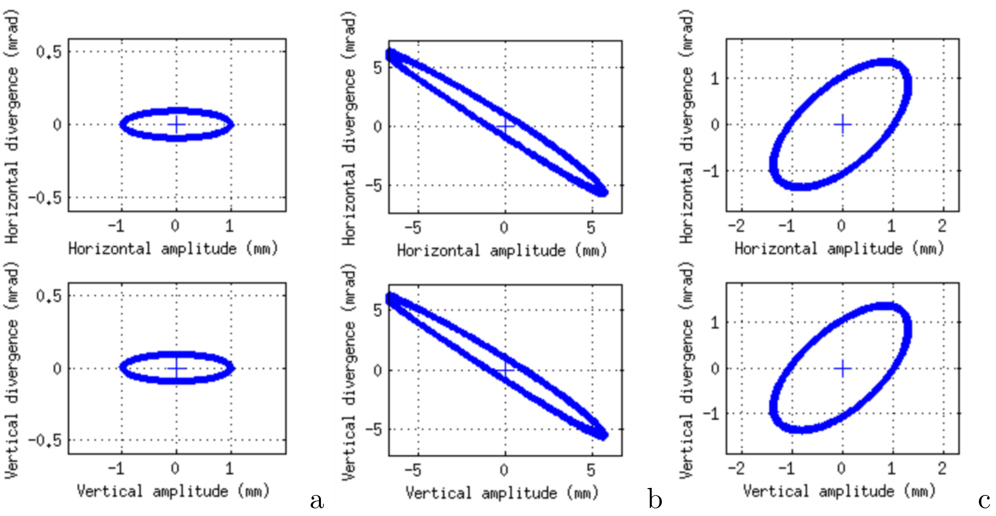

FIGURE 2.1: Horizontal and vertical phase space motion of a particle of transverse coordinates $(x, x', y, y') = (1\,\mathrm{mm}, 0, 1\,\mathrm{mm}, 0)$ along a DBA section of the current SOLEIL lattice: (a) in the middle of a straight section, (b) after a focusing quadrupole and (c) after the last dipole of the DBA.

From Eq. (2.16), the motion in the $(u, u')$ phase-space is elliptical, as illustrated in Fig. 2.2. The area of this ellipse is directly linked to the action $J$:

$$A = \oint u' du = 2\pi J_u \tag{2.17}$$

In a loss-free storage ring, the area is an invariant of motion: as the shape of the ellipse varies along the ring, its area remains constant. Figure 2.1 shows examples of the phase space trajectory of a particle at three locations of the SOLEIL current storage ring: in the middle of a straight-section, after a focusing quadrupole and after the last dipole of a Double Bend cell.

#### 2.1.1.5 Geometric Emittance

The trajectory of a particle in the $(u, u' = \frac{du}{ds})_{u\in\{x,y\}}$ plane describes an elliptic trajectory, as illustrated in Fig. 2.2, in the so-called linear regime. This trajectory can be normalised into a circular motion of radius $\sqrt{2\beta J}$ using the following coordinates:

$$\begin{cases} u = \sqrt{2J_u\beta_u(s)}\cos(\phi_u) \\ \tilde{p_u} = \beta_u u' + \alpha_u u = -\sqrt{2J_u\beta_u(s)}\sin(\phi_u) \end{cases} \tag{2.18}$$

To find a $s$-independent description of the phase-space motion, the area of the circular trajectory is normalised by $\beta_u$:

$$\mathcal{F}(u, u')_{u\in\{x,y\}} = \frac{1}{\beta_u}\left(u^2 + (\beta_u u' + \alpha_u u)^2\right) = \gamma u^2 + 2\alpha_u\beta_u u u' + \beta_u u'^2 \tag{2.19}$$

This equation equals twice the action $J_u$, and therefore is an invariant of the motion. It is called a Courant-Snyder invariant. The trajectory of a particle is described by

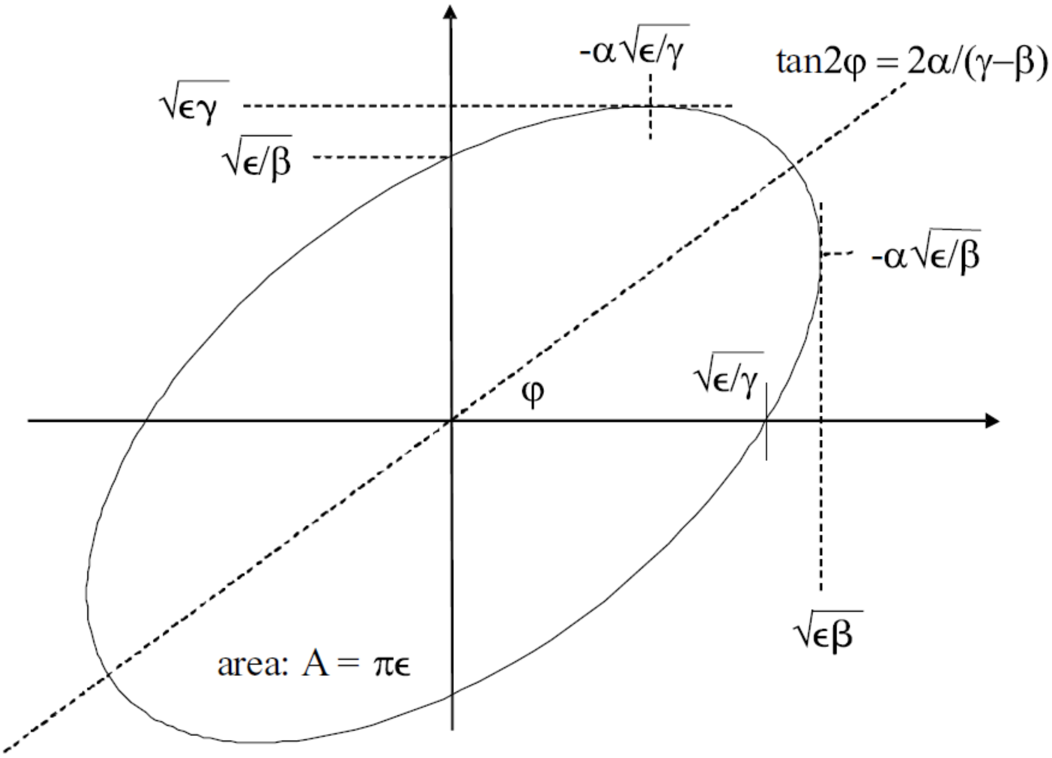

FIGURE 2.2: Representation of the Twiss functions and geometric emittance on the elliptical trajectory in the transverse phase space. From [53].

$F(u, u')_{u\in\{x,y\}} = \epsilon$, where $\epsilon$ is the geometric emittance. The area of the phase space ellipse is $\pi\epsilon$.

### 2.1.2 Off-momentum transverse motion

The previous sections mentioned the trajectory of a particle of momentum $\mathbf{p}_0$[eV/c], travelling through the ring on the ideal orbit. It is the synchronous or reference particle. In the realistic case of a non-monochromatic beam, the particles have different energies and momenta. They are defined by their relative momentum or energy deviation $\delta = \frac{\Delta p}{p_0}$. If $\delta \neq 0$, the particles are said to be off-momentum, else, on-momentum. The momentum spread defines the range of momenta inside a beam. The motion of such particles in the $(\phi, \delta)$ plane, or longitudinal motion, is discussed in the chapter 5.

#### 2.1.2.1 Dispersion and off-momentum closed orbit

The bending forces perceived by off-momentum particles depend on their momentum. For simplicity, the bending forces considered are only applicable to the horizontal plane. In this direction, the motion of off-momentum particles is described by the inhomogeneous Hill's equation below:

$$x'' + (K + \Delta K)x = \frac{\delta}{\rho(s)} \tag{2.20}$$

with $K + \Delta K = \left(\frac{1}{\rho(s)^2} + k_1(s)\right) + \left(-\frac{2}{\rho(s)^2} - k_1(s)\right)\delta$, $\rho$[m] and $k_1[\mathrm{m}^{-2}]$ the bending radius and focusing strength experienced by the reference particle of momentum $p_0$, and $\delta = \frac{\Delta p}{p_0}$ . The derivation of this inhomogeneous equation can be found here [54].

The general solution of the inhomogeneous Hill's equation is a superposition of a solution of the homogeneous equation and a particular solution satisfying Eq. (2.20). The solutions are expressed as:

$$x = x_\beta + D_x\delta \tag{2.21}$$

where $x_\beta$ is a solution of the homogeneous equation of motion (2.9), describing the betatron oscillations around the new closed orbit, defined by $D_x\delta$. $D_x$ is the dispersion function. At the lowest order in $\delta$, it is the solution of:

$$D_x'' + (K + \Delta K)D_x = \frac{1}{\rho} \tag{2.22}$$

Further orders will be discussed in Chapter 5. As $K$ and $\rho$[m] are periodic functions, so is the dispersion.

**Matrix formalism** Again, the equation of the dispersion can be expressed using matrices: $\begin{pmatrix} D_x(s) \\ D_x'(s) \end{pmatrix} = M_{s_0\to s}\begin{pmatrix} D_x(s_0) \\ D_x'(s_0) \end{pmatrix} + \begin{pmatrix} d \\ d' \end{pmatrix}$, with $(d, d')$ a particular solution. The transfer matrices of different elements can be updated into $3\times3$ matrices, including the dispersive components:

$$M_{s_0\to s} = \begin{cases} \begin{pmatrix} \cos(\sqrt{K}l) & \frac{1}{\sqrt{K}}\sin(\sqrt{K}l) & \frac{1}{\rho K}(1-\cos(\sqrt{K}l)) \\ -\sqrt{K}sin(\sqrt{K}l) & \cos(\sqrt{K}l) & \frac{1}{\rho\sqrt{K}}\sin(\sqrt{K}l) \\ 0 & 0 & 1 \end{pmatrix} & K > 0 \\ \begin{pmatrix} \cosh(\sqrt{|K|}l) & \frac{1}{\sqrt{|K|}}\sinh(\sqrt{|K|}l) & \frac{1}{\rho|K|}(-1+\cosh(\sqrt{|K|}l)) \\ -\sqrt{|K|}\sinh(\sqrt{|K|}l) & \cosh(\sqrt{|K|}l) & \frac{1}{\rho\sqrt{|K|}}\sinh(\sqrt{|K|}l) \\ 0 & 0 & 1 \end{pmatrix} & K < 0 \\ \begin{pmatrix} \cos(\frac{l}{\rho}) & \rho\sin(\frac{l}{\rho}) & \rho(1-\cos(\frac{l}{\rho})) \\ -\frac{1}{\rho}\sin(\frac{l}{\rho}) & \cos(\frac{l}{\rho}) & \sin(\frac{l}{\rho}) \\ 0 & 0 & 1 \end{pmatrix} & K = \frac{1}{\rho^2} \\ \begin{pmatrix} 1 & l & 0 \\ 0 & 1 & 0 \\ 0 & 0 & 1 \end{pmatrix} & K = 0 \end{cases} \tag{2.23}$$

with $l = s - s_0$. The new coordinate vector is $\begin{pmatrix} u(s) \\ u'(s) \\ \delta \end{pmatrix}_{u\in\{x,y\}}$ .

### 2.1.2.2 Radiation damping of the betatron motion

The emission of radiation by a relativistic electron occurs in the form of a cone of half-angle $\frac{1}{\gamma_L}$, with $\gamma_L$[n.d.] the Lorentz factor. The electrons' recoil in the opposite direction of emission induces a change in their momenta: $\partial p = \frac{\partial E}{c}$, with $\partial E$ the emitted energy. The variation results in a different effective focusing force on the particles, resulting in a change in their amplitude $A$ such as $u_\beta = A\cos(\phi_u)$. The amplitude change per revolution is characterised by the damping coefficients: $\frac{\Delta A}{A} = \alpha_u, u \in \{x, y\}$, with $\alpha_x = (1-\mathcal{D})\frac{U_0}{2T_0E}$ and $\alpha_y = \frac{U_0}{2T_0E}$, where $U_0$ is the energy loss (*cf* Eq. (1.7)), $T_0$ the revolution period and $\mathcal{D}$ the damping partition:

$$\mathcal{D} = \frac{1}{2\pi}\oint D_x(s)\left(\frac{1}{\rho^2 + 2K(s)}\right)_{dipoles} \tag{2.24}$$

in the case of an isomagnetic ring. Complete derivation of the damping equations can be found in [55, 56]. The radiation damping coefficients are all ratio of the factor $\frac{U_0}{2T_0E}$, and after normalisation define the damping partition number, $\mathcal{J}_{u\in\{x,y,E\}}$:

$$\begin{cases} \mathcal{J}_x = 1 - \mathcal{D} \\ \mathcal{J}_y = 1 \\ \mathcal{J}_E = 2 + \mathcal{D} \end{cases} \tag{2.25}$$

#### 2.1.2.3 Quantum excitation and emittance

The radiation emission in bending magnets yields to a quantic excitation of the betatron motion, characterised by the dispersion. Indeed, the off-momentum closed orbit $D_x\delta$ is shifted by the emission of a quanta, and varying the betatron amplitude by: $\partial x_\beta = -D_x\frac{\partial E}{E_0}$, with $\partial E$ the energy of the emitted quanta. Such a variation modifies the Courant-Snyder invariant of Eq. (2.19), and tends to grow the beam sizes.

**Emittance of an electron beam in a storage ring** The averaged amplitude growth is $\mathcal{H}\left(\frac{\partial E}{E_0}\right)^2$ with:

$$\mathcal{H} = \alpha_x D_x^2 + \gamma_x D_x D_x' + \beta_x D_x'^2 \tag{2.26}$$

The $\mathcal{H}$-function is a Courant-Snyder invariant, but not in the dipoles magnets, where dispersion is created. Adding the damping effect mentioned in 1.2.3.2 as described in the previous section for the betatron motion, the Root-Mean Square (RMS) width $\sigma_x$ and emittance $\epsilon_x$ reach an equilibrium between the quantum excitation and the radiation damping (*cf* 2.1.2.2):

$$\epsilon_x = \frac{\sigma_x^2}{\beta_x} = C_q\frac{\gamma_L^2}{J_x\rho}\langle\mathcal{H}\rangle_{\text{bending magnets}} \tag{2.27}$$

where $C_q$ constant, $\gamma_L = \frac{E}{E_0}$ the Lorentz factor, $J_x$ the action variable, $\rho$ the bending radius. The emittance created by a dipole can be minimised to the Theoretical Minimum Emittance (TME). Discussion is detailed in section 2.2.1.

#### 2.1.2.4 Momentum compaction factor $\alpha_C$

The dispersive aspect of the off-momentum motion modifies the closed orbit of the off-momentum particles: since they perceive different bending radius, their perception of the dispersion differs as well. The lengths of their closed orbits therefore differs from the length of the ideal orbit: the off-momentum particles will complete their revolution before or after the synchronous particle, depending on their energy, as in Eq. (1.9). To synchronise the beam, the variation of the path length has to be monitored. The path length $\Delta C$ is the integration of a small displacement along the ring:

$$\Delta C = \oint_{ring} \sqrt{\left(1 + \frac{x}{\rho}\right)^2 + x'^2 + y'^2 ds} \simeq C_0 + \oint_{ring} \frac{x}{\rho}\, ds \text{ , to the first order} \tag{2.28}$$

The variation of path length with energy is defined as the momentum compaction factor $\alpha_C$:

$$\frac{\Delta C}{C_0} = \alpha_C \left(\frac{\Delta p}{p_0}\right) \tag{2.29}$$

Considering the lowest order in energy deviation, the momentum compaction $\alpha_C$ is expressed with the dispersion and bending radius along the lattice:

$$\alpha_C = \frac{1}{C_0} \oint \frac{D_x}{\rho} \tag{2.30}$$

#### 2.1.2.5 Chromaticity and tune shift

From Eq. (2.20), the focusing strength perceived by off-momentum particles also varies with the energy deviation. This variation equals the effect of a quadrupole gradient error of $-k_1\delta$, resulting in the following variation in the betatron tunes, also called tune shift $\Delta\nu$:

$$\Delta\nu_u = \left(-\frac{1}{4\pi} \int_{ring} k_u(s)\beta_u(s)ds\right) \delta \tag{2.31}$$

with $u \in \{x, y\}$, $k_u$ the quadrupole strength, and $\beta_u$ the Twiss function.

The chromaticity $\xi$ is the variation of the tune shift $\Delta\nu$ with the energy deviation $\delta$. The first-order chromaticity is defined as:

$$\xi \equiv \frac{d(\Delta\nu)}{d(\frac{\Delta p}{p_0})} \tag{2.32}$$

The chromaticity created in the focusing magnets is called the natural chromaticity $\xi_{nat}$. It is expressed as: $\xi_{nat_u} = -\frac{1}{4\pi} \int_{ring} k_u(s)\beta_u(s)ds$. If the chromaticity is left uncorrected, the momentum spread of the beam could lead to a tune shift, enough to possibly cross a resonance, which could lead to the loss of particles. Since the chromaticity is created by a quadrupole strength variation of $-k_1\delta$, its correction requires a magnet which the focusing (defocusing) strength increases (decreases) linearly with the momentum. Such compensation can be achieved using sextupoles, which are introduced in the Appendix B.

### 2.1.3 Resonances

Analogically to oscillators, the number of oscillations per turn can critically enhance the amplitude of a particle, to a point where the particle exceeds the limits of the stability area, and is lost within a short number of turns. Indeed, if the betatrons oscillations are in phase with the synchrotron revolution, the particles will experience the same kicks at the same phases, which will therefore add constructively. This is a resonance phenomenon. Resonances occur when the linear combination of betatron tunes in both planes reaches an integer. This defines the resonance condition:

$$pQ_x + qQ_y = n \tag{2.33}$$

with $p$,$q$ and $n$ integers, and $\gcd(p, q) = 1$. Resonances are referred to with the triplet $(p, q, n)$, with $|p| + |q|$ their resonance order. Note that the resonance condition is stable with integer translation; the condition is verified for the fractional parts : $p\{Q_x\} + q\{Q_y\} = n$.

An interesting particularity appears for periodic rings. Indeed, if a ring is composed of N identical cells, the total betatron tune over the ring is N times the betatron tune of one cell. Therefore, a linear combination of the betatron tunes, where $p \wedge q = 1$ can only be a multiple of the periodicity N, reducing the possible systematic resonances to:

$$pQ_x + qQ_y = \mathbf{N} \times n \tag{2.34}$$

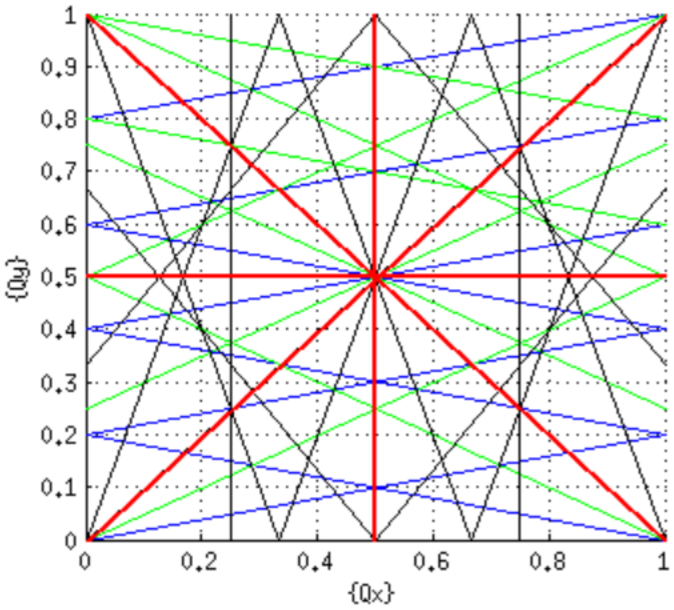

FIGURE 2.3: Example of a resonance diagram. Red lines draw the first-order resonances $Q_{x/y} \in \frac{1}{2}\mathbb{N}$, and the coupling resonances, where $\{Q_x\} = \{Q_y\}$. Second-order resonances are in blue, green for the third orders, and black for the fourth orders.

The visualisation of both the working point $(Q_x, Q_y)$ and the neighbour resonances is to draw a resonance diagram. Figure 2.3 illustrates a resonance diagram up to the fourth order in terms of fractional parts of the betatron tunes. The more resonances excited, the less stability area available in terms of tunes: during the tune shift, particles will be excited and lost, reducing the transverse stability area, and the beam lifetime (see 3.3.4).

**Effect of the sextupoles on the transverse motion and Resonance Driving Terms** The addition of sextupoles in the linear lattice and the inclusion of the dispersion updates the Hamiltonian of the transverse motion into:

$$H = \frac{p_x^2 + p_y^2}{2} - \frac{1}{\rho}\delta + \frac{1}{2}K_x x^2 + \frac{1}{2}K_y y^2 + \frac{k_2}{3}(x^3 - 3xy^2) \tag{2.35}$$

To identify any resonance limiting the dynamic, the non-linear and energy-dependent Hamiltonian of Eq. (2.35) is averaged over a large number of turns. Any remaining component leading to a non-bounded motion therefore is resonant. The averaged Hamiltonian in the case of thin quadrupole and sextupole magnets is divided into Fourier sums, to distinguish the betatron phases:

$$\langle H(\phi_x, J_x, \phi_y, J_y, s, \delta)\rangle_{\phi_{x,y}} \propto \nu_x J_x + \nu_y J_y + \sum h_{jklmp} \tag{2.36}$$

where $h_{jklmp}$ is a resonant driving term (RDT). Linear RDTs are composed of linear quadrupolar and sextupolar contributions, as follows:

$$\begin{aligned} h_{jklmp} \propto & \sum_{\text{sextupoles}} (k_2 L)\beta_x^{\frac{j+k}{2}} \beta_y^{\frac{l+m}{2}} D_x^p \mathrm{e}^{i(j-k)\phi_x + i(l-m)\phi_y} \\ & - \sum_{\text{quadrupoles}} (k_1 L)\beta_x^{\frac{j+k}{2}} \beta_y^{\frac{l+m}{2}} D_x^p \mathrm{e}^{i(j-k)\phi_x + i(l-m)\phi_y} \end{aligned} \tag{2.37}$$

The two first phase-independent RDTs refer to the linear chromaticity, $h_{11001}$ and $h_{00111}$ (*cf* 2.1.2.5). In a higher-order of perturbation, proportional to $(k_2 l_{sext})^2$, five phase-independent terms arise: two second-order chromaticities $\xi_u^{(2)} \equiv \frac{d^2\nu_u}{d\delta^2}$, and three terms describing the tune shift with amplitude, *i.e.* the variation of the horizontal and vertical tunes with the actions $J_x$ and $J_y$. The other terms are complex, of average:

$$\langle h_{jklmp}\rangle_{\phi_{x,y}} = \frac{|h_{jklmp}|}{2\sin(\pi[(j-k)\nu_x + (l-m)\nu_y])} \tag{2.38}$$

Those first-order Resonant Driving Terms (RDT) have to be compensated to avoid any resonance excitation. A thin sextupole kicks the particle, changing its momentum by $p_u := p_u - \frac{k_2 l_{sext}}{2}u^2$. The resonances excited by the sextupoles are classified according to their polynomial dependency on the sextupole strength $k_2$: this is the perturbation order of the resonances. Table 2.1 lists the first- and second-order sextupolar resonances, along with the corresponding RDT, for a mirror symmetry lattice, which means the complex part of the RDTs are null.

TABLE 2.1: Sextupolar resonances, classified by orders, and linked to their corresponding Resonant Driving Term.

| First-order sextupolar resonances | |
|---|---|
| Resonance | R.D.T. |
| $\nu_x$ | $h_{21000}$ |
| $3\nu_x$ | $h_{30000}$ |
| $\nu_x$ | $h_{10110}$ |
| $\nu_x + 2\nu_y$ | $h_{10200}$ |
| $\nu_x - 2\nu_y$ | $h_{10020}$ |
| $2\nu_x$ | $h_{20001}$ |
| $2\nu_y$ | $h_{00201}$ |

| Second-order sextupolar resonances | |
|---|---|
| Resonance | R.D.T. |
| $4\nu_x$ | $h_{40000}$ |
| $4\nu_y$ | $h_{00400}$ |
| $2\nu_x$ | $h_{31000}$,$h_{20110}$, $h_{00310}$ |
| $2\nu_y$ | $h_{01110}$ |
| $2\nu_x + 2\nu_y$ | $h_{20210}$ |
| $2\nu_x - 2\nu_y$ | $h_{20020}$ |

Second-order sextupolar resonances corresponds to a ”crosstalk” between two sextupole fields. It is computed with the Hamiltonian of two turns. Corresponding RDTs are the product of the linear RDTs of Eq. (2.37). Therefore, the first-order resonances are the source of all resonances: N-order RDTs correspond to the product of N first-order resonant driving terms. All resonances can then be minimised or even cancelled by using only a fixed number of sextupole families for instance.

## 2.2 Properties of ultra-low emittance lattices

This section introduces the Theoretical Minimum Emittance, which states the conditions for a minimum creation of emittance within a dipole. Among those, a non-zero dispersion, which increases the electron beam size at the insertion devices, thus reducing their brilliance and quality (*cf* sec. 1.2.2). The minimum emittance achieved with a zero-dispersion input condition is three times as high as the TME, and is achieved by a Chassman-Green lattice.

Towards the $4^{\text{th}}$ generation storage rings, ultra-low emittance can be achieved by using novel lattice designs such as Multi-Bend Achromats (MBA) where the number of dipoles per ring is increased, thus reducing their angle and the creation of dispersion. Further reduction of the emittance is achieved with novel types of magnets, such as combined-function dipoles, reverse bends and longitudinally variable bending magnets.

### 2.2.1 Theoretical minimum emittance

The creation of emittance is driven by the $s$-averaged value of the $H$ function in the dipoles. Considering a single dipole, the emittance creation can be minimised by identifying the optimum Twiss parameters, the dispersion and its derivative at the entrance of the dipoles which minimise the $\mathcal{H}$-function. The minimum emittance achievable is called the Theoretical Minimum Emittance (TME) $\epsilon_{TME}$:

$$\epsilon_{TME} = \frac{1}{12\sqrt{15}} \frac{C_q \gamma_L^2 \theta^3}{\mathcal{J}_x} \propto \frac{E^2}{N_{bend}^3} \tag{2.39}$$

where $\gamma_L$[n.d.] the Lorentz factor, $\theta$ the bending angle, $\mathcal{J}_x$ the damping partition number, $F$, $C_q$ physical constants, $E$[eV] the nominal energy and $N_{bend}$ the number of dipoles. The TME depends on the cubic power of the bending angle: the more dipoles in a storage ring, the lower the TME. Figure 2.4 gives the optics of an example TME cell available in OPA, a single-particle dynamics code developed by Andreas Streun [57].

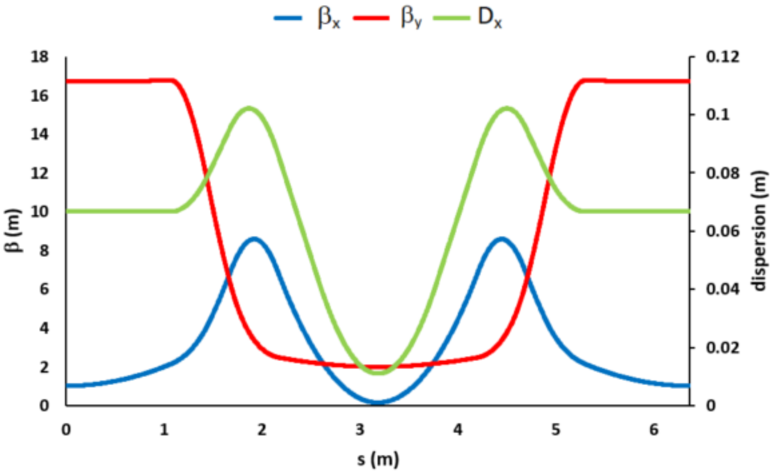

Figure 2.4: Example of a Theoretical Minimum Emittance (TME) cell available in OPA [57].

### 2.2.2 Double Bend Achromat and Triple Bend Achromat

The achieved TME in a single dipole requires a non-zero dispersion at both the entrance and, by mirror symmetry, the exit of the magnet: this could be problematic in the straight sections, where the dispersion should be naught or small enough to achieve a small electron beam size at the insertion devices. The null dispersion condition imposes the use of an achromat lattice.

**Achromatic principle** Achromat lattices are types of lattices composed of $n$ repetitive cells. Their transfer matrices are free of any non-linearities in the transverse motion and up to a certain order. Modified first- and second-order achromats are widely used in today's facilities. The first-order achromat theorem states that a lattice composed of $n$ repetitive cells is achromatic to the first-order if and only if its transfer matrix $M$ verifies: $M^n = I$, with $I$ the identity matrix. The achievement of this condition is independent from the dispersion: its value is therefore uniquely determined by the periodic conditions of the lattice. The achromatic condition is extended to the second-order, when $n > 3$ [58]. Higher-order theory is available in the literature [59].

**Chasman-Green lattice and Triple Bend Achromat** The addition of the achromatic condition to the minimum emittance created in a single dipole results in the following achromat minimum emittance $\epsilon_{DBA}$:

$$\epsilon_{DBA} = \frac{1}{4\sqrt{15}} \frac{C_q \gamma_L^2 \theta^3}{J_x} \tag{2.40}$$

which is three times higher than the TME of Eq. (2.39), due to the reduction of the freedom degrees by two, when imposing the achromatic condition. Using a mirror dipole and including a focusing quadrupole form a Double Bend Achromat (DBA) or a Chasman-Green lattice [60, 61]. A layout of such lattice is displayed on the left side of Fig. 2.5, from [62]. In that case, the dispersion is zero both at the entrance and at the end of the cell.

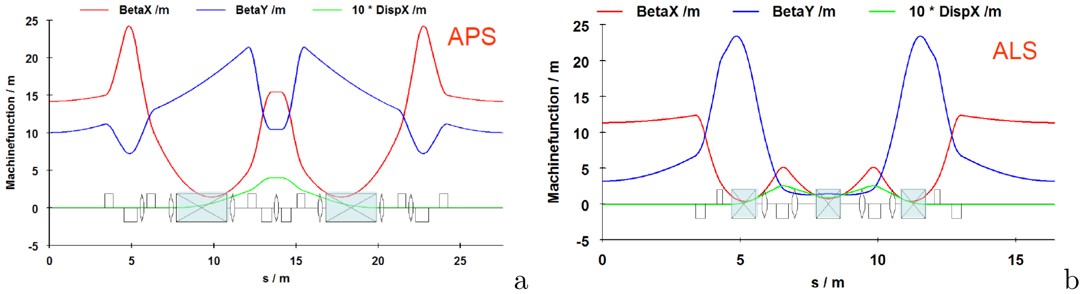

FIGURE 2.5: Example of (a) the Advanced Photon Source (APS) Chasman-Green lattice and (b) the Advanced Light Source (ALS) TBA lattice, from [62].

Further reduction of the emittance can be achieved by including an additional dipole. The length of the external dipoles has to be reduced by about a third, to restore the achromatic condition. This lattice is called a Triple Bend Achromat (TBA). Comparison of the performances of a non-modified Chasman-Green lattice and a TBA lattice is available in [63, 64]: the averaged achieved emittance is 2.5 times lower in TBA lattices. Furthermore, the achromatic condition of the Double Bend structure generates a high natural horizontal chromaticity. Indeed, the minimum emittance of a Chasman-Green lattice, in Eq. (2.40), is achieved with a very low horizontal $\beta$-function in both bending magnets, requiring strong sextupoles for correction and even stronger for machines operating with a slightly positive chromaticity, thus reducing the dynamic aperture and the lattice performances [65].

**Modified Chasman-Green lattice** Modification of the achromat principle can further reduce the emittance: allowing an increase in dispersion in the straight sections releases the tight achromatic conditions and gets the lattice closer to the TME condition. Table 2.2 compares the achieved emittances of some third-generation storage rings using the Chasman-Green achromat lattice and its modified version. Figure 2.6 compares the Chasman-Green lattice with its modified version for the Advanced Photon Source (APS) storage ring (from [62]): an increase up to 10 cm dispersion in the

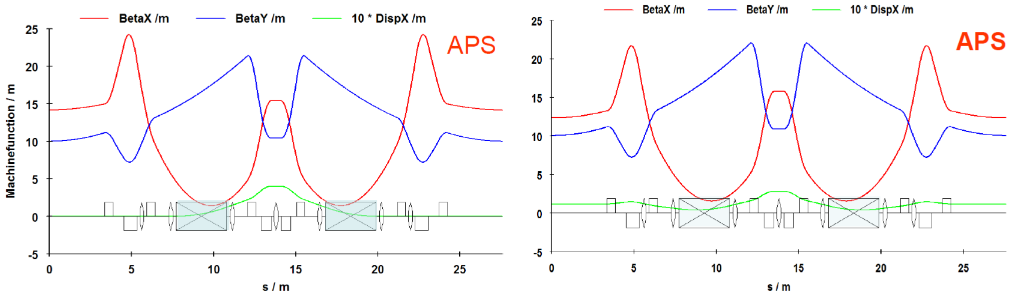

FIGURE 2.6: Comparison of the optic functions of a Chasman-Green lattice and its modified equivalent for the APS storage ring, (from [62]).

straight section allowed a reduction of the emittance from an original 7 nm.rad with a Chassman-Green lattice, to 2.5 nm.rad with the modified optics.

TABLE 2.2: Emittance reduction with the application of modified Chasman-Green lattices in third-generation storage rings.

| Storage ring | Chasman-Green optics | Modified DBA |
|---|---|---|
| ESRF | 7 nm.rad | 3.8 nm.rad |
| APS | 7.5 nm.rad | 2.5 nm.rad |
| SPring8 | 4.8 nm.rad | 3.0 nm.rad |
| SOLEIL | 4.8 nm.rad | 3.9 nm.rad |
| SPEAR3 | 18 nm.rad | 9.8 nm.rad |

Both the control of the $\beta$-functions in the middle of the straight sections and the reduced electron emittances increase the brilliance of the X-ray emission of the insertion devices, despite the non-zero dispersion [66, 67]. Many synchrotrons decided to operate in a modified Chasman-Green lattice for those reasons [68–71]. Table 2.3 gathers different $3^{\mathrm{rd}}$ generation storage rings, their lattice type, energy and emittance.

TABLE 2.3: Examples of synchrotron storage rings using either a DBA, a modified DBA or a TBA lattice, their energy and achieved natural horizontal emittance.

| Name | Location | $E$(GeV) | Circumference (m) | Achromat | $\epsilon_x$ (nm.rad) |
|---|---|---|---|---|---|
| ALBA | Spain | 3 | 268.8 | m-DBA | 4.3 |
| ALS | USA | 1.5- 1.9 | 196.8 | TBA | 2.0 |
| BESSY II | Germany | 1.72 | 240 | m-DBA | 6 |
| CLS | Canada | 2.9 | 171 | m-DBA | 18.0 |
| DIAMOND | UK | 3 | 560 | m-DBA | 3.17 |
| ELETTRA | Italy | 2.4 | 259 | m-DBA | 7.0 |
| ESRF | France | 6 | 844 | m-DBA | 4.0 |
| SLS | Switzerland | 2.4 | 288 | TBA | 5.50 |
| SOLEIL | France | 2.75 | 354 | m-DBA | 3.9 |
| SPring-8 | Japan | 8 | 1434 | m-DBA | 2.4 |

### 2.2.3 Multi-Bend Achromats

Following the logic of Theoretical Minimum Emittance lattices, the future $4^{\text{th}}$ generation light sources should be based on several bending magnets per achromatic cell. First steps evaluated the theoretical minimum emittance of a Quadrupole-Bend Achromat (QBA) [72]: the implementation of combined-function dipole magnets allows a further the reduction of the modified-QBA's minimum emittance. A further increase in the number of dipoles reduces the achievable theoretical minimum emittance. Imposing the achromatic condition, the design is named a Multi-Bend Achromat (MBA) lattice [73, 74]. According to Eq. (2.40), the emittance gain using a MBA lattice as compared to a DBA/TBA lattice is roughly cubic in the number of dipoles, as illustrated in Fig. 2.7. To highlight the number of dipoles in a MBA lattice, such a lattice is called $N$-BA, with $N$ the number of dipoles. A 5BA lattice then is a MBA composed of 5 dipoles in each cell.

**Example of the SOLEIL storage ring** The current lattice of the SOLEIL synchrotron is a modified DBA lattice, of which the main machine parameters were presented in the section 1.5.2. Its natural emittance is 3.9 nm.rad and 4 nm.rad including the insertion devices. Increasing the number of dipoles will roughly change the emittance by the factor $\left(\frac{N_{MBA}}{N_{DBA}}\right)^3$ - where N denotes the number of dipoles in each configuration. The achievable natural emittance of a 7BA lattice applied to SOLEIL 2.75 GeV storage ring could be as low as 100 pm.rad. Figure 2.7 estimates the emittance gain from DBA/TBA lattices with the number of dipoles in the future MBA lattices.

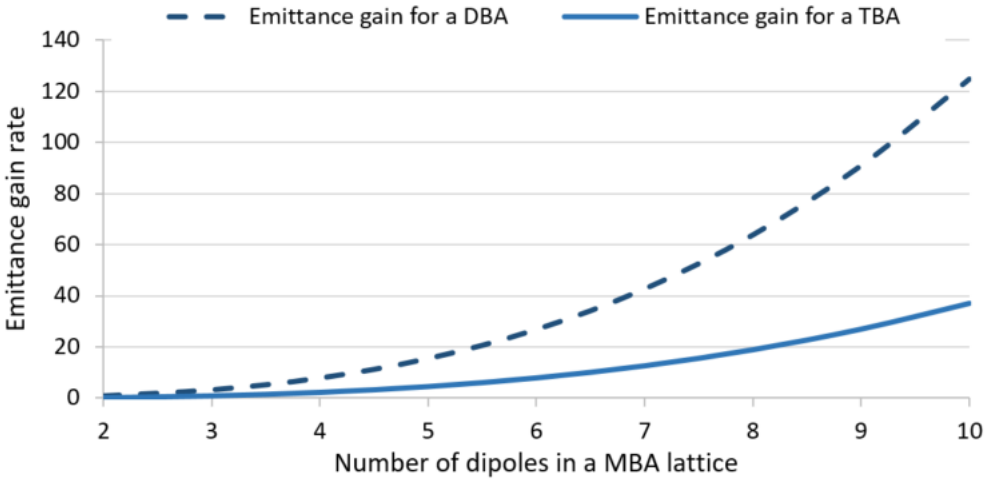

FIGURE 2.7: Rough emittance gain from the current DBA (dotted line) or TBA (solid line) lattices, to a MBA lattice with the same nominal energy.

**First fourth-generation storage ring** The first $4^{\text{th}}$ generation storage rings, implementing a MBA scheme was built in MAX IV (Lund, Sweden) [75], SIRIUS (Brazil - under completion) for their 3 GeV storage ring and ESRF-EBS (France) for a 6 GeV storage ring [76]. The case of ESRF-Extremely Brilliant Source (ESRF-EBS) is detailed in 2.3.1. With a 7BA lattice of 20-fold symmetry, MAX IV achieved a natural low emittance of 330 pm.rad over a 528 m circumference [77]. Figure 2.8 illustrates the $\beta$-function and dispersion of the 7BA lattice of MAX-IV [78]. The level of dispersion dropped from $\simeq$ 10 cm to $\simeq$ 8 cm maximum dispersion. Moreover, the horizontal $\beta$-functions, of the order of 10 m in third-generation storage rings, are now below 4-5 m in the core lattice, downsizing the horizontal size of the beam.

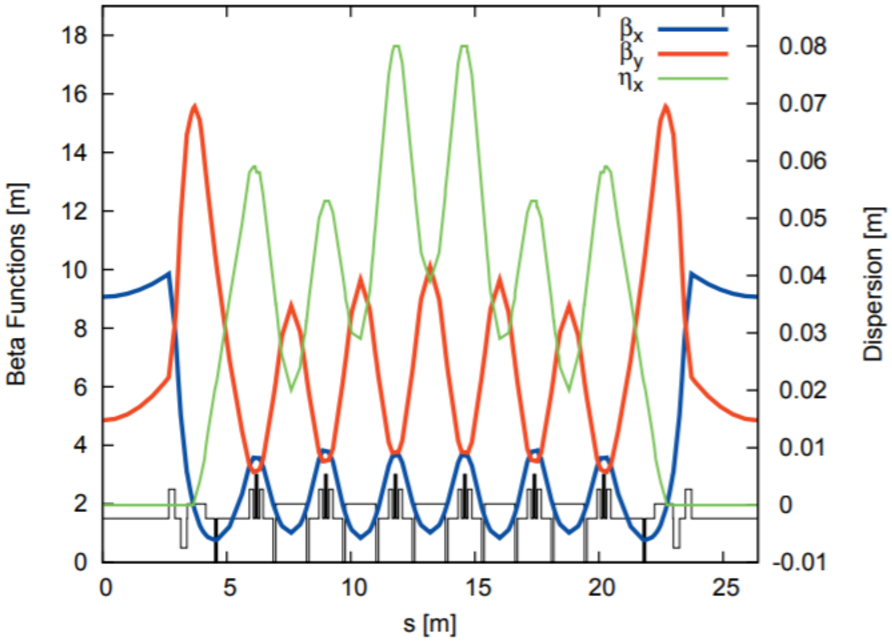

FIGURE 2.8: Layout of the MAX IV 3 GeV storage ring 7BA lattice, from [78].

Allying DBA cells with TME cells, the synchrotron PEP-X decreased its emittance from 49 nm.rad at 3.1 GeV in PEP-II to 0.37 nm.rad natural emittance, at 4.5 GeV, further reduced down to 0.09 nm.rad with the insertion of damping wigglers [79].

### 2.2.4 Novel magnets and techniques for further reduction of the emittance

Several light source facilities worldwide are considering an upgrade of their storage ring. The majority of them study the possibility of an upgrade while conserving the same tunnel *i.e.* the same circumference as their current storage ring as well as their nominal energy. The use of MBA lattices reduces the achievable Theoretical Minimum Emittance (TME), but depending on the storage ring parameters and the number of requested straight sections, the emittance may still remain higher by an order or two than the diffraction limit in Eq. (1.15). This subsection explores different techniques foreseen or already implemented to further reduce the emittance of fourth generation storage ring lattices.

#### 2.2.4.1 Reduction of the nominal energy

As the theoretical minimum emittance depends quadratically on the nominal energy, low energy machines achieve lower emittance. Nevertheless, change in the nominal energy shifts the synchrotron radiation energy range, which may not be suitable for synchrotron radiation users. While many upgrade investigations conserve the same nominal energy, some reduced it, such as the APS-U (from 7 to 6 GeV) and SPring8-II (from 8 to 6 GeV), and compensate the energy shift of their radiation range by reducing the period of their insertion devices [80].

#### 2.2.4.2 Round beam

A round beam is an electron beam of equal dimensions in the horizontal and the vertical plane, in at least one location of a storage ring lattice. It is especially useful in storage-ring-based colliders, to increase the collision cross-section [81].

For fourth-generation storage ring light sources where the natural vertical emittance is negligible compared to the horizontal emittance, a round beam could further decrease the effective size of the produced photon beam, using the principle of matching both phase spaces described in 1.4.1.2. It could locally imitate a diffraction limited source. Furthermore, the use of a round beam could reduce the density of particles in the horizontal plane, and decrease the probability of collective particle scattering events (*cf* 3.3.4). Its interest was demonstrated in a workshop held at SOLEIL in June 14-15, 2017 [82].

**Möbius ring** A round beam can be designed at a specific location of the ring, using the Möbius principle. First described by R. Talman [83, 84] and simulated on the Cornell Electron Storage Ring (CESR) ring [81], skew quadrupoles rotated at 45 degrees are inserted in a straight section of the lattice: the horizontal and vertical component are inverted each turn, and their emittance is equally parted between the two planes [85, 86]. An interesting effect is the chromaticity sharing resulting of the exchange: the damping rates depend on both chromaticities. This effect was measured for weak coupling on the CESR [87].

**Local creation of a round beam** Different techniques can be used to produce a round beam [88]. Local creation of a round photon beam can be achieved at specific beamlines, by creating emittance adapters with solenoids [89] or with the use of focusing mirrors to shape an undulator source [90, 91]. The emittance adapter described in [89] was simulated on SOLEIL and MAX IV [92]. It required the insertion of skew quadrupole triplets to match the $\beta_x$- and $\beta_y$-functions at the centre of the straight section, where the undulator with solenoid is placed. Their achieved reduction in the beam size and increase in the photon density is displayed in Fig. 2.9.

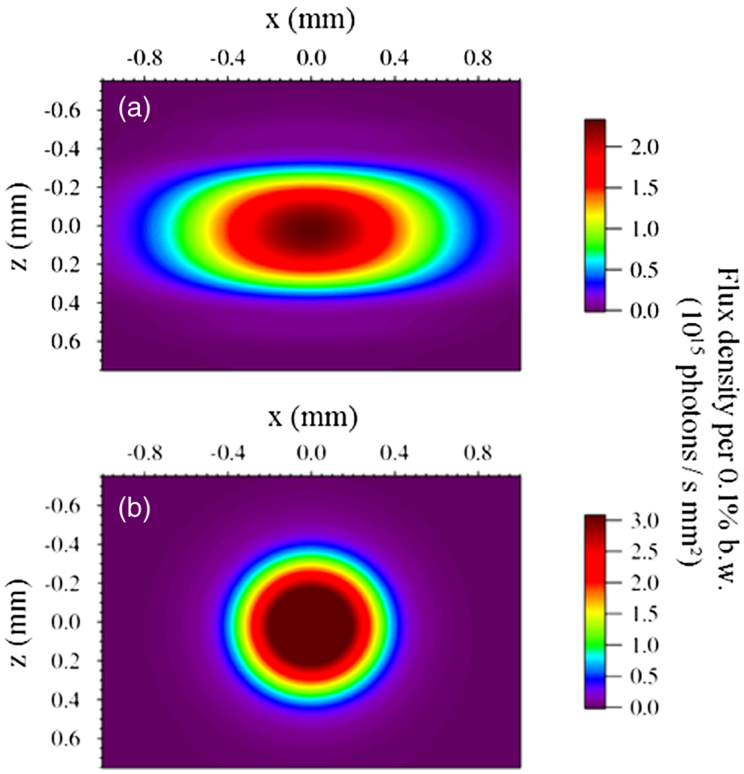

FIGURE 2.9: Locally achieved round beam with the use of an emittance adapter (simulation), from [93].

**Coupling resonance $\{\nu_x\} = \{\nu_y\}$** The coupling resonance $\{\nu_x\} = \{\nu_y\}$ can also be exploited, by setting the tunes on it and exciting it[94]: in that case, energy exchange occurs between the transverse planes, resulting in equal emittances $\epsilon_x = \epsilon_y$. The exchange of oscillation amplitudes between the horizontal and the vertical plane can be achieved with the use of skew quadrupoles. The coupled emittances are [95]:

$$\begin{cases} \epsilon_x = \dfrac{\epsilon_{tot}}{1+\tau} \\ \epsilon_y = \dfrac{\epsilon_{tot}}{1+\frac{1}{\tau}} \end{cases} \tag{2.41}$$

with $\tau$ the coupling parameter. For a full coupling $\tau = 100\%$, both emittances are equal, creating a round beam at the insertion device, provided the $\beta$-functions are identical.

#### 2.2.4.3 Damping wigglers

Already used in some third-generation storage rings such as PETRA-III and NSLS-II, further reduction of emittance can be achieved using damping wigglers. Such wigglers enhance the damping effect described in Sec. 1.2.3.2, by creating more radiation losses in the storage ring: the emittance reduction thus depends on the period length of the wiggler, its peak magnetic field and its total length. While this effect is easy to implement, the compensation for the increased losses might prove difficult in tight ultra-low emittance lattices, where the number of RF cavities is limited as is the available space for the wigglers themselves.

#### 2.2.4.4 Novel bending magnets

The first part of this chapter introduced and studied the effects of single magnetic elements: constant-field dipoles, quadrupoles and sextupoles. This section introduces different types of bending magnets which limit the creation of emittance directly at its source: from combined-function magnets to dipoles of longitudinally varying field.

**Combined-function dipoles** To optimise their effect and their occupation, single elements can be superposed into one magnet, combining the single-element effects. The modified QBA lattice mentioned earlier already included a quadrupole superimposed on a bending magnet to maintain low radiation integrals [72]. The main combined-function magnet considered in today's upgrades is the addition of a small defocusing quadrupolar field to a dipole. Unless stated otherwise, the dipoles encountered in this thesis are combined-function dipoles, integrating a defocusing quadrupole strength, which brings the magnet closer to the TME cell configuration (*cf* 2.2.1).

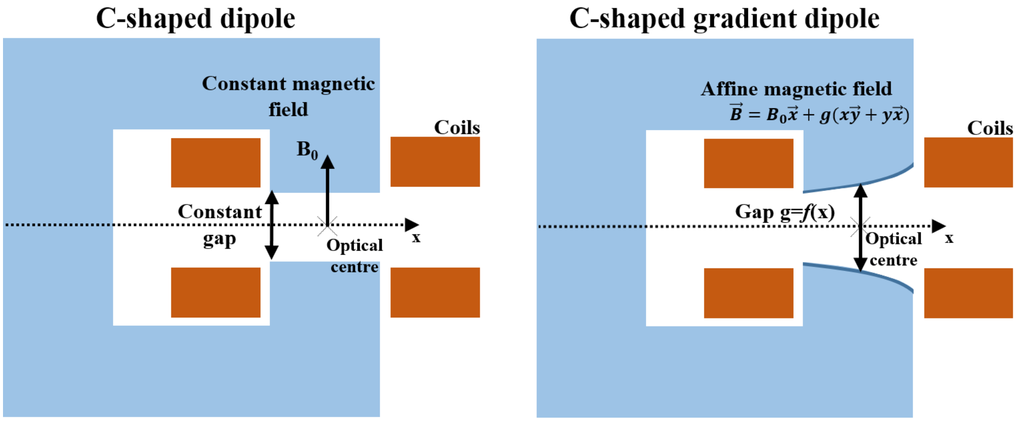

FIGURE 2.10: Comparison of the transverse view of (left) a standard C-shaped dipole of constant magnetic field and (right) a gradient dipole of defocusing strength with a gap dependent on the horizontal position.

Although first combined-function dipoles had a superimposed quadrupole, like in Fig. 2.10, the fourth-generation version requires stronger quadrupolar gradient. Design of such magnets are explored with permanent dipoles, with for instance a permanent triangular-shaped pole in the transverse plane, which provides both a bending and a defocusing force, as designed for the ALS upgrade [96]. Some lattices shift the magnetic axis of a defocusing quadrupole from the design closed orbit to create a dipolar field, like in APS upgrade [97]. Another method is to design a dipole with a gap varying with the horizontal axis, as used in the MAX IV storage ring [78]. Figure 2.10 compares schematics of the transverse cut of a standard C-shaped dipole with a MAX IV-type gradient dipole.

**Reverse bending magnets** Reducing the emittance implies minimising the integral sum of the $\mathcal{H}$-function within all the dipoles. The minimum emittance achievable is the TME (2.2.1). In a fixed MBA lattice, further reduction of the emittance can be achieved by controlling the dispersion function at the entrance of the dipole magnets, to approach the TME conditions. Reverse bending magnets, or antibends, are quadrupole magnets of which centre is shifted horizontally from the optical axis, creating a dipolar field of resulting negative angle. The link between the horizontal shift $\Delta x$ and the created angle $\theta_{reverse}$ is expressed as:

$$\theta_{reverse} = -k_1 l_{quad} \Delta x \tag{2.42}$$

where $k_1[\mathrm{m}^{-2}]$ is the quadrupolar strength, $l_{quad}$ the length of the quadrupole magnet. As an example, let us take a quadrupole magnet of length 0.25 m, and a strength of 10 $\mathrm{m}^{-2}$. For a required reverse bending angle of $-0.5$ degree, the quadrupole magnet should be shifted by 3.5 mm towards the centre of the storage ring. Inserting such a magnet before a regular dipole inverts the dispersion curve and variation, thus allowing the control of the dispersion at the entrance of a dipole: such a node can help minimise the $\mathcal{H}$-function in the dipoles. Furthermore, the reverse bend increases the damping partition number $\mathcal{J}_x$, which participates in decreasing the horizontal natural emittance. The comparison of the minimum emittance using the TME principle in a constant-field dipole cell and in an anti-bend cell was done in [98], resulting in a lower emittance achieved with a reverse bend. Further study of the reverse bends is conducted in the sections dedicated to the lattice design for the SOLEIL storage ring, in the sections 3.1 and 3.2.

**Longitudinal-gradient dipoles** The term Longitudinal-Gradient Bend (LGB) refers to a dipole of varying field with the longitudinal position $s$: the corresponding variation of the bending radius $\rho(s)$ allows the manipulation of the dispersion creation inside the magnets, controlling the variation of the $\mathcal{H}$-function inside the dipole. Depending on the variation function of the dipole field, the achieved emittance can be lower than the TME case [99]. Analytical studies of such dipoles are available in [100], where, in an example case, the minimum emittance achieved in the achromatic condition was three times lower than the DBA case.

Although no study regarding LGB is conducted in this thesis, further reduction of emittance, if necessary, could be achieved by replacing the homogeneous dipoles with longitudinal gradient dipoles, as demonstrated in [99, 101]. Discussion on such a magnetic field is conducted in [102].

### 2.2.5 Implication of the reduction of emittance

Ultra-low emittance is achieved by a continuous control of the beam envelope $(\beta, \alpha)$ and of the dispersion along the storage ring, to reduce the average value of the $\mathcal{H}$-function in the dipoles. Using a MBA lattice limits the creation of emittance (*cf* 2.2.3), by reducing

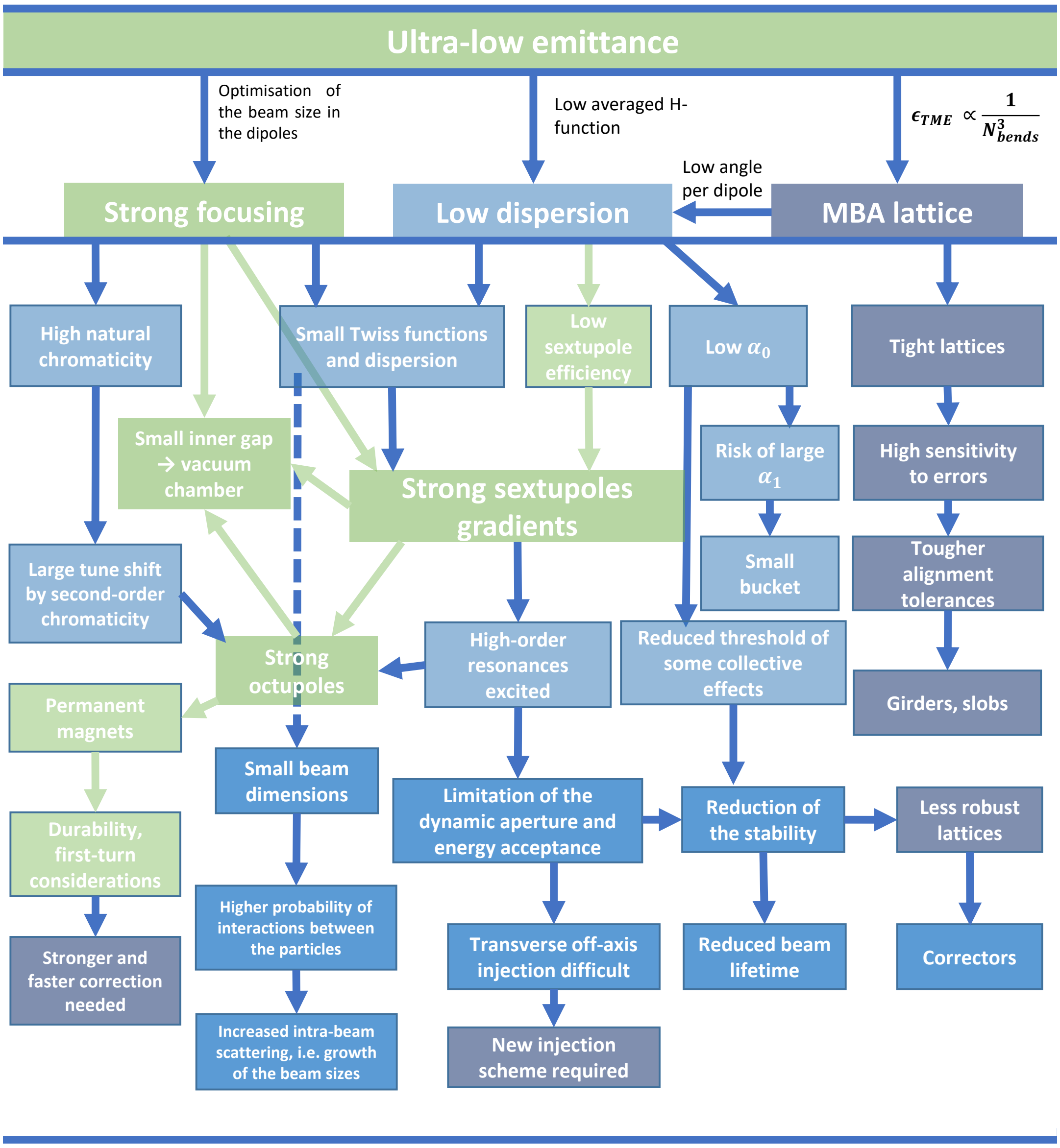

FIGURE 2.11: General effects of the reduction of emittance, and expected difficulties in ultra-low emittance lattices.

the bending angle per dipole, following the relation between the TME with the number of bending magnets, in Eq. (2.39).

The Twiss parameters at the entrance of the dipoles have to be controlled as well, to minimise the creation of emittance: focusing quadrupoles are implemented to ensure low $\beta$-functions and an even lower dispersion. The strong gradients require new magnet designs, with lower inner gaps, of the order of a few millimetres: a compromise has to be found between the vacuum pumping requirements and the magnet design.

Nonetheless, the strong focusing leads to large natural chromaticities. To correct them under such low dispersion levels, strong sextupoles are to be expected. Their large strengths will perturb the beam dynamics, by further exciting higher-order resonances, which have to be minimised for the dynamics and beam lifetime. Figure 2.11 summarises the implication of such a reduction of the emittance.

Maintaining stability and a large dynamic aperture requires that the sextupole-induced non-linearities are controlled: this can be achieved by modelling the linear lattice such as to compensate the negative sextupolar effects.

## 2.3 Including the chromaticity correction into the linear design of ultra-low emittance lattices

Sextupolar elements are necessary to correct chromaticity. However, such elements introduce additional higher-order aberrations which may dramatically decrease the dynamic aperture of the synchrotron. To control and counteract disruptive nonlinear effects of sextupoles, lattice designs are sought to minimise or even mask the nonlinear effects of sextupoles. Two distinct ultra-low emittance schemes have been developed to this end in the light source community and shall be presented in details in the following sections. Nowadays, the following chromaticity correction schemes are being considered for the ultra-low emittance lattices:

- A first scheme was developed by Pantaleo Raimondi for the ESRF-Extremely Brilliant Source (ESRF-EBS) lattice (2.3.1). It combines a Chasman-Green lattice with the non-interleaved principle, which compensates a sextupolar kick by its symmetric counterpart. All sextupoles are therefore located under two symmetric dispersion bumps, globally correcting the chromaticity.
- A second scheme works on both symmetry and betatron tunes: using one unit cell to build a whole period, the betatron tunes of each unit cell is fixed in order to cancel most geometric resonances up to the third order. This is a High-Order Achromat (HOA) (2.3.2). Each unit cell has its pair of sextupoles, making a local chromaticity correction.

### 2.3.1 Non-interleaved sextupole lattice

The first scheme considered was developed by Pantaleo Raimondi for the upgrade of the ESRF synchrotron, the ESRF-Extremely Brilliant Source (ESRF-EBS). The upgrade aims at providing a completely new 6 GeV storage ring of 844 m to fit in their current tunnel. Both the original periodicity of 32 and the position of their beamlines must be conserved. Their first stored beam [103] occurred in December 2019.

The layout of an arc of the ESRF-EBS lattice is displayed in Fig. 2.12. This novel lattice inhomogeneously distributed the bending magnets in the arc, allowing the creation of two dispersion bumps at its extrema. Under the bumps are located the sextupoles, for an optimum corrective efficiency. Furthermore, additional space is available for other non-linear magnets, such as additional sextupole families for resonances control or octupoles to correct the tune shift. The phase advance between the two dispersion bumps allows the application of the non-interleaved principle, which is explained below.

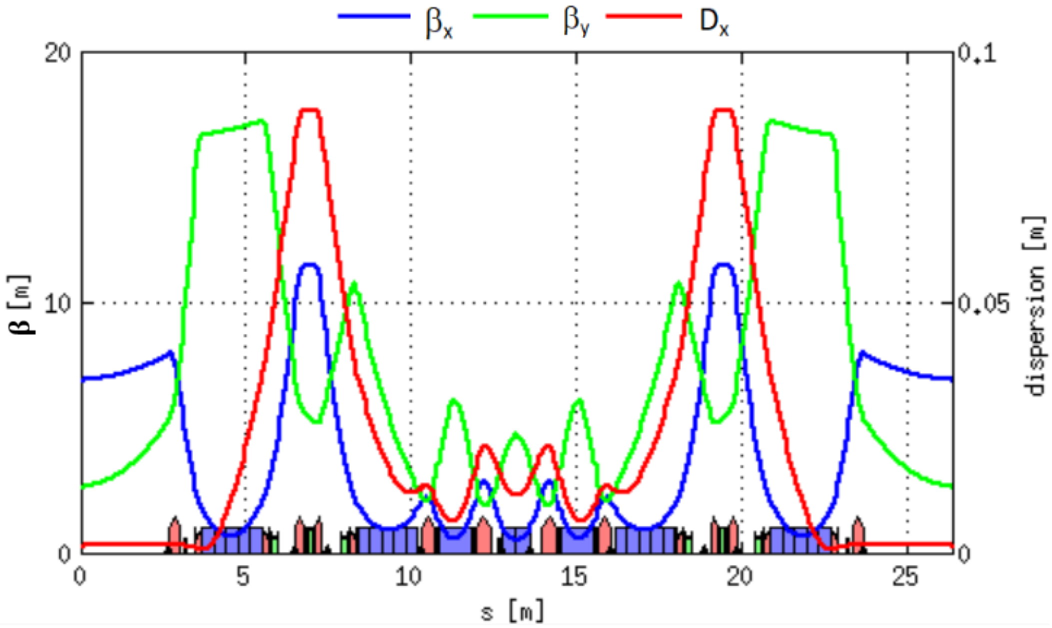

FIGURE 2.12: Example of the non-interleaved lattice designed for the ESRF-EBS upgrade, one arc of the ring. Edited from [41].

This minus identity $(-I)$ core lattice, delimited by the centre of both dispersion bumps, makes the overall lattice resembles a Double Bend Achromat (DBA). The combination of all those factors names this lattice a Hybrid Multi-Bend Achromat (HMBA) lattice. The lattice parameters can be found in the ESRF Orange book [41]. Some are gathered in Table 2.4.

TABLE 2.4: ERSF-EBS 7BA hybrid lattice with a 32-fold symmetry, for their 6 GeV storage ring.

| | |
|---|---|
| Energy | 6 GeV |
| Circumference | 844 m |
| Natural Emittance $\epsilon_x$ | 132 pm.rad |
| Betatron tunes $(Q_x, Q_y)$ | (76.21, 27.34) |
| Momentum compaction factor $\alpha_0$ | $8.50 \times 10^{-5}$ |
| Energy loss per turn | 2.52 MeV |

**Non-interleaved principle** Described in [58] and [104], the method implements two identical sextupoles in a linear lattice, where the phase advance between them is an odd multiple of $\pi$ in the horizontal plane:

$$(\Delta\phi_x, \Delta\phi_y) = ((2p+1)\pi, q\pi) \tag{2.43}$$

with $p, q \in \mathbb{N}$. This condition makes the transfer matrix between the sextupoles equivalent to a negative identity transport matrix, or $-I$ transformation. Therefore, as illustrated in Eq. (2.44), if the sextupole are placed at symmetric positions, where their Twiss functions and dispersion are equal, the second sextupolar kick $K_{S_2}$ seen by the particles will strictly be opposite to the first kick $K_{S_1}$, making both of them transparent to the particles at the end of the lattice,

$$\begin{pmatrix} x \\ p_x \end{pmatrix} \longrightarrow_{S_1} \begin{pmatrix} x \\ p_x - K_{S_1} \end{pmatrix} \longrightarrow_{-I} \begin{pmatrix} -x \\ -(p_x - K_{S_1}) \end{pmatrix} \longrightarrow_{S_2} \begin{pmatrix} -x \\ -p_x + (K_{S_1} - K_{S_2}) \end{pmatrix} \tag{2.44}$$

This allows correction of chromaticity while cancelling the integral of sextupoles on-momentum. In that case, the stability of the particles is ensured, and the dynamic aperture is therefore larger for the on-momentum case.

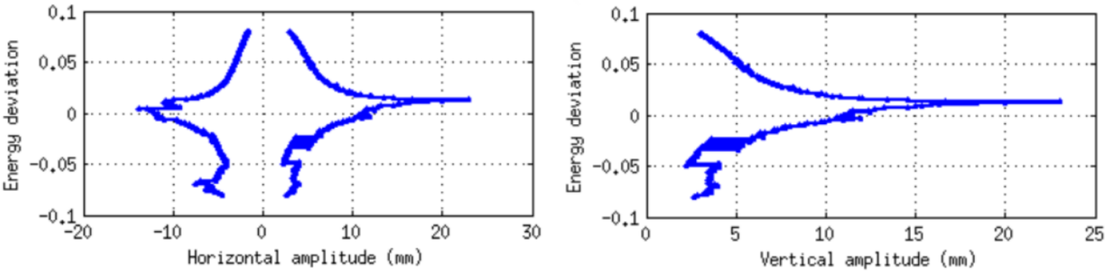

FIGURE 2.13: Effect of the non-interleaved sextupole scheme on the on-momentum dynamic aperture in the horizontal plane (left) and the vertical plane (right) with energy deviation, exposed by the variation of the maximum amplitude per energy deviation of the ESRF-EBS lattice (2.12).

Figure 2.13 displays the dynamic aperture with energy in both transverse planes, of the ESRF-EBS lattice. The cancellation of the sextupolar kicks highly increases the on-momentum dynamic aperture: it is three times as large as the averaged off-momentum horizontal limits. The non-interleaved principle is adapted in the vertical, where the condition can be extended to a multiple of $\pi$ only, which is enough to minimise the vertically dependent first-order RDTs [105].

Nonetheless, the inhomogeneous repartition of the sextupoles in such a lattice increases the higher-order chromaticities [106]. Those orders can be managed by increasing the sextupoles pairs under the dispersion bumps, for compactness and lack of space. This means that the non-interleaved condition can not be respected for each sextupole family. This problem can be alleviated by applying the non-interleaved condition to the strongest sextupole families.

### 2.3.2 High-order achromat lattice

Another chromaticity correction method is the so-called High-Order Achromat (HOA) lattice. It is based on a sextupole arrangement which makes the effect of the sextupoles transparent to the beam along the MBA lattice. From a DBA/TBA lattice, the number of dipoles per achromat has been increased, but not the achromatic order. From [58], a lattice of transfer matrix $M$ is achromatic to the second order if the minimum $n \in \mathbb{N}$

for which $M^n = I$ is strictly greater than 3. Increasing the order of the achromat using more dipole magnets can be done by building the period from unit cells of identical and fixed phase advance, thus cancelling all resonances after completion of a fixed number of unit cells. The HOA concept is illustrated in Fig. 2.14 which depicts the magnetic arrangement of an unit cell.

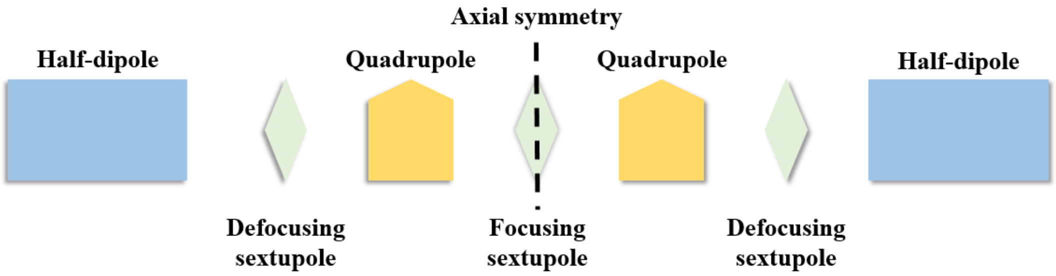

Figure 2.14: Scheme of a unit cell for a High-Order Achromat lattice.

The proposed High-Order Achromat MBA lattices are composed of M identical cell blocks, named unit cells. Each unit cell includes two half dipoles, two reverse bends, a focusing sextupole and two defocusing sextupoles, as depicted in Fig.2.14. Sextupoles are distributed in the lattice to correct chromaticity locally over each unit cell, thus reducing the discrepancy between the different energy deviations in the particle beam.

The cancellation of geometric and chromatic resonances is ensured by a specific choice and tight control of the phase advances over a unit cell. For example, the 7BA lattice for both ALS-U [49] and SLS-II [48] have a fixed unit cell phase advance of $(\nu_x, \nu_y) = (\frac{3}{7}, \frac{1}{7})$, cancelling resonances up to the third order. A discussion on the possible phase advances is made in Sec. 3.2.3.

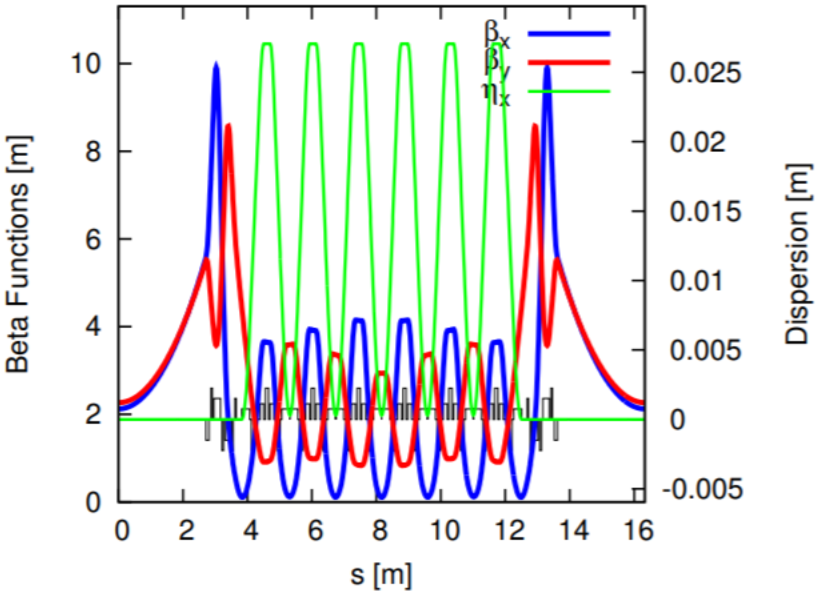

Figure 2.15: Twiss parameters and layout of a 7BA HOA period for the ALS storage ring, from [49].

HOA-based lattices have been extensively used for the upgrade of many synchrotron storage rings. For instance, HOA-based MBA lattices were designed for MAX IV by J. Bengtsson [78], A. Streun also applied such correction concept to the upgrade of the Swiss Light Source II (SLS-II) [48] and S. Leeman applied it for the Advanced Light Source - Upgrade (ALS-U) [49] , although the chosen lattice for ALS-U is a 9BA lattice [107]. Figure 2.15 illustrates the 7BA HOA lattice developed for the ALS storage ring, and Table 2.5 gathers its main parameters.

Table 2.5: ALS-U 7BA HOA lattice proposal with a 12-fold symmetry, for their 2 GeV storage ring.

| | |
|---|---|
| Circumference | 196 m |
| Emittance $\epsilon_x$ | 89 pm.rad |
| Tunes per period $(\nu_x, \nu_y)$ | (3.28, 1.20) |
| Momentum compaction factor $\alpha_0$ | $-1.25 \times 10^{-4}$ |
| Reverse bending angle | -1.27 degrees |
| Energy loss per turn | 38 keV |
| $(\beta_x, \beta_y)$ @ID | (2.5, 2.5) m |

## 2.4 Conclusion

In this chapter we reviewed the necessary theoretical elements to understand the challenging development of fourth-generation synchrotron light sources. To decrease their emittance below 100 pm.rad, Multi-Bend Achromat (MBA) lattices are widely used. Further reduction of the emittance can be achieved with the use of novel magnets, such as reverse bends or longitudinal-gradient dipoles. Local adaptation of the beam sizes can modulate the apparent emittances, and transfer the horizontal energy to the vertical plane, making a round beam, for which several methods were introduced.

The spatially tight ultra-low emittance lattices present several challenges, starting from the lattice design to its optimisation, and related to other accelerator fields, such as vacuum and alignment for instance. Some limitations were discussed in 1.4.4. This chapter limited its scope to the design and perceived nonlinear optimisation limitations. The conservation of small beam sizes to keep an ultra-low emittance naturally requires strong focusing, producing large natural chromaticities. The necessarily strong sextupoles to correct the former are foreseen to limit the dynamics and stability of such lattices. To compensate for the inclusion of strong sextupoles, two main lattice schemes were developed. One is the hybrid lattice applying the non-interleaved principle, with two dispersion bumps for both a compensation of the sextupole kicks and a higher sextupole efficiency. The other is the HOA lattice, of which the inherent phase advances cancel or rather minimise the resonant driving terms over a period. Both schemes are applied to the SOLEIL 2.75 GeV upgrade storage ring, and compared in the next chapter.

# Chapter 3

# Ultra-low emittance schemes for SOLEIL upgrade

The MBA lattices integrating chromaticity correction schemes such as the two introduced in the previous section were applied to the SOLEIL storage ring. Specific constraints for the case of the SOLEIL upgrade were taken into account. This section reviews and compares the linear lattices, and their first nonlinear limitations. While the hybrid lattice was designed by one of my SOLEIL colleagues, A. Loulergue [108], I was one of the initiators in the development of a suitable HOA lattice for the SOLEIL storage ring. All studies and lattices presented in this section are the outcomes of my own analysis, unless stated otherwise.

**Constraints of the SOLEIL upgrade** The upgrade of the storage ring aims at decreasing the natural horizontal emittance of the electron beam below 100 pm.rad, while conserving its main characteristics. Its nominal energy should be conserved, to maintain the current energy range of the synchrotron radiation on the beamlines. Furthermore, the new lattice should fit in the current tunnel of the storage ring, fixing its circumference.

Table 3.1: General constraints applied to the ultra-low emittance lattice design for the upgrade of the SOLEIL storage ring.

| | |
|---|---|
| Storage ring energy | 2.75 GeV |
| Circumference | 354 m |
| Emittance | $< 100$ pm.rad |
| Straight section length | $> 4.4$ m |
| $(\beta_x, \beta_y)$ @ID | (1-3, 1-3) m |

Further constraints are imposed by the necessary RF cavities and insertion devices in the straight sections. To better match the electron beam in the insertion devices, the $\beta$-functions should remain low in the middle of the straight sections. This chapter studies and discusses the application of the two ultra-low emittance lattice schemes introduced in 2.3. As a study case, both schemes will be used in the design of 7BA lattices, with a 20-fold symmetry.

## 3.1 Non-interleaved scheme applied to the SOLEIL case

Figure 3.1 presents the layout of a 7BA hybrid lattice designed for the SOLEIL upgrade by A. Loulergue [108]. The two external dipoles were moved away from the core, to allow the growth of two dispersion bumps of 8 cm; under each of them are located five sextupoles. The matching of the bump is ensured by one antibend, which is split in two to locate a focusing sextupole in between, for increased efficiency and phase advance matching following the non-interleaved principle. The tight core is composed of four repetitive cells, which alternate dipoles and reverse bends.

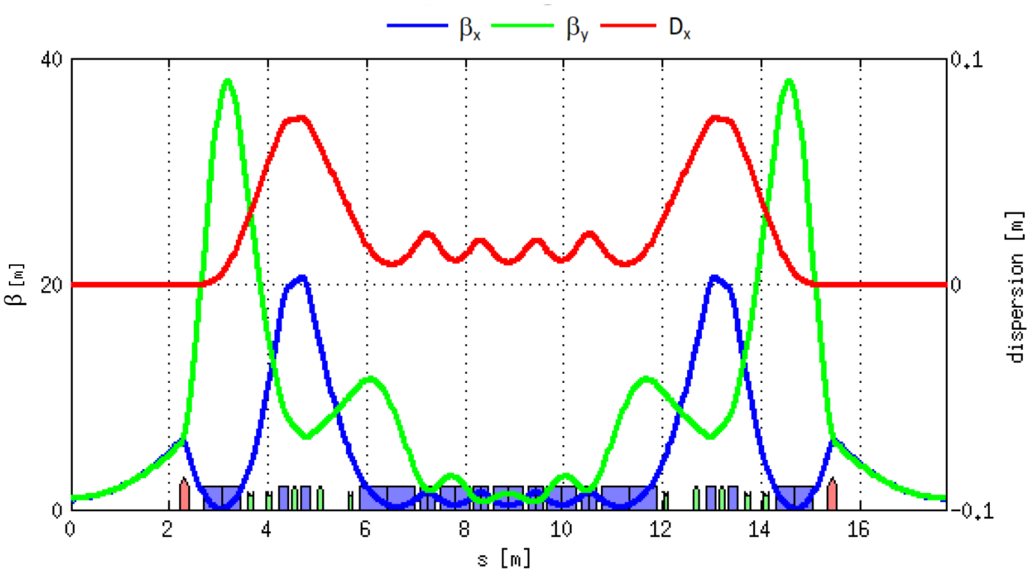

FIGURE 3.1: Twiss functions and magnet layout of the 7BA hybrid lattice for the SOLEIL 2.75 GeV storage ring, available in [108].

The dispersion-free section, necessary for the insertion devices, is created with a reduced length of the external dipoles, and by modulating its distance with the external antibend. The $\beta$-functions are matched at the middle of the straight section with only a focusing quadrupole and the external combined-function dipole.

### 3.1.1 Inclusion of reversed bends

To further reduce the emittance creation in the dipoles, reverse bending magnets are inserted in the lattice, in place of the core focusing quadrupoles. Their angle is to be adjusted, to minimise the emittance over the whole lattice. The exercise was made for the hybrid lattice, as illustrated in Fig. 3.2. A program was written in Accelerator Toolbox (A.T.) [109] which expands the emittance and the momentum compaction variations with regard to the reverse bending angles, over a hybrid period. This program assumes the reverse bending angles to be identical. The total angle was continuously corrected to restore the right period angle.

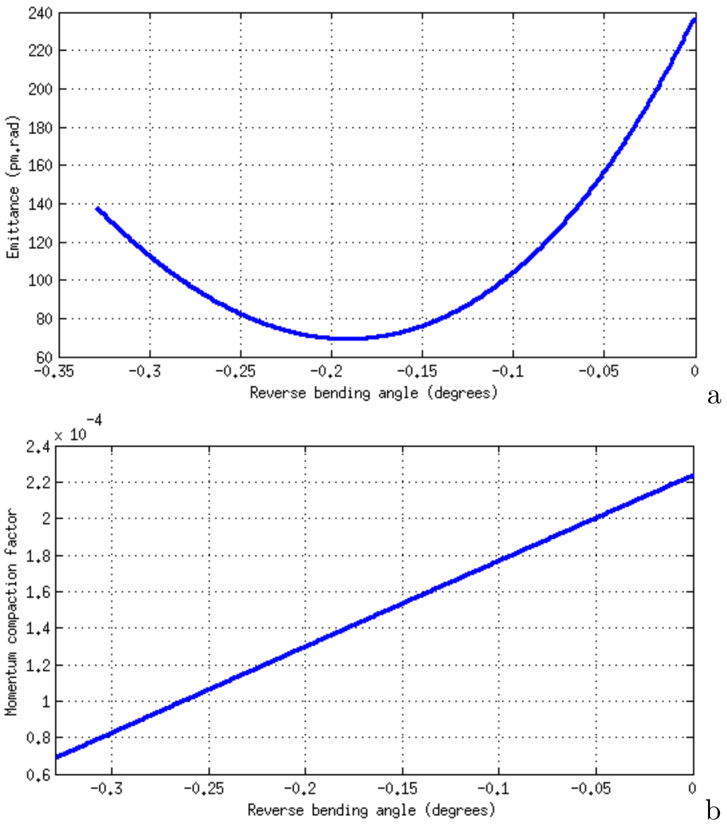

FIGURE 3.2: Effect of reversed bending magnets in a hybrid lattice on its emittance (a) and momentum compaction factor(b).

The emittance reaches a minimum of $\simeq$ 70 pm.rad for an antibend angle of $-0.18$ degrees, in Fig. 3.2 (a). The existence of the minimum is due to the parabolic dependence of the $\mathcal{H}$-function with the dispersion. In Fig. 3.2 (b), the momentum compaction factor depends linearly on the dispersion versus the bending radius: therefore, the increase in the reverse bending angle increases the negative ratio dispersion versus bending radius in the antibends, thus reducing the momentum compaction factor. For an angle of $-0.18$ degrees in the antibends, where the minimum emittance is achieved, the momentum compaction factor values $1.376 \times 10^{-4}$, which is large enough to be considered stable.

### 3.1.2 General characteristics of the 7BA hybrid lattice proposal for the SOLEIL upgrade

Table 3.2 gathers the general characteristics of the 7BA hybrid lattice designed for the upgraded SOLEIL storage ring. The high tunes and large chromaticities are the result of the strong focusing. The lattice includes reverse bending magnets, of angle $-0.160$ degrees in place of the inner focusing quadrupoles: the natural horizontal emittance achieved is 72 pm.rad, a reduction of a factor 54 with respect to that of the current SOLEIL lattice. The $-I$ transformation occurs between the two dispersion bumps with a fixed phase advance of $(3\pi, \pi)$, which ensures the compensation of the sextupole kicks located under the bump. The core dipoles are 1.2 m long, both to ensure a low natural emittance and low losses. The total energy loss per turn is $20 \times 15.5\,\text{keV} = 310\,\text{keV}$, which is three times lower than the current SOLEIL lattices - dipoles only.

Table 3.2: SOLEIL 2.75 GeV 7BA (-I) lattice, 20-fold symmetry.

| | |
|---|---|
| Emittance $\epsilon_x$ | 72 pm.rad |
| Tunes per period $(\nu_x, \nu_y)$ | (2.76, 0.91) |
| Momentum compaction factor $\alpha_0$ | $1.47 \times 10^{-4}$ |
| Reverse bending angle | -0.160 degrees |
| Energy loss per period | 15.5 keV |
| $(\beta_x, \beta_y)$ @ID | (1.0, 1.0) m |

The $\beta$-functions in the middle of the straight sections are matched at $(\beta_x, \beta_y) = (1.0, 1.0)$ m using only the last 0.72 m-long dipole and an additional focusing quadrupole, leaving space for the a possible harmonic sextupole or octupole. The choice of the $(\beta_x, \beta_y)$ functions relies on the beam matching considerations described in 1.4.1.2. For an undulator of 4 m, the matching is ensured for $\beta = \frac{L}{\pi} \simeq_{L=4\,\text{m}} 1.27\,\text{m}$.

### 3.1.2.1 Transverse dynamic apertures

The $-I$ transformation largely increases the on-momentum dynamic aperture, as illustrated in Fig. 3.3. The trajectory of the particles was simulated during 1000 turns in the transverse plane, in the momentum deviation range $\delta = \pm 10\%$. The physical apertures were set to 5 mm on each plane, with no alteration of the dynamic area.

As expected, the non-interleaved principle creates a distinct peak around $\delta = 0$ in the horizontal and vertical dynamic apertures. Yet, the presence of several sextupoles under the dispersion bump perturbs the compensative effects of the set phase advance. The peak is non-discreet and is in the real lattice, defined by a zone in the vicinity of the on-momentum particle. As several sextupoles are located under the same bump, they each other perturb the non-interleaved principle of the others, therefore annulling the complete cancellation theoretically expected. Nevertheless, compensation occurs, and still enlarges the on-momentum dynamic aperture, both in the horizontal and vertical planes.

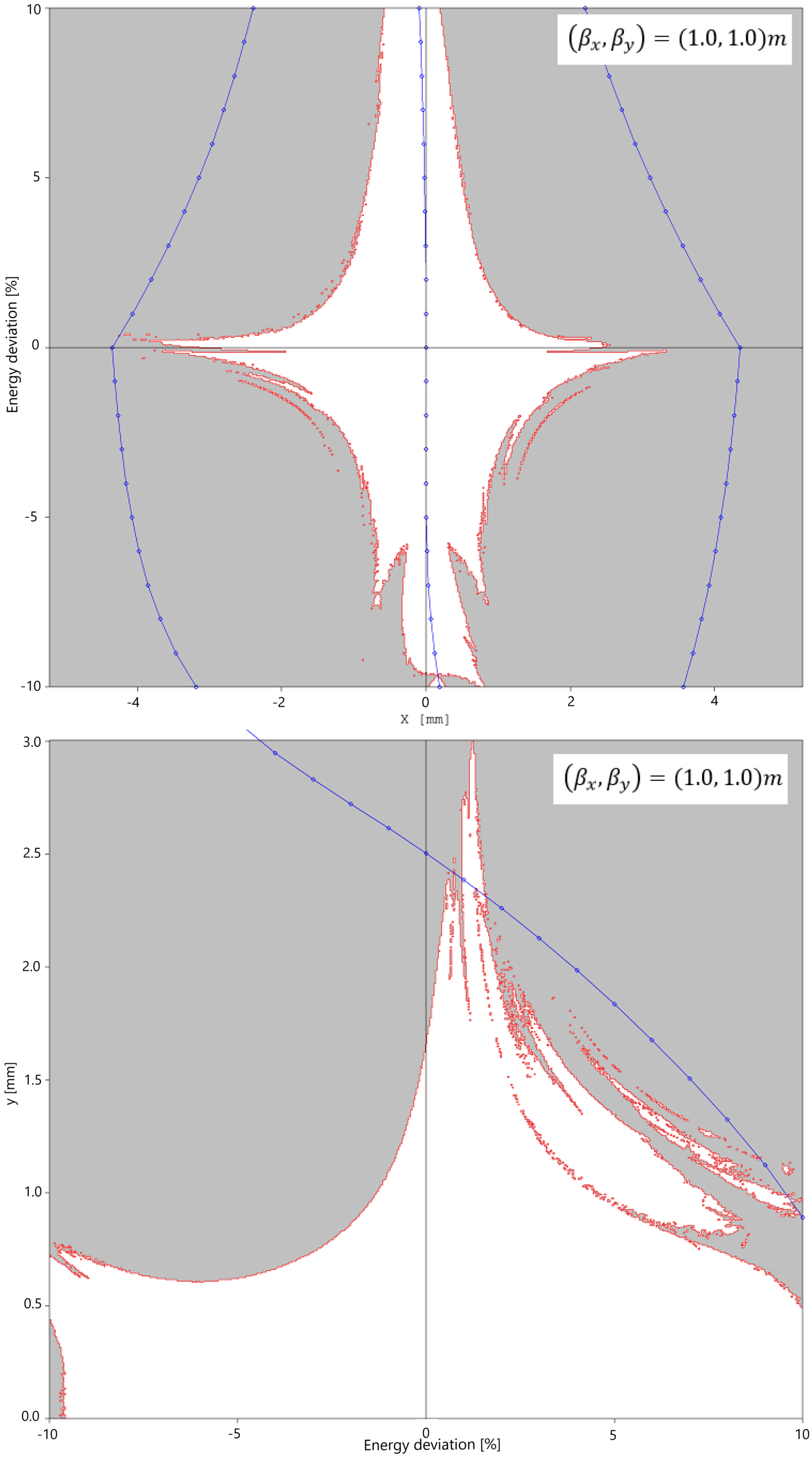

FIGURE 3.3: Horizontal dynamic apertures with energy deviation of the 7BA hybrid SOLEIL lattice.

## 3.2 Design of a 7BA HOA lattice for SOLEIL storage ring

Further analysis of the reduction of dynamic aperture with the 6D tracking in the hybrid lattice motivated me to study and develop a High-Order Achromat (HOA) lattice. I was in charge of implementing this scheme, taking into account the SOLEIL tunnel constraints, and designed several proposals. This section describes the process followed and required considerations.

### 3.2.1 Study of an unit cell

As discussed in section 2.3.2, the design of a HOA lattice starts with an unit cell, in which the phase advance is fixed. The choice of the phase advance is discussed in 3.2.3.

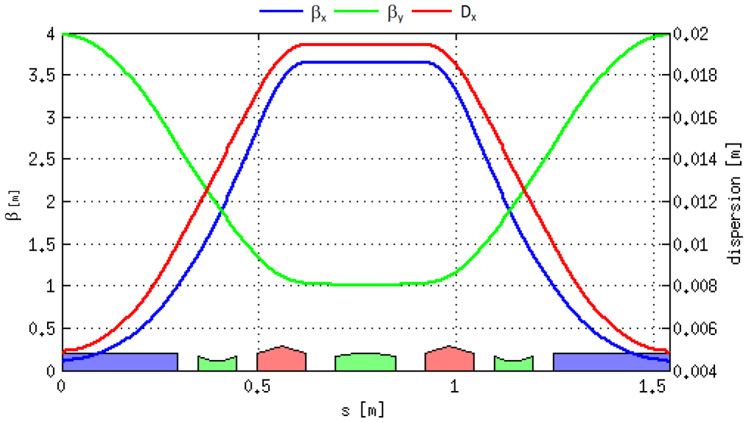

FIGURE 3.4: Twiss parameters and layout of a HOA unit cell, of which phase advance is $(\nu_x, \nu_y) = (\frac{3}{7}, \frac{1}{7})$ and a 0.30 m long half-dipole.

A unit cell is a symmetric FODO-like cell: it is composed of two focusing quadrupoles per dipole. The defocusing is ensured by combined-function dipoles. The distance between linear magnets and their strengths fix the phase advance. Chromaticities are corrected locally: the unit cell introduces a focusing sextupole in its centre, where the relation between $\beta_x$ and $\beta_y$ is maximum, and two defocusing sextupoles between the quadrupoles and the dipoles. Altogether, one unit cell is composed of six magnets. Figure 3.4 displays the Twiss parameters and the layout of an HOA unit cell, of fixed phase advance $(\nu_x, \nu_y) = (\frac{3}{7}, \frac{1}{7})$, with a half-dipole of 0.30 m long. The resulting total length of the unit cell is 1.55 m.

The emittance created in an unit cell depends on both its phase advance and the length of the bending elements. Together they determine the periodic conditions of the Twiss functions and dispersion. Figure 3.5 shows the variation of emittance in relation to the length of the half-dipole. Calculations were conducted using A.T., developed at the ESRF. The unit cell considered was composed of two focusing quadrupoles, each 0.125 m long.

The bending angle was kept constant during the whole process. Step by step, the dipole length was decreased, from 0.4 m to 0.2 m. The phase advance of the unit cell was

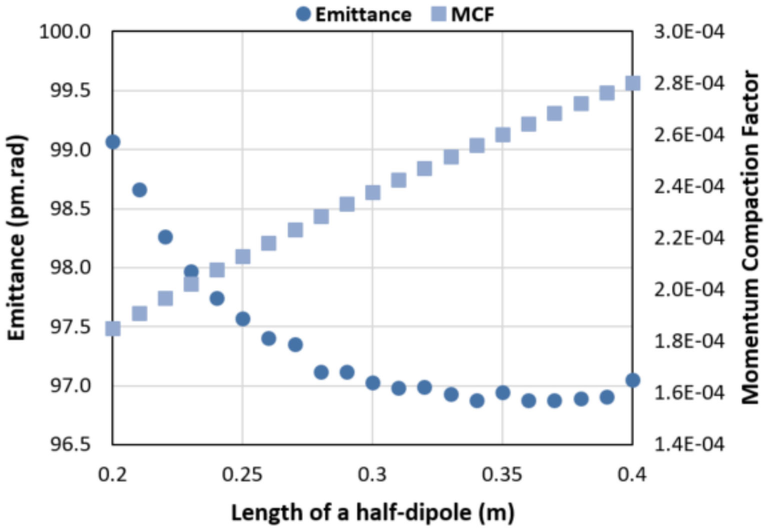

FIGURE 3.5: Variation of the emittance and the momentum compaction factor (MCF in the figure) with the unit cell half-dipole length.

matched at each step, to the fixed value $(\nu_x, \nu_y) = (\frac{3}{7}, \frac{1}{7})$, using the quadrupoles and the defocusing strengths of the dipoles. The value of the emittance rapidly decreases from 0.2 m to 0.3 m, to reach a plateau. The shorter the dipoles, the higher the quadrupole strengths to match the phase advance. The new periodic condition imposed a lower dispersion at the start of the unit cell. Yet, the large variation of the dispersion to reach its central value increased the emittance created in the dipoles.

When the plateau is reached at about $l_{dip} = 0.30$ m, the interesting value to look at is the variation of the momentum compaction factor, which increases with the length of the half-dipole. Yet, the limitations imposed by the total circumference of the ring prevent long dipoles for the design of a 7BA lattice. Indeed, a 7BA period is limited to $354/20 = 17.7\,\text{m}$, among which a 4.5-5 m straight section, leaving 13.2 m for the magnets. Assuming the total matching sections of the same length as an unit cell, the maximum length of a HOA unit cell is $13.2/(7-8) = 1.6 - 1.8\,\text{m}$ for a 4.5 m straight section. To ensure a large enough straight section and space for the matching section, the half-dipoles were set at a length of 0.30 m, for a unit cell of length 1.55 m.

### 3.2.2 Inclusion of reverse bends

Since a compromise must be reached between the emittance $\epsilon_x$ and the momentum compaction factor $\alpha_C$, previously described in 3.1.1, Figure 3.6 compares the variation of the emittance and the momentum compaction factor whilst increasing the reverse bending angle. The total angle was continuously corrected to restore the right period angle. The emittance reaches its minimum of 35 pm.rad for an antibend angle of $-0.6$ degrees. For an angle of $-0.6$ degrees in the antibends, the value of the momentum compaction factor surrounds $5 \times 10^{-5}$, which is lower than the ideal value of $1 \times 10^{-4}$ (*cf* Table 3.1).

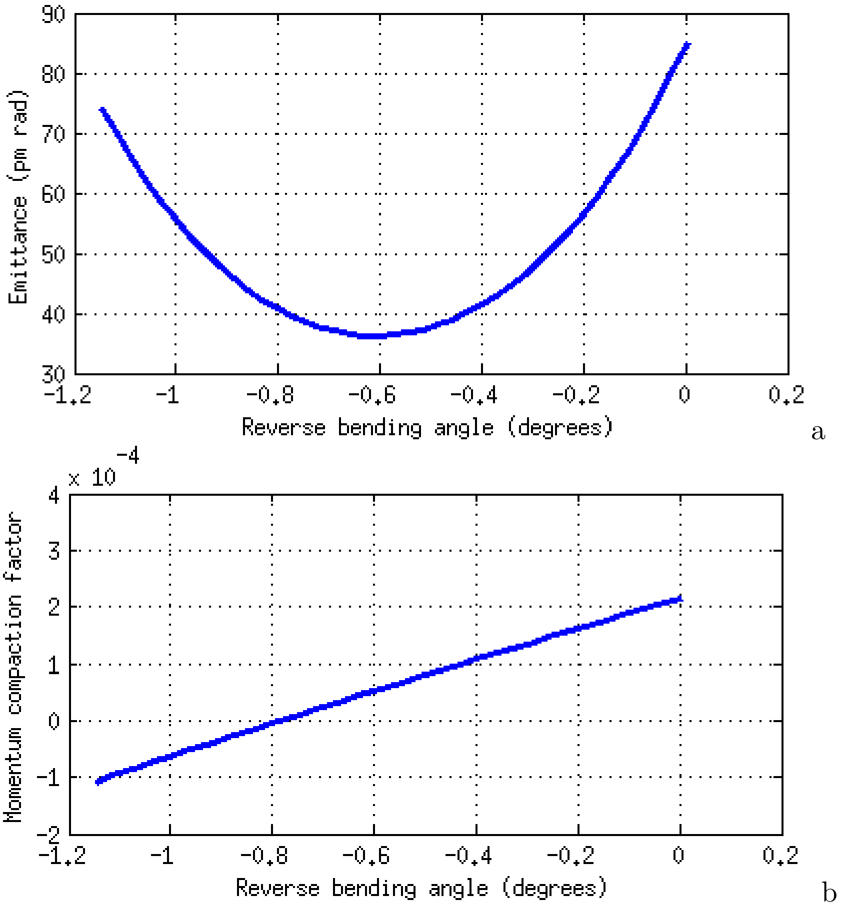

FIGURE 3.6: Effect of reverse bends in a HOA lattice on its emittance (a) and momentum compaction factor (b).

This comparison does not include the contribution of the matching and dispersion-free straight sections to the momentum compaction factor, which forms about a third of the 7BA period, further reducing it. To compensate the absence of dispersion in the above two sections, a higher momentum compaction factor is needed in the unit cells. Furthermore, such a low emittance is not required: constraints suggest an emittance of $\simeq 70$ pm.rad. Therefore, the reverse bending angle was set at $-0.10$ degrees, where the emittance is 53 pm.rad, and the momentum compaction factor $1.55 \times 10^{-4}$. The value of the emittance will slightly increase when implementing the achromatic condition, in sec. 3.2.4, and approach the natural horizontal emittance of the hybrid lattice.

Figure 3.7 compares the Twiss functions and the dispersion of the unit cell in Fig. 3.4 without (top) and with the inclusion of reverse bending angle (bottom). The dispersion knows an offset with the addition of the reverse bends: it is as low as 4 mm at the entrance of the dipoles, with a decreased slope, compared to a value of 5 mm and a higher slope in the basic unit cell.

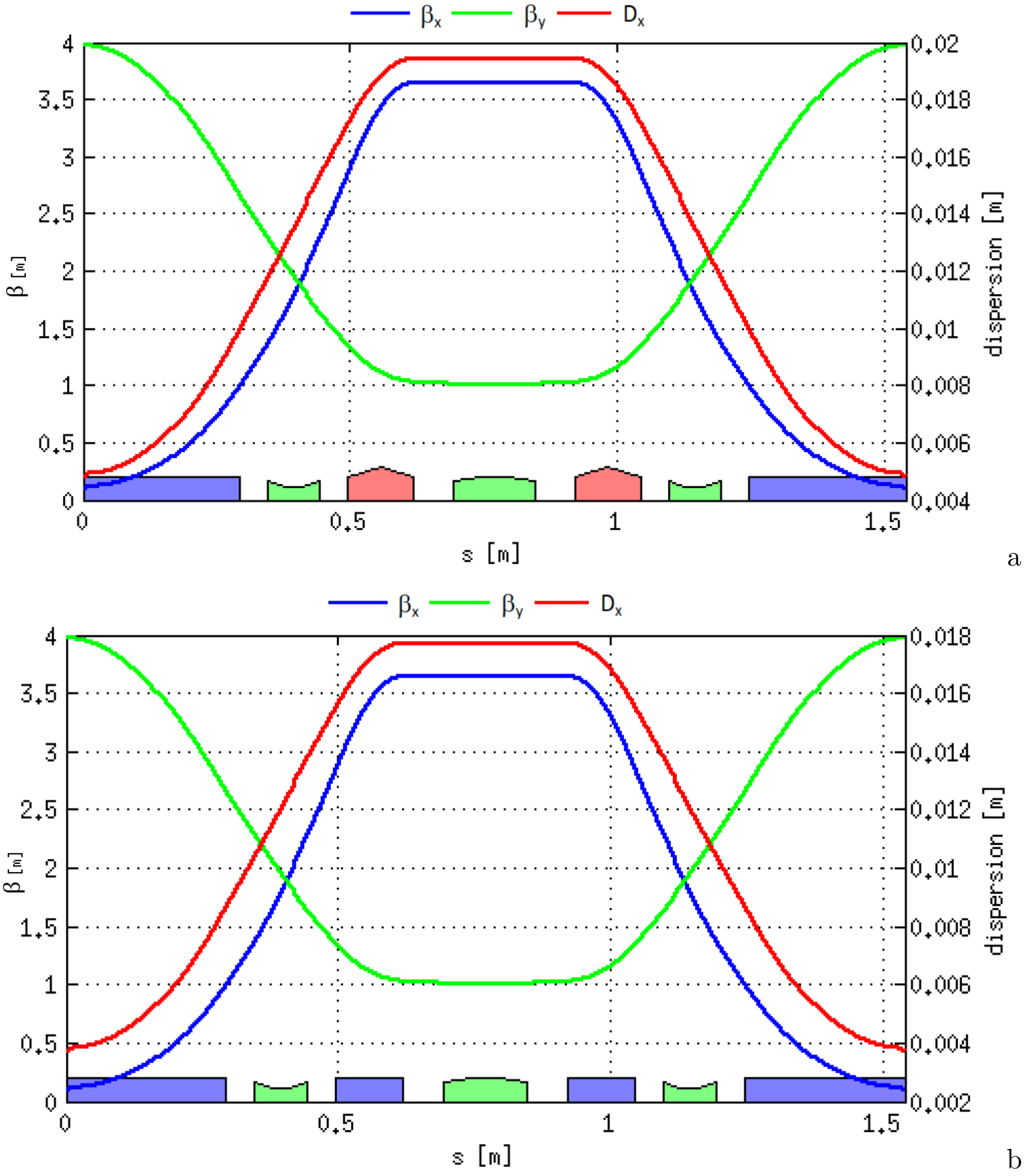

FIGURE 3.7: Twiss parameters and layout of a HOA unit cell, which phase advance is $(\nu_x, \nu_y) = (3/7, 1/7)$, a half-dipole of length 0.30 m (a) without and with (b) a reverse bending angle of $-0.10$ degrees in the inner bends.

### 3.2.3 Choice of the unit cell phase advance

The phase advance plays an essential role in the performances of a HOA lattice, as it ensures the cancellation of perturbative resonances. Ref. [48] discusses the depth of such cancellation over a 5BA and a 7BA HOA lattices. The phase advance chosen in the literature, $(\nu_x, \nu_y) = (\frac{3}{7}, \frac{1}{7})$ cancels geometric resonances up to the second-order in perturbation, over a set of seven unit cells.

#### 3.2.3.1 Discussion for a 7BA lattice

To understand the phase advance over an unit cell, I listed their possible values for a 7BA HOA lattice, which cancel at least the first-order resonances in terms of sextupolar strength, and computed the geometric resonances. For the repetition of seven cells, the phase advances considered are $(\frac{a}{7}, \frac{b}{7})$, with $b < a < 7$. Notice that the vertical phase advance is kept smaller than the horizontal one, to prevent unnecessary increase of the chromaticity by forcing a large vertical tune. It applies to the horizontal tune as well: if possible, it is to be kept as low as possible, thus I chose to limit the investigation to $\nu_x < 0.5$.

Table 3.3: Investigation of the geometric and chromatic resonances excited by different phase advances of a HOA unit cell.

| $\nu_y$ —$\nu_x$ | 1/7 | 2/7 | 3/7 |
|---|---|---|---|
| 1/7 | $2\nu_x - 2\nu_y$ | $\nu_x - 2\nu_y$ | $\nu_x - 4\nu_y$, $3\nu_x + 2\nu_y$ |
| 2/7 | $\nu_x - 4\nu_y$, $3\nu_x + 2\nu_y$ | $2\nu_x - 2\nu_y$ | $\nu_x + 2\nu_y$ |
| 3/7 | $\nu_x + 2\nu_y$ | $\nu_x + 4\nu_y$, $3\nu_x - 2\nu_y$ | $2\nu_x - 2\nu_y$ |

Mathematically, for no geometric resonance to be triggered, linear combinations of $a$ and $b$ should not be a multiple of 7. Table 3.3 summarises the excited resonances per couple of phase advances. In blue are highlighted third-order resonances in perturbation, limiting the possible phase advances to a single possibility: $(\nu_x, \nu_y) = (\frac{3}{7}, \frac{1}{7})$. The full resonance table of this case is in Table 3.4.

To further justify this choice, the dependence of emittance on each phase advance is analysed. Figure 3.8 displays the variation of the emittance of the HOA unit cell illustrated in Fig. 3.4, with regards to its horizontal (a) and vertical (b) phase advance around the working point $(\nu_x, \nu_y) = (\frac{3}{7}, \frac{1}{7})$. The betatron phase advances are matched with the quadrupole strengths of the unit cell. The horizontal phase advance is scanned in the range $[\frac{1}{7} : \frac{3.4}{7}]$, with a fixed vertical phase advance $\nu_y = \frac{1}{7}$. The emittance decreases with the horizontal phase advance, to a minimum plateau at around $\nu_x \in [0.4 : 0.43]$, before further increase, due to the proximity of the half-integer resonance. The emittance is here function of the focusing forces in the unit cell which both influence on the $\beta$-functions and the dispersion function.

Table 3.4: Variation of the first-order chromatic resonances and up to the third-order perturbation resonances over a 7BA HOA cell, with a fixed phase advance of $(\nu_x, \nu_y) = (\frac{3}{7}, \frac{1}{7})$ per unit cell.

| | | | **First order** | | | | | | **Second order** | | | | **Third order** | | | | |
|---|---|---|---|---|---|---|---|---|---|---|---|---|---|---|---|---|---|
| | | | **Geometric** | | | | **Chromatic** | | **Geometric** | | | | **Geometric** | | | | |
| **Cell** | $\nu_x$ | $\nu_y$ | $\nu_x$ | $3\nu_x$ | $\nu_x - 2\nu_y$ | $\nu_x + 2\nu_y$ | $2\nu_x$ | $2\nu_y$ | $4\nu_x$ | $4\nu_y$ | $2\nu_x - 2\nu_y$ | $2\nu_x + 2\nu_y$ | $5\nu_x$ | $\nu_x - 4\nu_y$ | $\nu_x + 4\nu_y$ | $3\nu_x - 2\nu_y$ | $3\nu_x + 2\nu_y$ |
| **1** | **0.429** | **0.143** | 0.429 | 1.286 | 0.143 | 0.714 | 0.857 | 0.286 | 1.714 | 0.571 | 0.571 | 1.143 | 2.143 | -0.143 | 1.000 | 1.000 | 1.571 |
| **2** | **0.857** | **0.286** | 0.857 | 2.571 | 0.286 | 1.429 | 1.714 | 0.571 | 3.429 | 1.143 | 1.143 | 2.286 | 4.286 | -0.286 | 2.000 | 2.000 | 3.143 |
| **3** | **1.286** | **0.429** | 1.286 | 3.857 | 0.429 | 2.143 | 2.571 | 0.857 | 5.143 | 1.714 | 1.714 | 3.429 | 6.429 | -0.429 | 3.000 | 3.000 | 4.714 |
| **4** | **1.714** | **0.571** | 1.714 | 5.143 | 0.571 | 2.857 | 3.429 | 1.143 | 6.857 | 2.286 | 2.286 | 4.571 | 8.571 | -0.571 | 4.000 | 4.000 | 6.286 |
| **5** | **2.143** | **0.714** | 2.143 | 6.429 | 0.714 | 3.571 | 4.286 | 1.429 | 8.571 | 2.857 | 2.857 | 5.714 | 10.714 | -0.714 | 5.000 | 5.000 | 7.857 |
| **6** | **2.571** | **0.857** | 2.571 | 7.714 | 0.857 | 4.286 | 5.143 | 1.714 | 10.286 | 3.429 | 3.429 | 6.857 | 12.857 | -0.857 | 6.000 | 6.000 | 9.429 |
| **7** | 3.000 | 1.000 | **3.000** | **9.000** | **1.000** | **5.000** | **6.000** | **2.000** | **12.000** | **4.000** | **4.000** | **8.000** | **15.000** | **-1.000** | **7.000** | **7.000** | **11.000** |

Table 3.5: Variation of the first-order chromatic resonances and up to the third-order perturbation resonances over 11 unit cells, with a fixed phase advance of $(\nu_x, \nu_y) = (\frac{4}{11}, \frac{3}{11})$ per unit cell.

| | | | **First order** | | | | | | **Second order** | | | | **Third order** | | | | |
|---|---|---|---|---|---|---|---|---|---|---|---|---|---|---|---|---|---|
| | | | **Geometric** | | | | **Chromatic** | | **Geometric** | | | | **Geometric** | | | | |
| **Cell** | $\nu_x$ | $\nu_y$ | $\nu_x$ | $3\nu_x$ | $\nu_x - 2\nu_y$ | $\nu_x + 2\nu_y$ | $2\nu_x$ | $2\nu_y$ | $4\nu_x$ | $4\nu_y$ | $2\nu_x - 2\nu_y$ | $2\nu_x + 2\nu_y$ | $5\nu_x$ | $\nu_x - 4\nu_y$ | $\nu_x + 4\nu_y$ | $3\nu_x - 2\nu_y$ | $3\nu_x + 2\nu_y$ |
| **1** | **0.364** | **0.273** | 0.364 | 1.091 | -0.182 | 0.909 | 0.727 | 0.545 | 1.455 | 1.091 | 0.182 | 1.273 | 1.818 | -0.727 | 1.455 | 0.545 | 1.636 |
| **2** | **0.727** | **0.545** | 0.727 | 2.182 | -0.364 | 1.818 | 1.455 | 1.091 | 2.909 | 2.182 | 0.364 | 2.545 | 3.636 | -1.455 | 2.909 | 1.091 | 3.273 |
| **3** | **1.091** | **0.818** | 1.091 | 3.273 | -0.545 | 2.727 | 2.182 | 1.636 | 4.364 | 3.273 | 0.545 | 3.818 | 5.455 | -2.182 | 4.364 | 1.636 | 4.909 |
| **4** | **1.455** | **1.091** | 1.455 | 4.364 | -0.727 | 3.636 | 2.909 | 2.182 | 5.818 | 4.364 | 0.727 | 5.091 | 7.273 | -2.909 | 5.818 | 2.182 | 6.545 |
| **5** | **1.818** | **1.364** | 1.818 | 5.455 | -0.909 | 4.545 | 3.636 | 2.727 | 7.273 | 5.455 | 0.909 | 6.364 | 9.091 | -3.636 | 7.273 | 2.727 | 8.182 |
| **6** | **2.182** | **1.636** | 2.182 | 6.545 | -1.091 | 5.455 | 4.364 | 3.273 | 8.727 | 6.545 | 1.091 | 7.636 | 10.909 | -4.364 | 8.727 | 3.273 | 9.818 |
| **7** | **2.545** | 1.909 | 2.545 | 7.636 | -1.273 | 6.364 | 5.091 | 3.818 | 10.182 | 7.636 | 1.273 | 8.909 | 12.727 | -5.091 | 10.182 | 3.818 | 11.455 |
| **8** | **2.909** | **2.182** | 2.909 | 8.727 | -1.455 | 7.273 | 5.818 | 4.364 | 11.636 | 8.727 | 1.455 | 10.182 | 14.545 | -5.818 | 11.636 | 4.364 | 13.091 |
| **9** | **3.273** | **2.455** | 3.273 | 9.818 | -1.636 | 8.182 | 6.545 | 4.909 | 13.091 | 9.818 | 1.636 | 11.455 | 16.364 | -6.545 | 13.091 | 4.909 | 14.727 |
| **10** | **3.636** | **2.727** | 3.636 | 10.909 | -1.818 | 9.091 | 7.273 | 5.455 | 14.545 | 10.909 | 1.818 | 12.727 | 18.182 | -7.273 | 14.545 | 5.455 | 16.364 |
| **11** | 4.000 | 3.000 | **4.0** | **12.0** | **-2.0** | **10.0** | **8.0** | **6.0** | **16.0** | **12.0** | **2.0** | **14.0** | **20.0** | **-8.0** | **16.0** | **6.0** | **18.0** |

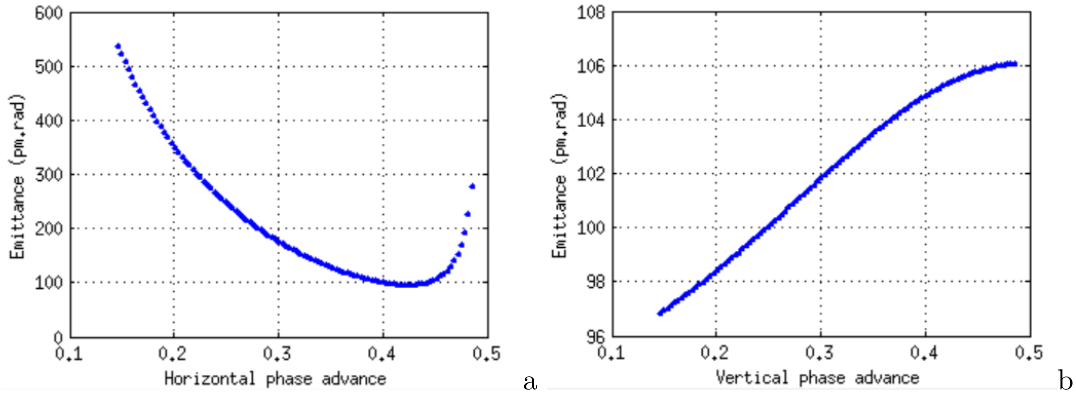

FIGURE 3.8: Variation of the emittance of a HOA unit cell of half-dipole 0.30 m, with regards to (a) its horizontal phase advance at a fixed vertical phase advance $\nu_y = \frac{1}{7} \simeq 0.1428$, and (b) its vertical phase advance with a fixed horizontal phase advance $\nu_x = \frac{3}{7} \simeq 0.4286$.

Similarly, the vertical phase advance is varied in the same range, with a fixed horizontal phase advance $\nu_x = \frac{3}{7}$. The emittance here seems proportional to the vertical phase advance, up until the vicinity of the integer and half-integer tune. While the variation of emittance with $\nu_x$ clearly states a minimum, its dependence with $\nu_y$ only comes from the dispersion creation in the dipole, and its defocusing quadrupolar strength. The smaller $\nu_y$ the lower the defocusing strength and the lower the emittance creation in the dipole. The minimum emittance is achieved for the working point $(\nu_x, \nu_y) = (\frac{3}{7}, \frac{1}{7})$.

#### 3.2.3.2 Alternative phase advances and MBA lattices

Nevertheless, two third-order geometric resonances remain. Cancellation of low-order resonances ensures their non-excitation by the sextupoles. Yet, the addition of necessary straight and matching sections perturbs the HOA strict phase advance rule. Moreover, the required straight sections are dispersion-free: a dispersion suppressor could perturb the phase advance (see 3.2.4).

To increase the number of combinations for the possible phase advances and possibly compensate the perturbation induced by the straight sections, this section discusses phase advances $(\nu_x, \nu_y) = (\frac{a}{p}, \frac{b}{p})$, with $a, b < p$ and $p$ prime. Further analysis is conducted for $p > 7$. The next smallest prime number after seven is 11, which can seem quite large - it would require an 11BA lattice, if the same rule is to be applied. To better compare the sets of phase advances, let us look for 11 close to $(\frac{3}{7}, \frac{1}{7})$, cancelling all geometric resonances, the third order included. Such a combination is $(\frac{4}{11}, \frac{3}{11})$: the full description of the resonances is in Table 3.5.

An example of an unit cell of phase advance $(\nu_x, \nu_y) = (\frac{4}{11}, \frac{3}{11})$ is displayed in Fig. 3.9, for a 0.30 m half-dipole and with a bending angle of $-0.10$ degrees. The resulting level of dispersion, fixed by the periodic condition, is higher than in the case $(\nu_x, \nu_y) = (\frac{3}{7}, \frac{1}{7})$, with an emittance of 73 pm.rad, instead of 53 pm.rad. The length of the dipole should be adjusted in this case, to monitor the emittance creation.

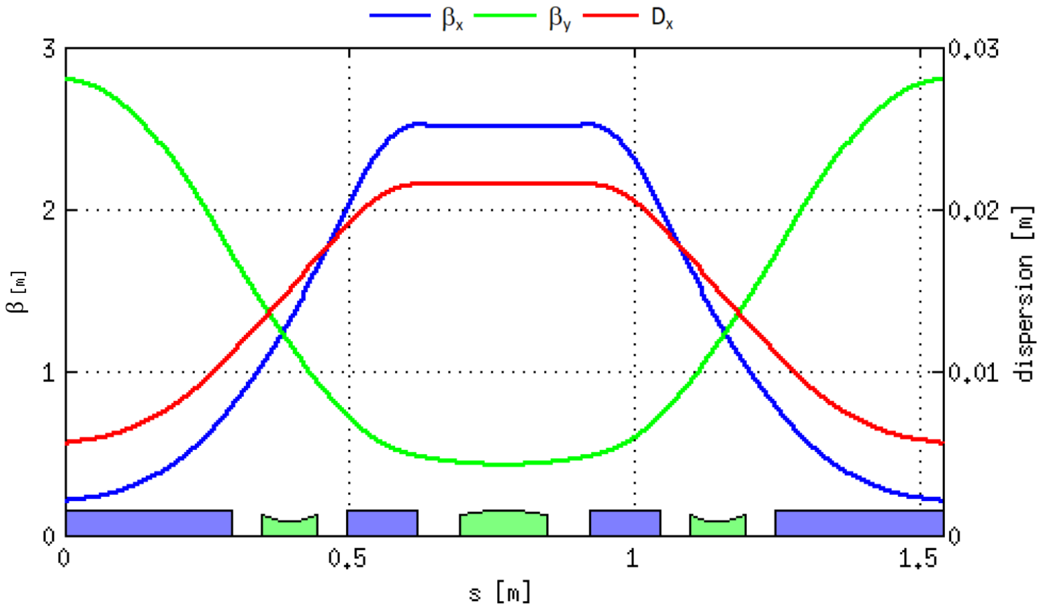

FIGURE 3.9: Unit cell with a half dipole of length 0.30 m, with a fixed phase advance $(\nu_x, \nu_y) = (\frac{4}{11}, \frac{3}{11})$.

To minimise losses and considering the minimum length of an unit cell, I designed a 9BA HOA lattice, with an unit cell phase advance of $(\nu_x, \nu_y) = (\frac{3}{11}, \frac{1}{11})$. The vertical tune is then minimised, and so is the natural vertical chromaticity. The horizontal tune is kept as a compromise between the length of the dipole and the lowest tune possible. Further analysis of this 9BA lattice is available in Appendix F.

### 3.2.4 Dispersion suppressor

To minimise the effect of this disruption on the HOA principle, two dispersion suppressors are discussed in this section. The first one is traditionally applied in MBA lattices and was introduced in the section (2.2.2), in the discussion of the passage from a DBA to a TBA lattice. The outermost dipoles are shortened by a factor close to 30%, allowing the dispersion to be lowered down to zero. Further matching is required using the quadrupoles available in the outer sections. Figure 3.10 illustrates the Twiss parameters after use of this method (top).

A second method aims at keeping the same phase advance in all dispersive cells, including the dispersion suppressor part of the period. To do so, the dispersion is cancelled by adjusting the angles of the extrema bending magnets, one dipole and one reverse bend. Since only the dispersion and the angles are varied by this method, the modification is transparent to the Twiss parameters thus the phase advance. The resulting extrema unit cell is displayed on the bottom of Fig. 3.10. After correction of the total angle, the new angles of the dipoles and antibends are: 1.5594 degrees (0.42 T) for core dipoles, 2.35 degrees (1.25 T) for extrema dipoles; -0.0975 degrees ($\Delta x = -0.89$ mm) for core antibends, -0.65 degrees ($\Delta x = -5.9$ mm) for extrema antibends.

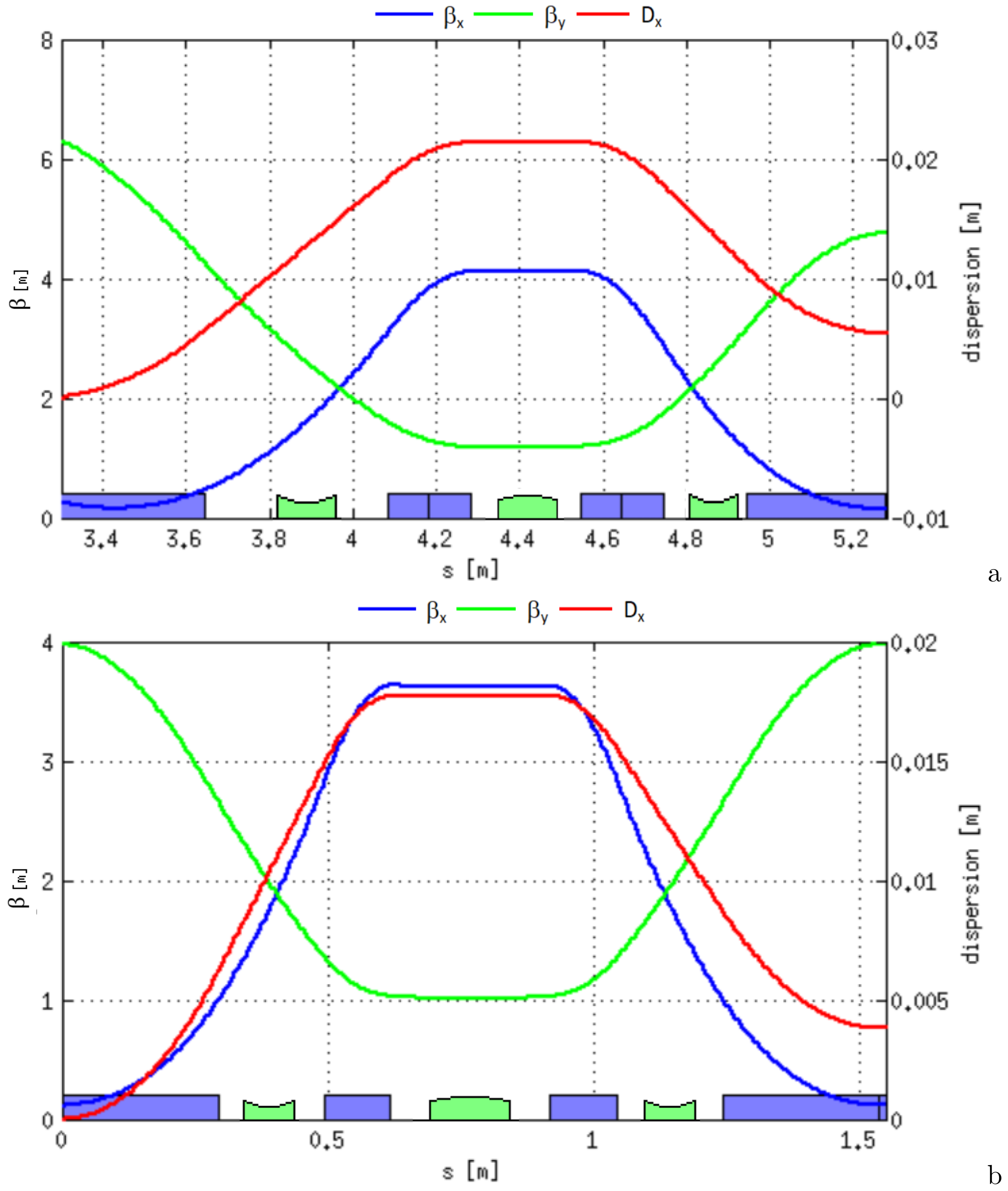

FIGURE 3.10: Matching of the dispersion-free zone by (a) reducing the extrema dipoles' length, and matching the Twiss parameters using the two last quadrupoles (b) modifying the bending angles, thus conserving the $\beta$-functions and the phase advance of the last unit cell.

Table 3.6 compares the main characteristics of the period designed out of both methods: their length, effect on the dynamic, and effect in the efficiency of the matching section required afterwards, to match the $\beta$-functions at the centre of the straight section. The characteristics of both lattices are similar. The traditional ”missing dipole” method has a higher horizontal tune, induced by the stronger focusing required to create the dispersion-free zone. The higher reverse bending angle of the angular method explains the difference in the momentum compaction factor and emittance.

Table 3.6: Comparison of main parameters for two methods for matching of the dispersion in a HOA lattice.

| | Traditional | Angular |
|---|---|---|
| Betatron tunes $(\nu_x, \nu_y)$ | (3.24, 1.15) | (2.57, 1.86) |
| Emittance | 76 pm.rad | 66 pm.rad |
| Momentum compaction factor $\alpha_C$ | $1.08 \times 10^{-4}$ | $5.50 \times 10^{-4}$ |
| Reverse bending angle | -0.048 degrees | -0.125 degrees |
| Energy loss | 20 keV | 27 keV |
| $(\beta_x, \beta_y)$ @ID | (2.7 m, 2.7 m) | (1.7 m, 1.7 m) |

The angular method was put in place to conserve the HOA principle over the dispersive area. Table 3.7 compares the values of the first-order Resonant Driving Terms (RDT) for both methods. The lattices were put at chromaticities $(\xi_x, \xi_y) = (-1, -1)$ using the core sextupole pairs. As expected, the RDTs of the angular method are satisfyingly low: the minimisation occurred thanks to the fixed phase advance of the unit cells.

Table 3.7: Values of the first-order resonant driving terms over one 7BA HOA period, for both dispersion suppressor methods. The chromaticity is fixed in both lattices to $(\xi_x, \xi_y) = (-1, -1)$.

| First-order sextupolar resonances | | Missing dipole | Angular |
|---|---|---|---|
| $\nu_x$ | $h_{21000}$ | 52.82 | 0.15 |
| $3\nu_x$ | $h_{30000}$ | 5.61 | 0.01 |
| $\nu_x$ | $h_{10110}$ | 11.20 | 0.41 |
| $\nu_x + 2\nu_y$ | $h_{10200}$ | 3.97 | 3.69 |
| $\nu_x - 2\nu_y$ | $h_{10020}$ | 7.26 | 0.64 |
| $2\nu_x$ | $h_{20001}$ | 1.04 | 5.93 |
| $2\nu_y$ | $h_{00201}$ | 0.93 | 1.17 |

In the case of the traditional missing dipole method, two RDTs predominate: $h_{21000}$, $h_{10110}$. Further minimisation is conducted on OPA. Table 3.8 compares the values of the RDTs and sextupoles (a) before and (b) after the minimisation. Small variations of the sextupoles are required to achieve the minimised RDTs below. Compared to the sextupoles of the angular method in the last columns, the values required for the traditional methods are either similar or lower, especially for the defocusing sextupoles.

Table 3.8: Values of the first-order resonant driving terms over one 7BA HOA period before and after optimisation, for the traditional ”missing dipole” dispersion suppressing method. The chromaticity is fixed in both lattices to $(\xi_x, \xi_y) = (-1, -1)$.

| First-order sextupolar resonances | | Before | After minimisation | Sextupoles | Before | After | Angular method |
|---|---|---|---|---|---|---|---|
| $\nu_x$ | $h_{21000}$ | 52.82 | 0.01 | SXF0 | $152.35\,\mathrm{m}^{-2}$ | $111.60\,\mathrm{m}^{-2}$ | $109.524\,\mathrm{m}^{-2}$ |
| $3\nu_x$ | $h_{30000}$ | 5.61 | 0.16 | SXD0 | $-93.2\,\mathrm{m}^{-2}$ | $-75.347\,\mathrm{m}^{-2}$ | $-121.50\,\mathrm{m}^{-2}$ |
| $\nu_x$ | $h_{10110}$ | 11.20 | 1.30 | SXF1 | $88.531\,\mathrm{m}^{-2}$ | $109.855\,\mathrm{m}^{-2}$ | $109.524\,\mathrm{m}^{-2}$ |
| $\nu_x + 2\nu_y$ | $h_{10200}$ | 3.97 | 5.69 | SXD1 | $-60.393\,\mathrm{m}^{-2}$ | $-69.344\,\mathrm{m}^{-2}$ | $-131.13\,\mathrm{m}^{-2}$ |
| $\nu_x - 2\nu_y$ | $h_{10020}$ | 7.26 | 1.45 | SX1 | $75\,\mathrm{m}^{-2}$ | $58.411\,\mathrm{m}^{-2}$ | $22.715\,\mathrm{m}^{-2}$ |
| $2\nu_x$ | $h_{20001}$ | 1.04 | 2.77 | SX2 | $-83.350\,\mathrm{m}^{-2}$ | $-64.624\,\mathrm{m}^{-2}$ | $-85.771\,\mathrm{m}^{-2}$ |
| $2\nu_y$ | $h_{00201}$ | 0.93 | 0.93 | | | | |

Figure 3.11 displays the transverse dynamic apertures of the 7BA HOA period, where the dispersion is suppressed by modifying the angles of the extrema dipoles and antibends. The good minimisation of the RDTs over the period, with no optimisation of the sextupoles, creates a highly homogeneous transverse stability area with regards to the energy deviation, with slight variations due to amplitude-dependent tune-shift terms, which can be corrected with the implementation of octupoles. The dynamic apertures for the standard method are displayed in Fig. 3.13. Although its dynamic aperture is not as symmetric as the angular method, the large on-momentum aperture is 1.5 times higher - considering the difference in the $\beta$-functions.

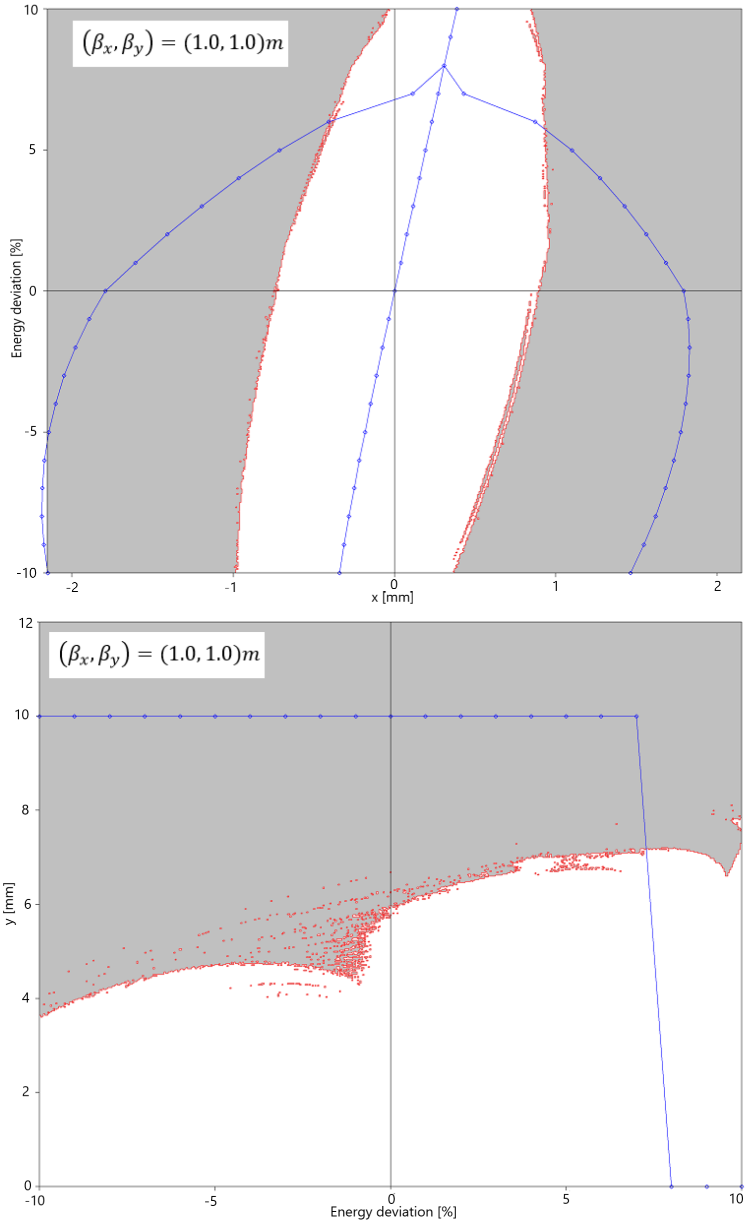

FIGURE 3.11: Transverse dynamic apertures achieved for a 7BA HOA lattice, of unit cell phase advance $(\nu_x, \nu_y) = (\frac{3}{7}, \frac{1}{7})$ and 0.6 m long dipoles, with the angular dispersion suppressor method.

Although the second method completely cancels the RDTs over a period, its matching of the $\beta$-function in the middle of the straight section proves more difficult and significantly increases the betatron tune. Moreover, the required angles for dispersion matching increase the energy loss. The standard dispersion suppressor leaves more space in the dispersive zone for nonlinear magnets, increasing the efficiency of the sextupoles. Its dipole could be lengthened to 0.4 m, as the matching section could be kept 1 m long, thus reducing the total losses over the period. For those practical reasons, this method is selected for the 7BA HOA SOLEIL storage ring proposal, to be compared with the hybrid lattice.

### 3.2.5 Layout of the 7BA HOA lattice proposal for the SOLEIL upgrade and general characteristics

The chosen HOA lattice for the upgrade studies of the SOLEIL storage ring is a 7BA lattice, composed of unit cells of betatron phase advances $(\frac{3}{7}, \frac{1}{7})$. Figure 3.12 displays the layout of the lattice, and its $\beta$-functions and dispersion, with thin sextupoles. Its general characteristics are available in Table 3.9.

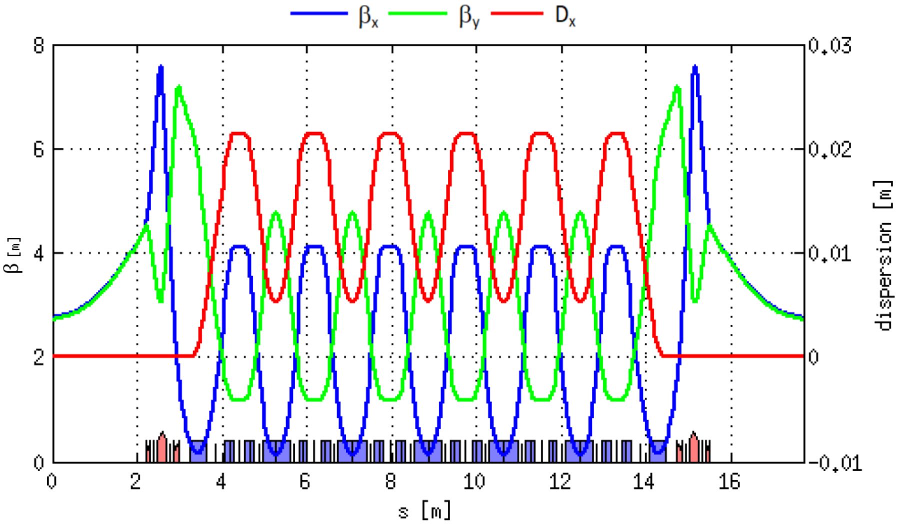

FIGURE 3.12: Twiss parameters and magnet layout of the 7BA HOA lattice for the SOLEIL 2.75 GeV storage ring.

Composed of five unit cells of phase advance $(\nu_x, \nu_y) = (\frac{3}{7}, \frac{1}{7})$, the variations of the $\beta$-functions are periodic in the core lattice. The HOA principle is perturbed by the dispersion suppressor cell, which integrates a longer half-dipole, placed further away from the antibend. Both their focusing strengths are varied for the matching of the dispersion, thus perturbing the phase advance of the half-cell. The dispersion reaches a maximum of 2.1 cm, at the centre of the core unit cells. The low $\beta$-functions do not exceed 7-8m in both planes: this induces larger betatron tunes and natural chromaticities, $(\xi_{x,\text{nat}}, \xi_{y,\text{nat}}) = (-7.18, -3.08)$. The $\beta$-functions are arbitrarily matched at $(\beta_x, \beta_y) = (2.7, 2.7)$ m at the centre of the straight section, placing the lattice near the beam matching requirements (*cf* sec. 1.4.1.2).

TABLE 3.9: SOLEIL 2.75 GeV 7BA HOA lattice proposal, 20-fold symmetry.

| | |
|---|---|
| Emittance $\epsilon_x$ | 76 pm.rad |
| Tunes per period $(\nu_x, \nu_y)$ | (3.24, 1.15) |
| Momentum compaction factor $\alpha_0$ | $1.09 \times 10^{-4}$ |
| Reverse bending angle | -0.048 degrees |
| Energy loss per period | 19.7 keV |
| $(\beta_x, \beta_y)$ @ID | (2.7, 2.7) m |

#### 3.2.5.1 Transverse dynamic aperture

The on-momentum dynamic aperture over 1000 turns of the present 7BA HOA lattice is displayed in Fig. 3.13 and 3.14. The dynamic aperture is calculated at the middle of the straight section. As expected with the minimisation of all first-order resonances following the HOA principle described in 3.2, the dynamic aperture of the 7BA HOA lattice is homogeneous with energy deviation, compared to that of the hybrid lattice. The cancellation of the first-order RDTs allows a transverse dynamic aperture frontiers driven by the tune shift, which can be further corrected with octupoles.

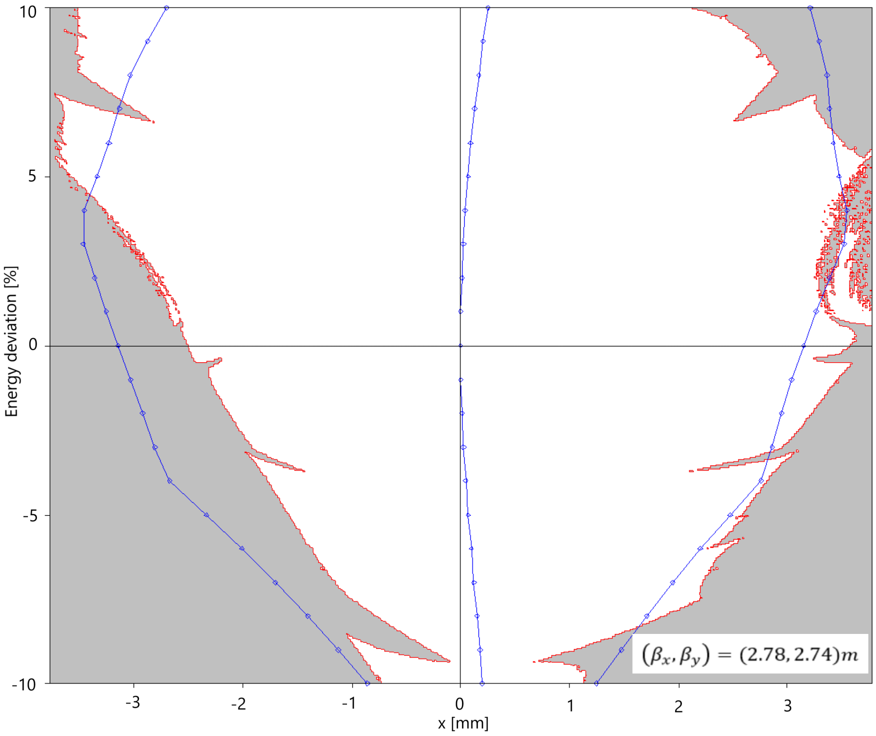

FIGURE 3.13: Horizontal dynamic aperture with energy deviation, for the chosen 7BA HOA lattice, of unit cell phase advance $(\nu_x, \nu_y) = (\frac{3}{7}, \frac{1}{7})$, and 0.8 m long dipoles. The dispersion-free is created with the ”missing dipole” method.

The HOA lattice presents a high stability in almost its entire dynamic aperture, ensuring the good cancellation of the sextupolar resonances. The transverse limits of the dynamic aperture are quasi-symmetric with the energy deviation, in both planes.

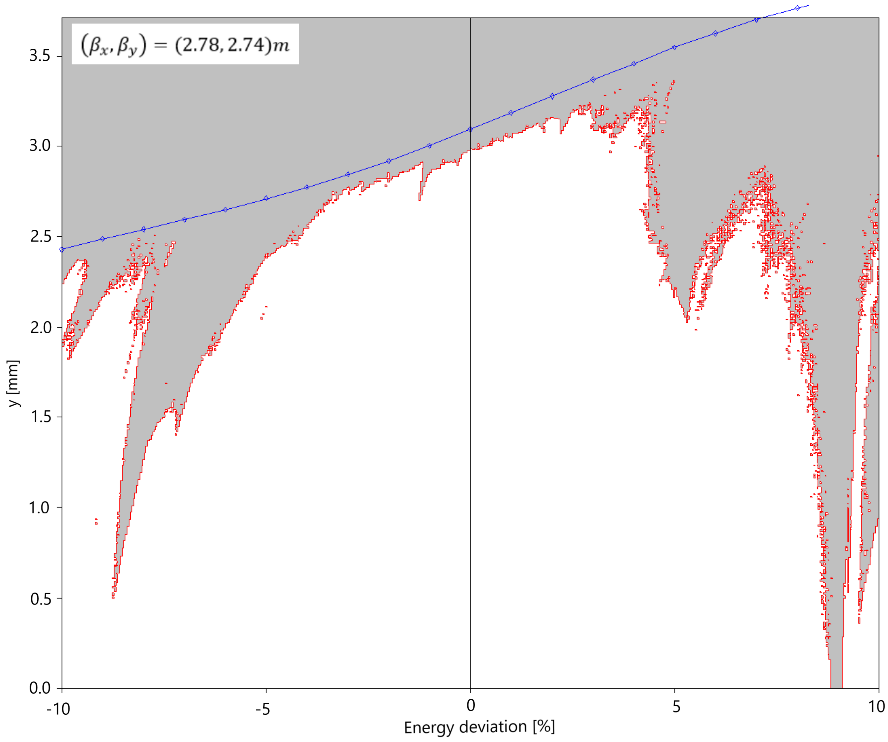

FIGURE 3.14: Vertical dynamic aperture with energy deviation, of the chosen 7BA HOA lattice, of unit cell phase advance $(\nu_x, \nu_y) = (\frac{3}{7}, \frac{1}{7})$, and 0.8 m long dipoles. The dispersion-free is created with the "missing dipole" method.

The on-momentum dynamic aperture reaches $\pm 2$ mm in the horizontal plane, $+3$ mm in the vertical plane, which remains lower than the hybrid lattice. Nonetheless, the performances off-momentum and the expected robustness of such lattice overcome the expectations of the hybrid lattice.

## 3.3 Comparison of the ultra-low emittance lattices with two different chromaticity correction schemes

This section summarises the important points of the detailed linear analysis of both ultra-low emittance 7BA lattices: a $-I$ hybrid lattice with a global correction of the chromaticity, and a HOA lattice with a local correction.

Their main characteristics are put side by side in the first part, linear mostly. The evolution process of both lattices are to be detailed, their efficiency in correcting the tune shift using octupoles, space, feasibility, manoeuvrability and robustness. All results presented in this section are the product of my own investigation. Their longitudinal dynamics are compared: further studies are conducted in this plane in Chapter (5).

### 3.3.1 Table of characteristics

Table 3.10 gathers the main linear parameters of both selected lattices adapted to the SOLEIL storage ring upgrade constraints. The targetted emittance are around 70 pm.rad, including small reverse bending angles. The betatron tunes are comparable, and fixed by the lattice scheme. The low vertical tune of the hybrid lattice is the result of strong focusing, which produces a high vertical natural chromaticity, comparable to its horizontal counterpart.

The $\beta$-functions at the centre of the straight section are of the same order, complying with the targeted electron beam size for the optimum electron-photon exchange (Eq. 1.16). Two differences remain: the momentum compaction factor and the energy loss. Despite having higher reverse bending angles than the HOA lattice, the hybrid lattice preserves a high momentum compaction factor thanks to its two dispersion bumps.

Table 3.10: Comparison of the main parameters of the designed 7BA Hybrid lattice and the 7BA HOA lattice for the study case of the SOLEIL upgrade.

| Scheme | Hybrid | HOA |
|---|---|---|
| Emittance $\epsilon_x$ | 72 pm.rad | 76 pm.rad |
| Tunes per period $(\nu_x, \nu_y)$ | (2.76, 0.91) | (3.24, 1.15) |
| Natural chromaticities $(\xi_x, \xi_y)$ | (-6.70, -6.25) | (-7.18, -3.08) |
| Momentum compaction factor $\alpha_0$ | $1.47 \times 10^{-4}$ | $1.0853 \times 10^{-4}$ |
| Reverse bending angle | -0.160/-0.165 degrees | -0.0477 degrees |
| Energy loss per period | 15.5 keV | 19.7 keV |
| $(\beta_x, \beta_y)$ @ID | (1.0, 1.0) m | (2.78, 2.74) m |

### 3.3.2 Magnetic characteristics

A major discrepancy between the two lattices is the number of sextupoles, and their strengths. Such information is available in Table 3.11. The hybrid scheme corrects the chromaticity globally, with sextupoles located under a dispersion bump. A minimum of two families are required per period, or six sextupoles magnets per period, considering the symmetry: two focusing and four defocusing sextupoles. The dispersion bump improves the efficiency of the sextupoles, thus reducing their required strengths. The HOA lattice inherently provides each of its unit cells with three sextupole magnets to correct the chromaticity directly at its source. For the 7BA HOA lattices considered, the minimum number of chromatic sextupoles rises to 18 per period, significantly higher than in the hybrid lattice.

Whilst the hybrid scheme optimises the chromatic correction and reduces the contribution of sextupoles in the lattice, the HOA scheme combines high natural chromaticity and low dispersion: the efficiency of its sextupoles is dramatically reduced. In addition, the large magnet occupation of the HOA lattice limits the length of the sextupole magnets, further limiting their efficiency. Managing the sextupoles will prove to be a non-trivial point in such a lattice. The lattice may make them transparent in terms of resonances, but does not optimise their chromaticity correction.

Table 3.11: Comparison of the composition in magnetic elements in the hybrid and the HOA lattice.

| | 7BA hybrid | 7BA HOA |
|---|---|---|
| Total number of magnets | 27 | 44 |
| of bends | 7 | 7 |
| of reverse bends | 8 | 12 |
| of focusing quadrupoles | 1 | 1 |
| of defocusing quadrupoles | 0 | 2 |
| of chromatic sextupoles (SF/SD) | 4/3 | 6/12 |
| of harmonic sextupoles | 0 | 2 |
| Magnet occupation | 50.41% | 58.88% |
| excluding $drifts < 0.15m$ | 66.01% | 77.67% |
| Core dipole lengths | 1.12 m/0.6 m | 0.8 m |
| Sextupole lengths | 0.10 m | SF: 0.20 m/ SD:0.10 m |
| Quadrupole strengths $k_1$ | | |
| in core bending magnets | $-4.14\,\mathrm{m}^{-2}$ | $-3.45\,\mathrm{m}^{-2}$ |
| in core reverse bends | $10.6\,\mathrm{m}^{-2}$ | $8.54\,\mathrm{m}^{-2}$ |
| in exterior bending magnets | $-1.15/-2.0\,\mathrm{m}^{-2}$ | $-1.49\,\mathrm{m}^{-2}$ |
| in exterior reverse bends | $3.3/3.7\,\mathrm{m}^{-2}$ | $6.70\,\mathrm{m}^{-2}$ |
| of the matching section | $-2.0/9.19\,\mathrm{m}^{-2}$ | $-9.48/10.76/-11.3\,\mathrm{m}^{-2}$ |
| Sextupole integrated strengths $k_2l$ | | |
| of focusing sextupoles | $15 \pm 5\,\mathrm{m}^{-2}$ | $125 \pm 25\,\mathrm{m}^{-2}$ |
| of defocusing sextupoles | $-20 \pm 5\,\mathrm{m}^{-2}$ | $-95 \pm 5\,\mathrm{m}^{-2}$ |

**Magnet occupation** The magnet occupation refers to the percentage of length occupied by the magnetic elements in a lattice. It gives an idea of the magnet density and the space available for the addition of corrective magnets - such as harmonic sextupoles and octupoles. With a higher number of sextupoles, the HOA lattice scores a magnet occupation of 58.88%, where the hybrid lattice stays at a 50.4% rate. The specificities of the SOLEIL upgrade require a distance of at least 5 cm between two magnets. Considering a minimum length of 5 cm for a sextupole or an octupole, I further excluded any drift space smaller than 15 cm, where no magnets could be included. The discrepancy between the magnetic occupation of both lattices is further increased: 66.0% in the hybrid case, 77.7% in the HOA case. The situation is even worse in the dispersive zone, where the magnet occupation of the HOA lattice reaches 100 %. The high occupation in the HOA lattice reduces the possible non-linear improvements of the lattice, such as the addition of sextupoles or octupoles in the dispersive zone. Therefore, nonlinear optimisation could require to increase the number of sextupole families, which could damage the HOA principle.

**Magnetic strengths** The quadrupole strengths $k_1[\mathrm{m}^{-2}]$ and sextupole integrated strengths $k_2l[\mathrm{m}^{-2}]$ of both lattices are displayed in Tab. 3.11.

Although the core quadrupole of the hybrid lattice are stronger than in the HOA case, the release of the optics for the creation of the dispersion bump alleviates the strong focusing of the $\beta$-functions, resulting in lower betatron tunes. The $\beta$-functions of the HOA lattice remain low in the core, as well as in the matching section, further increasing the betatron tunes.

In the case of the sextupoles, the strengths are higher by a factor 10 in the HOA lattice: the dispersion bump of the hybrid lattice reduces the necessary sextupole strength for the correction of chromaticity. The HOA lattice is tight: with a large magnetic occupation, the length of the sextupoles is limited by the total length of the unit cell. The low dispersion makes it harder for the sextupoles to correct the chromaticities, thus their strong strengths.

### 3.3.3 Transverse dynamics

The transverse dynamic apertures with energy deviation were already presented for both lattices, in Sec. 3.1.2.1 and 3.2.5.1 for the hybrid lattice and the HOA lattice respectively. This section compares some analysis of the off-momentum transverse beam dynamics for both lattices. The HOA lattice, in Fig. 3.13, presents a rather homogeneous acceptance with energy, without any optimisation of the sextupoles or the addition of any octupole: the cancellation of first- and second-order sextupolar resonances and the low tune-shift with momentum allow a large momentum acceptance of the HOA lattice. Yet, the on-momentum dynamic aperture remains low compared to that of the hybrid lattice. Further optimisation should enlarge both on- and off-momentum dynamic apertures and ensure symmetric apertures for $\pm\delta$. In the case of the hybrid lattice in Fig. 3.3, the dynamic aperture decreases rapidly with momentum deviation, as the tune shift with momentum rapidly reaches half an integer. Further optimisation of the hybrid lattice should aim at enlarging the momentum acceptance, for both transverse stability and beam lifetime.

#### 3.3.3.1 Tune shift with energy

The off-momentum stability has to be controlled for a stable beam and a high beam lifetime. The main source of off-momentum losses in single-particle dynamics is the transverse resonances. The control of the tune shift $\Delta\nu$ with energy deviation $\delta$ is necessary to increase the energy acceptance of a lattice. As a reminder, the variation of the tunes with energy deviation is described by the chromaticity:

$$\Delta\nu = \xi\delta = \xi^0\delta + \xi^1\delta^2 + \xi^2\delta^3 + \mathcal{O}(\delta^4) \tag{3.1}$$

**Higher-order chromaticities** Once the first-order chromaticity is corrected by the sextupoles (*cf* 2.1.2.5), the tune shift with energy is dominated by either the second-order or the third-order chromaticities. Minimisation of higher-order chromaticities can be done by increasing the number of sextupole families. The second-order chromaticities can be estimated by tracking the trajectory of off-momentum particles and extracting their tune variation with energy. Their exact expressions can be derived applying the canonical perturbation theory [110].

Table 3.12: Comparison of the second- and third-order natural chromaticities with a homogeneous correction of the first-order chromaticities.

| | Natural Chromaticities | | Homogeneous correction | |
|---|---|---|---|---|
| | HOA lattice | Hybrid lattice | HOA lattice | Hybrid lattice |
| $\xi_x^0$ | -7.181 | -6.705 | -0.002 | 0.04 |
| $\xi_y^0$ | -3.082 | -6.411 | 0.006 | 0.04 |
| $\xi_x^1$ | 46 | 49 | 9.2 | -3.4 |
| $\xi_y^1$ | 3.2 | 365 | 2.2 | 2.2 |
| $\xi_x^2$ | -1072 | -1514 | 26.5 | 5.2 |
| $\xi_y^2$ | -12.3 | -22180 | -15.7 | 22 |

Table 3.12 gathers the second- and third-order chromaticities for both lattices. Chromaticities are compared in the case of no sextupoles - natural chromaticities, and in the case of a homogeneous correction $(\xi_x^0, \xi_y^0) = (0, 0)$, where sextupoles of same polarity are identical. The second- and third-orders are extracted using a polynomial fit on the tune shift with momentum. For the purely linear lattices, they were computed for a range $\delta = \pm 2.2\%$ in the HOA lattice, and $\delta = \pm 0.7\%$ in the hybrid lattice. The corresponding tune shifts are displayed in Fig. 3.15 and 3.16. Indeed, the fractional part of the tune $\{Q_x\}$ reaches a half-integer value for $\delta \approx 2.3\%$ in the HOA case, $\{Q_y\}$ an integer for $\delta \approx 0.08\%$ in the hybrid case, limiting their energy acceptance.

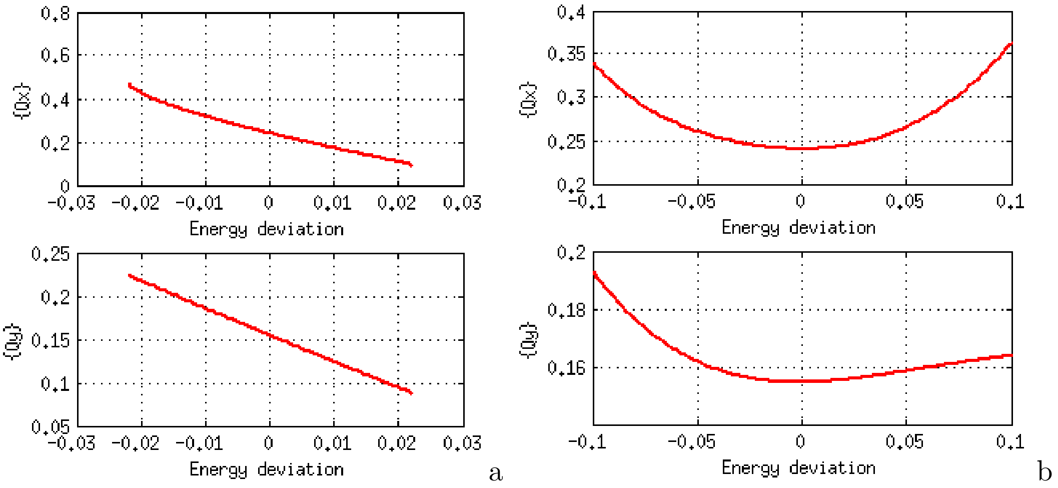

Figure 3.15: Tune shift with energy for the (a) natural chromaticities and (b) a homogeneous chromaticity correction for the HOA lattice.

**Tune shift with energy** The tune shift with energy deviation is tracked for both lattices, with all sextupoles off (a) for the HOA lattice, (c) for the hybrid lattice, and with homogeneously corrected chromaticities $(\xi_x^0, \xi_y^0) = (0, 0)$ (b) of the HOA lattice, (d) of the hybrid lattice, with only two chromatic sextupole families. The results are displayed in Fig. 3.15 for the HOA lattice and Fig. 3.16 for the hybrid case.

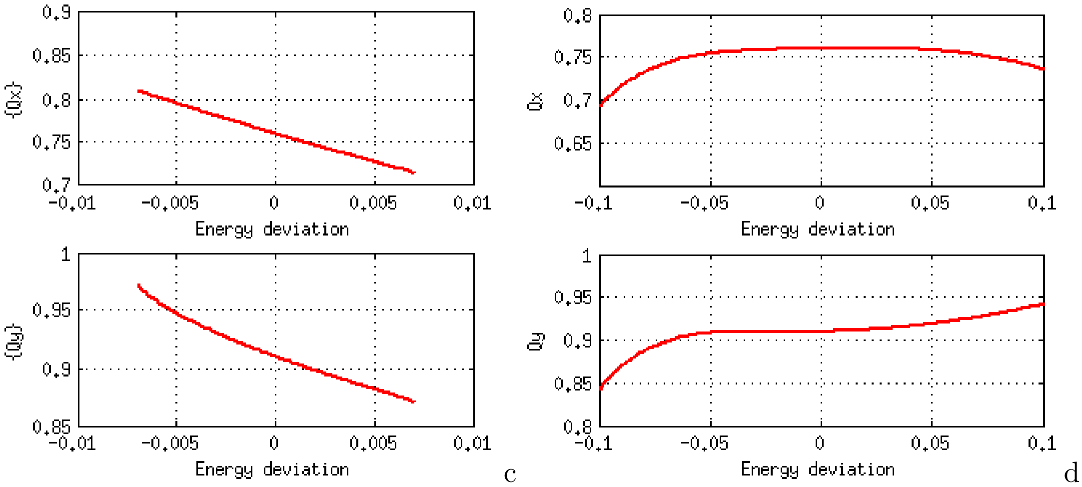

FIGURE 3.16: Tune shift with energy for the (c) natural chromaticities and (d) a homogeneous chromaticity correction for the hybrid lattice.

While the first-order chromaticities are corrected to zero, the HOA lattice tune shift with energy deviation is driven by the second-order chromaticity in the horizontal plane with a parabolic dependence: a variation of $+0.1$ over a $\delta = \pm 10\%$, which is a $+50\%$ variation on the tune. In the vertical plane, the effect of the second- and third-order combined induces a variation of $+0.04/+0.01$. The third order compensates the second in the range $\delta > 0$, flattening the dependence. The overall variation remains acceptable in terms of stability, as the the tunes remain in the half-integer window with a simple chromaticity correction. Further optimisation of the off-momentum dynamics will continue to flatten the tune shift, by increasing the number of sextupole families and by including octupoles. The conclusions are similar for the hybrid lattice, although the signs are opposite. The vertical tune shift of the hybrid lattice depends on the cubic order of the energy deviation, driven by the third order.

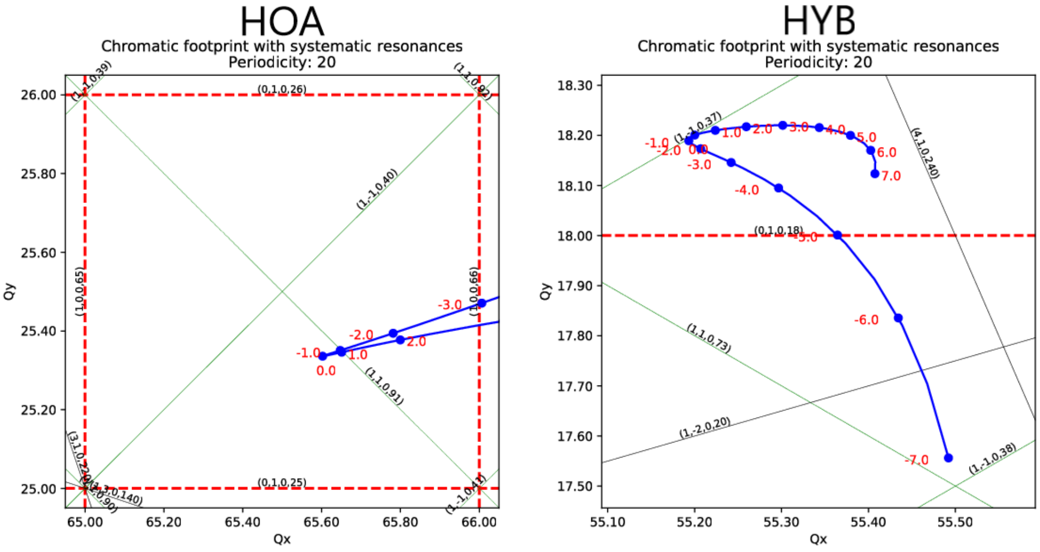

FIGURE 3.17: Resonance diagram for the (left) 7BA HOA lattice and (right) the 7BA hybrid lattice.

**Resonance diagram** Figure 3.17 displays the tune shift with energy for the 7BA HOA and hybrid lattices. Each lattice is only composed of two chromatic sextupole families, which corrected their chromaticities to $(0, 0)$. The tune shift is plotted on a resonance diagram, where the systematic resonances are displayed. Since both lattices present a periodicity of 20, the only excitable resonances have an order of multiple of 20 (*cf* sec. 2.1.3).

#### 3.3.3.2 Frequency map analysis

Figure 3.18 compares the Frequency Map Analysis (FMA) of the 7BA HOA and hybrid lattices. The frequency map analysis includes the transverse dynamic aperture and measures, for different coordinates $(x, y)$, the variation of the betatron tune after a defined number of turns, here 1000. The colour bar refers to the value of the diffusion index, defined as:

$$D_\nu = \frac{1}{N_{turns}} \times \log_{10}\left(\sqrt{(\nu_x(N) - \nu_x(N/2))^2 + (\nu_y(N) - \nu_y(N/2))^2}\right) \tag{3.2}$$

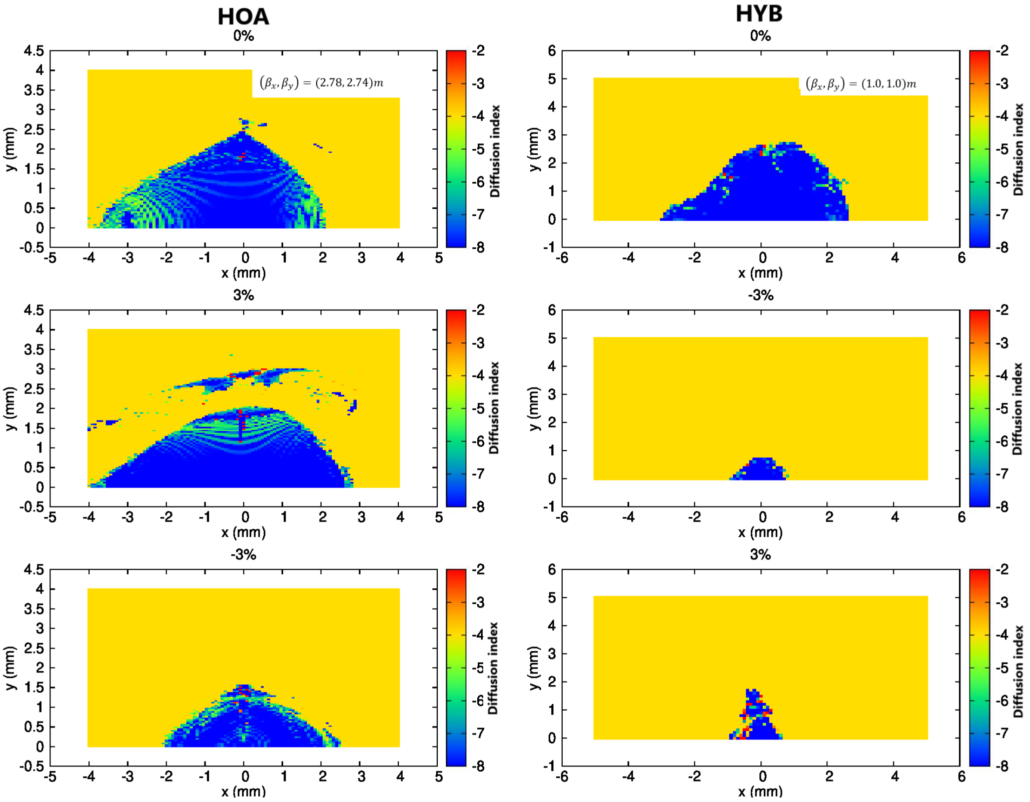

FIGURE 3.18: Frequency map analysis for three energy deviations of the (left) 7BA HOA lattice and (right) the 7BA hybrid lattice.

The FMA of both lattices is a study of their long term stability: green and red lines represent instabilities in the transverse plane: they are related to resonances excited by the off-axis particle oscillations. Figure 3.18 (a) gathers the FMA of the HOA lattice, at three energies, 0%, and ±3%. Such FMA was calculated thanks to a code developed by M. Ehrlichman for Bmad-MOGA [43]. The low variation of the tunes proves the high stability of such lattice and scheme, despite the green lines defining crossed resonances. Further optimisation should aim at increasing the negative off-momentum dynamic aperture, and limit the impact of the few resonances displayed. In Fig. 3.18 (b), the on-momentum and ±3% frequency map analysis of the hybrid lattice are presented: while the on-momentum is composed of a large blue thus stable area, thanks to the application of the non-interleaved principle, it is no longer the case for slight deviation in momentum, where the dynamic aperture drops because of crossed resonances (red dots).

#### 3.3.3.3 Reduction of the on-momentum dynamic aperture in 6D tracking

Including the Radio-Frequency (RF) system in the tracking simulation, the dynamic aperture of both ultra-low emittance lattices could be impacted. Indeed, the addition of RF cavities in the lattices triggers a longitudinal motion, independently described in Chapter 5. The oscillatory motion in the longitudinal plane, combined with the transverse motion induces the synchro-betatron oscillations. The included RF cavity in the lattices had a 1.1 MV voltage and 352.2 MHz frequency.

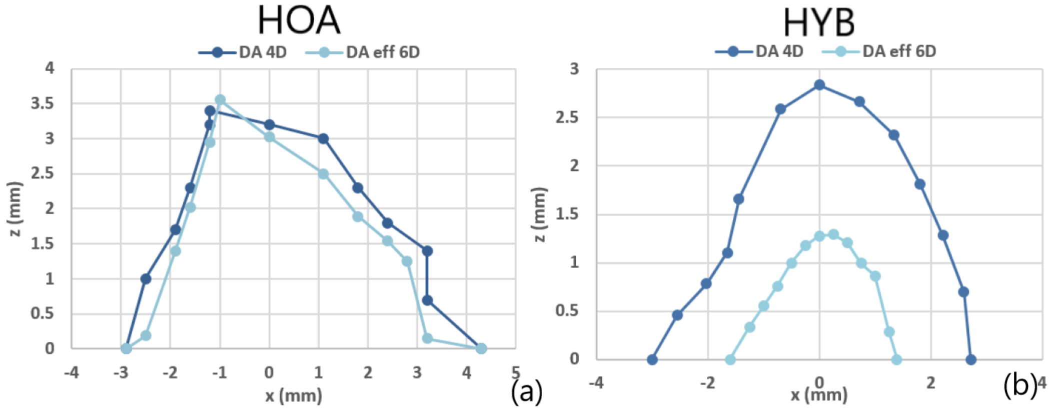

Figure 3.19: Comparison of the on-momentum dynamic apertures without and with RF cavities, for (a) the HOA lattice and (b) the hybrid lattice.

Figure 3.19 compares the on-momentum dynamic apertures without and with the addition of the RF cavities in the tracking, for both the HOA 7BA lattice (left in the figure) and the hybrid 7BA lattice (right in the figure). The on-momentum dynamic aperture is overall conserved with RF, in the HOA lattice. On the contrary, the hybrid lattice presents a drastic reduction of its on-momentum dynamic aperture with the consideration of the longitudinal motion. Indeed, since the on-momentum dynamic aperture is a peak in the overall dynamic aperture with momentum displayed in Fig. 3.3 for instance, small oscillations in energy deviation in the vicinity of $\delta = 0\%$ rapidly falls outside the transverse stability area. This effect is studied in the Chapter 6, where the first-order canonical perturbation theory is applied to describe the perturbed averaged trajectory of the particles, thus leading to the perturbed path length $\Delta C$.

#### 3.3.3.4 Impact of quadrupoles errors on the transverse dynamics

The robustness of the lattices regarding quadrupole errors is tested in this section. This analysis implements random quadrupole errors in the whole lattice, within the error range. The relative error is expressed as a percentage of the nominal value. The new strengths are therefore expressed as the following:

$$k_{err} = (1 + error \times \mathrm{rand}(\pm 1))k_{nom} \tag{3.3}$$

with $k_{err}$ the quadrupole strength including errors, $error$ the relative error, and $k_{nom}$ the nominal strength. Figure 3.20 gathers the variation of the on-momentum dynamic apertures after $N_t = 100$ turns, for a random draw of $N = 100$ rings and for three relative errors of ±0.1%, ±0.5% and ±1%. The left column is dedicated to a period of the HOA lattice, the right column to a period of the hybrid lattice. In red lines are the nominal dynamic apertures.

From an error of ±0.1% the HOA lattice presents a high resistance to the quadrupole errors. With an averaged ±0.1 mm, ±0.2 mm and ±0.3 mm lost in the horizontal and vertical amplitude, for an error of ±0.1%, ±0.5%, and ±1%, respectively, the lattice conserves a large enough stability area. The hybrid lattice dynamic aperture rapidly deteriorates with the quadrupoles errors, with an initial loss of about ±0.1 mm for errors of ±0.1%, to a third of its stability area of a relative error ±1%.

### 3.3.4 Touschek lifetime and Intra-Beam Scattering

Up to this section, the different studies conducted in this chapter considered the trajectory of a single particle. Here, we will introduce two necessary notions, which describe the stability of an electron beam: its lifetime and its equilibrium emittance, which take into account multi-particles. Those are part of a larger area in accelerator physics: the collective effects.

A beam is composed of several particles of the same charge, located around a reference particle. Electromagnetic collisions occur between the particles, during their synchrotron and betatron oscillations, in which particles exchange momenta. In the same logic as the quantum excitation, they could result in an increase in both transverse and longitudinal emittances.

**Beam scattering** These collisions are classified into two categories according to the largeness of the involved energy transfer. A large change in momentum, or large-angle scattering can lead to energy deviations larger than the energy acceptance of the ring, thus losing particles. It is called the Touschek scattering, for Touschek was the first to describe this phenomenon on AdA, in [111]. Small angle scattering leads to an overall

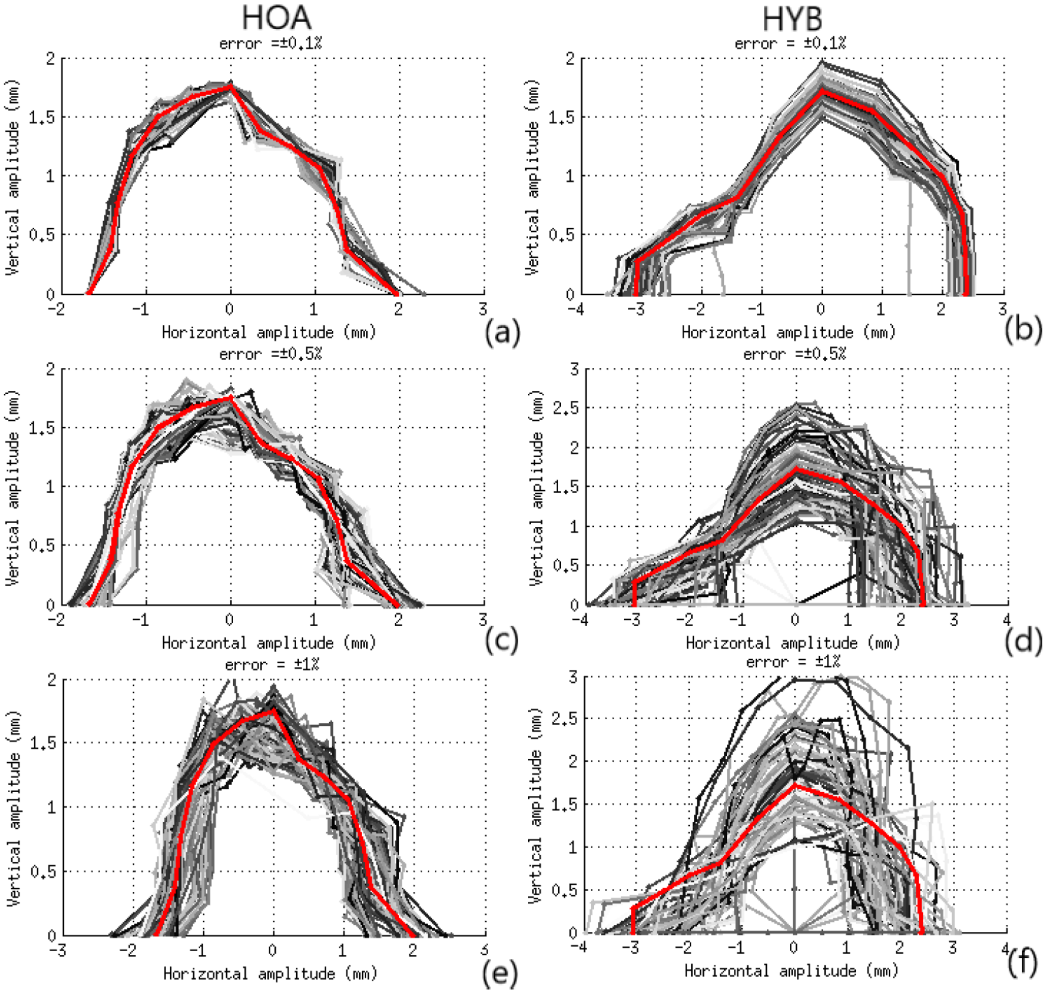

FIGURE 3.20: Impact of relative quadrupole field errors of ±0.1%, ±0.5% and ±1% on the 7BA HOA (left column) and the 7BA hybrid (right column) periods' on-momentum dynamic aperture, in the middle of the straight section, for a relative error of: (a) and (b) ±0.1%, (c) and (d) ±0.5% and (e) and (f) ±1%. In red is drawn the dynamic aperture of the nominal lattice, without errors.

increase in the beam emittance. It is the Intra-Beam Scattering (IBS), of which first theory was described in [112, 113].

**Beam lifetime** The beam lifetime is limited by two factors: the interaction of the electrons with the remaining gas in the vacuum chamber, and the interaction between the electrons of the same bunch. The first depends on the averaged pressure of the vacuum chamber, the total beam current and the transverse stability area. The beam lifetime of an ultra-low emittance electron beam is dominated by the probability of large angle Coulomb scattering between two electrons: indeed, in the larger scattering angle of two electrons in an beam, the more likely particles will experience an energy exchange that will take them out of the 6D acceptance, and therefore be lost. The probability of such scattering is expected to increase with the energy acceptance and decrease with particle density, determined by both the current per bunch and the bunch volume.

In third generation storage rings, the beam lifetime normally reaches tens of hours in a multibunch operation. The current status of the SOLEIL storage ring displays a beam lifetime higher than 20 h, for a beam total current of 500 mA and 416 bunches. In the case of ultra-low emittance lattices, with the reduced beam sizes and the predominance of non-linearities in the particle trajectory, the Touschek lifetime is reduced to the order of an hour, or even less [114]. Several methods are being studied to increase the Touschek lifetime. Some machine experimented calculation of the ultra-low emittance Touschek lifetime in the round beam case [115]. Some proposed to create vertical dispersion bumps, to distribute the particle density in the vertical plane [116].

Several formulae were developed to evaluate the beam lifetime[117]. In this section, calculations were conducted using the code ZAP[118]. The Touschek lifetime there is estimated using Bruck's formula:

$$(\tau_{1/2})_T^{-1} = \frac{\sqrt{\pi} r_0^2 c N_b}{\gamma^2 (\Delta p_x)^3 \epsilon_A V_b} F(\epsilon_A) \tag{3.4}$$

where $r_0$ is the Bohr radius, $c$ the speed of light, $N_b$ the number of bunches,$\gamma$ the Lorentz factor, $\epsilon_A = \left(\frac{1}{\Delta p_x}\left(\frac{\Delta p}{p}\right)\right)^2$ and $V_b$ the bunch volume.

This section estimates the dependence of both the Touschek lifetime and the Intra Beam Scattering on the emittance. To do so, I used the code ZAP, which allows the user to manually enter the value of the lattice emittance, and implement any coupling rate between the transverse planes. The calculations are instantaneous, as the momentum aperture is empirically input by the user. Despite the several imprecisions in ZAP calculations, this discussion's only interest lies in the variations of the beam lifetime and growth rate.

**Parameters** Calculations are made with the input parameters detailed in Table 3.13 and 3.14. The lattice used is the 7BA hybrid lattice developed for the SOLEIL tunnel (3.1). The simulations are conducted for a full ring at a full beam intensity $I_c$ = 500 mA, with 416 bunches of 1.42 nC each. The natural bunch length is 3.9 mm. The calculations are done with a simulated round beam, which reduces the large-angle scattering probability [115].

TABLE 3.13: General parameters of the 7BA hybrid lattice.

| | |
|---|---|
| Energy [GeV] | 2.75 |
| Circumference $C_0$ [m] | 354.1 |
| Revolution frequency $f_0$ [kHz] | 846.63 |
| Momentum compaction $\alpha_0$ | $1.47 \times 10^{-4}$ |
| Energy loss per turn $U_0$ [keV] | 310 |
| Natural RMS momentum spread | $8.63 \times 10^{-4}$ |
| Natural horizontal emittance [pm.rad] | 72 |
| Full coupling transverse emittance [pm.rad] | 49.0 |

Table 3.14: Calculation parameters for Touschek lifetime and IBS equilibrium emittance of the hybrid lattice using the ZAP code.

| | |
|---|---|
| Horizontal damping time $\tau_x$ [ms] | 9.847 |
| Vertical damping time $\tau_y$ [ms] | 20.943 |
| Horizontal emittance damping rate $\frac{2}{\tau_x}$ [s$^{-1}$] | 203.11 |
| Longitudinal damping time $\tau_e$ [ms] | 23.982 |
| Longitudinal emittance damping rate $\frac{2}{\tau_e}$ [s$^{-1}$] | 83.40 |
| **RF voltage $V_{RF}$ [MV]** | 1.00 |
| RF frequency $f_{RF}$ [MHz] | 352.20 |
| $V_{\text{rfp}}$ [MV/s] | $2.104 \times 10^9$ |
| Harmonic number h | 416 |
| Natural RMS bunch length [cm] | 0.390 |
| **Total beam current $I_{tot}$ [mA]** | 500 |
| **Number of bunches $N_b$** | 416 |
| Bunch current $I_b$ [mA] | 1.20 |
| Number of electrons per bunch $N_e$ | $8.861 \times 10^9$ |

#### 3.3.4.1 Touschek lifetime versus emittance

Figure 3.21 gathers the estimation of the Touschek lifetime in hours, when fully-coupled natural emittance varies. The momentum acceptance was kept constant along the ring, at 5%, thus giving a highly optimistic evaluation of the Touschek lifetime.

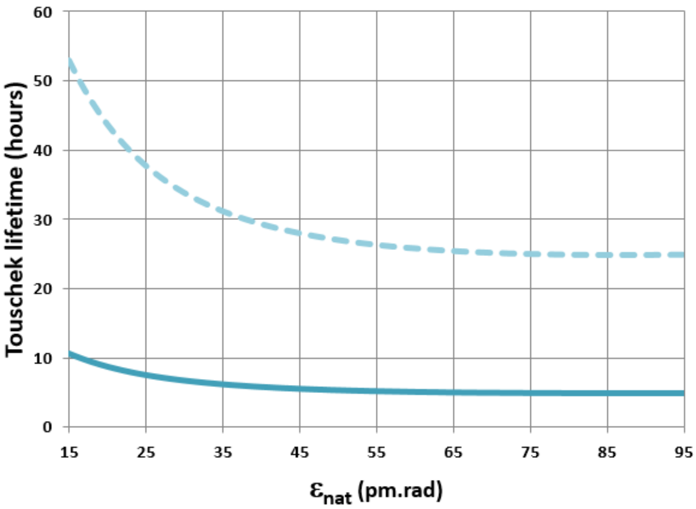

Figure 3.21: Variation of the Touschek lifetime with natural emittance for the 7BA hybrid lattice of 72 pm.rad natural emittance, 50 pm.rad emittance with full coupling. Calculations are made for two cases: of a natural bunch length (in plane line) and of a bunch lengthened 5 times, assuming the use of a harmonic cavity(in dashed line).

An interesting effect occurs when the fully-coupled emittance reaches values $< 40$ pm.rad: in this regime, the Touschek lifetime increases exponentially, even doubling the value of the plateau of high-emittances ($> 85$ pm.rad). When the beam size is smaller for highly-relativistic electrons, their momenta align, making large-angle scattering less likely. This effect is favourable for a large beam lifetime.

In the case of the 7BA hybrid lattice, the natural horizontal emittance is 70 pm.rad. The application of a round beam results in an effective horizontal emittance of 50 pm.rad, placing the fully-coupled lattice in the favourable regime at full current. As shown in Fig. 3.21, ultra-low emittance lattices could enter a favourable regime, where the Touschek lifetime is high enough for an easier machine operation. Current lattices, even in the case of round beam, are not in this regime.

#### 3.3.4.2 Intra Beam Scattering versus emittance

While Touschek scattering's probability decreases with smaller emittance, the probability of small angle Coulomb scattering which induces small-energy exchange rather increases, thus yielding to an expected increase of the beam emittance.

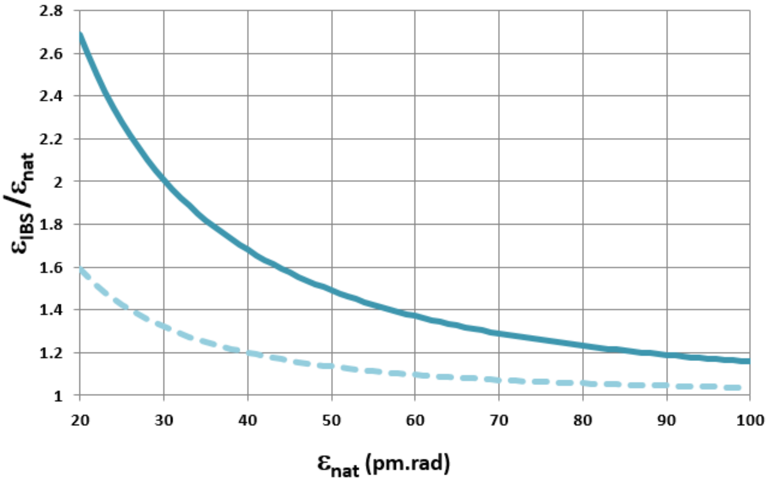

FIGURE 3.22: Emittance blow-up due to IBS with natural emittance in the case of a natural bunch length (in plane line) and of a bunch lengthened 5 times, assuming the use of a harmonic cavity(in dotted line), for the SOLEIL 7BA hybrid lattice.

Figure 3.22 compares the variation of the emittance blow-up due to IBS with the natural emittance of an ultra-low emittance lattice, with and without bunch lengthening. As expected, the rate of the emittance blow up increases rapidly when the emittance is decreased: the equilibrium emittance could be the double of the natural emittance.

**Bunch lengthening with a harmonic cavity** To mitigate this phenomenon, the particle density is decreased both longitudinally and transversally by lengthening the beam, using harmonic cavities[119, 120]. Third-harmonic cavities work at the third-harmonic of the RF frequency, and can lengthen the beam by about a factor of three and five in the ultimate limit. They proved to increase the Touschek lifetime of third-order storage ring lattices [121]. The resulting emittance blow-up is reduced by almost 2 in Fig 3.22 at the lowest emittances, for a lengthened bunch of 19.5mm.

#### 3.3.4.3 Energy acceptance and Touschek lifetime

The previous calculations were conducted under a constant and arbitrary momentum acceptance. In a real lattice, the momentum acceptance varies along the longitudinal position $s$. Ultra-low emittance lattices suffer from a general increase of the sextupole strengths, necessary to compensate the large natural chromaticities. Strong sextupole strengths excite more nonlinear resonances, even when compensated by the schemes under scrutiny (3.1 and 3.2). Precise calculation of the Touschek lifetime must scan the momentum acceptance along the lattice. Figure 3.23 verifies, using ZAP, the link between the beam lifetime and the momentum acceptance, and estimates the energy range to be optimised dynamically, to increase the Touschek lifetime.

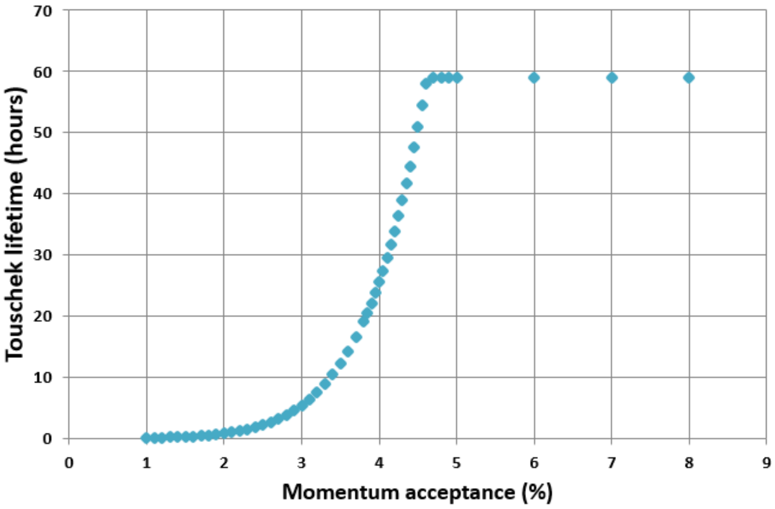

FIGURE 3.23: Evolution of the Touschek lifetime versus momentum acceptance. Simulation are made with ZAP, on the SOLEIL 7BA hybrid lattice at a fully-coupled horizontal emittance of 50 pm.rad.

A plateau is reached for an acceptance of $\simeq 4.8\%$, which depends on the RF voltage. Nevertheless, the Touschek lifetime remains higher with a higher momentum acceptance. Off-momentum optimisation should be conducted in the next chapter.

## 3.4 Conclusion

The ultra-low emittance schemes described in the section 2.3 were applied to the SOLEIL upgrade of its 2.75 GeV storage ring. The hybrid scheme was implemented by one of my colleagues, Alexandre Loulergue, while I contributed to the development of a HOA lattice. I then compared the main characteristics of both lattices, and their on- and off-momentum dynamics.

While the on-momentum dynamics is optimum in the hybrid lattice, its off-momentum dynamics require additional optimisation. Furthermore, the path length effect limits even its on-momentum dynamic aperture, when synchro-betatron oscillations are considered. On the contrary, the HOA lattice presents a strong robustness with regards to the energy deviation and implemented errors. Furthermore, since the HOA lattice is composed of small building blocks, it is easier to adapt itself to a given geometric constraint of the ring, by adjusting the number of the above basic blocks along the ring. Those characteristics make the HOA principle a highly interesting scheme to be applied on the SOLEIL storage ring, that already possesses a lack of symmetry. Nevertheless, the cost of the HOA lattice is higher in terms of magnet strengths and occupation: the force of the sextupole magnets were ten times higher than in the hybrid lattice, because of a reduced overall horizontal dispersion. Further analysis of both lattices are conducted in the next chapter: both lattices are implemented in a Multi-Objective Genetic Algorithm, to optimise their on- and off-momentum dynamic apertures.

# Chapter 4

# Nonlinear optimisation of ultra-low emittance lattices

The strong sextupoles, required for the correction of the natural chromaticities, perturb the dynamic and stability of the ultra-low emittance lattices. Further optimisation is therefore required to compensate the effect of the sextupoles and enhance the particles stability within the storage ring. Different methods and measures exist. For instance, the tune shift with energy can be corrected by minimising the second- and third-order chromaticities, by choosing the adequate strengths for the sextupoles [122]. Other codes look into the momentum acceptance along the ring, required for the calculation of the Touschek lifetime: it can be enhanced with the inclusion of harmonic sextupoles and octupoles in the lattice. Moreover, the analysis of the sextupole resonances can determine which resonance limits the transverse dynamic aperture [123].

Nonetheless, the increase in the sextupole strengths and the tight lattices make the new designs extremely nonlinear, which proves difficult to handle by hand, or with the codes used for the development of third-generation storage rings, which have either a limited number of variables, range, or consider the sextupoles in the thin lens approximation - which is no longer valid in the ultra-low emittance lattices presented, or do not take into account the octupoles as bulk magnets, or have a limited access to nodes which dramatically increases the required time for any optimisation with a high volume of variables. The use of novel numerical tools such as multi-objective algorithms allows nonlinear optimisations of the 6D dynamics and stability with a large number of variables, with a possible parallelisation.

## 4.1 Multi-objective genetic algorithm

Genetic algorithms are optimisations based on biological evolutionary processes of a population: natural selection, cross-over and mutation of an individual's genes. The algorithm studies a set number of individuals called a generation. The characteristics of each individual are called genes and can be subjected to different constraints. The performances or fitness of each individual are evaluated once the generation is complete and the individuals are ranked accordingly. Selection occurs and to restore the following generation, cross-over of two parental genes are used to birth a new individual. A mutation probability is implemented to scan the solution map.

The genetic algorithm used in the present thesis is a Multi-Objective Genetic Algorithm (MOGA) which optimises three objectives in a solution space defined by several constraints. The following section introduces the genetic algorithm steps and describes the specificities of the code MOGA used.

### 4.1.1 Introduction to MOGA-Bmad

The MOGA available with Bmad, an accelerator code developed at Cornell University ([124]), optimises the on- and off- momentum Dynamic Apertures (DA) using a set of sextupoles, while conserving the chromaticity. The principles of the optimisation, common to any MOGA algorithm, are detailed below, with a description of the input and output files, as well as the different analysis scripts provided in the package. The program is developed by M. Ehrlichman, in Cornell University [43]. A large part of the analysis scripts used were developed by him. The Bmad distribution was installed in the CEA cluster, Centre de Calcul Recherche et Technologie (CCRT) [125], available for SOLEIL staff.

#### 4.1.1.1 Theoretical environment

To control and lead the optimisation, targets should be defined: they are the objectives. The dynamic aperture of a storage ring is limited by either the magnetic fields and resonances, or the physical aperture of the vacuum chambers. The physical aperture is the vacuum chamber dimensions projected in the transverse plane $(x, y)$ through the Twiss functions. A dynamic aperture limited by the physical aperture is the best case scenario and it is currently the case with the current SOLEIL lattice. Nevertheless, as seen in Figure 3.13 and 3.3, ultra-low emittance lattices present strongly reduced dynamic apertures of the order $\pm 1\,\mathrm{mm}$ for $\beta_{x,y} = 1\,\mathrm{m}$, which are below the expected physical aperture of $5 - 10\,\mathrm{mm}$.

The dynamic apertures are usually calculated by tracking the particles turn by turn, scanning the transverse plane, and state the stability of the transverse coordinates if the particle survived the requested number of turns. To speed up the optimisation process, the estimation of the dynamic aperture is done by calculating its border. Instead of mapping the transverse plane, the border is evaluated by radially scanning the $(x, y)$ plane, for a certain number of angles, reducing the number of scans by a dimension. As the aim is to match or be larger than the physical aperture, if the dynamic aperture border is larger at one point, it will be treated as equal to the physical aperture within the code.

**Objectives** The objective value is defined as the distance between the real dynamic aperture and the linear dynamic aperture in the transverse plane $(x, y)$. Three objectives are available in MOGA-Bmad, one for three different energies, which can be fixed in the main file.

$$f_E(x) = \frac{1}{N_{angle}} \sum \frac{|L_{da} - L_{la}|}{L_{la}} \tag{4.1}$$

where $L_{da}$ is the border point of the dynamic aperture at a certain angle, $L_{la}$ the corresponding physical aperture, and $N_{angle}$ the number of radial angles used to scan the $(x, y)$ plane. By definition, the objective values are comprised between 1 and 0: 1 refers to an unstable area, 0 to a dynamic aperture as large as or larger than the physical aperture. Thus, the optimisation aims for objective values of 0, or the lowest possible for each energy.

**Constraints** Several constraints guide the optimisation. MOGA-Bmad distinguishes two types of constraints: the dominant constraints and the side constraints. Dominant constraints must not be violated: if so, the individual will not be considered as a suitable option within the algorithm. The dominant constraints are:

- the bounds on the sextupole strengths,
- the global bounds on the chromatic closed orbit - *i.e.* nonlinear dispersion for both non-zero energies,
- and the bounds on the chromatic footprint within set energy deviation and tune range.

The number of dominant constraints is fixed as an input: therefore, if the number of set dominant constraints is lower than the list here above, the rest of the constraints are considered as side constraints.

**Feasibility** First, the individual must comply with the dominant constraints, which states their feasibility: if all dominant constraints are verified, the individual is declared feasible, and further evaluation will follow. Otherwise, the individual is unfeasible, and receive a low rank. This parameter saves time, as only the feasible individuals will be evaluated.

**Solution space** Now, the values of those objectives are manipulated with the sextupoles magnets. Let us use $N_{sext}$ as the number of sextupole magnets defined as variables in the optimisation. The initial vectorial space $E_{sext}$, of dimension $N_{sext}$, gathers the strengths of each sextupoles. Indeed, a vector $x$ in $E_{sext}$ is composed as :

$$\forall i \in \{1 : N_{sext}\}, x_i = \left(k_1^i, \cdots, k_j^i, \cdots, k_{N_{sext}}^i\right) \tag{4.2}$$

with $(k_j)_{1 \leq j \leq N_{sext}} : \xi_{x,y} = \xi_{corr}$, the sextupole strengths.

Yet, the main constraints of MOGA-Bmad are the chromaticities, kept constant in both planes during the optimisation process. The effective variables and the optimisation vectorial space will then be the projection of the sextupoles space with regards to the plane where both chromaticities are constants. Any vector from this solution space is called an individual and its coordinates, genes. The genes, linked to the sextupole strengths, are to be varied in order to optimise the objective functions.

As the variable space has a higher dimension than the objective space, the expected results of the optimisation are not a Cauchy-Schwartz solution space, but a Pareto front: it is the frontier defined by the minimum distance of the vectorial space $E_{objs} = \{objs(1:3)/objs = f(x_i)_{i\in\{1:N_{sext}\}}, x \in E_{sext}\}$ and the optimum objectives space $E_{opt} = 0_{1\times3}$.

#### 4.1.1.2 Optimisation process

Multi-Objective Genetic Algorithm (MOGA) is based on the natural evolutionary process – as described by Charles Darwin. Solutions are gathered in generations: each solution is an individual whose genes are the sextupole strengths. When the generation is completed, the individuals are evaluated on their objective values and their feasibility. Then, they are ranked using the dominance relationship below. Half of the generation is then deleted, the remaining half used to breed new individuals. Cross-over of the parents genes is widely used to create new individuals, yet a probability of mutation is implemented, to scan the map and avoid stagnation around a local minimum. After the first generation has been either implemented manually or generated randomly, the sorting algorithm has to rank the solutions, in order to best fit the requirements of the optimisation. Ranking is based on the value of two parameters: the fitness and the strength, which are defined further down.

**Dominance relationship** After some generations, feasible individuals will arise. To rank them, an order rule is defined in the solution space : **the dominance relationship**. Let us take $x_1, x_2 \in S$, $S$ the solution space. $x_1$ dominates $x_2$ if and only if:

- $x_1$ is no worse than $x_2$ in all objectives
- $x_1$ is better than $x_2$ in at least one objective

which translates to the equation below:

$$\forall (x_1, x_2) \in S^2,\, x_1 >_S x_2 \longleftrightarrow \begin{cases} \forall E, f_E(x_1) \geq f_E(x_2) \\ \exists E : f_E(x_1) > f_E(x_2) \end{cases} \tag{4.3}$$

If $x_1 > x_2$ according to this relationship, $x_1$ is said to dominate $x_2$. $x_1$ is therefore called the $x_2$'s dominant, $x_2$ a dominated of $x_1$. Two individuals are said equivalent if none dominates the other. The orbit of an individual is then defined as the group of equivalent individuals.

**Fitness and strength** Now, to rank the feasible individuals, the natural parameter to take into account is the number of dominated per individual: it is defined as the strength. Then, the higher the strength, the better the performance of an individual in terms of objective functions, yielding to a higher rank.

Nonetheless, individuals with the same strength have to be compared, to distinguish the best individuals. Since their dominated have already been taken into account, we have to turn our scope to their dominants. At constant dominated, two individuals $x_1$ and $x_2$ have $N_1$ and $N_2$ dominants respectively. This means that they are dominated by $N_1$ and $N_2$ individuals respectively. If $N_1 > N_2$, then $x_1$ has a higher rank in its relationship orbit than $x_2$. Yet, this reasoning considers all dominants to be equal: their quality, *i.e.* their strength, is not taken into account. A new parameter is therefore defined: the fitness. It is the sum of the dominants' strengths for a given individual. A high fitness therefore leads to an individual dominated by strong dominants, regardless of their number.

In conclusion, two parameters are defined out of the dominance relationship: the fitness and the strength. The strength of an individual is the number of other individuals it dominates. The fitness of an individual is the sum of the dominants' strengths.

**Cross-over and mutation** Once the individuals are ranked according to both their strength and fitness parameters, the population is cut in half: following the principles of the Darwinian evolution theory, only the fittest and strongest individuals are kept into the optimisation. To restore the population, and potentially grow better individuals, the remaining half is mixed to brew new individuals. Here, we define a parental relationship in each generation. New individuals are created, like in breeding, by mixing the genes of two parents:

$$x^n(k) = c_1 x_1(k) + c_2 x_2(k) \tag{4.4}$$

with $c_1 + c_2 = 1$. Furthermore, to be sure to explore the solution map, and not stick to a local minimum, a probability of mutation in each gene is implemented: in that case, the mutated gene is generated randomly within the respect of the dominant constraints.

### 4.1.2 Summary of the algorithm

Figure 4.1 summarises the different steps of the multi-objective genetic algorithm. The convergence is entirely determined by the requested number of generations. The advancement of the optimisation can be followed by different analysis scripts written by M. Ehrlichman.

The convergence of the genetic optimisation is practically determined by the maximum number of generations set as an input. The evolution of the objective functions during the optimisation can be followed using either the output files and manually checking the good progress generation after generation, or analysis scripts dedicated to the optimisation. The success of the optimisation is determined by the Pareto front: the border of the solution space, where the objective values reached a compromise. Analysis of the solutions usually takes place after thousands of generation: it was noticed that

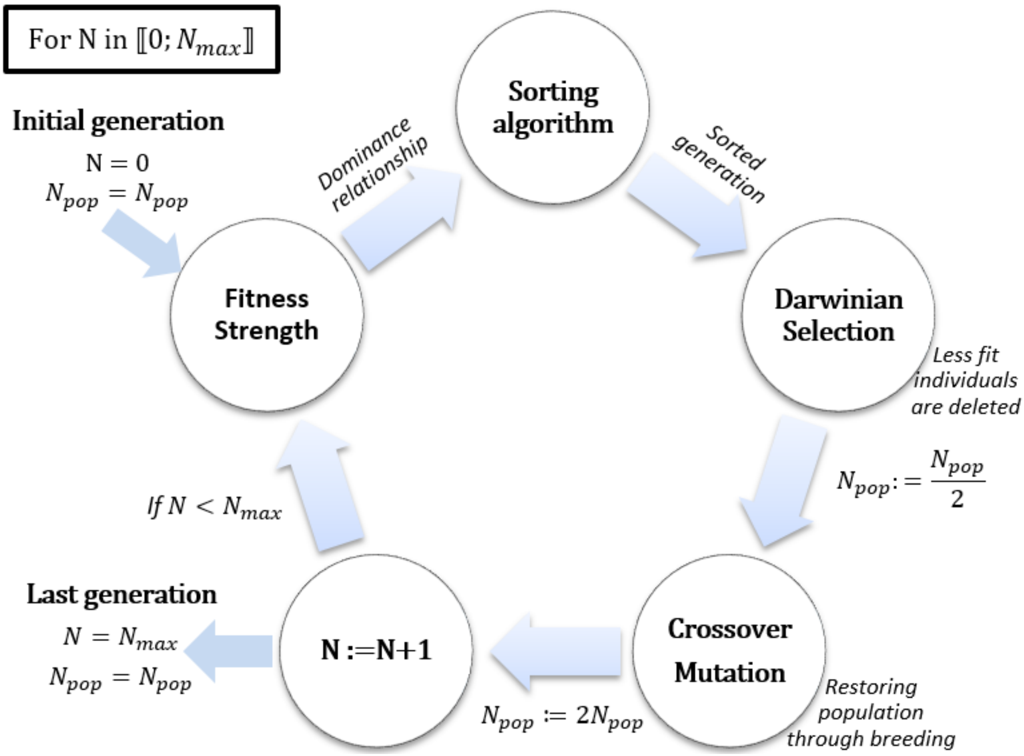

FIGURE 4.1: Scheme of the MOGA-Bmad algorithm process.

the optimisation quickly complies with the three first constraints, yet takes some time to constrain the chromatic footprint.

**Pareto front** After a fixed number of generations, the optimisation terminates. Ideally, the last generation forms a frontier in the objective space, drawing the minimised solutions for the problem at stake. Figure 4.2 displays an analysis available in the MOGA package developed by M. Ehrlichman [43], which compares the objective values two by two. The colours were changed to better appreciate the last generation, in red. The objective values equal 1 at the beginning of the optimisation. Generation after generation, their values are decreased, ideally reaching the zero-value, *i.e.* the level of the purely linear lattice.

In this example, the Pareto front is projected onto each objective plane: the red dots, corresponding to the last generation, allow us to comprehend the pursuit of the optimisation. The optimisation appears complete for the dynamic aperture at ±3%, but the on-momentum dynamic aperture is not stabilised. One would either relaunch an optimisation with an increased number of generations, or pursue the current optimisation by inserting the last generation as an input.

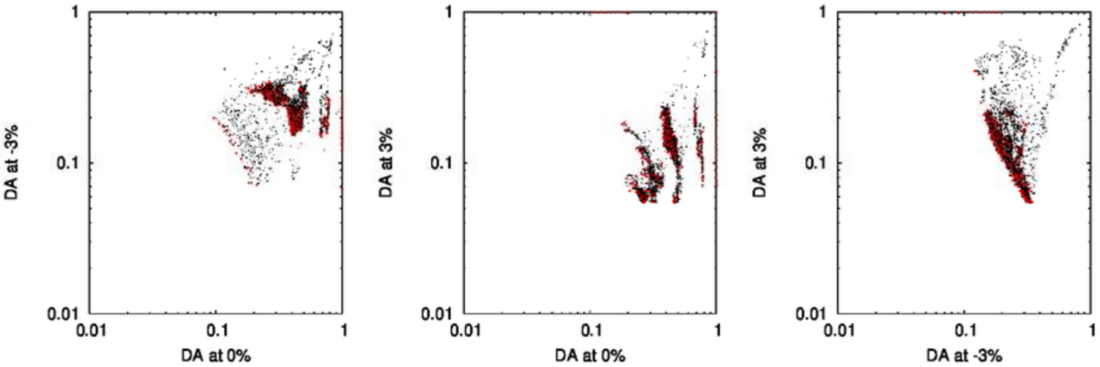

FIGURE 4.2: Comparison of the objective values for different generations, in an optimisation of a period of a 7BA 134 pm.rad SOLEIL lattice. The Pareto front is exposed by colouring the last generation in red.

## 4.2 Non-linear optimisation of the 20-fold symmetry ultra-low emittance lattices

Further comparison of the ultra-low emittance schemes under study requires optimising both lattices nonlinearly. MOGA-Bmad proved to be a good means to optimise on- and off-momentum dynamic apertures at certain energies, while conserving chromaticities. This section is dedicated to the nonlinear optimisation of the ultra-low emittance lattices introduced in the previous chapter: a 7BA hybrid lattice, based on the ESRF-EBS design, and a 7BA High-Order Achromat (HOA) lattice, as developed for ALS-U and SLS-II, both adapted for the SOLEIL storage ring upgrade. Studies of both linear lattices in the previous chapter distinguished different optimisation objectives for both lattices, additionally to the enlargement of the momentum acceptance for a longer beam lifetime.

The hybrid lattice presents a high on-momentum dynamic aperture, but its off-momentum performance drops quickly with the energy deviation. First optimisations tried to improve the on-momentum dynamic aperture to test out the $-I$ principle. Synchro-betatron oscillations are believed to limit the effective dynamic aperture of the lattice versus energy deviation (*cf* sec. 3.3.3.3). Further optimisation sets shall look at improving the dynamic aperture off-momentum to limit the effect of such oscillations.

The High-Order Achromat presents a rather homogeneous transverse dynamic aperture with energy deviation, which remains small compared to the hybrid lattice. Indeed, the strengths of its sextupoles remain too large and approach the electrostatic limit. Optimisation shall try to enlarge the dynamic apertures, while conserving its large energy acceptance, and reducing the sextupole strengths by increasing the number of families.

### 4.2.1 Optimisation of a hybrid lattice

The performances of the hybrid lattice are further optimised using MOGA-Bmad. Two types of optimisations were conducted. As the non-interleaved principle is not applied to all sextupoles, first runs focused on the on-momentum dynamic aperture and scanned the sextupole map to maximise the on-momentum dynamic aperture. A second optimisation will try to improve the off-momentum dynamic aperture, while conserving the on-momentum dynamic aperture.

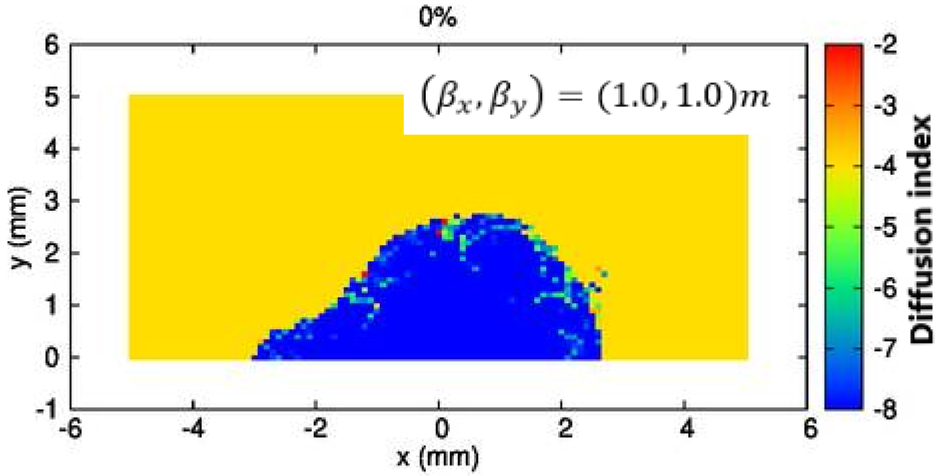

Figure 4.3: On-momentum dynamic aperture of the hybrid lattice, for $(\xi_x, \xi_y) = (0, 0)$.

Figure 4.3 recalls the large on-momentum dynamic aperture of the hybrid lattice, at the chromaticities $(\xi_x, \xi_y) = (0, 0)$ and at the middle of the straight section. To ease the comparison and the understanding of the optimisation results, Figure 4.4 displays the name and position of the variables of the following MOGA optimisations. They consist in five chromatic sextupole families and three octupole families of two individual magnets each, located at symmetric positions under the dispersion bumps of the hybrid lattice. The position of the octupoles were arbitrarily chosen next to the relevant sextupoles. Further analysis could slightly change their resulting strengths by placing them closer to the maximum dispersion. The sextupoles were kept as bold magnets in the MOGA optimisations, while the octupoles were defined as multipole magnets, of zero length.

Table 4.1 gathers the nominal values of the sextupole strengths before any MOGA optimisation. The chromaticity of the lattice is set to $(\xi_x, \xi_y) = (0, 0)$. The following MOGA optimisations will set the chromatic constraints to those values.

Table 4.1: Strengths of the sextupoles for the nominal lattice, before any optimisations. The strengths correspond to a chromaticity of $(\xi_x, \xi_y) = (0, 0)$, and follow the Bmad convention.

| Family | Strength | Family | Strength |
|---|---|---|---|
| sxd1e | $-430\,\mathrm{m}^{-2}$ | sxd2e | $-430\,\mathrm{m}^{-2}$ |
| sxf1e | $336.64\,\mathrm{m}^{-2}$ | sxf2e | $-210\,\mathrm{m}^{-2}$ |
| sxf3e | $208\,\mathrm{m}^{-2}$ | | |

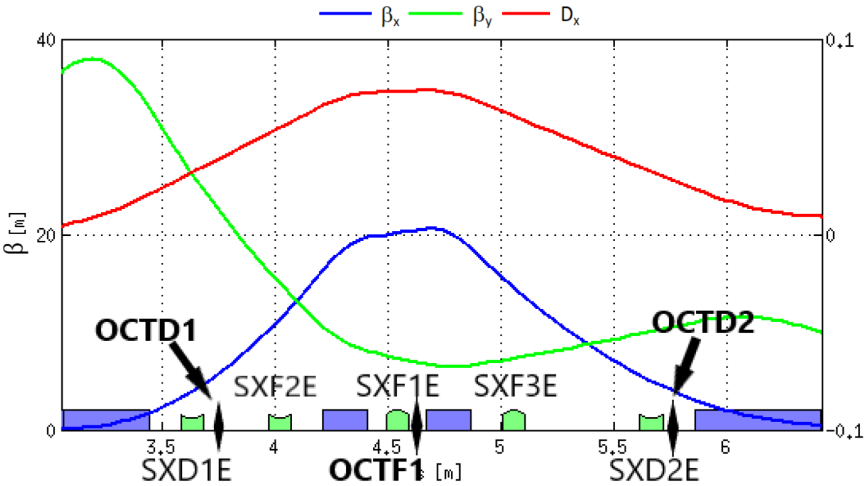

FIGURE 4.4: Position of the sextupoles and octupoles set as variables in the following MOGA optimisations. The hybrid lattice was zoomed in, around the dispersion bump. The octupoles are thin elements, which position is displayed using diamond-shaped figures.

#### 4.2.1.1 Optimisation of the on-momentum dynamic aperture

First optimisations tested the genetic algorithm process and tried to reproduce or even enlarge the on-momentum dynamic aperture of the hybrid lattice, for fixed chromaticities of $(\xi_x, \xi_y) = (0, 0)$. To do this optimisation, I used all sextupole families as chromatic sextupoles, and three octupole families located on the side of the chromatic sextupoles. The sextupole strengths were varied in the range $\pm 500\,\mathrm{m}^{-2}$, the octupoles $\pm 1000\,\mathrm{m}^{-3}$.

In MOGA, the optimisation of the dynamic aperture (DA) is conducted at three distinct energies. To concentrate the optimisation around the dynamic aperture, this optimisation worked at the energies 0% and ±0.1%. Figure 4.5 represents the evolution of the objective values along the 2000 generations of 200 individuals each. The red dots corresponds to the last generation. The objectives start at the top left hand corner, around the value (1,1) on each chart. A perfect optimisation would see its objective values vary from 1 to 0. After thousands of generation, the objective value stagnates onto a frontier, the Pareto front.

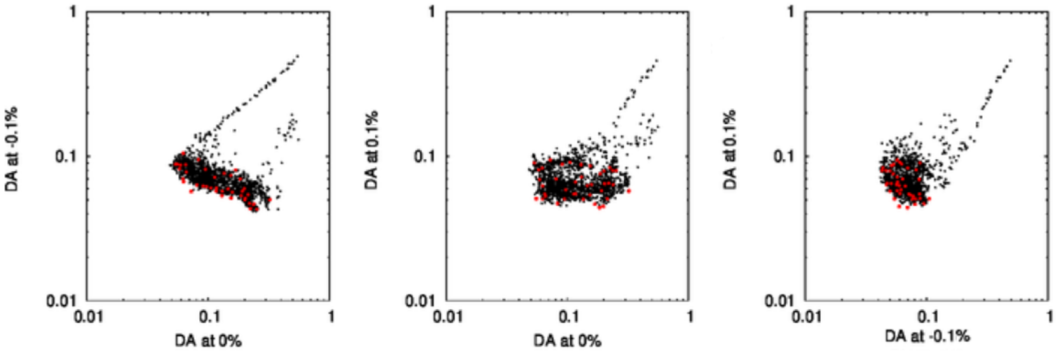

FIGURE 4.5: Evolution of the objective values along the optimisation. The last generation is plotted in red.

The values of the objectives are similar, regardless of the energy deviation. Figure 4.6 displays the typical dynamic apertures after 300 turns, obtained in the last generation of this optimisation. It corresponds to the seed 39860. The dynamic aperture is enriched with knowledge of the stability of the particle of coordinates $(x, y)$: the colours represent the decimal logarithmic power of the variation of the tune of such particles after a defined number of turns. The difference in colours is the expression of the tune variation caused by the vicinity of a resonance. They appear as green to red lines in Fig. 4.6.

It is interesting to note the aim of the optimisation failed: compared to the manually-optimised on-momentum dynamic aperture of Fig. 4.3, the results of the MOGA optimisation harmonised the slightly off-momentum dynamic apertures and the on-momentum DA. Furthermore, since it is part of the dominant constraints of MOGA, the chromatic footprint is changed. The conclusion of this test is that the non-interleaved principle remains in the optimisation, but this optimisation alone could not reproduce the manually-maximised on-momentum dynamic aperture: the variations of the dynamic aperture with the energy deviation in the vicinity of $\delta = 0\%$ are drastic, therefore $\pm 0.1\%$ was probably too large to enhance the on-momentum stability area.

To prepare the off-momentum optimisation, Figure 4.7 draws the tune shift with energy of the typical result of the on-momentum optimisation, for the range $\delta = \pm 7\%$. The chromatic footprint is part of the optimisation constraints and aims at containing the range $\pm 5\%$ into the half-integer quarter of the tunes. To do so, octupoles were included in the optimisation at the location indicated in Fig. 4.4: they were varied in the range $\pm 1000\,\mathrm{m}^{-3}$. Including the 20-fold symmetry within the display of the resonances, the off-momentum stability is only threatened by the integer and half-integer resonances, as well as the resonances $a\{Q_x\} + b\{Q_y\} \in \mathbb{Z}$, with $(a, b) \in \{(1, 1), (1, -1), (-1, 3)\}$. Although the tune shift with energy is well confined around the working point for particles with energy deviation $\delta = \pm 3\%$, the tune shift varies a lot for higher energy deviation. For the sake of both beam lifetime and injection, the off-momentum dynamic apertures are optimised in a second round of MOGA optimisations, and aims at confining the tune shift around the working point for $\delta = \pm 7\%$.

Table 4.2 lists the strengths of the sextupoles and octupoles of the selected seed 39860 of the optimisation in the vicinity of the on-momentum particle. The strengths of the defocusing sextupoles are similar to their nominal value, required for the correction of the chromaticity, $-430\,\mathrm{m}^{-2}$, as well as the strength of the main focusing sextupole, SXF1E, $336.64\,\mathrm{m}^{-2}$, with a slight increase from its nominal value. The two other sextupoles, SXF2E and SXF3E present respectively a slightly higher and reduced strength. The first octupole of the lattice, OCTD1, appear to be highly efficient for the control of the tune shift. Further comparison with other optimisation will confirm this observation.

#### 4.2.1.2 Optimisation of the off-momentum dynamic aperture

The second optimisation type for the hybrid lattice takes a look at the off-momentum stability. The first steps of this optimisation extended the energy range to $\pm 3\%$ and $\pm 5\%$.

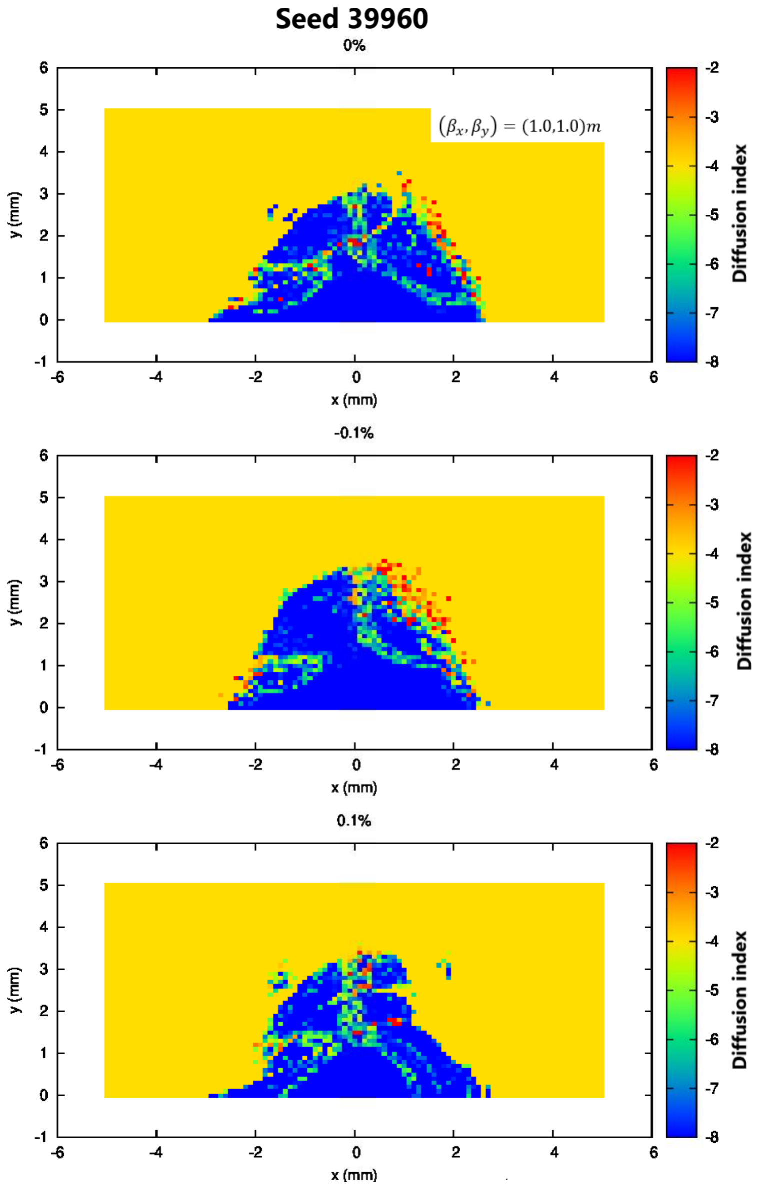

FIGURE 4.6: Typical dynamic apertures obtained at the last generation of the on-momentum optimisation conducted on the 7BA hybrid SOLEIL lattice. The frequency map analysis offers a clear view of the stability within the stable region. Seed 39960.

TABLE 4.2: Strengths of the sextupoles and octupoles of the Seed 39860, in the on-momentum optimisation of the hybrid lattice, at ±0.1%. The strengths are given following Bmad convention.

| Family | Strength | Family | Strength |
|---|---|---|---|
| sxd1e | $-424.17\,\mathrm{m}^{-2}$ | sxf3e | $129.47\,\mathrm{m}^{-2}$ |
| sxd2e | $-399.87\,\mathrm{m}^{-2}$ | octd1 | $-888.32\,\mathrm{m}^{-3}$ |
| sxf1e | $383.61\,\mathrm{m}^{-2}$ | octd2 | $168.49\,\mathrm{m}^{-3}$ |
| sxf2e | $-218.42\,\mathrm{m}^{-2}$ | octf1 | $204.01\,\mathrm{m}^{-3}$ |

As the tune shift with energy rapidly limits the off-momentum stability in the hybrid lattice (*cf* sec. 3.3.3.1), the following optimisations were conducted with octupoles placed at the beginning, middle and end of the dispersion bump. The variation range

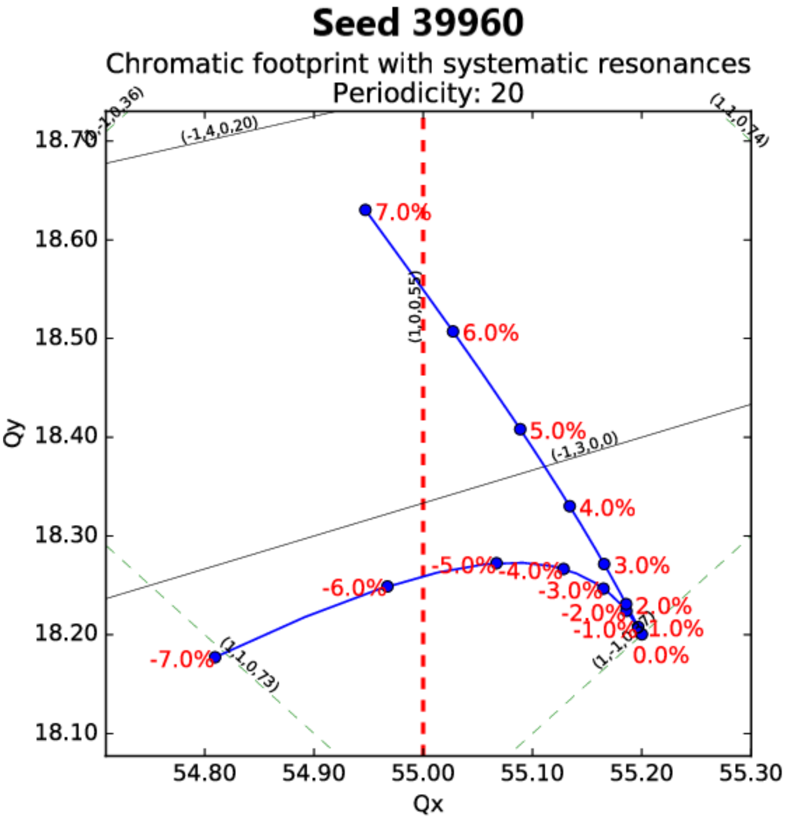

FIGURE 4.7: Tune shift with energy of the typical solution, Seed 39960, of dynamic apertures displayed in Fig. 4.6 and obtained at the last generation of the on-momentum optimisation conducted on the 7BA hybrid SOLEIL lattice.

of the chromatic sextupoles were increased to ±600 $\mathrm{m}^{-2}$. The octupole strength range was set to ±1000 $\mathrm{m}^{-3}$ for slight variations.

Figure 4.8 presents the evolution of the objective function for the optimisations at ±3% and ±5%. The optimisation varied the on-momentum dynamic aperture and the positive off-momentum deviation dynamic aperture.

The −3% and −5% dynamic apertures present slight variations as well: they are steps in the objective functions, which are the results of the octupoles in the optimisation. The objective functions of the negative energies are expected to increase only when brought closer to the working point, where there are less systematic resonances (*cf* Fig. 4.7).

Figure 4.9 displays a typical frequency map analysis obtained at the end of the optimisation in the energy range ±3% and ±5%. For the sake of homogeneity, all results presented for this optimisation correspond to the same individual, the seed 39751 for the ±3% optimisation and the seed 11419 for the ±5% optimisation. The on-momentum dynamic aperture is comparable to the results of the on-momentum optimisation conducted in the previous section, although the stability of the transverse region is enhanced. In both cases, the on-momentum dynamic aperture presents an equivalent stability area with a higher stability than the solution selected in the on-momentum optimisation (*cf* Fig. 4.6). Nonetheless, the off-momentum dynamic apertures remain less than a quarter of the on-momentum DA in terms of stable area. The +3% stability is threatened by

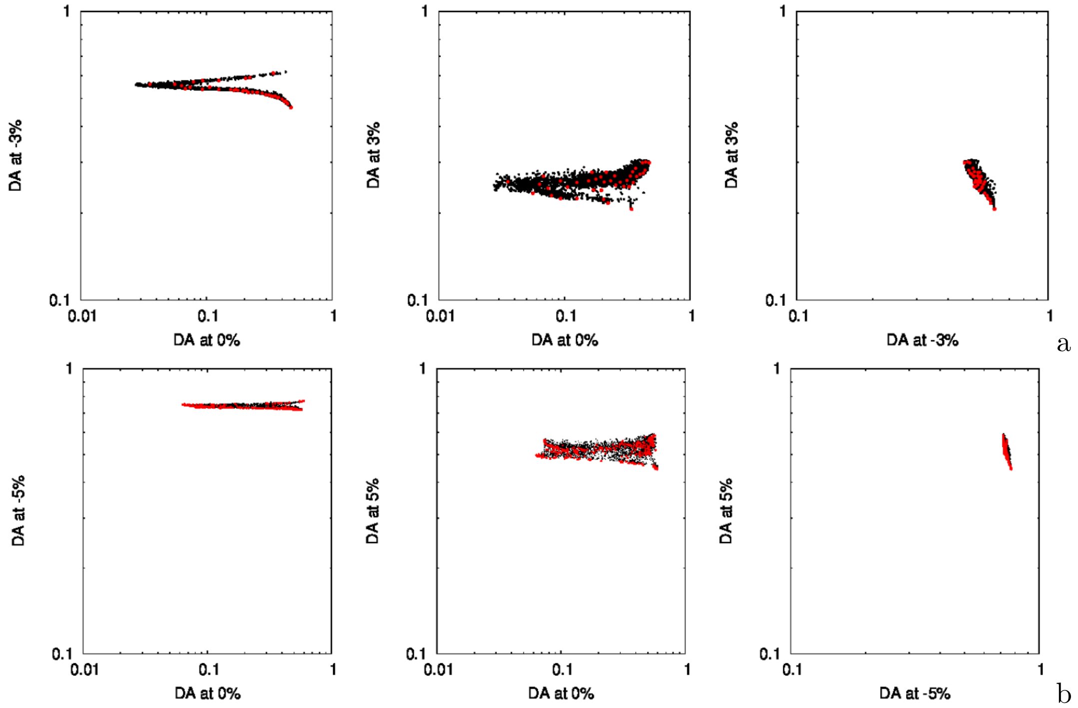

Figure 4.8: Comparison of the objective values for different generations, in an optimisation of the off-momentum dynamic apertures of a period of a 7BA hybrid SOLEIL lattice: (a) for the energies 0%, −3% and +3% and (b) 0%, −5% and +5%. The Pareto front is exposed by colouring the last generation in red.

a resonance, appearing in the FMA in the form of unstable particles and a triangular shape, which is spotted in the +5% DA as well.

Table 4.3 lists the strengths of the sextupoles and octupoles of the seed 39751, of the ±3% optimisation. Compared to the nominal strengths in Table 4.1, the sextupoles have similar strengths. The octupoles are to be compared with the on-momentum optimisation results. The repartition of the octupolar strengths seems to have increased, with a lower strength of OCTD1 and a higher strength of the two other octupoles.

Table 4.3: Strengths of the sextupoles and octupoles of the Seed 39751, in the off-momentum optimisation of the hybrid lattice, at ±3%. The strengths are given following Bmad convention.

| Family | Strength | Family | Strength |
|---|---|---|---|
| sxd1e | $-412.93\,\mathrm{m}^{-2}$ | sxf3e | $295.99\,\mathrm{m}^{-2}$ |
| sxd2e | $-457.23\,\mathrm{m}^{-2}$ | octd1 | $-679.22\,\mathrm{m}^{-3}$ |
| sxf1e | $298.82\,\mathrm{m}^{-2}$ | octd2 | $358.72\,\mathrm{m}^{-3}$ |
| sxf2e | $-241.75\,\mathrm{m}^{-2}$ | octf1 | $408.23\,\mathrm{m}^{-3}$ |

The resulting tune shift with energy is displayed in Fig. 4.10 (a). For the energies ±3%, the dynamic aperture remains small, compared to the on-momentum case. Although, as displayed in Fig. 4.10, the tune shift with energy was efficiently contained around the working point for a ±5% range. Further resonance analysis should be done to

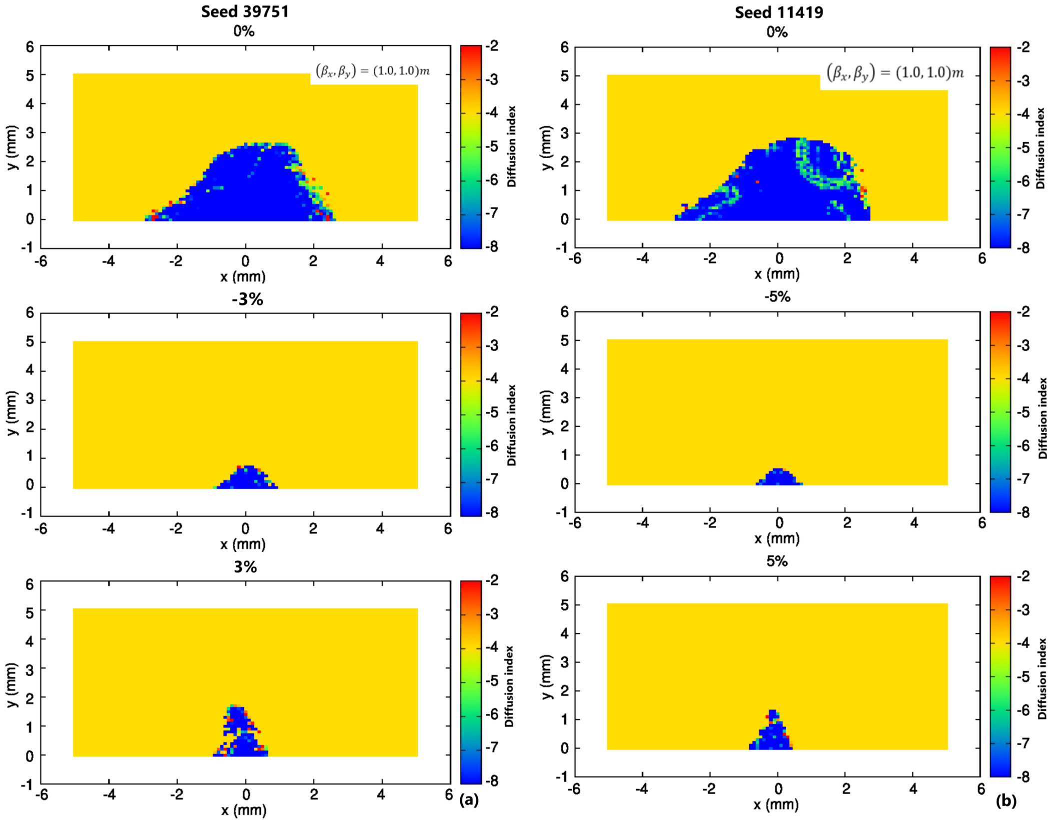

FIGURE 4.9: Frequency map analysis of (a) the seed 39751, which presents the largest dynamic aperture areas, out of the analysed individuals of the optimisation at ±3% and (b) during the optimisation of the on-momentum and ±5% momentum deviation dynamic apertures, the seed 11419.

understand the limitations in dynamic aperture, but were not conducted in the present thesis.

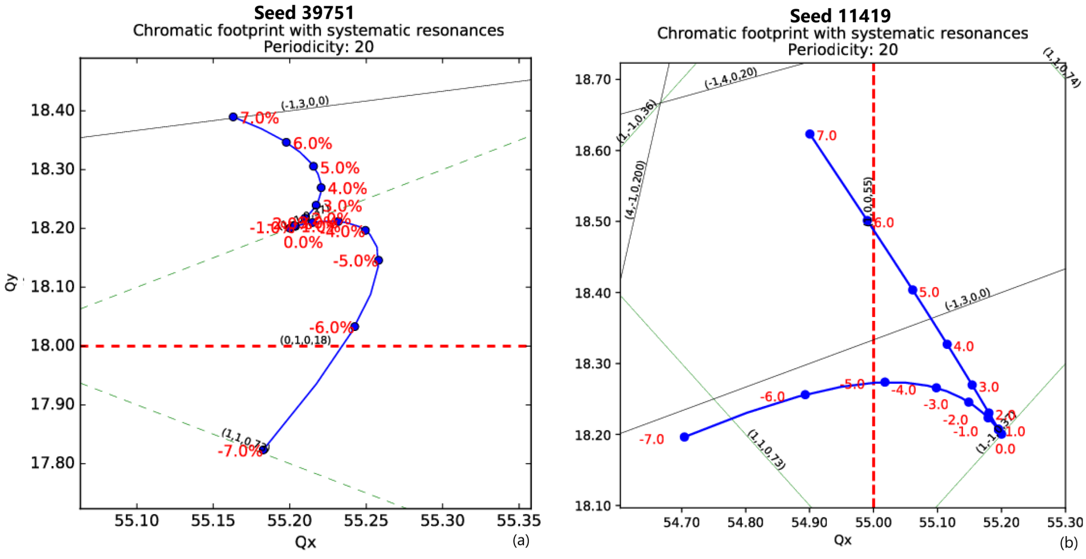

FIGURE 4.10: Chromatic footprint of (a) the solution 39751, of DA in Fig. 4.9, and (b) the solution 11419, of DA in Fig. 4.9.

Figure 4.10 (b) presents the tune shift with energy of the seed 39751 of the ±5% optimisation. Although the tune shift with energy should be contained thanks to the inclusion of octupoles, the particles at ±5% are close to the $-Q_x + 3Q_y = M$ and $Q_x = M$ resonances ($M \in \mathbb{Z}$), further limiting their stability. It is interesting to note that, despite a stronger constraint on the tune shift, which was set to include the ±7% particles in the off-momentum optimisation, where the value was set to ±5% in the on-momentum optimisation, the tune shift with energy is higher in the off-momentum optimisations. The low values of the off-momentum dynamic aperture is thought to have been prioritised by the algorithm, thus limiting its influence on the chromatic footprint constraints.

Table 4.4 gathers the strengths of the nonlinear elements in the seed 11419. All strengths are similar to the selected seed of the on-momentum optimisation, explaining the similar obtained tune shift with energy of Fig. 4.10 (b). The optimisation is believed to have stuck on the difficult increase in the −5% dynamic aperture, thus neglecting the control of the tune shift with energy.

TABLE 4.4: Strengths of the sextupoles and octupoles of the Seed 11419, in the off-momentum optimisation of the hybrid lattice, at ±5%. The strengths are given following Bmad convention.

| Family | Strength | Family | Strength |
|---|---|---|---|
| sxd1e | $-455.15\,\mathrm{m}^{-2}$ | sxf3e | $122.52\,\mathrm{m}^{-2}$ |
| sxd2e | $-395.93\,\mathrm{m}^{-2}$ | octd1 | $-852.53\,\mathrm{m}^{-3}$ |
| sxf1e | $372.56\,\mathrm{m}^{-2}$ | octd2 | $153.00\,\mathrm{m}^{-3}$ |
| sxf2e | $-177.41\,\mathrm{m}^{-2}$ | octf1 | $211.15\,\mathrm{m}^{-3}$ |

### 4.2.2 Optimisation of a HOA lattice

The High-Order Achromat (HOA) lattice is, if infinitely repeated, cancelling all resonant driving terms, up to the second- or third-order - depending on its inner phase advance (*cf* sec. 3.2.3), and provided the sextupoles are identical from one unit cell to another. Nevertheless, the introduction of straight sections and the attached matching sections perturbs the lattice dynamic and the nonlinearities previously annihilated start to arise.

Optimisation of the achromat should increase both on- and off-momentum apertures, by increasing the number of sextupole families to compensate for their resonances and the introduced linear perturbation, and eventually by adding octupoles in the lattice. Considering the nonlinear limitations previously described, the MOGA optimisation of the HOA lattice under study will focus on increasing the transverse energy acceptance and both the stability and the area of the transverse dynamic apertures.

Figure 4.11 presents the sextupole families and their position in the HOA lattice, which will be used as variables in the following optimisations. The defocusing sextupoles were kept as pairs in the core unit cell. The sextupole families were differentiated in the dispersion-suppressor half-cell: the difference in $\beta$-functions could change their efficiency, as well as extracting the half unit cell from the HOA principle considerations. Plus, it

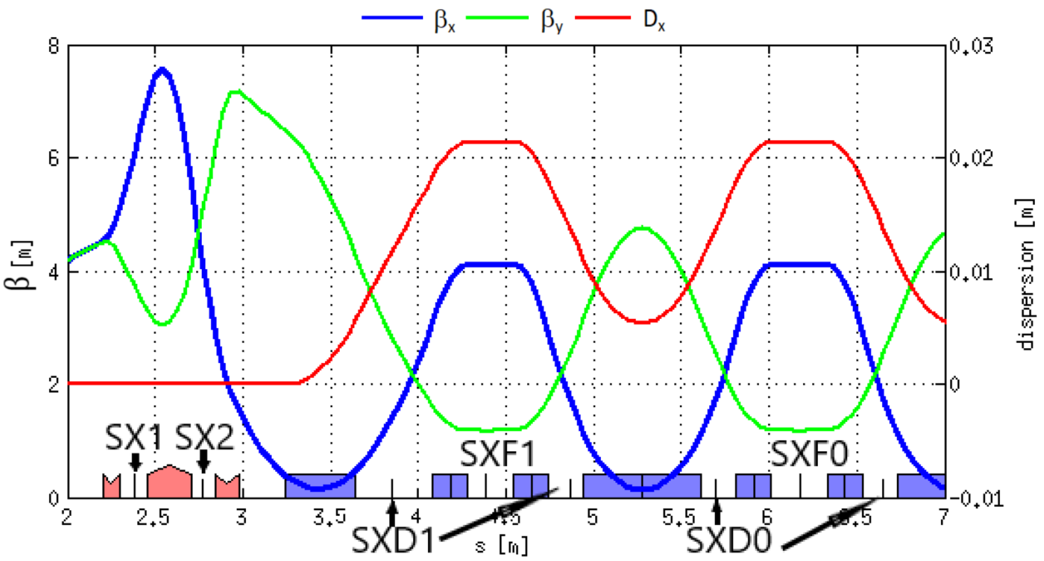

FIGURE 4.11: Position of the sextupoles set as variables in the following MOGA optimisations of the HOA lattice. The zoom corresponds to the outer matching section and dispersive area of the HOA lattice.

adds two nodes to the optimisation. Table 4.5 gathers their strengths for a corrected chromaticity of $(\xi_x, \xi_y) = (-1, -1)$, and a manual on-momentum optimisation using the harmonic sextupoles only, SX1 and SX2.

TABLE 4.5: Nominal strengths of the sextupoles and octupoles of the HOA lattice, with corrected chromaticities $(\xi_x, \xi_y) = (-1, -1)$. The strengths are given following Bmad convention.

| Family | Strength | Family | Strength |
|---|---|---|---|
| sxd0 | $-186.40\,\mathrm{m}^{-2}$ | sxf1 | $304.70\,\mathrm{m}^{-2}$ |
| sxf0 | $304.70\,\mathrm{m}^{-2}$ | sx1 | $150.00\,\mathrm{m}^{-2}$ |
| sxd1 | $-186.40\,\mathrm{m}^{-2}$ | sx2 | $-166.70\,\mathrm{m}^{-2}$ |

#### 4.2.2.1 Optimisation of the dynamic aperture at ±3% using four sextupole families

First steps optimised the off-momentum dynamic aperture at ±3%, while trying to conserve the good stability area on-momentum. To do so, the optimisation first only considered four sextupole families: two chromatic and two harmonic, in order to keep the chromatic sextupoles equal, so that their contribution to the resonances can be cancelled by the HOA principle (*cf* sect. 2.3.2). In that case, the sextupoles SXD1 and SXF1 are kept identical to their correspondent in the core unit cells, SXD0 and SXF0 respectively. Since MOGA-Bmad fixes the chromaticity - which was fixed to $(-1, -1)$ for all optimisations conducted on the HOA lattice, the chromatic sextupole strengths are therefore fixed by this condition. The aim of such an optimisation is to find a suitable set of harmonic sextupoles to further enhance the on-momentum and off-momentum dynamic aperture, at ±3% arbitrarily. To do so, their strength were bounded to $\pm 200\,\mathrm{m}^{-2}$.

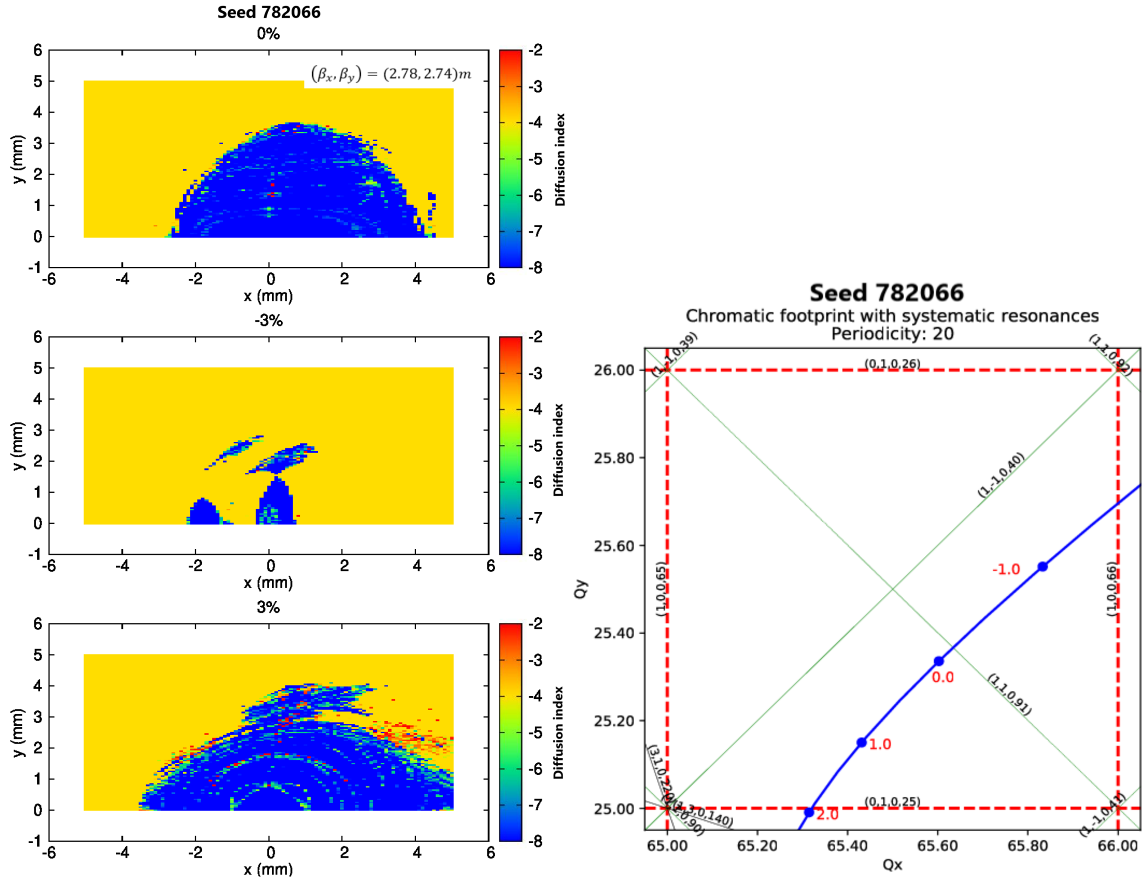

FIGURE 4.12: Typical solution obtained during the optimisation of the on-momentum and ±5% momentum deviation dynamic aperture of the 7BA SOLEIL HOA lattice: (left) FMA of the seed 782066 and (right) its chromatic footprint.

Figure 4.12 (a) displays a typical FMA for the individuals obtained through this optimisation. It corresponds to the seed 782066. Considering that the non-optimised dynamic apertures were larger in the positive energy deviation than the on-momentum, the FMA of the particles at +3% is reduced but remains equal to the on-momentum aperture. The dynamic aperture at −3% suffers from the large tune shift with energy, which is not controlled in the optimisation, as Fig. 4.12 (b) illustrates. Indeed, the absence of octupoles and the few number of nodes in the optimisation limit the effect of the sextupole variations on the tune shift with energy.

Table 4.6 lists the sextupole strengths of the selected seed 782066. The slight variations in SXD0 and SXF0 are due to the difference in calculations from Bmad and A.T. for thin sextupoles. This difference compels the use of the same code for analysis of the MOGA results, to avoid any alteration in the expected performances.

Table 4.6: Strengths of the sextupoles and octupoles of the seed 782066, extracted from a first optimisation of the HOA lattice at the set energies 0% and ±3%. Only two chromatic families were used. The strengths are given following Bmad convention.

| Family | Strength | Family | Strength |
|---|---|---|---|
| sxd0 | $-202.92\,\mathrm{m}^{-2}$ | sx1 | $49.22\,\mathrm{m}^{-2}$ |
| sxf0 | $300.41\,\mathrm{m}^{-2}$ | sx2 | $-57.90\,\mathrm{m}^{-2}$ |

#### 4.2.2.2 Optimisation of the tune shift using octupoles

An additional optimisation was conducted with the inclusion of octupoles near the chromatic sextupoles. The sextupoles in the dispersion suppressor cells were differentiated to include two nodes in the optimisation: as the $\beta$-functions of such cells, and therefore their phase advance, were not preserved when creating the dispersion-free zone, they can be considered outside of the compensative HOA principle. The octupoles were varied in the range $\pm 5000\,\mathrm{m}^{-3}$, to locate the most efficient position.

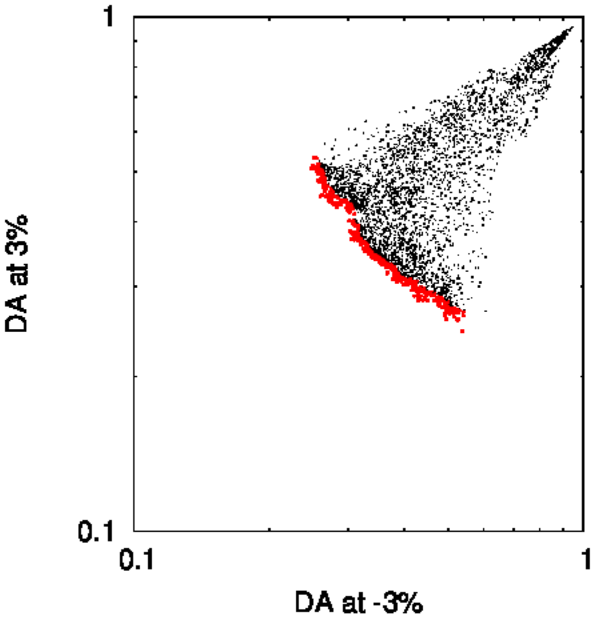

Figure 4.13: Comparison of the off-momentum objective functions during and at the end of the optimisation (red dots).

The chromatic sextupoles' strengths remained in the range $\pm 600\,\mathrm{m}^{-2}$, which sign was fixed positive for focusing sextupoles, negative for defocusing sextupoles. The harmonic sextupoles were limited to $\pm 500\,\mathrm{m}^{-2}$. Figure 4.13 shows the progress of the optimisation, by comparing the off-momentum objective functions. The red dots correspond to the last generation.

The progress of this optimisation lies both at +3% and −3%. Compared to the results of the previous optimisation, which was conducted without octupoles, the evolution of the −3% objective function proves the tune shift with energy is being contained by the added octupoles. Figure 4.14 (a) illustrates the frequency map analysis of a typical solution selected in the last generation. Compared to Fig. 4.12, the dynamic aperture at 3% is limited by the integer resonance: even though the constraint on the chromatic footprint was set to ±7%, the optimisation only contained the ±3% range.

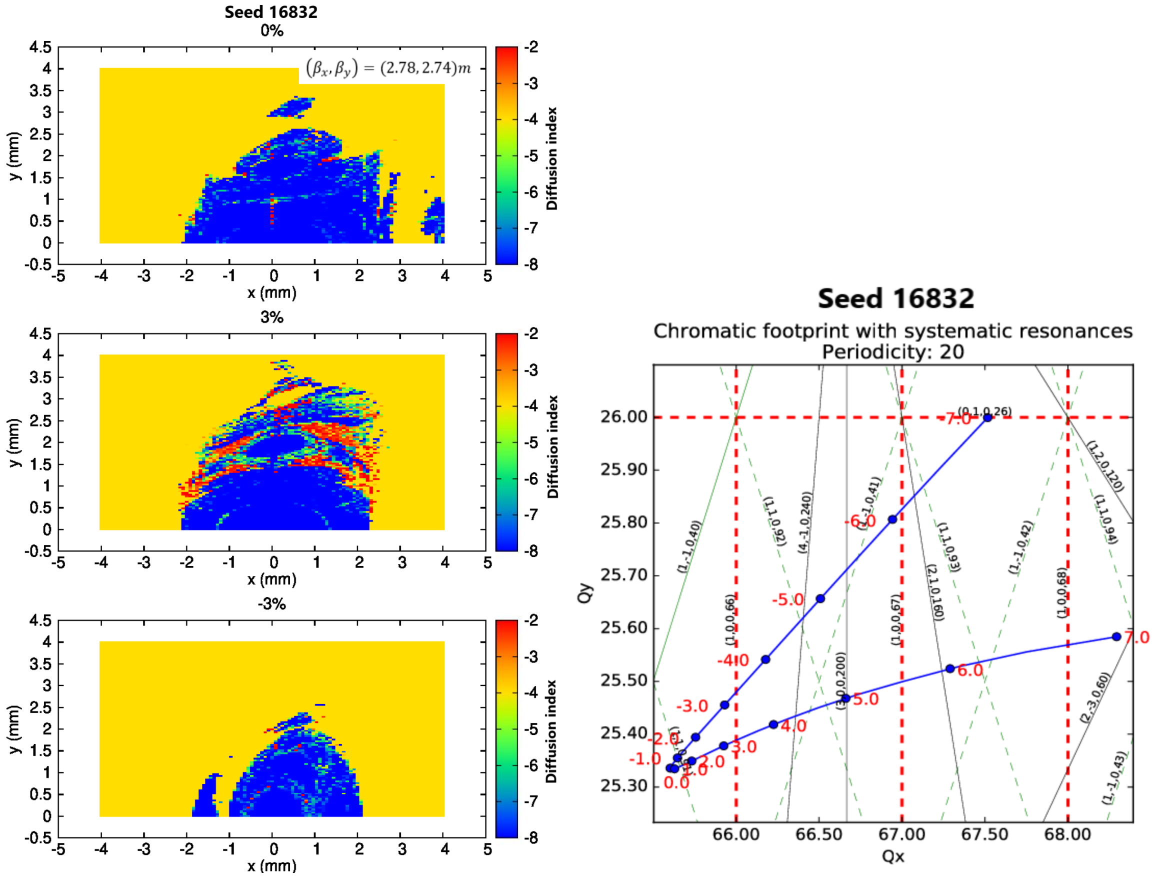

FIGURE 4.14: Typical solution obtained during the optimisation of the on-momentum and ±3% momentum deviation dynamic apertures, of the 7BA SOLEIL HOA lattice. The seed 16832 is characterised with its FMA (left) and chromatic footprint (right).

Despite the limitation at +3%, the use of octupoles helped control the tune shift with energy, which put the tunes at −3% further away from the integer resonance, which was limiting its stability in the last optimisation. Figure 4.14 (b) displays the chromatic footprint on a tune diagram, exhibiting the systematic resonances for a 20-fold symmetry lattice.

Table 4.7 gathers the nonlinear strengths of the seed 16832. Since the optimisation could optimise the dynamic aperture at −3% with no resonance limitation, the strengths of the sextupoles appear slightly higher than their nominal values, which only aimed at correcting the chromaticities. The strengths of SXD1 and SXF1 are higher than the core sextupoles, which optimised strengths are closer to their nominal values. The octupoles implemented reach strengths as high as 4700 m$^{-3}$, which confirms the need for control of the tune shift to increase the energy acceptance and beam lifetime.

Table 4.7: Strengths of the sextupoles and octupoles of the seed 16832, extracted from an optimisation of the HOA lattice at the set energies 0% and ±3%. Four chromatic sextupole families were used, along with two octupole families, located on the core sextupoles. The strengths are given following Bmad convention.

| Family | Strength | Family | Strength |
|---|---|---|---|
| sxd0 | $-244.91\,\mathrm{m}^{-2}$ | sxd0 $[k_3 l]$ | $-920.4\,\mathrm{m}^{-3}$ |
| sxf0 | $335.04\,\mathrm{m}^{-2}$ | sxf0 $[k_3 l]$ | $4741\,\mathrm{m}^{-3}$ |
| sxd1 | $-306.38\ \mathrm{m}^{-2}$ | sxf1 | $398.89\,\mathrm{m}^{-2}$ |
| sx1 | $86.0\,\mathrm{m}^{-2}$ | sx2 | $-104\,\mathrm{m}^{-2}$ |

### 4.2.3 Conclusion on the MOGA optimisation of the ultra-low emittance schemes

The conservation of both principles, the non-interleaved principle and the HOA principle proves to be difficult in the designed lattices.

**On the use of MOGA for the optimisation of the 7BA hybrid lattice** In the case of the hybrid lattice, the presence of secondary sextupoles under the dispersion bumps increases the nodes in the nonlinear optimisation but perturbs the non-interleaved principle. The dynamic aperture remains maximised in the vicinity of the on-momentum particles, yet the resulting transverse acceptance is smaller both in the vertical and horizontal plane, compared to the one obtained with a pure non-interleaved lattice. The inclusion of secondary sextupoles remains for the off-momentum dynamics need to be maximised, for stability and beam lifetime considerations.

First optimisations aimed at enhancing the on-momentum dynamic aperture, to potentially find a larger acceptance than with the non-interleaved sextupoles. No individual found had a higher on-momentum dynamic aperture than the nominal lattice, despite the use of all sextupole families and octupoles.

Further studies aimed at increasing the off-momentum dynamic apertures, at ±3% and ±5% in different runs. Unfortunately, no found solutions could match the off-momentum dynamic aperture to the level of the on-momentum DA. Further resonance analysis is required to understand the limitations off-momentum. Furthermore, optimisation of the off-momentum dynamic apertures led to a small reduction of the on-momentum dynamic aperture as well.

**On the use of MOGA for the optimisation of the 7BA HOA lattice** In the case of the HOA lattice, different optimisations were conducted to test the robustness of the lattice. First optimisations aimed at keeping the chromatic sextupoles identical, to preserve the HOA principle. Only two harmonic sextupoles were implemented to optimise the on- and off-momentum aperture. The absence of octupoles led to an uncontrolled tune shift with energy, which limited the optimisation.

To increase the number of nodes, a second optimisation differentiated the sextupoles in the dispersion suppressor cell. Nonetheless, the tune shift remains unconstrained.

Therefore, octupoles were added at the location of the core sextupoles; they were coded as an octupolar component of the sextupoles. The tune shift could then be constrained within a half-integer window around the working point, which allowed an enhanced off-momentum stability, away from systematic resonances.

## 4.3 4-superperiod HOA-based lattice for the SOLEIL upgraded storage ring

The current SOLEIL storage ring is surrounded by 29 beamlines. Amongst them, two 180 m-long beamlines Anatomix and Nanascopium, were built in 2012. They work in the hard X-ray range. Their implementation required the adaptation of the straight section SDL13 into canted optics, described in the section 1.5.3 and displayed in Fig. 4.15.

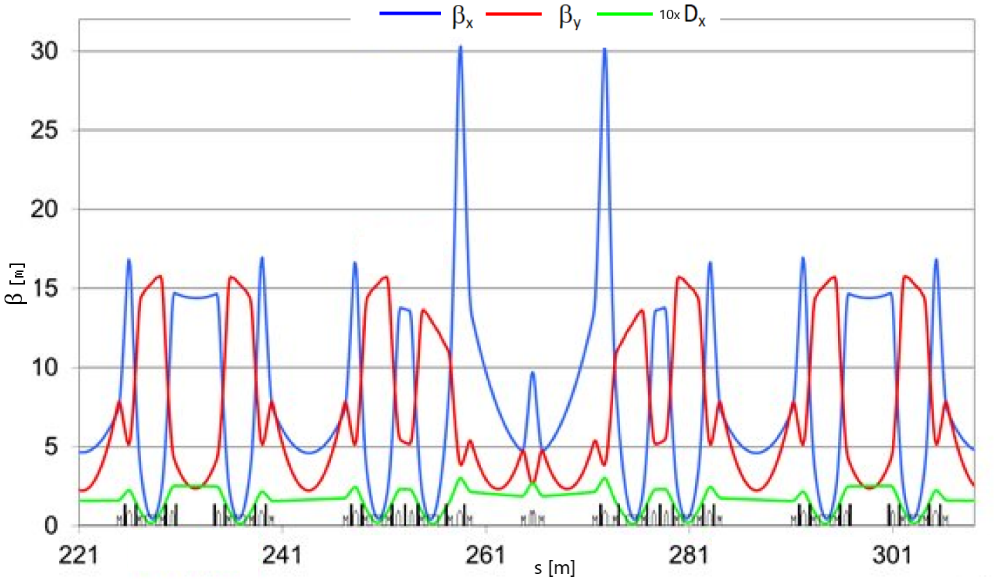

FIGURE 4.15: $\beta$-functions around the SOLEIL SDL13 straight section, where canted optics were implemented for the two long SOLEIL beamlines, Anatomix and Nanoscopium.

The SOLEIL upgrade project aims at maintaining the beamlines positions. The beamline MARS, where radioactive samples are tested and which required an authorisation from the Agence de Sûreté Nucléaire (ASN), along with the long beamlines should keep their current positions. To include two undulators in one straight section in the canted optics for ANATOMIX and NANOSCOPIUM, larger straight sections are required: the symmetry of the ultra-low emittance lattices under study is decreased from 20 to 4. New designs include two types of straight sections: four long straight sections of 6 m for the long beamlines, RF cavities, injection and extraction and regular straight sections of 4 m for the other insertion devices.

### 4.3.1 Layout of a 4-superperiod HOA lattice

Following the new recommendations two 4-superperiod 7BA lattices were designed : one hybrid and one HOA-based. Both include two types of straight sections: long 6 m straight sections for the injection/extraction, the RF cavities and the two long beamlines on canted optics, and smaller 4 m straight sections for the other insertion devices. I designed several 4-superperiod HOA lattices, 7BA and 9BA. The 9BA version is available in the Appendix F. Figure 4.16 compares the Twiss functions and dispersion of the 7BA hybrid and 7BA HOA 4-superperiod lattices.

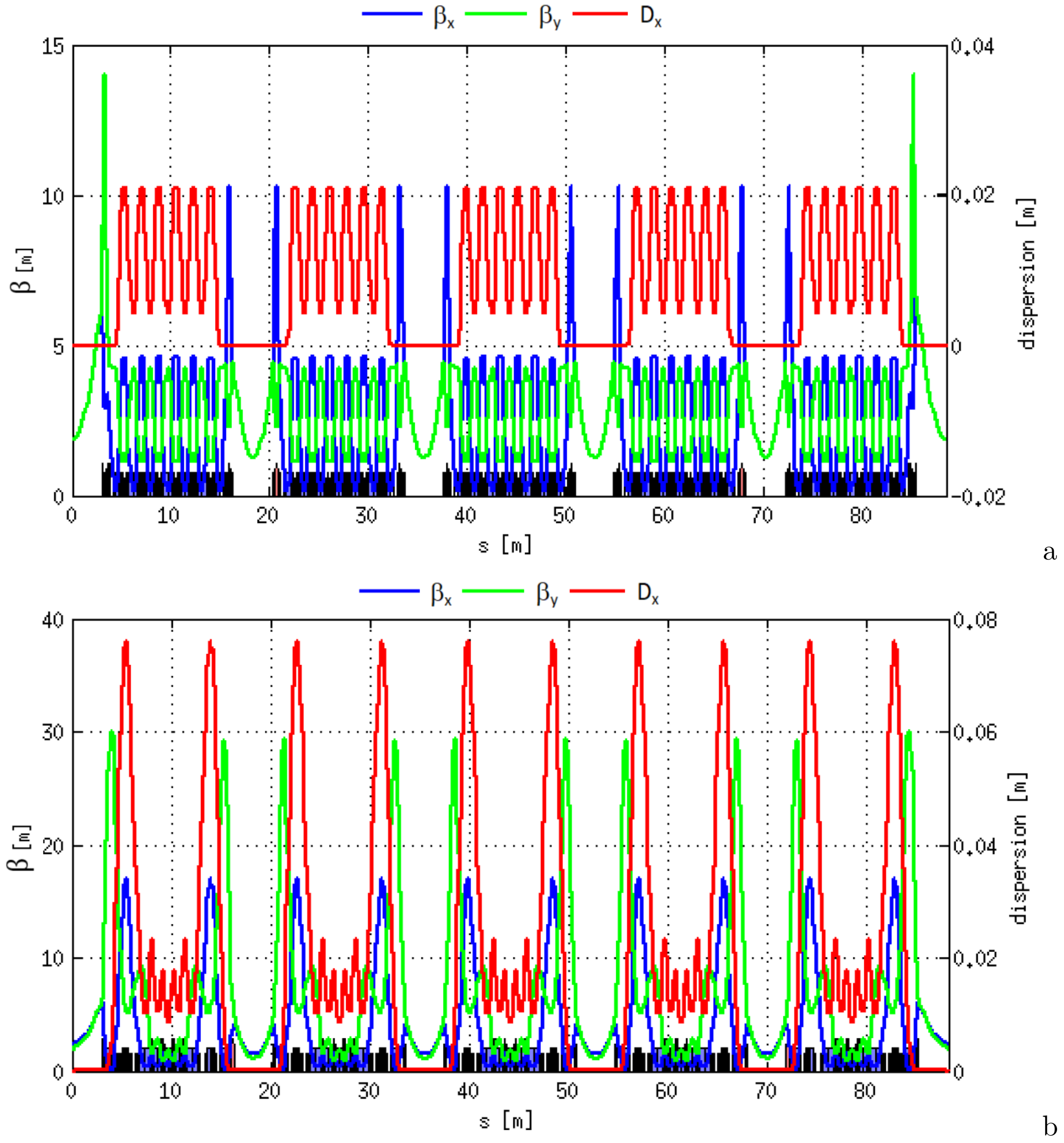

FIGURE 4.16: Twiss parameters and magnet layout of the (a) 7BA HOA and (b) 7BA hybrid 4-superperiod lattices for the SOLEIL 2.75 GeV storage ring.

Table 4.8 compares the main characteristics of both lattices. Despite the reduced length per period, the main characteristics were maintained in the hybrid case, such as the natural horizontal emittance and the momentum compaction factor. The design of

Table 4.8: General characteristics of the hybrid and HOA 4-superperiod lattices for the SOLEIL 2.75 GeV storage ring.

| | 4-superperiod hybrid | 4-superperiod HOA |
|---|---|---|
| Emittance $\epsilon_x$ | 77 pm.rad | 72 pm.rad |
| Tunes per superperiod $(\nu_x, \nu_y)$ | ( .20, .45) | (16.85, 6.46) |
| Momentum compaction factor $\alpha_0$ | $1.54 \times 10^{-4}$ | $6.68 \times 10^{-5}$ |
| Reverse bending angle | -0.165 degrees | -0.146 degrees |
| Energy loss per turn | 312 keV | 536 keV |
| Magnet occupation<br>excluding $drifts < 0.15$m | 50.8%<br>64% | 64.1%<br>90.7% |
| $(\beta_x, \beta_y)$ @ID in LS | (2.5,2.1) m | (1.9, 1.9) m |
| $(\beta_x, \beta_y)$ @ID in SS | (1.5, 1.1) m | (1.7, 1.7) m |

a HOA 4-superperiod lattice increases the tightness of the lattice. The easy matching in the short straight sections allows an increased length of the unit cells, with dipoles of 0.8 m. The angular dispersion suppressor method is adopted (*cf* sec. 3.2.4), which explains the increase in the reverse bending angle, to recover a low emittance and a reduced momentum compaction factor, compared to the 20-fold case. Compared to the 20-fold symmetry where the magnet occupation was 66% in the hybrid case and 78% in the HOA case when the drifts smaller than 0.15 m were excluded from the calculations, the magnetic occupation of the 4-superperiod lattices is of 64% in the hybrid case, and as high as 90% in the HOA case.

The $\beta$-functions are matched at $\simeq (1,1)\,$m in all short straight sections for both lattices for beam matching considerations (*cf* sec. 1.4.1.2), and $\simeq (2,2)\,$m in the long straight sections, where the conditions are no longer critical. An additional quadrupole was required in both lattices to match the low $\beta$-functions at the middle of the long straight sections. Figure 4.17 is a zoom of the Twiss parameters of the 7BA period between the middle and long straight sections, for both the hybrid and HOA 4-superperiod lattices.

### 4.3.2 Study of the feasibility of the longitudinal injection scheme

Alongside the additional constraints reducing the symmetry, the injection scheme of the ultra-low emittance lattices is under discussion. The current SOLEIL injection scheme is transverse off-axis. In that case, the injected beam would be bent by a septum and kicked off-axis at a certain horizontal position $x_{inj}$ using a Multipole Injector Kicker (MIK). The injected beam is damped, turn by turn, towards the machine axis. Nonetheless, not to perturb the stored beam, the injected beam needs to be injected at a high horizontal shift, which falls out of the current transverse stability of the ultra-low emittance lattices under study. To keep the current injection scheme of the SOLEIL storage ring, the $\beta$-functions can be raised in a long straight section, to locally increase the transverse acceptance and inject the beam off-axis. Nonetheless, the damping partition number $\mathcal{J}_x$ of such lattices is close to 2, which induces an increased damping time and a higher

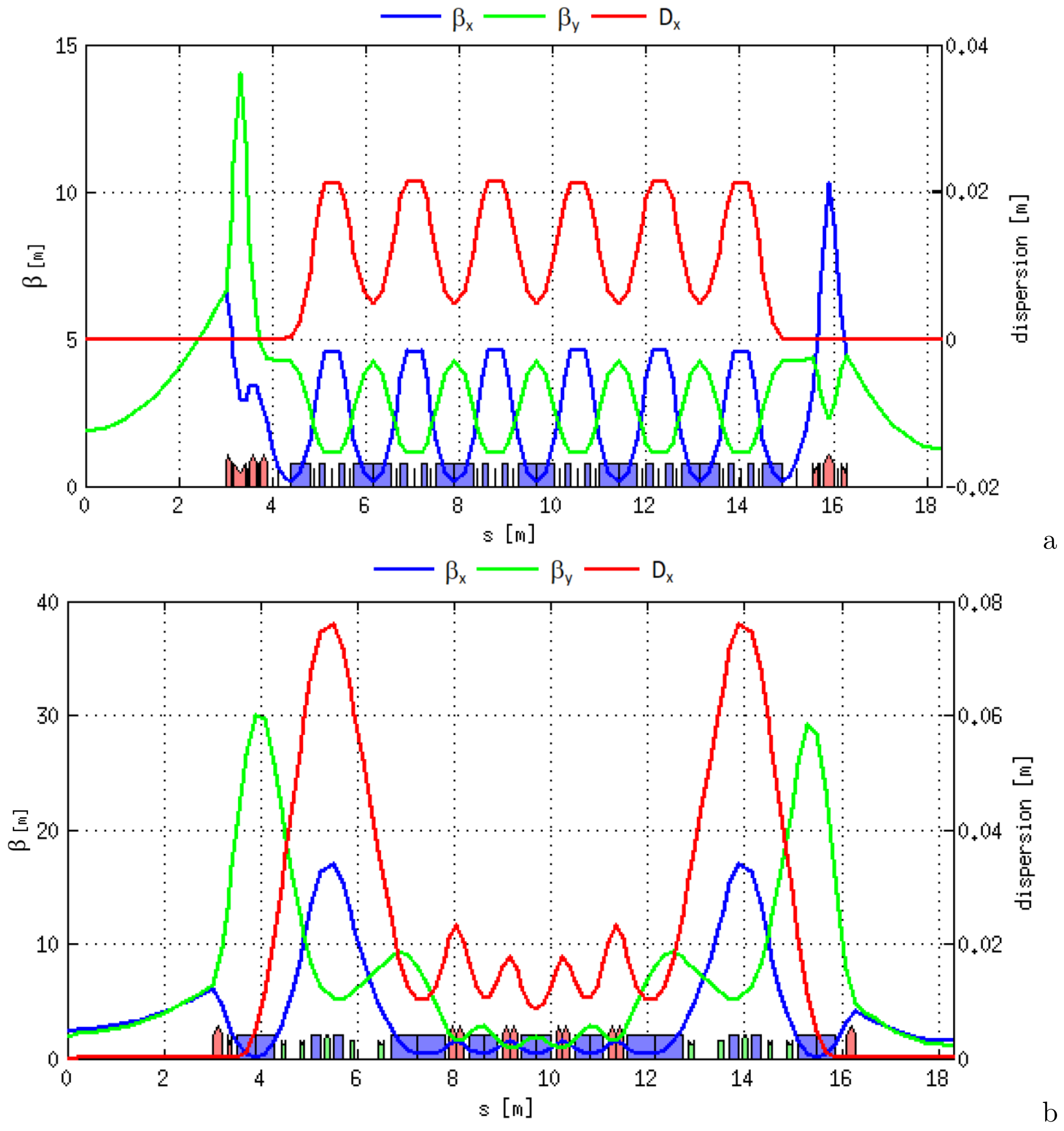

FIGURE 4.17: Twiss parameters and magnet layout of the (a) 7BA HOA and (b) 7BA hybrid 4-superperiod lattices around the long straight section.

number of turns to damp the injected beam, further increasing the probability of losses. Additionally, it also decreases the natural horizontal emittance. Although this scheme is studied amongst the Beam Dynamics group of SOLEIL, I did not participate in the optimisation of such a lattice.

Another scheme consists in swapping the beams. To prevent intensity losses in the stored beam, it is extracted, after a defined number of turns, from the storage ring and replaced with a new beam. This principle is called the swap-out injection. Its implementation is required where no top-up injection can be used, which depends on the machine parameters. The extracted beam can be placed in an accumulator ring, where it shall be damped and re-accelerated before being injected again in the machine [97]. Such a method requires the design and implementation of an accumulator ring, in the same tunnel as the storage ring. The SOLEIL upgrade aims at conserving its current injection modes, including the top-up system, and has therefore not considered this type of injection for its upgraded lattices.

A last scheme consists in injecting the beam directly on-axis, but shifted in energy. Using the off-momentum closed orbit $D_0\delta$, the injected beam could be kicked onto a chromatic closed orbit using a Multipole Injector Kicker (MIK), and is detailed in the following section. I participated in the adaptation of the linear lattice to this injection scheme and the nonlinear optimisation to increase both the off-momentum dynamic aperture and the injection efficiency.

#### 4.3.2.1 Longitudinal on-axis injection

This section describes the basic elements required to understand the longitudinal on-axis injection, and the particularities of the scheme studied for SOLEIL upgrade. The first part presents the nonlinear kicker which should be used to kick the injected beam onto the designated chromatic closed orbit. The required energy deviation is fixed by the dimensions and characteristics of the kicker: to benefit from a maximum magnetic field, the injected beam should be horizontal shifted at a set $\Delta x$. The use of this method requires a dispersion bump in the injection section: the bump differentiates the chromatic orbits around the magnetic peak of the nonlinear kicker. The higher the dispersion bump, the lowest the energy deviation required to match the closed orbit at the required horizontal shift. Two types of dispersion bumps are compared, and one of them is ran in MOGA, to try and optimise the transverse dynamic aperture at the required energy deviation, and at its opposite value.

#### 4.3.2.2 Multipole-Injector Kicker and injection parameters

To do so, the system first bends the beam using a thick septum and a thin septum, then a Multipole-Injector Kicker (MIK), which finally kicks the beam onto the relevant chromatic orbit. An ongoing collaboration between SOLEIL and MAX IV developed a MIK for the injection of MAX IV [126, 127]. Figure 4.18 illustrates the ideal magnetic field of such a nonlinear kicker: the injected beam benefits from a large magnetic field which kicks it transversally towards the corresponding off-momentum chromatic closed orbit. The MIK should be transparent to the stored beam, therefore have a naught magnetic field around the machine axis.

In reality, the nonlinear magnetic field of a MIK approaches that of a sextupole magnet, as displayed in Figure 4.19. This MIK corresponds to the result of the collaboration between SOLEIL and MAX IV, and was designed for MAX IV injection. The plateaux are located at ±10 mm [127]. To prevent a perturbation on the stored beam, the plateaux should be located as far away as possible from the axis $x = 0\,\mathrm{mm}$. Nonetheless, the transverse dynamic aperture prevents a large horizontal shift, which limits the horizontal position of the injected beam. In the case of the MAX IV injection, the injected beam was shifted at 4.66 mm, and benefits from a 39 mT magnetic field for its top-up injection [128]: the injected beam is therefore not placed on the plateau, but

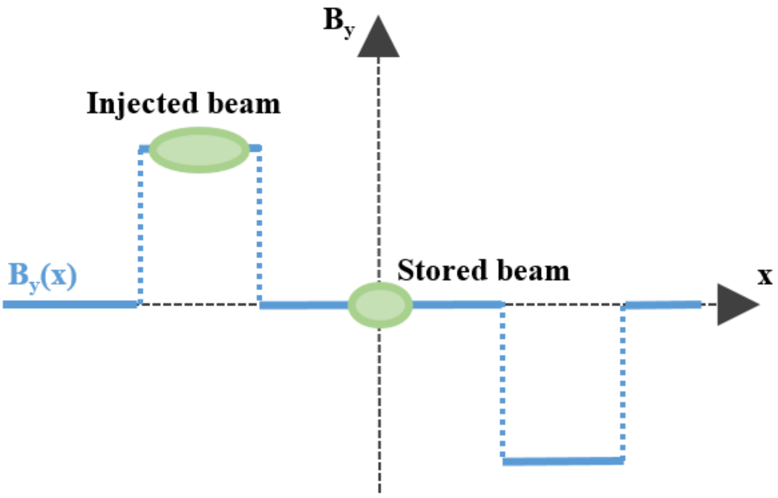

FIGURE 4.18: Schematic of the ideal magnetic field of a Multiple-Injector Kicker (MIK). The injected beam is shifted horizontally and benefits from a positive magnetic field, which kicks the beam onto its chromatic closed orbit. The magnetic field of a MIK should be naught on-momentum, as not to perturb the stored beam.

benefits from the maximum slope. In that case, the level of the plateau is high enough to provide a large slope around the required horizontal shift. Nevertheless, the injected beam has an horizontal size $\Delta x \neq 0$, which spreads the injected beam onto the slope: the extremities of the injected beam do not receive the same kick.

The main limitation induced by the nonlinear MIK is the distance between the plateaux and the axis $x = 0\,\text{mm}$. Such a distance monitors the length of the naught plateau around the stored beam: a close plateau renders difficult the maintenance of a naught magnetic field for the stored beam, and can induce perturbation for the furthest particles of the stored beam, which makes the injection no longer transparent. The SOLEIL Pulsed Magnet group managed to produce a MIK of maximum field at $x = -3.5\,\text{mm}$. The field is sextupolar around the maximum, with a field variation of $\pm 10\%$ for a $\pm 0.5\,\text{mm}$ variation around the extrema.

The injected beam trajectory has to be prepared before entering the MIK. For example, the current MIK envisioned for the injection of SOLEIL upgrade has its magnetic field peak at $\pm 3.5\,\text{mm}$ horizontal shift. The injected beam is therefore bent by a septum at the entrance of the straight section, before entering the MIK where it will be kicked onto an off-momentum chromatic closed orbit.

#### 4.3.2.3 On the dispersion bumps

The use of the longitudinal scheme requires specific changes in the linear lattice. To cope with the horizontal shift limit imposed by the MIK, and the limited energy acceptance of the ultra-low emittance lattice, several schemes are approached. The first follows the steps described by M. Aiba et al. [39], and aims at kicking the injected beam on a set chromatic closed orbit. The choice of the energy deviation depends on the injected beam size, the stored beam and the distance between both closed orbits, as the injected beam

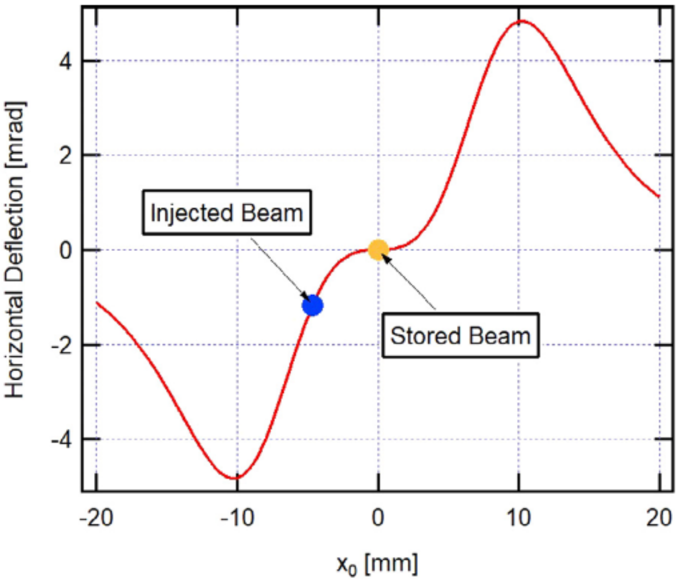

Figure 4.19: Example of the nonlinear magnetic field of the SOLEIL-MAX IV collaborative MIK. The plateaux are located at ±10 mm, from [127].

should not interact with the stored beam. To increase the distance between the closed orbits, a dispersion bump is created on a straight section. The lowest energy complying with those parameters was set at $\delta = -6\%$ for the ultra-low emittance lattices presented. Three methods I developed to create a dispersion bump are explored in this section. To comply with the requirements in terms of distance of the chromatic closed orbits imposed by both the magnetic field of the MIK and its gap, the dispersion bump should be as high as possible.

A first method to create a dispersion bump is to manipulate the angle of the last dipole and the last reverse bend, allowing a natural increase in the dispersion. Figure 4.20 illustrates a 5 cm dispersion bump included in one long straight section of the previous 4-superperiod 7BA HOA lattice. The inclusion of the dispersion bump drops the symmetry down to 1. This method conserves $\beta$-functions of the external half-cell, and thus does not affect the HOA principle. The total angle is restored by multiplying the whole superperiod by a proportional factor. The periodic conditions were recovered thanks to the quadrupolar triplets in the matching sections.

A 5 cm dispersion bump distances the chromatic closed orbit of an off-momentum particle by $D_0\delta$, which equals 3 mm for an energy deviation of 6% for instance. The energy deviation corresponding to a closed orbit at $-3.5$ mm at the centre of the MIK is $-7\%$ with this dispersion bump, which is too high to optimise. Although the longitudinal energy acceptance is higher than ±10%, the off-momentum transverse dynamics at such large energy deviation is limited by the large tune shift with energy which crosses systematic resonances. Since the test optimisations conducted on the HOA and hybrid 20-fold symmetry lattices proved the need of a large dedicated time to increase, step by step, the off-momentum stability, the maximum feasible energy deviation at the MIK is

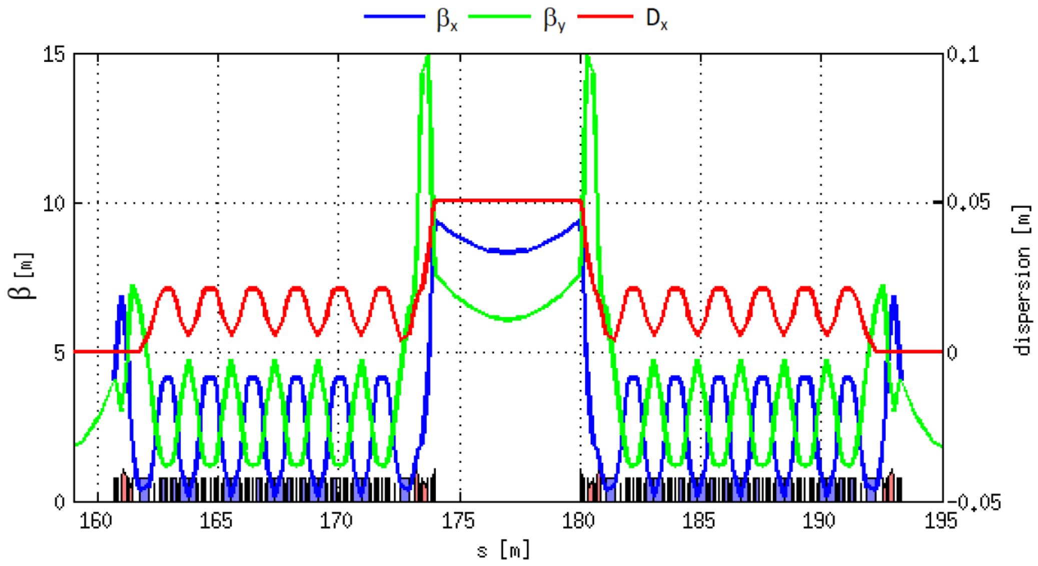

Figure 4.20: Twiss parameters and magnet layout of the 7BA HOA lattice for the SOLEIL 2.75 GeV storage ring.

set at −4/5%. Therefore, the level of the dispersion bump is increased up to 8 cm and 10 cm.

Table 4.9: Evolution of the emittance for different dispersion bump levels, created using the external dipoles and reverse bends only.

| Dispersion level | Bending Angle | Reverse Bending Angle | Ring emittance |
|---|---|---|---|
| $\eta_{bump} = 5\,\text{cm}$ | 0.073 rad | −0.0026 rad | 74 pm.rad |
| $\eta_{bump} = 8\,\text{cm}$ | 0.1007 rad | −0.0036 rad | 100 pm.rad |
| $\eta_{bump} = 10\,\text{cm}$ | 0.1191 rad | −0.0043 rad | 150 pm.rad |

Nonetheless, such a manipulation increases the dispersion at the last dipole, and therefore increases emittance. Table 4.9 compares the resulting natural horizontal emittance of the ring, after inclusion of different levels of dispersion bumps. The set limit in emittance for the upgrade of the SOLEIL storage ring, which is 100 pm.rad, is reached for a dispersion bump of 8 cm, which corresponds to a required energy deviation of $\delta = -4\%$ at the centre of the MIK. The methods for creation of the dispersion bump will now be compared for a dispersion peak of 8 cm.

A second method modifies the angle of the last dipole and adjusts the $\beta$-functions in the middle of the straight section to recover the periodic conditions. Figure 4.21 displays the resulting Twiss functions and dispersion. The emittance here rose to 110 pm.rad, which is slightly higher than with the previous method.

Table 4.10 states the bending angle of the last dipole and the quadrupolar strength of the matching triplets, required for the creation of the bump displayed in Fig. 4.21. Since the number of variables is limited to four, the $\beta$-functions at the middle of the straight section could not be kept at their nominal values: they rose to $(\beta_x, \beta_y) = (7.3, 6.8)\,\text{m}$.

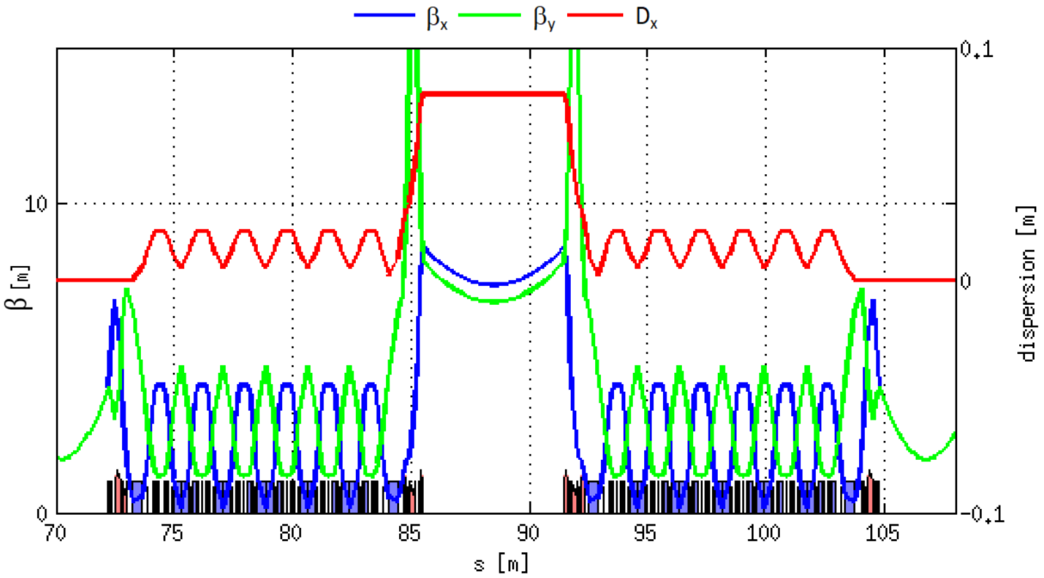

FIGURE 4.21: Twiss parameters and dispersion bump of 8 cm for a 7BA HOA 4-superperiod lattice, using the external dipoles' angles and the quadrupolar triplets.

TABLE 4.10: Variation of the matching parameters for the creation of the dispersion bump in Fig. 4.21.

| Name | Parameter | Value |
|---|---|---|
| bd1out | Bending Angle | 0.10510 rad |
| qd01f | Defoc. strength | $15.3244\,\mathrm{m}^{-2}$ |
| qd02f | Defoc. strength | $13.875\,\mathrm{m}^{-2}$ |
| qf02f | Foc. strength | $-9.81889\,\mathrm{m}^{-2}$ |

Another method lengthens the external dipole to recover the symmetric condition at the dispersion bump, at the image of the dispersion suppressor ”missing dipole” method. This frees the quadrupole triplet and allow their use for the matching of the $\beta$-functions at the middle of the straight section. Figure 4.22 displays the results of such optimisation.

The resulting $\beta$-functions are $(\beta_x, \beta_y) = (1.8, 1.5)\,\mathrm{m}$. Table 4.11 gathers the variations of the matching parameters. The length of the external dipoles was increased by 20%, to satisfy the periodic condition on the dispersion. Nonetheless, the longer dipole has a larger contribution to the emittance, which rises to 412 pm.rad.

TABLE 4.11: Variations of the matching parameters for the creation of the dispersion bump in Fig. 4.22.

| Name | Parameter | Value |
|---|---|---|
| bd1out | Bending Angle | $0.1168\,\mathrm{rad} \longrightarrow 0.1309\,\mathrm{rad}$ |
| bd1out | Length | $0.4\,\mathrm{m} \longrightarrow 0.486\,\mathrm{m}$ |
| qd01f | Defoc. strength | $15.26\,\mathrm{m}^{-2} \longrightarrow 16.59\,\mathrm{m}^{-2}$ |
| qd02f | Defoc. strength | $12.69\,\mathrm{m}^{-2} \longrightarrow 17.17\,\mathrm{m}^{-2}$ |
| qf02f | Foc. strength | $-9.54\,\mathrm{m}^{-2} \longrightarrow -10.97\,\mathrm{m}^{-2}$ |

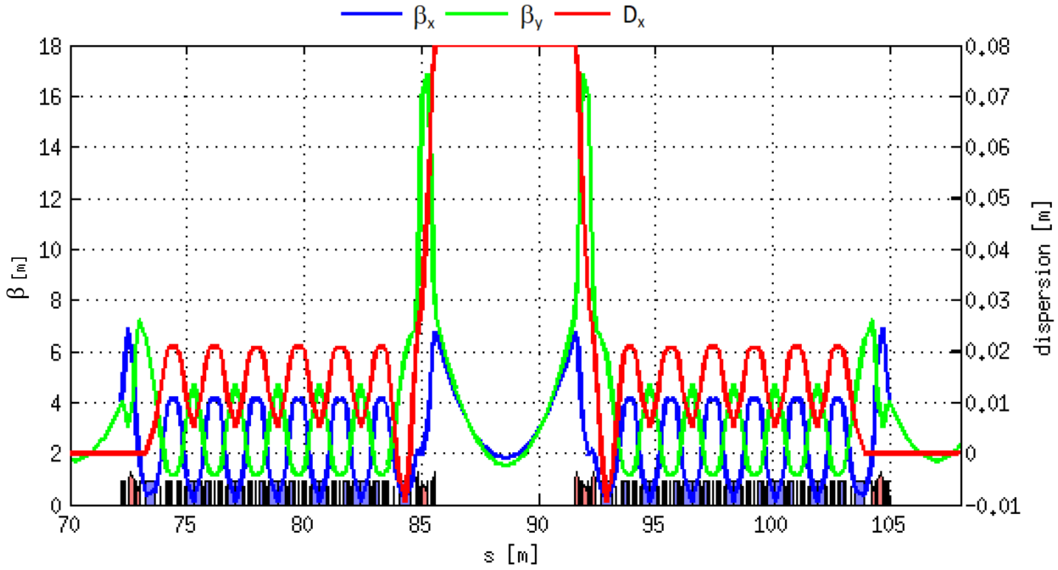

FIGURE 4.22: Twiss parameters and dispersion bump of 8 cm for a 7BA HOA 4-superperiod lattice, using the external dipole and reverse bend angles, lengthening the external dipoles, and matching the $\beta$-functions thanks to the quadrupole triplets.

## 4.4 Non-linear optimisation of a 7BA-4BA lattice for the upgrade of the SOLEIL storage ring

On the current storage ring, the positions of the long beamlines and the MARS beamline are not symmetric. Therefore, the 4-superperiod cannot exactly conserve both positions. The exploration of the storage ring upgrade led my colleague Alexandre Loulergue to design several MBA-NBA lattices based on HOA cells [129]. His investigations, conjugated with the conservation of the beamline positions - or integration of the lattice in the tunnel, led to a 7BA-4BA lattice, whose Twiss $\beta$ functions and dispersion are displayed in Fig. 4.23. This lattice is the baseline of the SOLEIL upgrade, and will be described in the Conceptual Design Report (CDR) (due end 2020).

### 4.4.1 Layout and main characteristics

Table 4.12 lists the main characteristics of the 7BA 4BA HOA 4-superperiod lattice. The baseline lattice is composed of an alternance of 7BA HOA periods and 4BA HOA cells, which follows the deflection repartition of the current storage ring, alternating 22.5 degrees and 11.25 degrees cells. The HOA principle was conserved, as the phase advance of the unit cells composing the 7BA and the 4BA are identical. Nonetheless, numerical exploration of the unit cells phase advance found an optimum set, $(\nu_x, \nu_y) = (0.408, 0.143)$, which does not correspond to the theoretical principle described in sec. 3.2.3, $(\nu_x, \nu_y) = (\frac{3}{7}, \frac{1}{7})$.

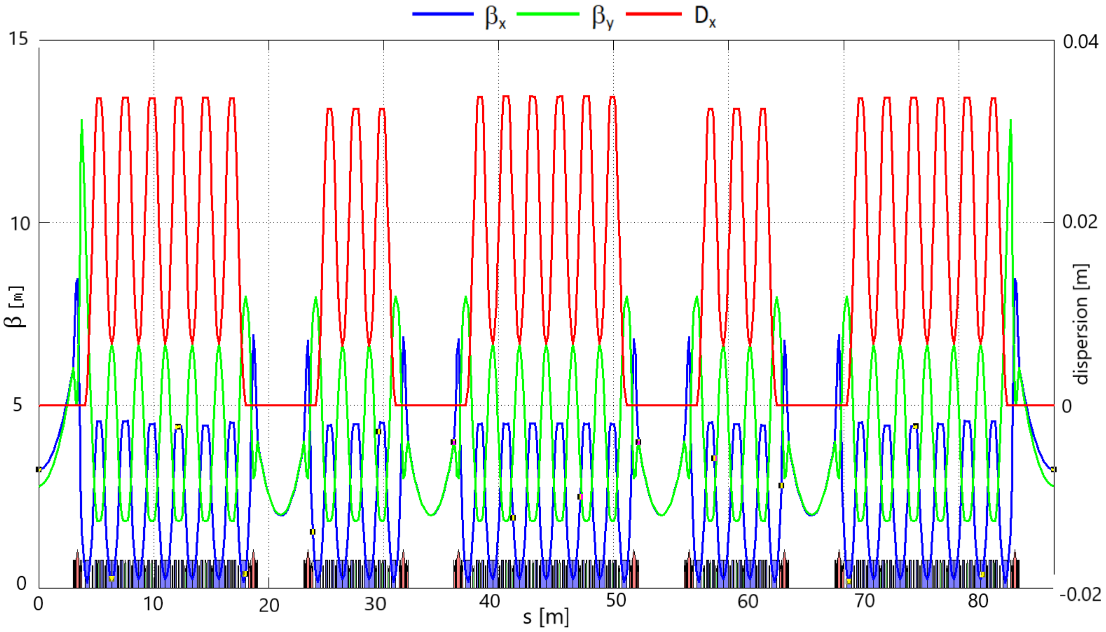

FIGURE 4.23: Twiss parameters of the 7BA 4BA HOA 4-superperiod lattice for the SOLEIL upgrade.

TABLE 4.12: SOLEIL 2.75 GeV 7BA 4BA HOA lattice proposal, 4-fold symmetry.

| | |
|---|---|
| Circumference | 354.0 m |
| Energy | 2.75 GeV |
| Emittance $\epsilon_x$ | 79 pm.rad |
| Tunes per period $(\nu_x, \nu_y)$ | (54.42, 18.42) |
| Momentum compaction factor $\alpha_0$ | $9.40 \times 10^{-5}$ |
| Reverse bending angle | -0.048 degrees |
| Energy loss per turn | 480 keV |
| $(\beta_x, \beta_y)$ @ID | (1.1-1.3, 1.1-1.7) m |
| $(\beta_x, \beta_y)$ Long straight section | (3.2, 3.2) m |

### 4.4.2 Insertion of a high-$\beta_x$ for transverse off-axis injection

Further study of all ultra-low emittance lattices evaluates the feasibility of two injection schemes, described in sec. 4.3.2. The 7BA 4BA 4-superperiod lattice was adapted to both of them. In this subsection is presented the layout of the injection section for transverse off-axis injection, available in Fig. 4.24. This lattice adaptation was designed by Alexandre Loulergue [130].

Since the betatron amplitude is proportional to $\sqrt{\beta}$ in both planes, the horizontal acceptance can be enlarged by increasing the $\beta_x$-function locally. In the case of the 7BA-4BA HOA lattice, the $\beta_x$-function was increased in a long straight section, from 3.2 m to 11.5 m, which corresponds to a factor 1.9 in horizontal transverse acceptance.

Further increase of the horizontal acceptance in that section was obtained by optimising the dynamic aperture contour using the nearby sextupoles and octupoles. Figure

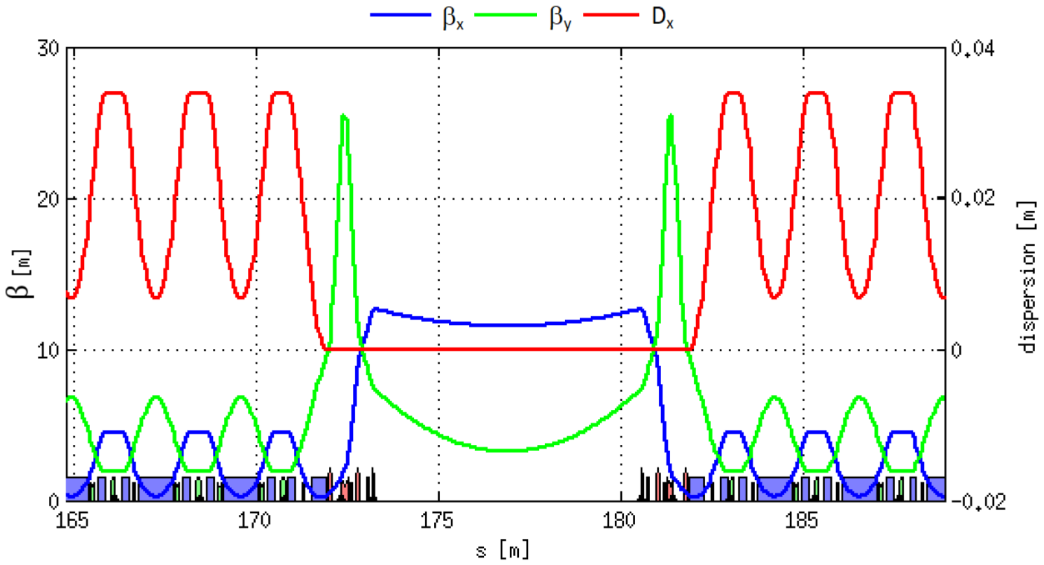

FIGURE 4.24: Layout of the injection section for transverse off-axis injection. The high-$\beta_x$ allows a local increase of the horizontal acceptance.

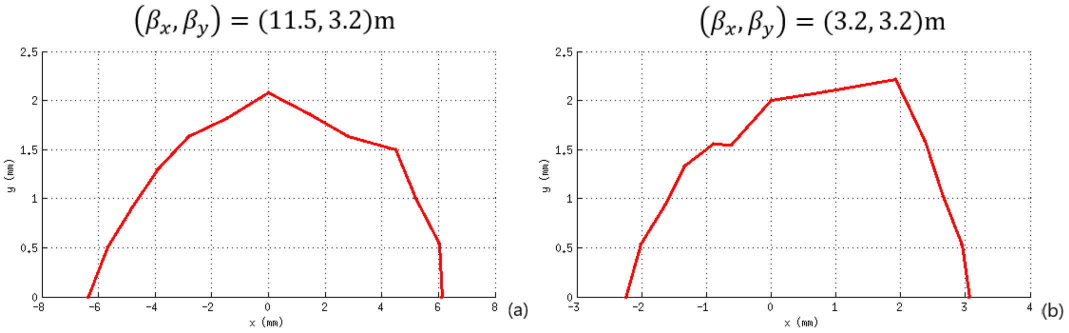

FIGURE 4.25: On-momentum transverse dynamic aperture (a) in the middle of the injection section, $\beta_x = 11.5$ m and (b) in the middle of a regular long straight section, $\beta_x = 3.2$ m, after a thousand turns.

4.25 displays the on-momentum transverse dynamic aperture in the middle of the injection section, and compares it to the DA in the middle of a non-specific long straight section at $\beta_x = 3.2$ m, for a thousand turns. The resulting transverse acceptance remains at around 2 mm vertically, and was increased from $-2/+3$ mm to $\pm 6$ mm horizontally. The enlarged horizontal acceptance allows the off-axis injection of a beam at $-4/5$ mm for instance.

### 4.4.3 Insertion of a dispersive area for longitudinal on-axis injection

The inclusion of a dispersion bump in this lattice was done by Ryutaro Nagaoka. The external reverse bend and dipole quadrupolar strengths were decreased, to allow an averaged 5 cm dispersion in the external dipole. After a drift of 2.5 m long, a quadrupole doublet is inserted, to further kick the dispersion up and match the symmetric condition at the middle of the straight section. This method limits the increase in emittance, which rises to 90 pm.rad only, for a dispersion bump of 16 cm. Figure 4.26 zooms in the optics around the dispersion bump.

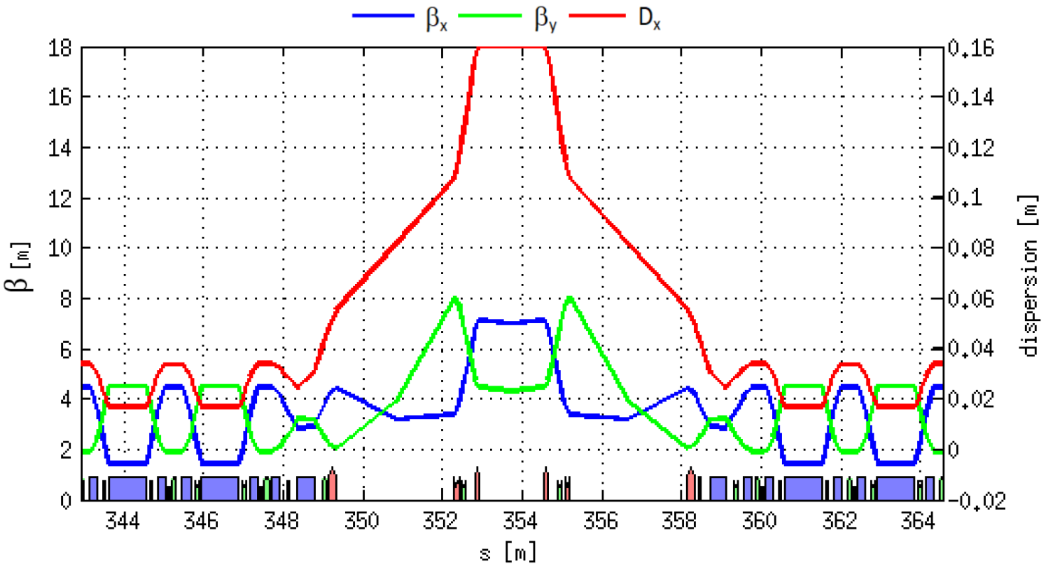

FIGURE 4.26: Twiss parameters and dispersion bump of 16 cm created for the 7BA-4BA HOA SOLEIL lattice. The inclusion of two pairs of quadrupoles allows an extra increase of the dispersion, up to 16 cm, in the centre of the straight section, where the Multipole Injector Kicker should be inserted.

The MIK should be inserted in between the quadrupole doublets, in a 1 m-long section. With a bump of 16 cm, the momentum deviation required to place its chromatic orbit on the maximum magnetic field produced by the MIK at $x = -3.5$ mm in the centre of the kicker, is $\delta = \frac{-3.5\,\text{mm}}{160\,\text{mm}} = -2\%$.

## 4.5 Evaluation of the nonlinear dispersion at the position of the septum in the 7BA-4BA lattice with a 16 cm dispersion bump

As described in section 4.3, the creation of a dispersion bump in a straight section has two main effects. First, it increases the emittance of the lattice, with variations depending on the method employed. The use of bending magnets to create the dispersion bump drastically increases the emittance, as the level of dispersion in those magnets arises. The method employed for the creation of a 16 cm dispersion bump for the 7BA-4BA HOA lattice limits the increase in emittance as the large part of the bump is created by two quadrupole doublets. Second, the addition of a dispersion bump increases the off-momentum deviation from the design orbit, which could therefore fall out of the physical limits of the vacuum chamber: for instance, for a chamber radius of 5 mm and 10 mm, the corresponding energy deviation in the case of a 16 cm bump is ±3.1% and ±6.2%.

Higher-order dispersion components participate in the dispersion bump required for the on-axis longitudinal injection, either by increasing the effective bump at a given momentum deviation, or decreasing it. In the first case, the consideration of the nonlinear dispersion would alleviate the required linear dispersion bump and limit its effect on the emittance, which should be looked at for the methods described in 4.3.2.3.

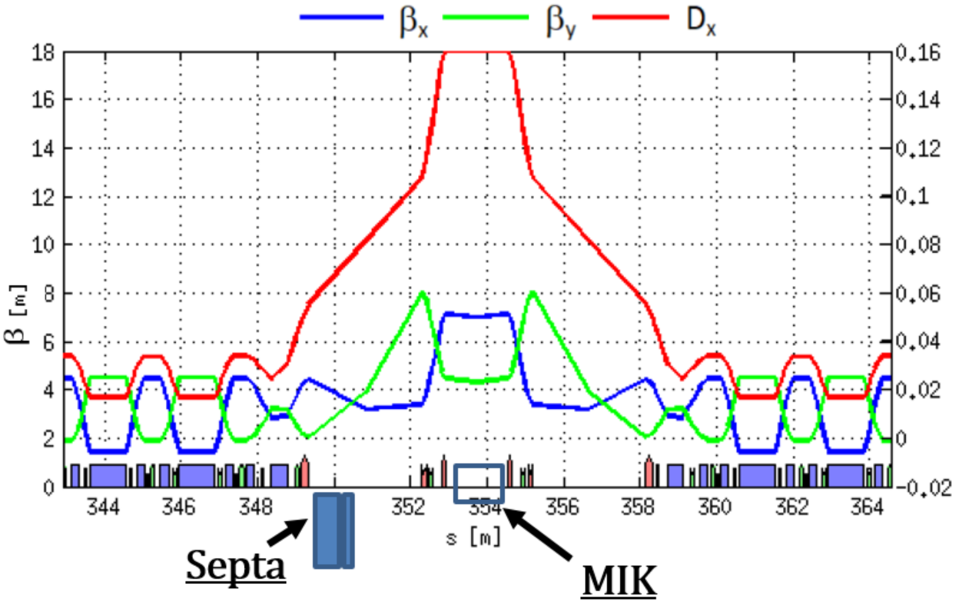

FIGURE 4.27: Position of the septum and the MIK in the injection section of the 7BA 4BA SOLEIL lattice. The current dispersion bump is at 16 cm.

In the case of the 7BA-4BA lattice including a 16 cm dispersion, future explorations aim at decreasing the linear dispersion bump, to increase the beam-stay-clear zone at the septa, which should be located at the very beginning of the injection section. Currently, the prior bending is provided by a thick and a thin septa, which bend the injected beam before the MIK. The total length of both septa is $\simeq 1\,\mathrm{m}$. The exit of the septa is located at $\simeq 3.5\,\mathrm{m}$ of the injection point.

In the current configuration, the septa are located at $\Delta x = -8\,\mathrm{mm}$ from the machine axis, with a level of dispersion of about 5 to 7 cm. The horizontal shift corresponds to a chromatic closed orbit at an energy deviation of $\delta \simeq -(11\,\mathrm{to}\,16)\%$. In the case of constructive nonlinear dispersion, the shift of the chromatic closed orbit is further increased per energy deviation. If the energy deviation is of the order of the energy acceptance, the septa should be moved backwards, not to perturb the stored beam and limit the momentum acceptance, which would reduced the beam lifetime. In that case, the injected beam will arrive at a higher horizontal position to the MIK, which would then require a stronger magnetic field *i.e.* a higher bending angle for it to be kicked onto the same chromatic closed orbit. Currently, the possible bending angles achieved with the SOLEIL MIK are limited to 1-3 mrad.

Since the nominal energy acceptance is limited to $\pm 2\%$ at the bump, the trajectory of off-momentum particles is described thanks to the higher-order dispersions. To control the dimensions of the injected beam at the location of the septum, the linear and higher-order dispersion are thus numerically calculated.

### 4.5.1 Minimisation script

The analytical calculation from [131] of the nonlinear dispersions up to the second order are derived and tested in the section 5.3.2 of the present thesis. The necessary scripts were written in Accelerator Toolbox, and compared with the variation of the closed orbit. The variation of the dispersion with the momentum deviation is exhibited as follows:

$$D_x = D_0 + D_1\delta + D_2\delta^2 + ... \tag{4.5}$$

Since the 7BA-4BA lattice comprises a high number of magnets, which drastically increases the calculation time, the minimisation script tracks the closed orbit of off-momentum particles at $\delta = \pm 0.1\%$ and extracts the first-order dispersion $D_1$ with a second-order polynomial fit. The chromatic orbit of a particle of momentum deviation $\delta$ varies in the injection straight section with the nonlinear dispersion. Figure 4.28 displays the evolution of the first-order dispersion with the longitudinal position $s$ for half the injection section of the 7BA-4BA HOA lattice and the beginning of the 7BA cell. The dipoles and the straight sections were sliced into ten identical pieces during the tracking, to provided a clearer view of the first-order dispersion variations.

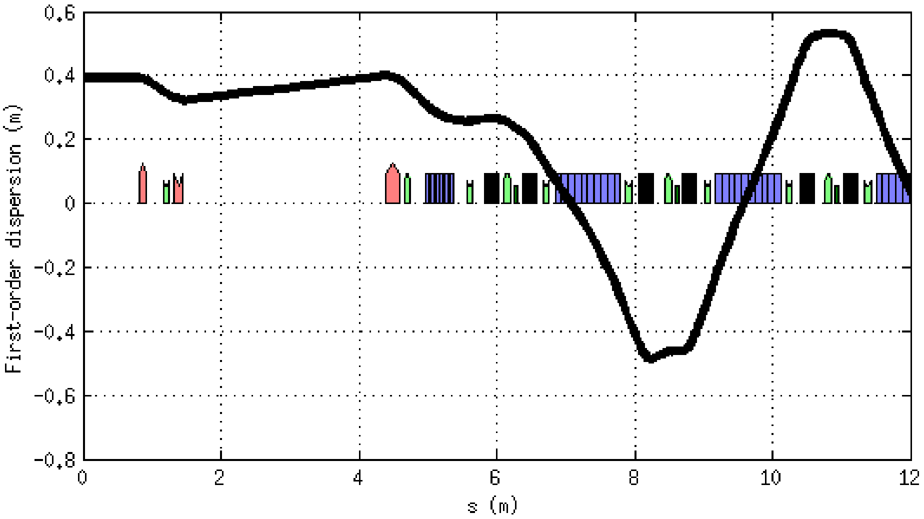

FIGURE 4.28: First-order dispersion extracted from the closed orbit along half the injection section.

At the septum, located at ≃ 3.5 m away from the injection point, the current value of the first-order dispersion equals $D_1 = 368 - 392\,\mathrm{mm}$. The energy deviation corresponding to the chromatic closed orbit at the transverse location of the septa therefore verifies:

$$D_0\delta + D_1\delta^2 = -\Delta x = -8\,\mathrm{mm} \tag{4.6}$$

which corresponds to $\delta = -11.6/+11.7$, *i.e.* $\delta = -1160/+1170\%$ at $D_1 = 392\,\mathrm{mm}$. Since $D_1 > 0$, all values in between the zeroes of Eq. (4.6) are negative, meaning that the realistic closed orbits do not reach the limit value of $\Delta x = -8\,\mathrm{mm}$. Furthermore, the equation (4.6) has solutions if and only if $D_1 > \frac{D_0^2}{4|\Delta x|}$ which corresponds to $D_{1,limit} \simeq 150\,\mathrm{mm}$.

Figure 4.29 displays the closed orbit variation with the energy deviation at the location of the septa, for $D_0 = 70\,\mathrm{mm}$ and $D_1 = 400\,\mathrm{mm}$, in the energy deviation range $\delta = \pm 20\%$. No off-momentum particles approach the $-8\,\mathrm{mm}$ limit.

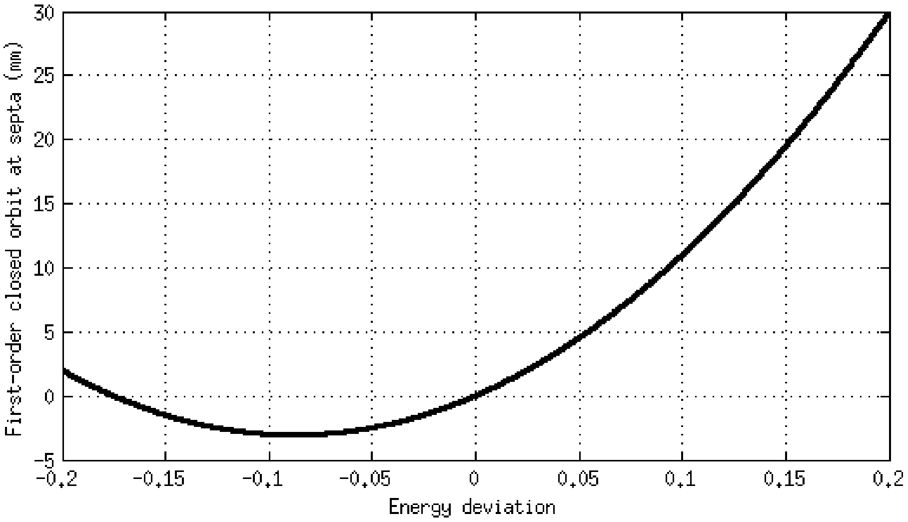

FIGURE 4.29: First-order closed orbit variation with energy deviation at the location of the septa.

Nonetheless, the nonlinear optimisations conducted with MOGA do not take this point into account. In case of limited energy acceptance because of the septum, I wrote a script in A.T. which evaluates the first-order dispersion and tries to minimise it. Despite the limit defined by Eq. (4.6) and the problem characteristics, the script aims at getting as close to the linear lattice as possible. In that case, the values of energy deviation verifying Eq. (4.6) gets larger when the first-order dispersion is close to zero, meaning the septa should not be a limiting factor in the energy acceptance.

### 4.5.2 Proof of principle and results

Using the sextupoles of the whole lattice, the first-order dispersion can be manipulated around the injection point. A scanning script was written in A.T., and evaluates the value of the first-order dispersion at the location of the septa. A hundred sets of sextupoles were generated, with strengths varying in a 100% range around their nominal value. Figure 4.30 displays the values of the first-order dispersion at the septa, for all the generated rings, with $D_0 = 70\,\mathrm{mm}$ and $\Delta x = -8\,\mathrm{mm}$.

The first-order dispersion closer to 0 at the septa is $D_1 = -96\,\mathrm{mm}$, of the order of the zeroth-order dispersion. The relative variation of the sextupole strengths of the

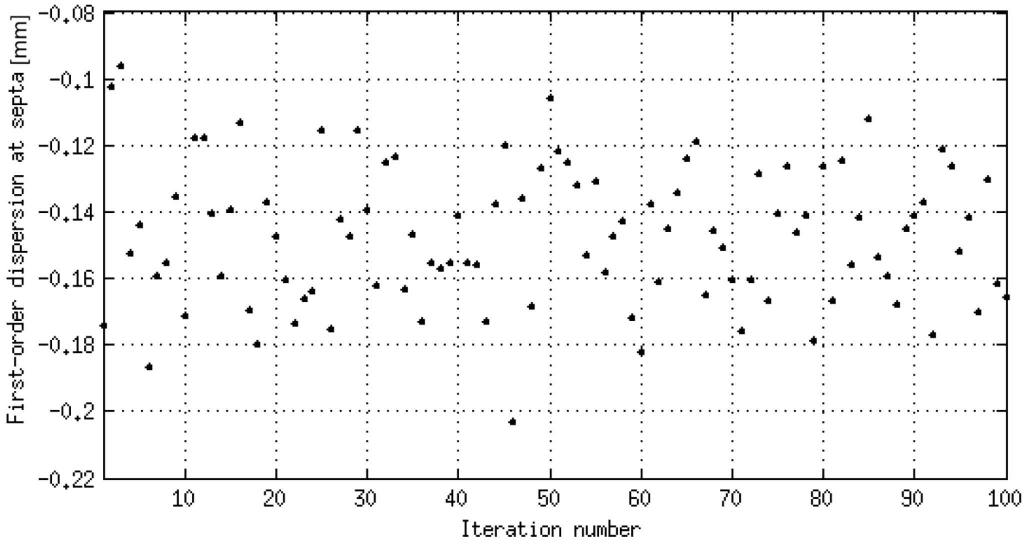

FIGURE 4.30: Evolution of the first-order dispersion during the sextupole strengths scan, at the location of the septa.

optimised ring with regards to the nominal ring are displayed in Fig. 4.31. Their variations are high, compared to their nominal values. Further analysis would be required to optimise the created ring, in terms of transverse dynamics.

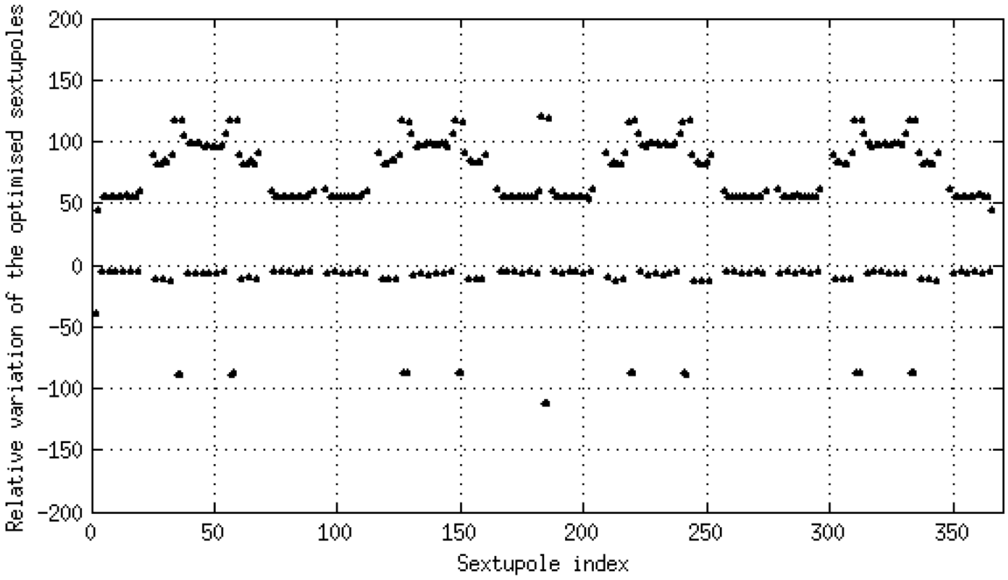

FIGURE 4.31: Relative variation of the sextupole strengths along the ring, with regard to their nominal values.

## 4.6 Conclusions

The use of MOGA-Bmad differs from MOGA-Elegant, which was extensively used in the optimisation of the current SOLEIL storage ring[132]. In terms of objectives, MOGA-Bmad optimises the on- and off-momentum dynamic apertures, while MOGA-Elegant optimises the on-momentum dynamic aperture and the Touschek lifetime directly. For time considerations, MOGA-Bmad is faster per individual than MOGA-Elegant: considering the larger lattices in terms of number of magnets and number of variables, this favours the use of MOGA-Bmad. Another point is that no stable point is necessary to start the optimisation in MOGA-Bmad, while a input set of sextupole strengths is required for MOGA-Elegant: this can be difficult to implement in tight lattices, where the stability is not always guaranteed off-momentum. Although no stable point is required, in hundreds of generations, MOGA-Bmad can find a feasible candidate and further start the optimisation.

Such genetic algorithm to optimise both the on- and off-momentum dynamic aperture of the ultra-low emittance lattices studied in the SOLEIL upgrade boosts the nonlinear optimisation process and provides acceptable solutions. Using MOGA-Bmad, developed by M. Ehrlichman [43], further complementary remarks could be found in the comparison of the two chromatic correction schemes which are being compared since the Chapter 3. While the HOA lattice appears easy and flexible to optimise, the hybrid lattice is limited to its non-interleaved principle, which maximises the on-momentum dynamic aperture but does not apply to the off-momentum dynamics.

**Feasibility of the injection schemes** As the SOLEIL upgrade constraints evolved into including the position of the long beamlines, ANATOMIX and NANOSCOPIUM, 4-superperiod lattices were designed: a hybrid-based lattice, and a HOA-based lattice. Breaking the symmetry did not perturb the basic principle of each scheme, but the increase in the number of systematic resonances further limited the transverse dynamics. While the hybrid 4-superperiod lattice proved to be difficult to implement in the tunnel, a 7BA-4BA HOA lattice was designed to preserve the position of all current beamlines.

Two types of injection are discussed in the SOLEIL upgrade project. The current transverse off-axis injection can be used in the 7BA-4BA with the inclusion of a high-$\beta$ straight section. Another scheme aims at injecting the beam directly on-axis, onto an off-momentum closed orbit: it is the longitudinal on-axis scheme. The use of a Multipole-Injector Kicker (MIK) requires the insertion of a 16 cm dispersion bump in the 7BA-4BA lattice. The current specifications of the MIK place the septa close to the machine axis. Therefore, a further analysis of the nonlinear dispersion is required, and a minimisation script was written in Accelerator Toolbox (A.T.) to decrease the value of the first-order dispersion at the location of the septa. By scanning the strengths of the nearby sextupoles, and conserving the linear chromaticity, the first-order dispersion could be decreased, with no control on the transverse dynamics.

# Chapter 5

# 6D nonlinear optimisation using multi-objective genetic algorithm

As stated in the section 2.2.5, the reduction of the transverse emittances influences greatly other linear parameters, such as the dispersion and the momentum compaction factor. In particular, the latter is of the utmost importance in the control of collective effects and longitudinal stability. Furthermore, a low linear momentum compaction factor might be overtaken by a larger second-order part, thus reducing the energy acceptance in the synchrotron motion and limiting the beam stability. The bucket of such ultra-low emittance lattices could be entirely driven by the higher-orders of the momentum compaction factor $\alpha_C$: this is the topic of this chapter.

The convention used in this chapter is the following. The momentum compaction factor is defined as the slope of the pathlength with regards to the energy deviation and as such, it is expressed as:

$$\alpha_C = \alpha_0 + 2\alpha_1\delta + 3\alpha_2\delta_2^2 \tag{5.1}$$

with $\alpha_0$ the zeroth-order, $\alpha_1$ the first-order and $\alpha_2$ the second-order momentum compaction factors.

## 5.1 Initial motivation and problematic

First steps into the upgrade projects for the SOLEIL storage ring produced a 5BA lattice, of emittance 80 pm.rad. Figure 5.1 illustrates the magnet arrangement and the Twiss functions of the 5BA lattice with 24-fold symmetry. Its main characteristics can be found in Table 5.1. The ultra-low emittance is achieved with a low dispersion of maximum value 5.6 cm, reaching a low zeroth-order momentum compaction factor of $2.1044 \times 10^{-5}$. The low dispersion nature was pronounced by the inclusion of reverse bending magnets of angle $-0.28$ degrees between the external dipoles and $-0.38$ degrees in the core of the lattice which decreased the natural horizontal emittance down to 80 pm.rad.

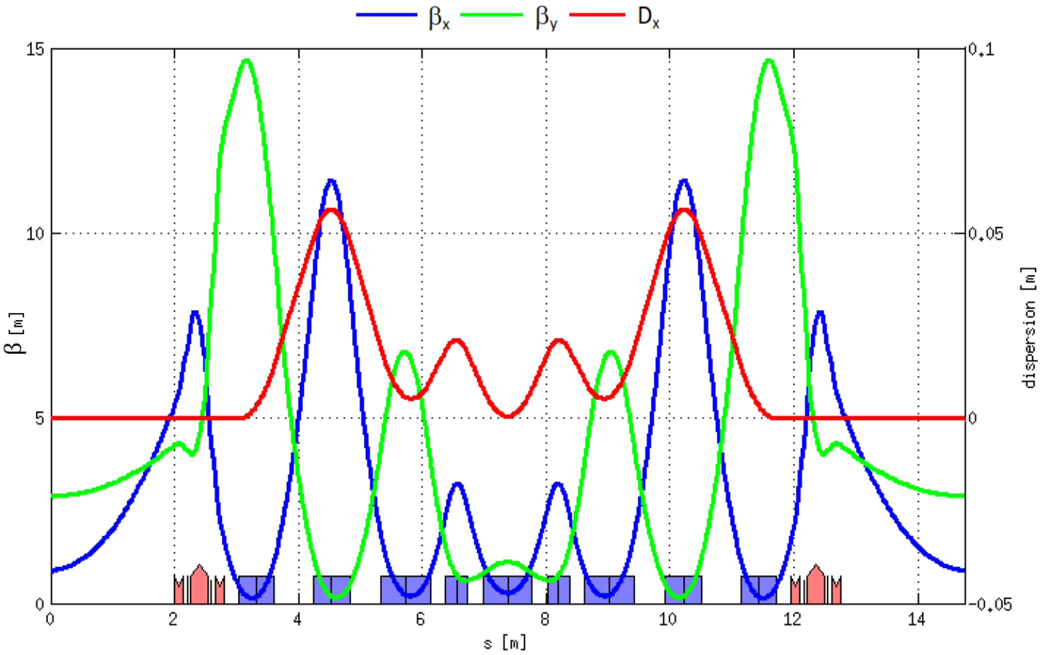

Figure 5.1: Twiss functions of the SOLEIL 5BA lattice under study, of emittance 80 pm.rad.

Table 5.1: General characteristics of the SOLEIL 2.75 GeV 5BA lattice, 24-fold symmetry.

| | |
|---|---|
| Emittance $\epsilon_x$ | 80 pm.rad |
| Tunes per period $(\nu_x, \nu_y$ | (2.21, 1.54) |
| Natural chromaticities $(\xi_x, \xi_y)$ | (-6.1, -4.8) |
| Momentum compaction factor $\alpha_0$<br>$\alpha_1$ | $2.1044 \times 10^{-5}$<br>$5.3435 \times 10^{-4}$ |
| Reverse bending angle | -0.28/-0.38 degrees |
| Energy loss per turn | 22.8 keV |
| $(\beta_x, \beta_y)$ @ID | (0.9, 2.9) m |

Analysis of the feasibility of the on-axis longitudinal injection described in the section 4.4.3 on the 5BA lattice pointed out its small bucket and its narrow energy acceptance of $\simeq \pm 2\%$. Fig. 5.2 displays the longitudinal phase space of the 5BA lattice which corresponds to lines of equal-energy Hamiltonian, i.e. $\mathcal{L} = \{(\phi, \delta) \in \mathbb{R}^2 \backslash H(\phi, \delta) = E, E \in \mathbb{R}\}$. The black line corresponds to the linear separatrix function which is supposedly a closed bucket, the other colours serve no other purpose than readability. The predominance of the first-order momentum compaction factor $\alpha_1 = 5.3435 \times 10^{-4}$ in the 5BA lattice reduces the linear bucket stability down to $(\pm 10\,\text{degrees}, \pm 2\%)$.

Ultra-low emittance lattices have an overall smaller dispersion and weaker bending magnets than third-generation storage rings, inducing a strong reduction of the zeroth-order momentum compaction factor $\alpha_0 = \frac{1}{C_0} \int_0^{C_0} \frac{\eta_{disp}}{\rho}$. A too small $\alpha_0$ can be the cause of several instabilities: the threshold of many collective effects depends linearly

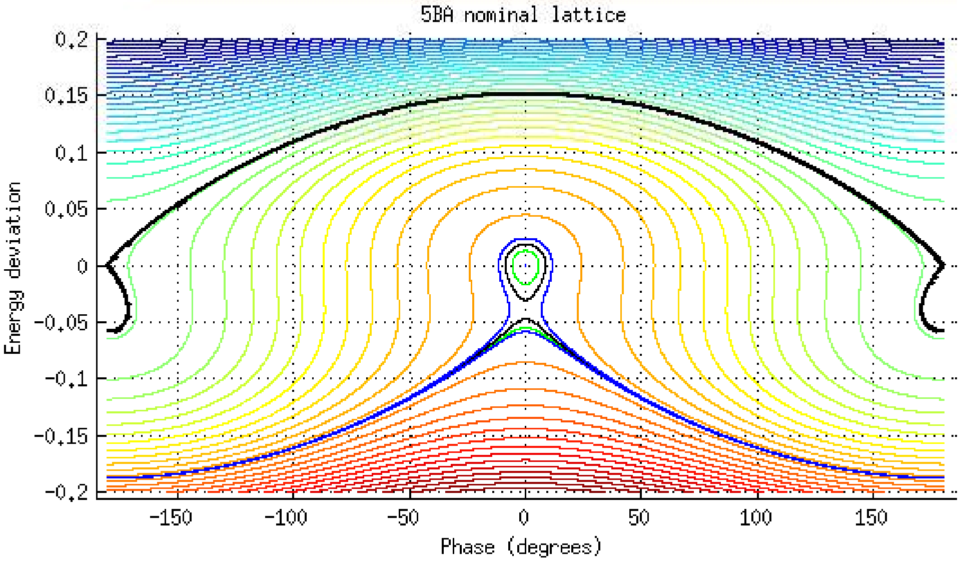

Figure 5.2: Longitudinal phase space of the 5BA lattice, of $\alpha_0 = 2.1044 \times 10^{-5}$ and $\alpha_1 = 5.3435 \times 10^{-4}$.

with $\alpha_0$, such as micro-bunching instabilities. In terms of dynamic, the off-momentum particles of $\delta \neq 0$ oscillate longitudinally: it is the synchrotron motion. The stability of such motion depends directly on the variation of the momentum compaction factor with the energy deviation $\delta$. Furthermore, a small $\alpha_0$ can be overtaken by the first-order momentum compaction $\alpha_1 = \frac{1}{2}\frac{d\alpha_C}{d\delta}$ which strongly reduces the longitudinal stability area and creates small buckets, alike the case of the 5BA lattice.

This chapter describes the longitudinal phase space in terms of the momentum compaction factor with its three lower-order terms to understand the linear synchrotron motion and the possible destructive effect of a large first-order momentum compaction factor. Later, different methods are studied to overcome this problem. The first method is based on the second-order momentum compaction factor and was suggested by Maher Attal [133] in his thesis. The second and third methods were developed on my initiative: the approach aims at minimising the first-order momentum compaction directly by using the sextupole strengths. The second method scans the sextupole strengths within a defined range in hopes of finding a ring of reduced $\alpha_1$. The inefficiency of the method, which scans a large high-dimensional window to find a minimum with no other intelligence - amongst other limitations that will be defined in the relevant section, encouraged to include the minimisation of $\alpha_1$ into the pre-existing MOGA-Bmad which will include the transverse dynamic optimisation, lacking in the other methods.

## 5.2 Towards the second-order longitudinal Hamiltonian

The significantly diminished bucket of the 5BA lattice pointed out the effect of the strong reduction of the zeroth-order momentum compaction factor in ultra-low emittance lattices on the energy acceptance. This section recalls the basics of the longitudinal Hamiltonian dynamics and demonstrates the destructive effect of a high first-order momentum compaction factor. The following section shall provide solutions to correct it.

### 5.2.1 Synchrotron equation of motion

The effect of the acceleration by RF cavities is described as the synchrotron motion. The energy variation of off-momentum particles make them oscillate around the synchronous particle of phase $\phi_s$. The principle of a RF system is introduced in the Appendix (A). Non-synchronous particles are defined by their phase $\phi$ and their energy deviation $\delta = \frac{\Delta p}{p_0}$, with $\mathbf{p}$[eV/c] their momentum and $\mathbf{p}_0$[eV/c] the momentum of the synchronous particle.

$$\begin{cases} \dot{\delta} = \dfrac{\omega_0}{2\pi\beta_L^2 E} eV_{RF}(\sin(\phi) - \sin(\phi_s)) \\ \dot{\phi} = -h\Delta\omega = h\eta_0\delta \end{cases} \tag{5.2}$$

with $\eta_0$ the zeroth-order slip factor, $\omega_0$ is the revolution angle frequency, $E$ the nominal energy, $\beta_L$ the relative speed, $e$[C] the charge of an electron and $V_{RF}$[V] the RF voltage. Linked by the above equations, $(\phi, \delta)$ are a pair of conjugate phase-space coordinates of the longitudinal motion. The difference in angular frequency can be expressed in terms of trajectory radius $R$: $\frac{\Delta\omega}{\omega_0} = \frac{\beta R}{\beta_0 R_0} - 1$. The mean radius varies with the energy deviation and the momentum compaction factor $\alpha_C$, as described in 2.1.2.4:

$$\alpha_C = \frac{1}{R_0}\frac{dR}{d\delta} = \alpha_0 + 2\alpha_1\delta + 3\alpha_2\delta^2 + ... \equiv \frac{1}{\gamma_T^2} \tag{5.3}$$

where $\gamma_T mc^2$ is the transition energy: it corresponds to the particle energy for which the revolution frequency is independent of the particle momentum variations. Similarly, the angular frequency variation with energy deviation is described by the slip factor $\eta_p$:

$$\eta_p = \frac{1}{T_0}\frac{dT}{d\delta} = -\frac{1}{\omega_0}\frac{d\omega}{d\delta} = \eta_0 + \eta_1\delta + \eta_2\delta^2 + ... \tag{5.4}$$

with $T_0$[s] the nominal revolution time. The slip factor orders are linked with the momentum compaction factor with:

$$\begin{cases} \eta_0 = \alpha_0 - \dfrac{1}{\gamma_0^2} \\ \eta_1 = \dfrac{3\beta_0^2}{2\gamma_0^2} + \alpha_1 - \alpha_0\eta_0 \\ \eta_2 = -\dfrac{\beta_0^2(5\beta_0^2 - 1)}{2\gamma_0^2} + \alpha_2 - 2\alpha_0\alpha_1 + \dfrac{\alpha_1}{\gamma_0^2} + \alpha_0^2\eta_0 - \dfrac{3\beta_0^2\alpha_0}{2\gamma_0^2} \end{cases} \tag{5.5}$$

In the case of highly relativistic particles where $\gamma_0 \gg 1$ and $\beta_L \simeq 1$, the slip factor is equivalent to the momentum compaction factor. The slip factor will be used in all longitudinal Hamiltonians to respect their temporal independent variable. They are merged otherwise. In the linear approximation, the angular frequency difference is expressed as $\Delta\omega = -h\eta_0\omega_0\delta = \left(\frac{1}{\gamma^2} - \frac{1}{\gamma_T^2}\right)$. In the light of this equation, the transition energy corresponds to a revolution frequency independent of the particle momentum: it is the isochronous condition. Below the transition energy, a higher energy particle ($\delta > 0$) has a higher revolution frequency. Above, it has a smaller revolution frequency and appears to have a negative mass.

### 5.2.2 Synchrotron motion

In this section, the lattice is assumed perfectly linear thus the momentum compaction factor is then constant regarding the momentum deviation. This section neglects the damping effect of the radiation losses on the synchrotron motion. This will set the basis of our study. The equations (5.2) can be derived from the Hamiltonian below:

$$H_0 \equiv \frac{h\omega_0\eta_0}{2}\delta^2 + \frac{e\omega_0 V}{2\pi\beta_L^2 E}\left[\cos(\phi) - \cos(\phi_s) + (\phi - \phi_s)\sin(\phi_s)\right] \tag{5.6}$$

where time is the independent variable. In the case of small-amplitude oscillations, the equation of motion can be linearised into:

$$\frac{d^2(\phi - \phi_s)}{dt^2} = \frac{h\omega_0^2 eV_{RF}\eta_0\cos(\phi_s)}{2\pi\beta_L^2 E}(\phi - \phi_s) \tag{5.7}$$

The oscillations remain stable as long as the frequency is real; the stability condition for the synchrotron oscillations is $\eta_0\cos(\phi_s) < 0$ and was first described in [1, 2]. The angular synchrotron frequency $\omega_s$ is $\omega_0\sqrt{\frac{heV_{RF}|\eta_0\cos(\phi_s)|}{2\pi\beta_L^2 E}}$. The number of synchrotron oscillations per turn or synchrotron tune $Q_s$ is the ratio between the synchrotron frequency and the synchronous frequency:

$$Q_s = \frac{\omega_s}{\omega_0} = \sqrt{\frac{heV_{RF}|\eta_0\cos(\phi_s)|}{2\pi\beta_L^2 E}} \tag{5.8}$$

**Description of the phase space** The Hamiltonian $H_0$ has two fixed points: a Stable Fixed Point (SFP) at $(\phi_s, 0)$ and an Unstable Fixed Point (UFP) $(\pi - \phi_s, 0)$ around which a small perturbation leads to the loss of the particle. The stability area of the

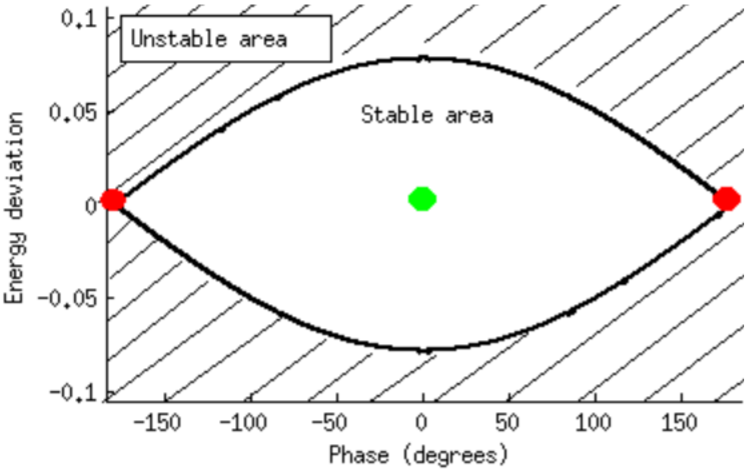

FIGURE 5.3: Schematic of a longitudinal phase space $(\phi, \delta)$. In green is the stable fixed point, in red the unstable fixed points: the contour of its Hamiltonian draws the frontier (in black) of the stability area.

longitudinal phase space is then delimited by the unstable fixed points and the particles of equal energy. The term "energy" here refers to the value of the Hamiltonian $H_0$. The fixed points and the stability area are represented in Fig. 5.3. That frontier is called the separatrix of equation $H(\phi, \delta) = H_0(\pi - \phi_s, 0)$, expanded in:

$$\frac{h\eta_0}{2}\delta^2 + \frac{eV}{2\pi\beta^2 E}\left[\cos(\phi) + \cos(\phi_s) + [\phi - (\pi - \phi_s)]\sin(\phi_s)\right] = 0 \qquad (5.9)$$

To further ease our reading and lighten the equations to come, let us define the following function:

$$f : (\phi, \phi_s) \longmapsto \cos(\phi) + \cos(\phi_s) + [\phi - (\pi - \phi_s)]\sin(\phi_s) \qquad (5.10)$$

Figure 5.4 illustrates the variations of the defined function, for different $\phi_s \in [\frac{\pi}{2}, \pi]$. The complete variations of the function $f : (\phi, \phi_s)$ are available in the Appendix G.

**Energy acceptance and bucket area** The separatrix has two turning points both on the $\delta = 0$ line:

$$\{(\phi_c, 0); (\pi - \phi_s, 0)\}$$

where $\phi_c$ is the phase satisfying the following conditions :

$$\begin{cases} cos(\phi_c) + (\phi_c) * \sin(\phi_s) = \cos(\phi_s) + (\pi - \phi_s)\sin(\phi_s) \\ \phi_c \in [-(\pi - \phi_s), \pi - \phi_s[ \end{cases} \qquad (5.11)$$

Since the polynomial dependence in $\delta$ is even and monomial in the separatrix equation (5.9), the link between $\delta$ and $\phi$ is straightforward. From Eq. (5.10), the area of the stable area expands into the following equation:

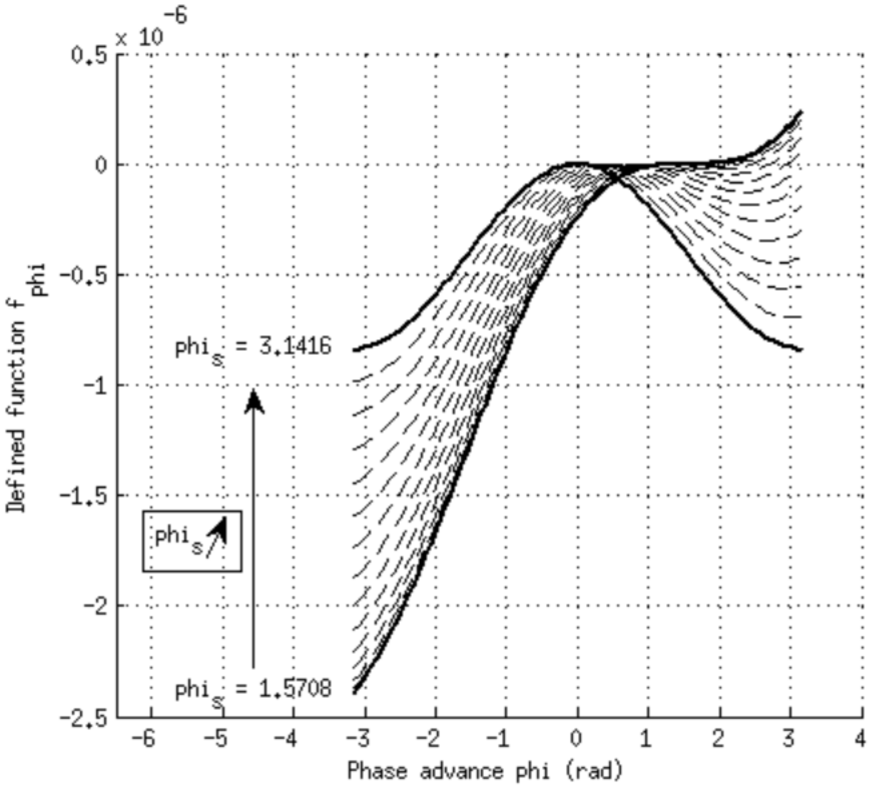

FIGURE 5.4: Variation of the function $f : (\phi, \phi_s)$ over a period $[-\pi, \pi]$ for different $\phi_s \in [\frac{\pi}{2}, \pi]$.

$$A_0 = 2\int_{\phi_c}^{\pi-\phi_s} \delta d\phi = 2\sqrt{\frac{eV}{h|\eta_0|\pi\beta^2 E}} \int_{\phi_c}^{\pi-\phi_s} \sqrt{-f(\phi,\phi_s)} d\phi \tag{5.12}$$

and the maximum momentum deviation, obtained for $\phi = \phi_s$ is:

$$\delta_{0,\,\max} = \sqrt{\frac{eV}{h|\eta_0|\pi\beta^2 E}} \sqrt{|f(\phi_s, \phi_s))|} \tag{5.13}$$

Figure 5.5 illustrates the longitudinal phase space for different momentum compaction factors along with different energy levels. In black is represented the separatrix for each case.

The resulting stability area keeps increasing with $\frac{1}{|\alpha_0|}$, as expected from Eq. (5.12) and (5.13). Ultra-low emittance lattices of which momentum compaction factor $\alpha_0$ is smaller due to a decreased dispersion, should present both a larger bucket area and a higher energy acceptance, both being inversely proportional to the slip factor and the momentum compaction factor. Figure 5.5 illustrates this dependence by drawing three purely linear buckets for two different $\alpha_0$. Nonetheless, the smaller $\alpha_0$ the stronger the destructing effect induced by $\alpha_1$.

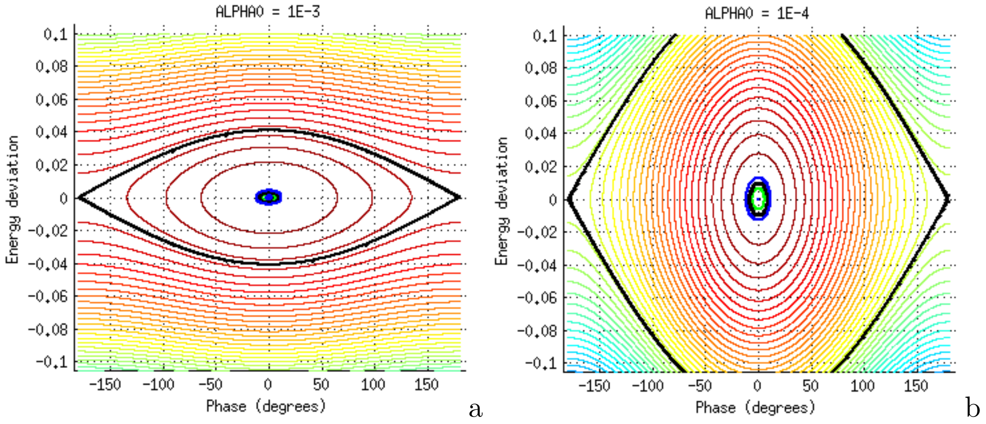

FIGURE 5.5: Longitudinal phase spaces of fixed range $(\phi, \delta) \in [-\pi, \pi] \times [\pm 10\%]$ axis for different first order momentum compaction factors (a) $\alpha_0 = 1 \times 10^{-3}$ and (b) $\alpha_0 = 1 \times 10^{-4}$. The lower $\alpha_0$, the larger $\delta_{0,\,\mathrm{max}}$.

#### 5.2.2.1 Mapping equations and synchrotron damping

In circular accelerators, RF acceleration occurs at a specific location in the storage ring. The synchrotron motion is more realistically described by the sequences $(\phi_n, \delta_n)_{n \in \mathbb{N}}$, with $n$ the number of turns. The corresponding equations are the mapping equations:

$$\begin{cases} \delta_{n+1} = \delta_n + \dfrac{eV}{2\pi\beta^2 E}(\sin(\phi_n) - \sin(\phi_s)) \\ \phi_{n+1} = \phi_n + h\eta_0\delta_{n+1} \end{cases} \tag{5.14}$$

Indeed, once a particle of coordinates $(\phi_n, \delta_n)$ crosses the RF system, it is either decelerated or accelerated depending on the sign of $(\phi_s - \phi_n)$ (*cf* 1.1.2). The new phase is derived from the new momentum deviation $\delta_{n+1}$. All stable motion is bounded in the $(\phi, \delta)$ plane: it is the stability area, represented in Fig. 5.3.

### 5.2.3 First-order longitudinal plane

This section reviews the effect of the first-order in momentum compaction factor $\alpha_1$, on the longitudinal stability area. Its destructive effect, when larger than $\alpha_0$, highly reduces the energy acceptance and disturbs the stability. The total momentum compaction in this subsection is:

$$\alpha_C = \alpha_0 + 2\alpha_1\delta \tag{5.15}$$

A corresponding Hamiltonian includes the effect of the first-order element in the mapping equations (5.14):

$$H_1 = \frac{h\eta_0}{2}\delta^2 + \frac{h\eta_1}{3}\delta^3 + \frac{eV}{2\pi\beta^2 E} f(\phi, \pi - \phi_s) \tag{5.16}$$

This Hamiltonian, in addition to the linear fixed points, has a second line of buckets at the energy deviation $\delta = -\frac{\alpha_0}{\alpha_1}$, with reversed stability of the fixed points: $(\phi_s, \delta)$ here is unstable, $(\pi - \phi_s, \delta)$ stable. Figure 5.6 is the longitudinal phase space of the current

SOLEIL lattice without the losses due to the insertion devices, with $\alpha_0 = 4.16 \times 10^{-4}$ and $\alpha_1 = 4.50 \times 10^{-3}$ at a RF voltage of 3 MV.

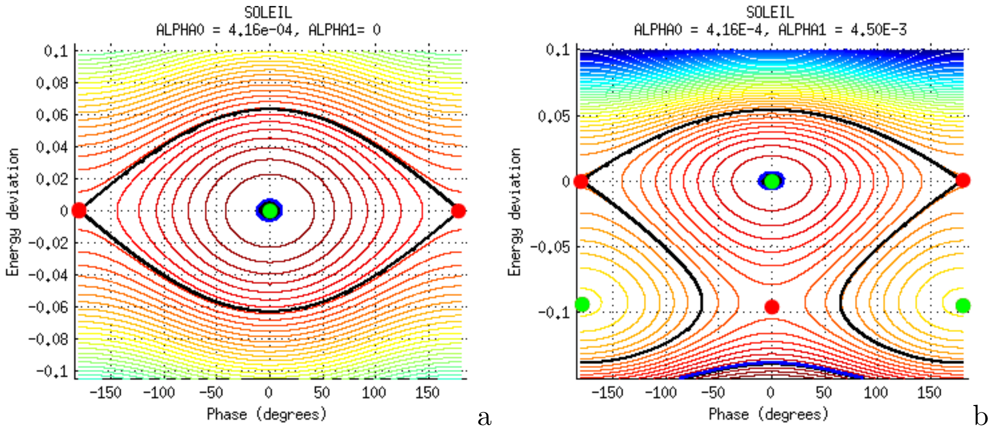

FIGURE 5.6: Second order longitudinal phase space of the current SOLEIL storage ring, (a) $\alpha_0 = 4.16 \times 10^{-4}$ without any other order and (b) including the second-order $\alpha_1 = 4.50 \times 10^{-3}$. The stable (in green) and unstable (in red) fixed points are displayed in the second-order case (b). The separatrices are in black in each phase space. SFP are marked with green dots, UFP with red dots.

In the case where an overlap exists between the two bucket lines, the energy level adds destructively in the vicinity of the unstable fixed points, reducing the width of the bucket, as observed in Fig. 5.6 (b). This effect is illustrated in Fig. 5.7. The bucket lines are nevertheless independent, provided the ratio $\frac{\alpha_0}{\alpha_1}$ is larger than the maximum energy deviation $\delta_{max}$, which is expressed in the next paragraph. The fixed points are displayed with the following colour code: green dots correspond to stable fixed points, red dots to unstable fixed points.

Figure 5.7 illustrates the destructive effect of the first-order momentum compaction factor $\alpha_1$ by progressively increasing its value for a fixed zeroth-order $\alpha_0 = 1.0 \times 10^{-4}$. The decrease in the ratio $\frac{\alpha_0}{\alpha_1}$ closes the gap between the two bucket lines $\delta = 0$ and $\delta = -\frac{\alpha_0}{\alpha_1}$. Once the buckets are mixed, the unstable fixed point at $\delta = -\frac{\alpha_0}{\alpha_1}$ reduces the stable area of the linear buckets at $\delta = 0$.

**Maximum momentum deviation and bucket area** Even in the optimum case of a large $\frac{\alpha_0}{\alpha_1}$ ratio, $\alpha_1$ will reduce the energy acceptance of the lattice. Indeed, the dependence of the separatrix on $\delta$ is now asymmetric: depending on the sign of $\alpha_1$, either $\delta_{1,\,\max}$ or $\delta_{1,\,\min}$ will be dramatically reduced. Since changing the sign of $\alpha_1$ is equivalent to flipping the longitudinal phase space with $\delta := -\delta$, let us assume $\alpha_1 > 0$. The extremum momentum deviation of the second-order separatrix satisfies:

$$\frac{h\eta_0}{2}\delta_{1,\,\max}^2 + \frac{h\eta_1}{3}\delta_{1,\,\max}^3 + \frac{eV}{2\pi\beta^2 E} f(\phi_s, \phi_s) = 0 \tag{5.17}$$

From Eq. (5.13), the previous equation becomes:

$$\delta_{1,\,\max}^2 + \frac{2}{3}\frac{\eta_1}{\eta_0}\delta_{1,\,\max}^3 = \delta_{0,\,\max}^2 \tag{5.18}$$

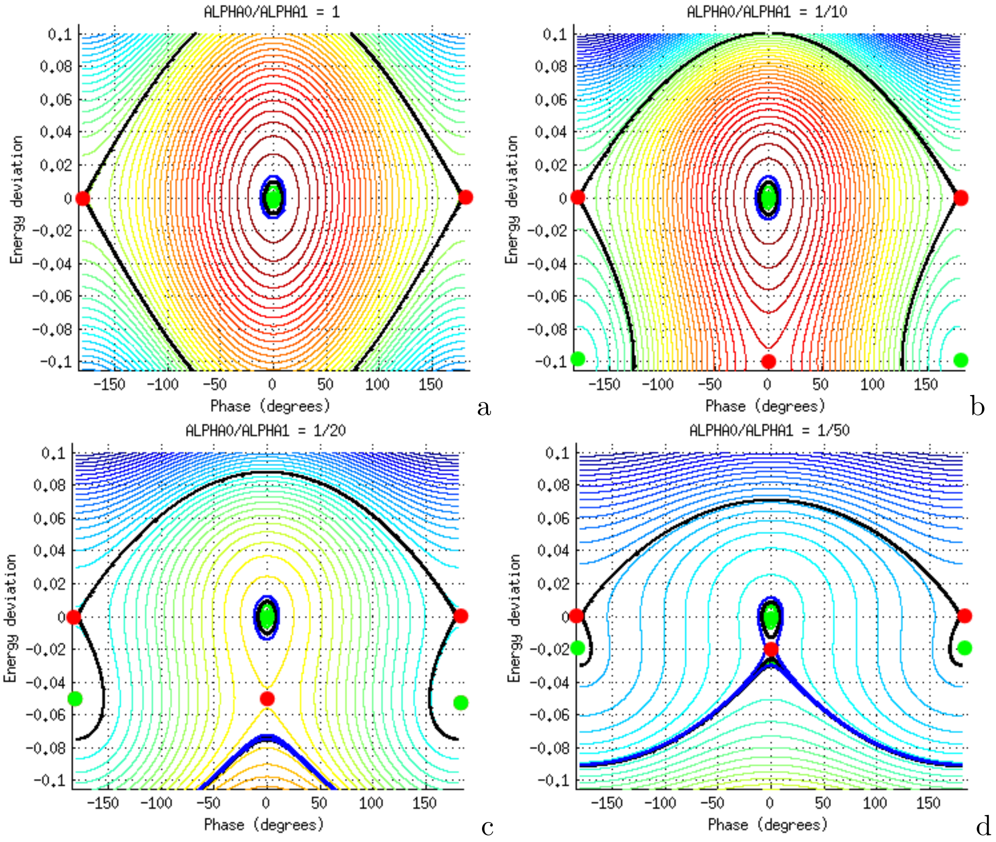

FIGURE 5.7: Illustration of the destructive effect of $\alpha_1$ on the longitudinal phase space for a fixed arbitrary $\alpha_0 = 1 \times 10^{-4}$ and for different ratios (a) $\frac{\alpha_0}{\alpha_1} = 1$ (b) $\frac{\alpha_0}{\alpha_1} = \frac{1}{10}$, (c) $\frac{\alpha_0}{\alpha_1} = \frac{1}{20}$ and (d) $\frac{\alpha_0}{\alpha_1} = \frac{1}{50}$. SFP are marked with green dots, UFP with red dots.

Therefore, the larger the ratio $\frac{\eta_0}{\eta_1}$ the higher the maximum energy. It is the contrary for the minimum energy deviation. Indeed $\delta_{1,\,\mathrm{min}}$ is negative and also verifies Eq. (5.18): then the lowest $\frac{\eta_0}{\eta_1}$ provides a higher $|\delta_{1,\,\mathrm{min}}|$. In ultra-low emittance lattices, no further control is exerted on $\alpha_1$. Among the lattices under study, it is always larger than $\alpha_0$ and their ratio $\simeq 0.1$. The second bucket line interferes with the linear bucket line, leading to either a reduction and alteration of the bucket shape or to its destruction.

### 5.2.4 Case of a second-order symmetric bucket, $\alpha_1 = 0$

Before increasing the general longitudinal Hamiltonian to the second-order in momentum compaction factor, let us study the contribution of the second-order momentum compaction factor $\alpha_2$ on the linear bucket. The considered momentum compaction factor is therefore purely symmetric in $\delta$ and is:

$$\alpha_C = \alpha_0 + 3\alpha_2\delta^2 \tag{5.19}$$

**Symmetric second-order Hamiltonian** The Hamiltonian describing the second-order symmetric bucket is from Eq. (5.24):

$$H_{sym} = \frac{h\eta_0}{2}\delta^2 + \frac{h\eta_2}{4}\delta^4 + \frac{eV}{2\pi\beta^2 E} f(\phi, \pi - \phi_s) \tag{5.20}$$

Its fixed points are the linear SFP$_0$ $(\phi_s, 0)$ and UFP$_0$ $(\pi - \phi_s, 0)$, and two additional fixed points SFP$_2$ $(\phi_s, -\frac{\alpha_0}{\alpha_2}))$ and UFP$_2$ $(\pi - \phi_s, -\frac{\alpha_0}{\alpha_2}))$. Unlike the second-order case in section 5.2.3, the second bucket line adds constructively to the linear one, allowing a symmetric enlargement of the original bucket in the energy direction. Figure 5.8 illustrates this effect.

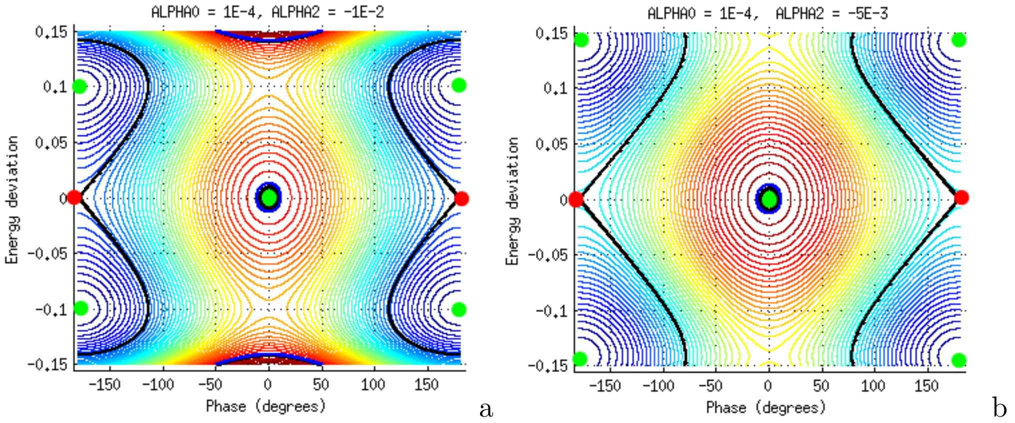

FIGURE 5.8: Effect of the second-order momentum compaction factor $\alpha_2$ on the bucket size, with a arbitrarily set $\alpha_0 = 1\times10^{-4}$ and (a) $\alpha_2 = -1\times10^{-2}$ and (b) $\alpha_2 = -5\times10^{-3}$. SFP are marked with green dots, UFP with red dots.

**Energy acceptance** If the second bucket line is far away enough, the maximum energy deviation on the separatrix verifies:

$$\delta^2_{2,\,\max} + \frac{\eta_2}{2\eta_0}\delta^4_{2,\,\max} = \delta^2_{0,\,\max} \tag{5.21}$$

The energy acceptance can therefore be symmetrically increased when $\eta_0\eta_2 < 1$.

### 5.2.5 Second-order mapping equations and Hamiltonian

In this section, the momentum compaction factor reads:

$$\alpha_C = \alpha_0 + 2\alpha_1\delta + 3\alpha_2\delta^2 \tag{5.22}$$

The mapping equations including all studied orders of the momentum compaction factor are:

$$\begin{cases} \delta_{n+1} = \delta_n + \dfrac{eV}{2\pi\beta^2 E}(\sin(\phi_n) - \sin(\phi_s)) \\ \phi_{n+1} = \phi_n + h(\eta_0\delta_{n+1} + \eta_1\delta^2_{n+1} + \eta_2\delta^3_{n+1}) \end{cases} \tag{5.23}$$

The Hamiltonian expressed with a second-order slip factor is, from Eq. (5.23):

$$H = \frac{h\eta_0}{2}\delta^2 + \frac{h\eta_1}{3}\delta^3 + \frac{h\eta_2}{4}\delta^4 + \frac{eV}{2\pi\beta^2 E} f(\phi, \pi - \phi_s) \tag{5.24}$$

#### 5.2.5.1 Fixed points of the second-order Hamiltonian

The fixed points of this Hamiltonian verify:

$$\begin{cases} \dot{\delta} = \dfrac{eV}{2\pi\beta^2 E}\left(\sin(\phi) - \sin(\phi_s)\right) = 0 \\ \dot{\phi} = h(\eta_0\delta + \eta_1\delta^2 + \eta_2\delta^3) = 0 \end{cases} \tag{5.25}$$

The first condition is valid when $\sin(\phi) = \sin(\phi_s)$, for the phases $\phi = \phi_s$ and $\phi = \pi - \phi_s$, modulo $2\pi$. The second condition is verified by $(\phi, \delta)$, such as: $\delta = 0$ or $\delta$ solution of $\left(\eta_2 X^2 + \eta_1 X + \eta_0 = 0\right)$. Let us define the polynom $P(X) = \left(\eta_2 X^2 + \eta_1 X + \eta_0\right)$. The latest condition exposes three cases:

- <u>P has no zeros in $\mathbb{R}$</u>: this case is equivalent to $\eta_1^2 < 4\eta_2\eta_0$. If this condition is verified, the polynom $P(X) = \eta_2 X^2 + \eta_1 X + \eta_0$ has no zeros in $\mathbb{R}$. Therefore, the Hamiltonian in Eq. (5.24) has only two fixed points which are also the linear Hamiltonian fixed points:

| Order | $\phi$ | $\delta$ | Type |
|---|---|---|---|
| Linear fixed points | $\phi_s$ | 0 | SFP |
| | $\pi - \phi_s$ | 0 | UFP |

  The equation of the separatrix is similar to the linear case in Eq. (5.9):

$$Q(\delta) + \frac{eV}{2\pi\beta^2 E}[\cos(\phi) + \cos(\phi_s) - (\pi - \phi - \phi_s)\sin(\phi_s)] = 0 \tag{5.26}$$

  with $Q(X) = \frac{\eta_2}{4}X^2\left(X^2 + \frac{4}{3}\frac{\eta_1}{\eta_2}X + 2\frac{\eta_0}{\eta_2}\right)$, of discriminant $\Delta_Q = \frac{16}{9}(\eta_1^2 - 4.5\eta_2\eta_0)$ is negative.

- <u>$P$ has a unique zero $z$,</u> $\eta_1^2 = 4\eta_0\eta_2 \implies z = -\frac{\eta_1}{2\eta_2}$. The Hamiltonian H of Eq. (5.24) has four fixed points:

| Order | $\phi$ | $\delta$ | Type |
|---|---|---|---|
| Linear fixed points | $\phi_s$ | 0 | SFP |
| | $\pi - \phi_s$ | 0 | UFP |
| Non-linear fixed points | $\phi_s$ | $-\frac{\eta_1}{2\eta_2}$ | UFP |
| | $\pi - \phi_s$ | $-\frac{\eta_1}{2\eta_2}$ | SFP |

  This specific situation resembles the first-order case; the stable area is therefore determined by the ratio $\frac{\eta_1}{2\eta_2}$.

- $\underline{P \text{ has two zeros in } \mathbb{R}}$, *i.e.* $\eta_1^2 > 4\eta_2\eta_0$: $\delta_\pm = -\frac{\eta_1}{2\eta_2}\left(1 \pm \sqrt{1-4\frac{\eta_2\eta_0}{\eta_1^2}}\right)$. The Hamiltonian of Eq. (5.24) has six fixed points:

| Order | $\phi$ | $\delta$ | Type |
|---|---|---|---|
| Linear fixed points | $\phi_s$ | 0 | SFP |
| | $\pi-\phi_s$ | 0 | SFP |
| Nonlinear fixed points | $\phi_s$ | $\delta_+$ | SFP |
| | $\pi-\phi_s$ | $\delta_+$ | UFP |
| | $\phi_s$ | $\delta_-$ | SFP |
| | $\pi-\phi_s$ | $\delta_-$ | UFP |

In this case, the linear bucket can be modified by the SFP $(\phi_s, \delta_+)$ and $(\phi_s, \delta_-)$ depending on their distance with $\delta = 0$. The distance between the two secondary buckets lines defined by $\delta_+$ and $\delta_-$ can be monitored using $\delta_+ + \delta_- = -\frac{\eta_1}{\eta_2}$.

#### 5.2.5.2 Mapping equations

From the mapping equations including the zeroth- and first-order slip factors, Riabko *et al.* [134] described the first-order longitudinal phase space by switching to a canonical plane. This section summarises my attempts to extend their method to the second-order Hamiltonian in Eq. (5.24). From the mapping equations (5.23), the following differential equation is verified by $\delta$, similarly to [134]:

$$\ddot{\delta} + \nu_s^2\delta + \nu_s^2\frac{\eta_1}{\eta_0}\delta^2 + \nu_s^2\frac{\eta_2}{\eta_0}\delta^3 = 0 \tag{5.27}$$

Changing the time variable as well as the longitudinal variable as in [134] and defining $x = -\frac{\eta_1}{\eta_0}\delta$ and $t = \nu_s\theta$, the equation (5.27) can be expressed in terms of $x$ as:

$$\ddot{x} + x - x^2 + \frac{\eta_2\eta_0}{\eta_1^2}x^3 = 0 \tag{5.28}$$

Compared to Riabko's paper, a higher order in $x$ was added, which has a coefficient $\frac{\eta_2\eta_0}{\eta_1^2}$ and which corresponds to the second-order term in the Hamiltonian. The derivative variable for the description of the phase space area is expressed as:

$$p = \frac{dx}{dt} = \frac{\eta_1}{\eta_0^2}\nu_s\phi \tag{5.29}$$

Considering the longitudinal variables $(x, p)$, the second-order Hamiltonian $H(\phi, \delta)$ becomes:

$$H = \frac{p^2}{2} + \frac{x^2}{2} - \frac{x^3}{3} + \frac{\eta_2\eta_0}{4\eta_1^2}x^4 \tag{5.30}$$

Following the process described in [134], one can derive the differential equation verified by the longitudinal variable $x$ at a fixed energy Hamiltonian $E$:

$$\left(\frac{dx}{dt}\right)^2 = -\frac{\eta_2\eta_0}{2\eta_1^2}x^4 + \frac{2}{3}x^3 - x^2 + 2E \tag{5.31}$$

Facing this analytic curve of order 4, one can derive this equation and find:

$$\frac{d^2x}{dt^2} = x(1 - x + \frac{\eta_2\eta_0}{\eta_1^2}x^3) \tag{5.32}$$

Unlike the case of the paper, where the phase space $(x, p)$ was described by an elliptic curve of known solutions, the equation (5.32) is not solvable to my knowledge but numerical derivation of the specific cases is possible. Figure 5.9 gives examples of the phase space described by Eq. (5.32) for different ration $\frac{\eta_2\eta_0}{\eta_1^2}$.

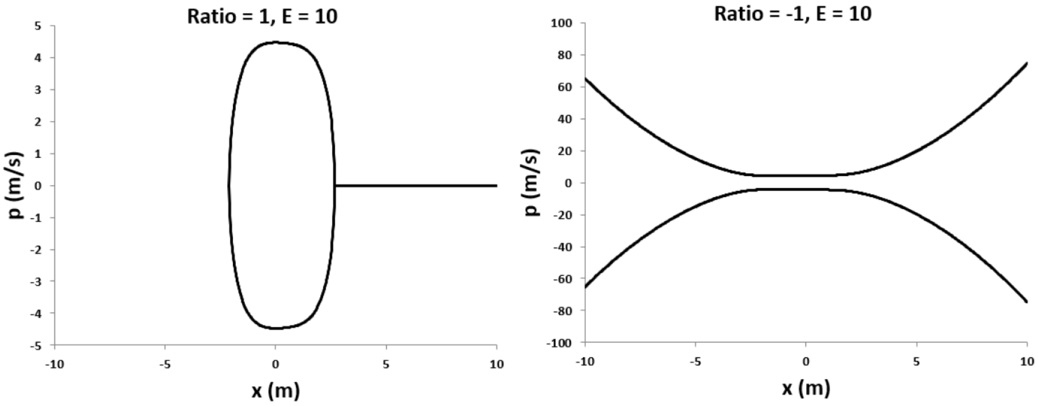

FIGURE 5.9: Phase-space $(x, p)$ of the second-order Hamiltonian, following [134], with (a) a ratio $\frac{\eta_2\eta_0}{\eta_1^2} = 1$ and (b) $\frac{\eta_2\eta_0}{\eta_1^2} = -1$. In both cases, the energy of the Hamiltonian E in Eq. (5.32) was arbitrarily set at 10.

As the resulting phase space is not easily described from the second-order Hamiltonian there derived, the attention is turned onto the high-order momentum compaction factor.

## 5.3 Higher-order momentum compaction factor

To control the longitudinal phase space and its stability while optimising the lattice, the higher-order momentum compaction factor was derived and investigated. Once the higher-orders in $\alpha_C$ were known and controlled, one could shape the bucket to match their expectations. This section follows the previous notations and deals with the three first-orders of the studied quantities.

### 5.3.1 Integral expressions

The momentum compaction factor can be expressed in terms of magnetic strengths and dispersion. To do so, one shall expand the pathlength $\Delta C$ in higher-order of momentum deviation $\delta$:

$$\Delta C = \oint \sqrt{x'^2 + y'^2 + (1 - hx)^2} ds \simeq \oint \left( \frac{x'^2 + y'^2}{2} - hx + hx \frac{x'^2 + y'^2}{2} \right) ds \tag{5.33}$$

with $\mathrm{h} = -\frac{1}{\rho}[\mathrm{m}^{-1}]$ . Distinguishing the betatron amplitude $x_\beta$ and the off-momentum component, the different orders in momentum compaction factor can find their integral expression as functions of the higher-order dispersions: $D_x = D_0 + D_1\delta + D_2\delta^2$. The full derivation is available in [133] for instance.

$$\begin{cases} \alpha_0 = \dfrac{1}{C_0} \displaystyle\int_0^{C_0} -hD_0 \, ds \\ \alpha_1 = \dfrac{1}{C_0} \displaystyle\int_0^{C_0} \left[ \dfrac{D_0'^2}{2} - hD_1 \right] ds \\ \alpha_2 = \dfrac{1}{C_0} \displaystyle\int_0^{C_0} \left[ D_0' D_1' + h \dfrac{D_0 D_0'^2}{2} - hD_2 \right] ds \end{cases} \tag{5.34}$$

### 5.3.2 Analytic expressions of the higher-order dispersion

To compute the higher-order momentum compaction factor, the dispersion and its derivatives are needed up to the second- and the first-order respectively. The definition of the higher-order dispersion is recalled in Eq. 5.36. First, the differential equation of each order is derived. Afterwards, considering the inherent periodicity of the dispersion function, the solutions of the differential equations are derived using Fourier series. From [131], the differential equation verified by the horizontal amplitude is, including the dependence in momentum deviation:

$$\begin{aligned} x'' + (h^2 + k_1)x = &- h(\delta - \delta^2 + \delta^3 - ...) + (k_1 + 2h^2)x(\delta - \delta^2 + \delta^3 - ...) \\ &- \frac{1}{2}k_2 x^2 (1 - \delta + \delta^2 - ...) - \frac{1}{2} h x'^2 (1 + \delta + \delta^2 + ...) + ... \end{aligned} \tag{5.35}$$

with $h[\mathrm{m}^{-1}] = -\frac{1}{\rho}$, $k_1$ the quadrupolar strength, $k_2$ the sextupolar strength. The differential equations verified by the different orders in dispersion are extracted from Eq. (5.35) by exhibiting the betatron motion and dispersion contribution in the amplitude $x$ and isolating each order in energy deviation $\delta$. Indeed,

$$x = x_\beta + D_0\delta + D_1\delta^2 + D_2\delta^3 + ... \tag{5.36}$$

#### 5.3.2.1 Linear dispersion $D_0$

The linear dispersion $D_0$ defines the off-momentum closed orbit, from the deflection in dipoles and combined-function magnets (*cf* sec. 2.1.2.1). It verifies the differential equation:

$$D_0'' + (h^2 + k_1)D_0 = -h \tag{5.37}$$

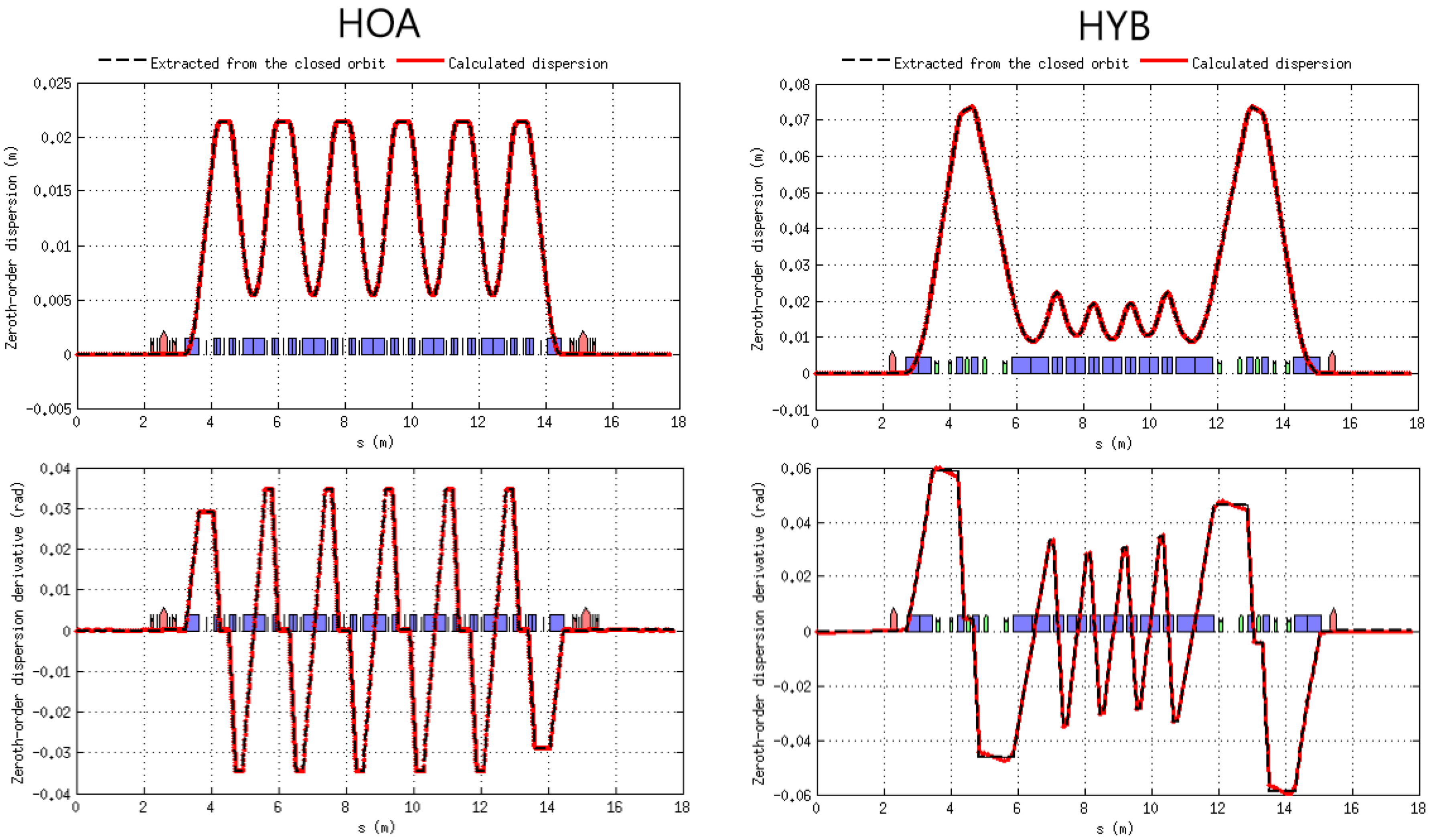

FIGURE 5.10: Comparison of the analytically-calculated (top) linear dispersion $D_0$, (bottom) its derivative $D_0'$ (in red) with the extracted values from tracking the orbits variation (in black), for two ultra-low emittance lattices: the 7BA HOA (left column) and the 7BA hybrid (right column) 20-fold symmetry for SOLEIL.

From [131, 135], the dispersion is Fourier-expanded with respect to the betatron phase advance $\phi$. Since all the lattices considered include a mirror symmetry, the phase is set at 0 in the middle of the straight section and the Fourier series include only the cosine component. The Fourier series of the linear dispersion and its derivative $D_0'$ are:

$$\begin{cases} D_0 = \sqrt{(\beta_x)} \sum_{n=0}^{\inf} F_{0n} \dfrac{\cos(n\phi)}{\nu_0^2 - n^2} \\ D_0' = -\dfrac{1}{\nu_0 \sqrt{(\beta_x)}} \sum_{n=0}^{\inf} n F_{0n} \dfrac{\sin(n\phi)}{\nu_0^2 - n^2} - \dfrac{\alpha}{\beta} D_0 \end{cases} \tag{5.38}$$

where $\nu_0$ is the unperturbed betatron tune and $F_{0n}$ is the Fourier harmonics of $-h\nu_0^2\beta_x^{\frac{3}{2}}$, of expression:

$$F_{0,n>0} = a_n \int_0^{C_0} -h\sqrt{\beta(s)} \cos(n\phi(s)) ds \tag{5.39}$$

with $a_n = \frac{\nu_0}{2\pi}$ if $n = 0$, $\frac{\nu_0}{\pi}$ otherwise.

The analytical calculation of the linear dispersion shall be compared to the expected dispersion for two different lattices. The expected dispersion and the orders to follow are extracted from the off-momentum orbit: the orbit of two off-momentum particles at $\pm\delta$ is calculated, the lowest-order dispersion and higher orders are then extracted from the variation of the orbit with $\delta$.

Figure 5.10 compares the linear dispersion and its derivative along the SOLEIL 7BA HOA lattice and the SOLEIL 7BA hybrid lattice, analytically calculated in Eq. 5.37 and the expected dispersion function and derivative. The calculations were conducted with Fourier series of maximum harmonic $N = 1000$. For a better appreciation of the variations along the lattice, along with an increased precision in the integral calculations, all elements were sliced into 30 pieces. The analytical evaluation (in red dots) of the linear dispersion is in excellent concordance with the expected dispersion (in black), as is the derivative, for both lattices. Slight variations occur near the dispersion bumps of the hybrid lattices, which can be controlled by increasing the number of Fourier harmonics N.

Integrating the zeroth-order dispersion along the longitudinal position $s$, one finds the momentum compaction factor of the hybrid lattice: $\alpha_0 = 1.4677 \times 10^{-4}$. The expected value is $1.467 \times 10^{-4}$, with three digits precision. The agreement with a three digits precision remains in the case of the HOA lattice, where the calculated momentum compaction factor is $1.0856 \times 10^{-4}$, and the expected value $1.0853 \times 10^{-4}$. The matching results of both the dispersion and the momentum compaction factor in the zeroth-order, for two different lattices confirm both the method and the script. They are thus extended to the first- and second-order, for the calculation of the first- and second-order momentum compaction factors.

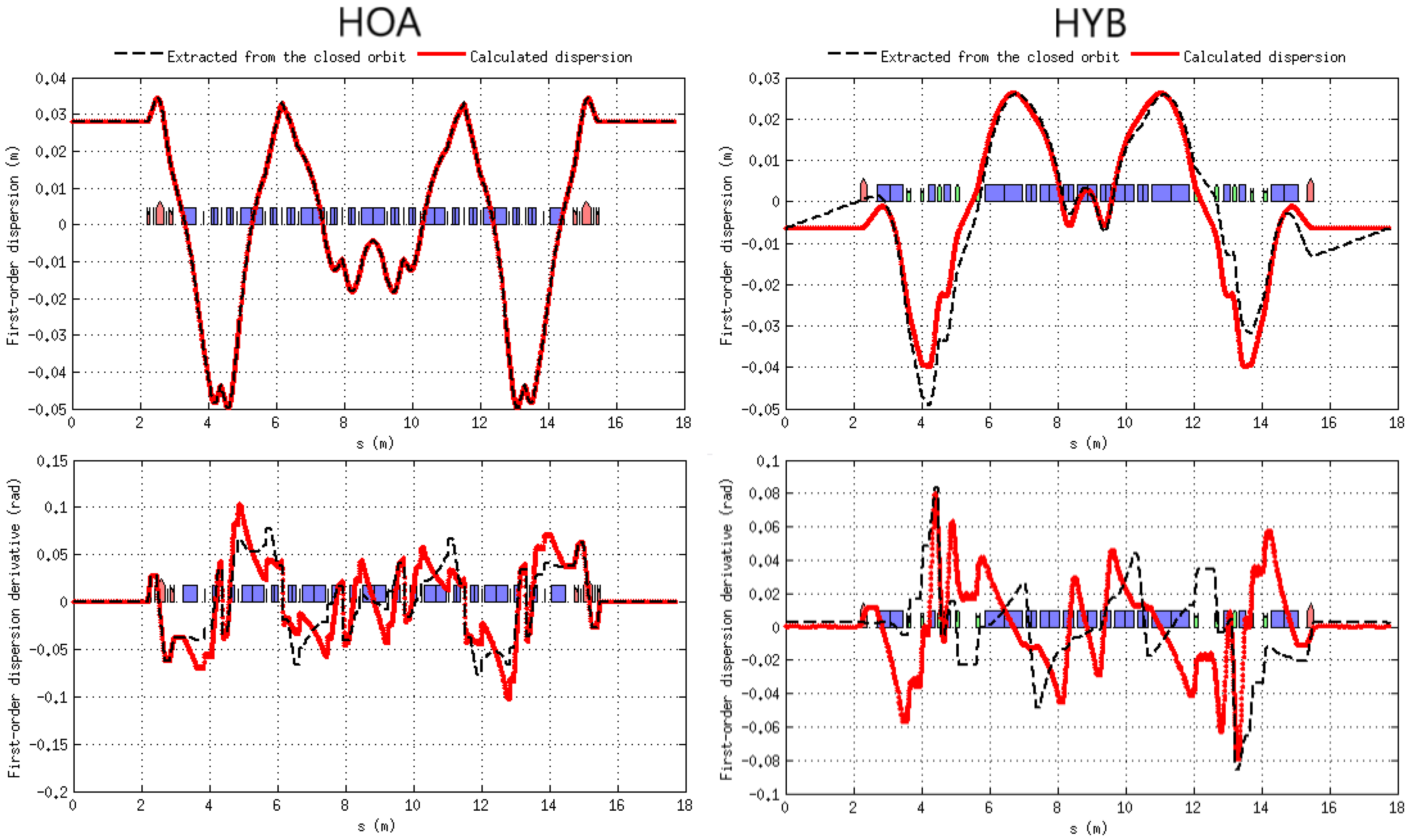

FIGURE 5.11: Comparison of the analytically-calculated (top) first-order dispersion $D_1$ ; (bottom) its derivative $D_1'$ (in red) with the extracted values from the orbits variation (in black), for two ultra-low emittance lattices: the 7BA HOA (left column) and the 7BA hybrid (right column) 20-fold symmetry for SOLEIL.

#### 5.3.2.2 First-order dispersion $D_1$

The first-order dispersion $D_1$ verifies the following differential equation:

$$D_1'' + (h^2 + k_1)D_1 = h + k_1 D_0 - \left(\frac{1}{2}k_2 + 2hk_1\right) D_0^2 - \frac{1}{2}hD_0'^2 - h'D_0D_0' \tag{5.40}$$

Similarly to the zeroth-order, the first-order part is expressed using the Fourier analysis described and applied in [131, 135]:

$$\begin{cases} D_1 = \sqrt{(\beta_x)} \displaystyle\sum_{n=0}^{\inf} (-F_{0n} + F_{1n}) \frac{\cos(n\phi)}{\nu_0^2 - n^2} \\ D_1' = -\dfrac{1}{\nu_0\sqrt{(\beta_x)}} \displaystyle\sum_{n=0}^{\inf} n(-F_{0n} + F_{1n}) \frac{\sin(n\phi)}{\nu_0^2 - n^2} - \frac{\alpha}{\beta}(D_1 + D_0) \end{cases} \tag{5.41}$$

where $F_{1n}$ is the Fourier harmonics of $-\nu^2\beta_x^{\frac{3}{2}}\eta_0\left[(k_1 + h^2) - \left(\frac{1}{2}k_2 - 2hk_1\right)\eta_0\right]$, including the influence of combined-function magnets. The expression of $F_{1n}$ is:

$$F_{1,n>0} = a_n \int_0^{C_0} \sqrt{\beta(s)}D_0(s)\left[k_1 - \left(\frac{1}{2}k_2 - 2hk_1\right)D_0(s)\right]\cos(n\phi(s))ds \tag{5.42}$$

with $a_n = \frac{\nu_0}{2\pi}$ if $n = 0$, $\frac{\nu_0}{\pi}$ otherwise.

Figure 5.11, similarly to Fig. 5.10, compares the analytical calculation of the first-order dispersion and its derivative $D_1'$, with the extracted values from the closed orbit. The calculations were conducted with Fourier series of maximum harmonic $N = 1000$, and all elements were sliced into 30 pieces. Both those values were chosen to match the zeroth-order momentum compaction factor with a $10^{-3}$ precision, as confirmed in the previous section.

**First-order derivative** In both cases, the first-order derivatives extracted from the orbits (c) and (d) appear wrong, as they do not represent the variation of the first-order dispersion: the additional treatment to extract the derivative here failed. To ensure the calculated derivative is correct, it is compared with the rate of change of the calculated first-order dispersion. The results for both lattices are displayed in Fig. 5.12, where the perfect agreement is shown - apart for a discontinuity at $s \simeq 3.8\,\mathrm{m}$ in the hybrid case-confirming the analytical calculation of the derivative.

#### 5.3.2.3 Second-order dispersion $D_2$

Finally, the second-order dispersion $D_2$ verifies the differential equation:

$$\begin{aligned} D_2'' + (h^2 + k_1)D_2 = & -h + k_1[D_1 - D_0] - \left(\frac{1}{2}k_2 + 2hk_1\right)[2D_0D_1 - D_0^2] \\ & - \frac{1}{2}\left[D_0'^2 + 2D_0'D_1'\right] + \left(\frac{3}{2}k_1 - 2h^2\right)D_0D_0'^2 \end{aligned} \tag{5.43}$$

Its Fourier series is:

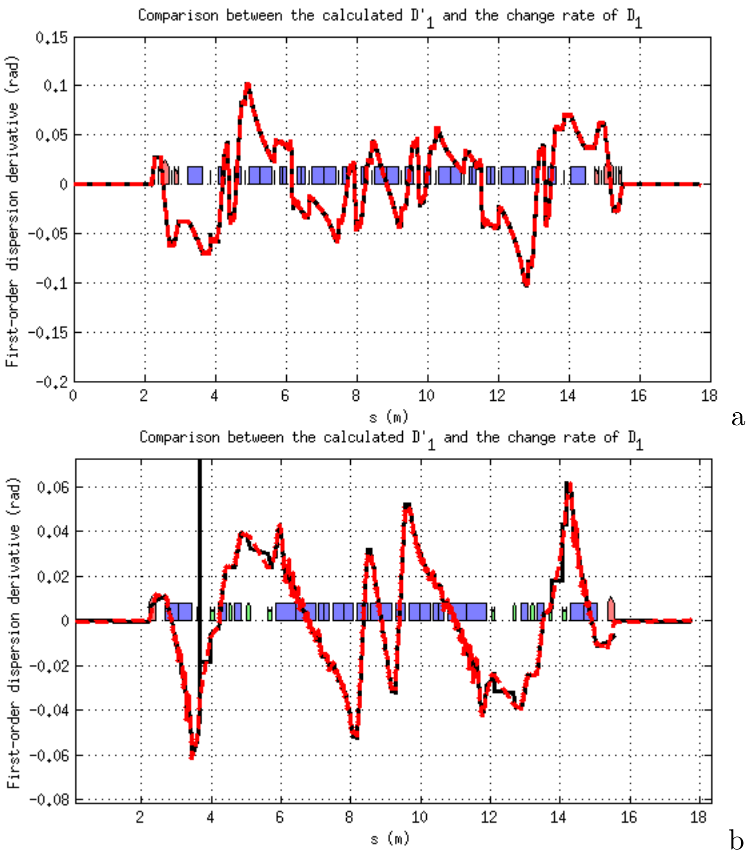

FIGURE 5.12: Comparison of the analytically-calculated first-order dispersion derivative $D'_1$ (in red) with the rate of change of the first-order dispersion $D_1$ (in black) for (left) the HOA lattice and (right) the hybrid lattice.

$$D_2 = \sqrt{(\beta_x)} \sum_{n=0}^{\inf} \left(F_{0n} - F_{1n} + F_{2n}\right) \frac{\cos(n\phi)}{\nu_0^2 - n^2} \tag{5.44}$$

where $F_{2n}$ the cosinusoidal Fourier harmonics of $-\nu^2 \beta_x^{\frac{3}{2}} \eta_1 \left[k_1 - \left(k_2 - 4hk_1\right) \eta_0\right]$, including the influence of combined-function magnets. The expression of $F_{1n}$ is:

$$F_{2,n>0} = a_n \int_0^{C_0} \sqrt{\beta(s)} D_1(s) \left[k_1 - \left(k_2 - 4hk_1\right) D_0(s)\right] \cos(n\phi(s)) ds \tag{5.45}$$

with $a_n = \frac{\nu_0}{2\pi}$ if $n = 0$, $\frac{\nu_0}{\pi}$ otherwise.

Figure 5.13 compares the analytical calculation of the second-order dispersion with the extracted values from the closed orbit. The derivative of the second-order was not analytically calculated, for it is not necessary in the calculations of the considered orders of the momentum compaction factor. The calculations were conducted with Fourier series of maximum harmonic $N = 1000$, and all elements were sliced into 30 pieces. The match is nearly perfect both the HOA and the hybrid case, with slight variations in the straight sections; such differences can be imputed to the loss of precision when using a second-order polynomial fit.

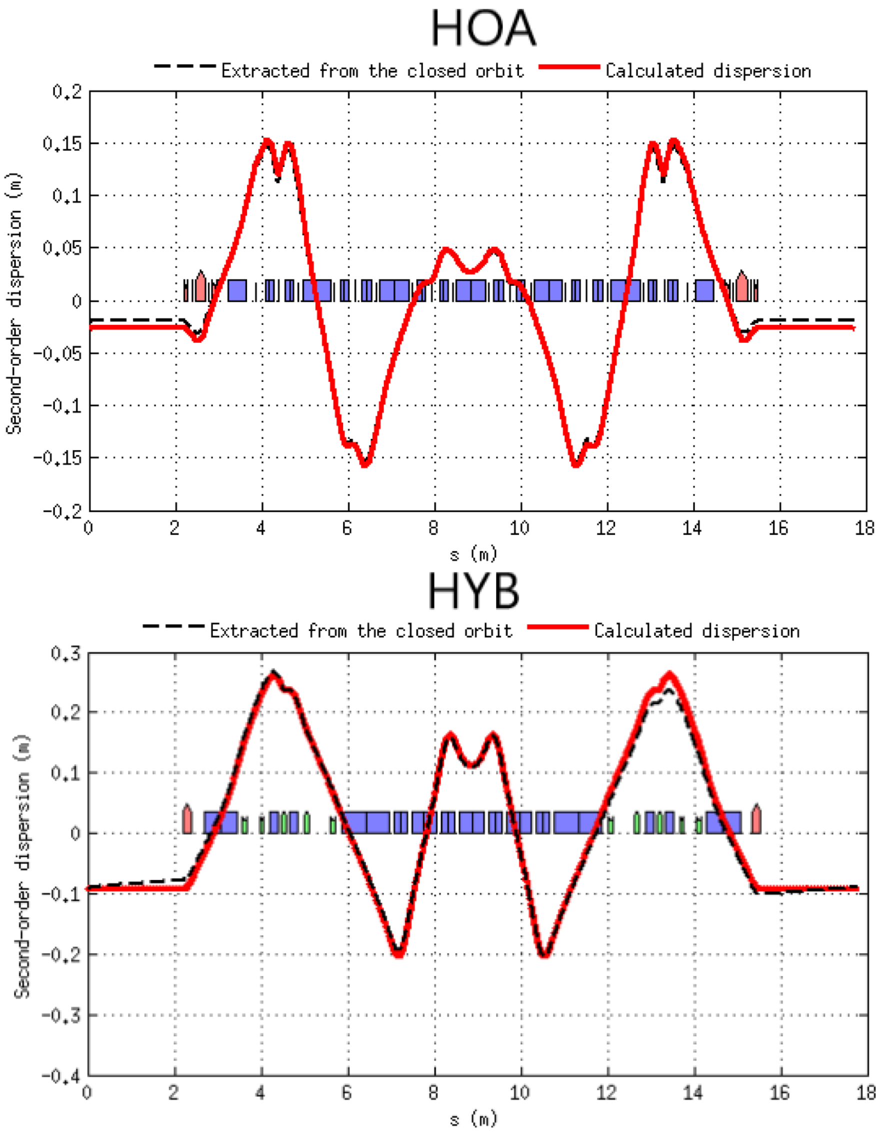

FIGURE 5.13: Comparison of the analytically calculated second-order dispersion $D_2$ (in red) with the extracted values from tracking the orbits variation (in black) for (a) the HOA lattice and (b) the hybrid lattice.

#### 5.3.2.4 Calculated momentum compaction factor

The calculated higher-order dispersions are integrated along the ring, complying with the integral expressions of the higher-order momentum compaction factor. Table 5.2 compares the orders in $\alpha_C$ extracted from the orbit by a polynomial fit of order 3 (left columns) available in A.T., and the calculated values (right columns) for the hybrid and HOA lattices.

Good agreement is found for the zeroth- and first-order, $\alpha_0$ and $\alpha_1$, to the $10^{-3}$ and $10^{-2}$ respectively, between the two calculation methods. The evaluation of the second-order differs between the two methods. The polynomial fit loses its precision for orders higher than two. Following the good agreement found in the nonlinear dispersion and the lowest-order calculation, the analytical value is believed to be the reference value.

Table 5.2: Comparison of the calculated and tracked first three-orders in momentum compaction factor for the 7BA hybrid and 7BA HOA lattices for SOLEIL.

| | HYBRID | | HOA | |
|---|---|---|---|---|
| MCF | Tracked | Calculated | Tracked | Calculated |
| $\alpha_0$ | $1.4673 \times 10^{-4}$ | $1.4677 \times 10^{-4}$ | $1.0853 \times 10^{-4}$ | $1.0856 \times 10^{-4}$ |
| $\alpha_1$ | $6.2004 \times 10^{-4}$ | $6.216 \times 10^{-4}$ | $1.7920 \times 10^{-4}$ | $1.7915 \times 10^{-4}$ |
| $\alpha_2$ | $-7.8838 \times 10^{-4}$ | $-7.914 \times 10^{-4}$ | $-3.5621 \times 10^{-4}$ | $-3.4654 \times 10^{-4}$ |

Increased precision of this value is achieved by increasing the number of harmonics in the Fourier expansion, as well as the number of slices per element of the ring, to better appreciate the Twiss function variations in the elements.

With the confirmed three lowest orders of the momentum compaction factor, a simple program was developed in A.T. to display the lines of equal Hamiltonian. The longitudinal phase space of both the HOA and the hybrid lattice could then be calculated. They are displayed in Fig. 5.14. As expected from the values of $\alpha_0$ and $\alpha_1$, which ratio equals 0.61 for the HOA 7BA and 0.24 for the hybrid lattice, the linear bucket is large enough and not perturbed in any way by the higher-order bucket lines. Nonetheless, an asymmetry exists in the hybrid bucket in the negative energy, and is due to the proximity of the first-order bucket line $\delta = -\frac{\alpha_0}{\alpha_1} = 0.24$.

## 5.4 Effect of the nonlinear magnets on $\alpha_1$ and $\alpha_2$

The optimisation of the higher-order momentum compaction factor is explored in this section with the use of nonlinear magnets: sextupoles and octupoles. Sextupoles influence both the first- and the second-order momentum compaction factor, while octupoles only have an effect on $\alpha_2$. From Eq. (5.34), the influence of such magnets is indirect. Indeed, $\alpha_1$ is influenced by the sextupoles from its second term, $-hD_1$: the sextupoles play a role in determining $D_1$, following Eq. (5.41). Similarly, the octupoles influence $\alpha_2$ through $D_2$, the sextupoles through $D_1'$.

The optimisation of the longitudinal stability area is explored through two means: either the increase of $\alpha_2$ to compensate the destructive effect of $\alpha_1$, or minimising the first-order $\alpha_1$ directly.

### 5.4.1 On the use of octupoles to optimise the bucket characteristics

As discussed in the section 5.2.3, the first-order momentum compaction factor, if large enough, perturbs the symmetry of the longitudinal plane, thus creating an atrophied bucket. Two methods are foreseen to minimise this effect.

A first method addressed by Maher Attal in his thesis [133] focuses on restoring the symmetry of the longitudinal plane by balancing the ratio $\frac{\alpha_0\alpha_2}{\alpha_1^2}$. By inserting octupoles in the a dispersive zone of the lattice, the second-order in momentum compaction factor can

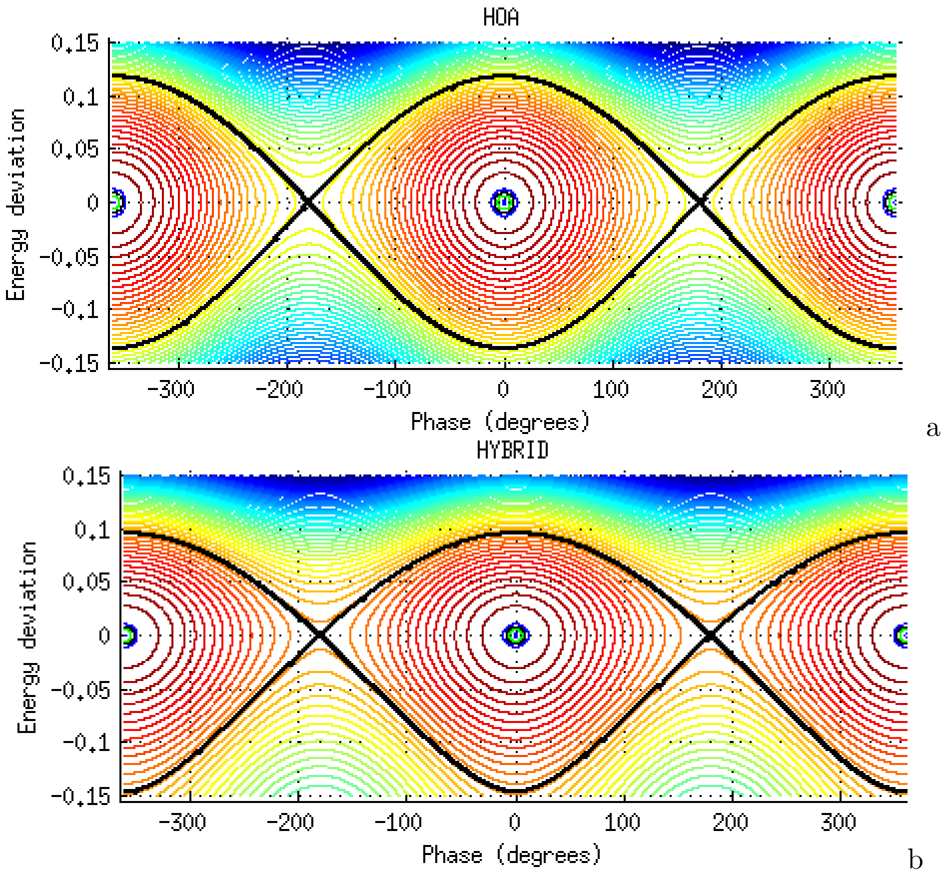

FIGURE 5.14: Comparison of longitudinal phase space of (a) the HOA 7BA lattice and (b) the hybrid 7BA lattice, with the calculated three lowest-order of the MCF.

be optimised to restore the symmetry of the bucket, thus compensating the effect of $\alpha_1$. As $\alpha_2$ is produced by all second-order magnets and above, the addition of octupoles in a lattice can increase the second-order momentum compaction factor with no alteration of the lowest orders.

Where this solution could work on some lattices - specifically in the case where the RF bucket is small, when the ratio $\frac{\alpha_0}{\alpha_1}$ is small, the restoration effect of $\alpha_2$ is neither efficient, nor always possible. It was applied on the 5BA lattice, described in the introduction of this chapter (5.1). Two octupoles were inserted at symmetric positions, on the side of the second dipole, to benefit from a large dispersion. Their location is displayed in Fig. 5.15.

The pathlength is tracked in A.T., and the orders of the momentum compaction factor are extracted with a polynomial fit:

$$\frac{\partial(\Delta C)}{\partial\delta} = C_0\alpha_C = C_0(\alpha_0 + 2\alpha_1\delta + 3\alpha_2\delta^2 + ...) \tag{5.46}$$

This allowed the evaluation of the second-order momentum compaction of the nominal lattice, which is $\alpha_2 = -1.5 \times 10^{-4}$, too low to have an influence on the RF bucket. Figure 5.16 displays the variation of the second-order momentum compaction factor with the strength of the octupole family.

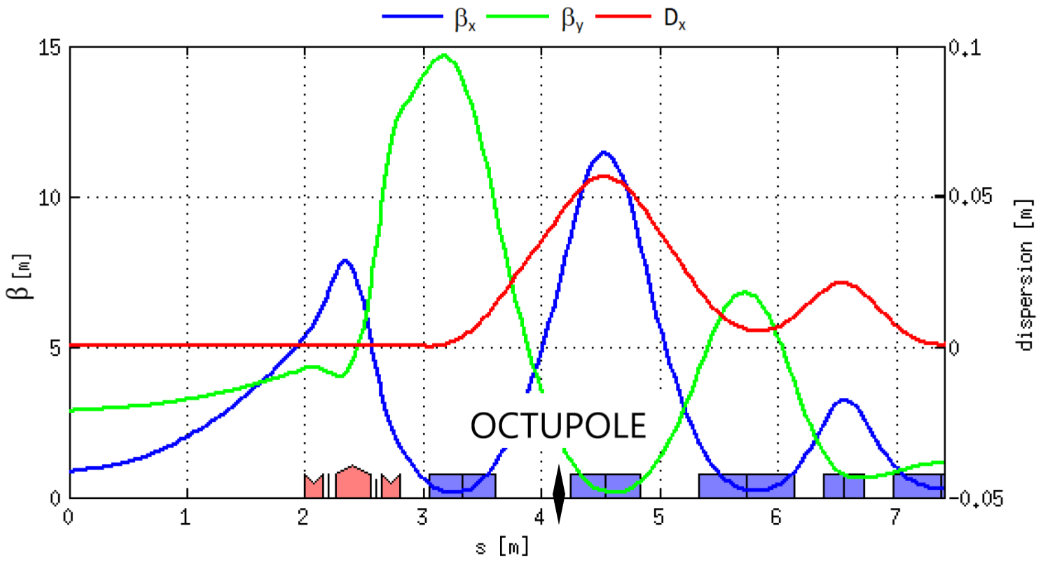

FIGURE 5.15: Location of the octupole for increase of the second-order momentum compaction factor.

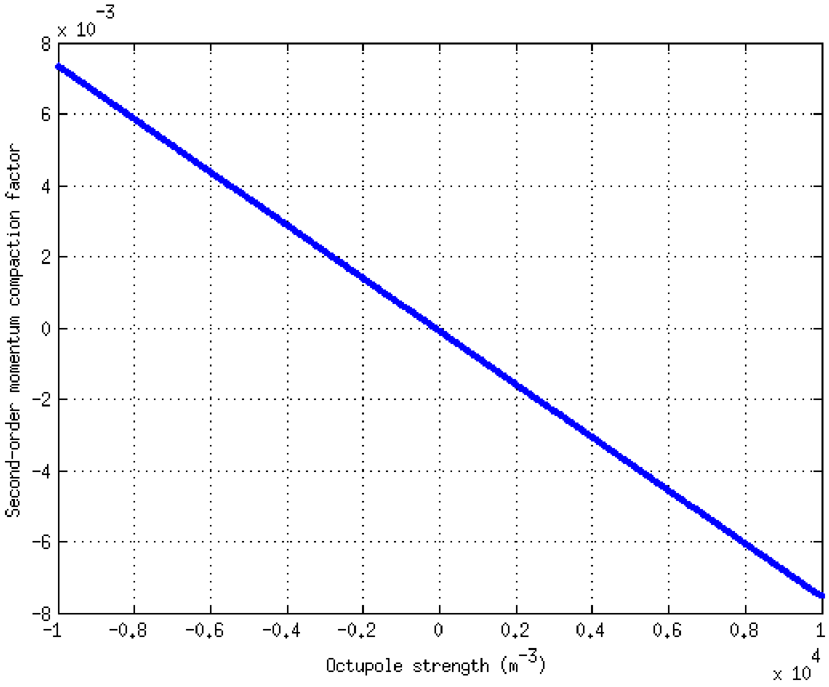

FIGURE 5.16: Variation of the second-order momentum compaction factor with the octupole strength.

The method is proved to vary $\alpha_2$. To specify which $\alpha_2$ is required to restore the RF bucket, Figure 5.17 compares the RF buckets for different second-order momentum compaction factors.

Therefore, the application of $-7000\,\mathrm{m}^{-3}$ strength to the octupoles increased the second-order momentum compaction factor and restored the linear bucket on Fig, 5.17 (c). Yet, to completely restore the symmetry of the linear bucket, the required octupole strength exceeds $-10000\,\mathrm{m}^{-3}$. Although this method can restore the RF bucket by

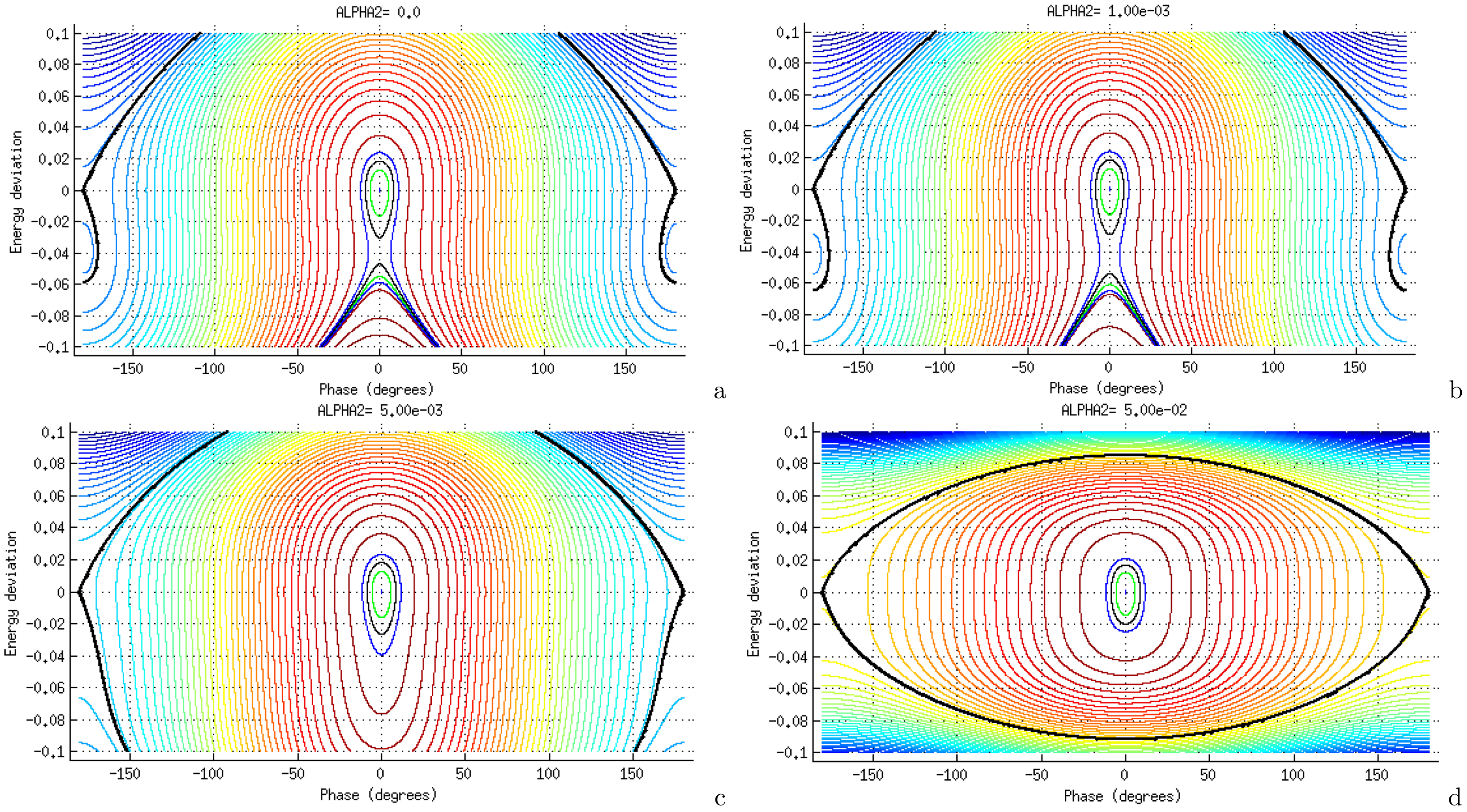

FIGURE 5.17: RF buckets of the 5BA lattice with $\alpha_0 = 2.10 \times 10^{-5}$ and $\alpha_1 = 5.35 \times 10^{-4}$, for (a) $\alpha_2 = 0$, (b) $\alpha_2 = 1 \times 10^{-3}$, (c) $\alpha_2 = 5 \times 10^{-3}$ and (d) $\alpha_2 = 5 \times 10^{-2}$.

increasing the second-order momentum compaction factor which compensates the effect of the first-order, the requirements for strong octupoles, in a lattice with little space, and a large tune shift which has to be further corrected, limits its application and its effectiveness.

### 5.4.2 Optimisation of the effect of $\alpha_1$ using sextupoles

Rather than introducing additional magnets in the tight lattices to increase $\alpha_2$, a second method aims at minimising $\alpha_1$ directly and restore the bucket acceptance. Since $\alpha_1 = \frac{1}{C_0}\int_0^{C_0}[\frac{D_0'^2}{2} - hD_1]ds$, the effect of the sextupoles on $\alpha_1$ is indirect: they affect the second-order dispersion only, in the presence of linear dispersion. Therefore, the minimisation of $\alpha_1$, if possible, with the sextupoles, requires the manipulation of $D_1$.

In this section, I explore the feasibility and efficiency of the minimisation of $\alpha_1$ with the sextupoles. The different tests were conducted on the HOA 7BA lattice: this lattice is inherently composed of a large number of sextupoles, which increases the freedom degrees of the minimisation process. The good knowledge of the lattice helps better understand the outputs of the scan. Once the minimisation was proved feasible and tested on the HOA lattice, the process was applied on the 5BA lattice.

#### 5.4.2.1 Variation of the second-order dispersion with sextupoles

To test the feasibility of this method, the sextupoles of the HOA 7BA lattice are randomly varied among a fixed range and under the constraint of constant chromaticities. The first-order dispersion is evaluated for each generated ring. All sextupoles are treated individually, to maximise the effect on the higher-order dispersion. For comparison with the nominal lattice, the program works under constant chromaticities. To do so, the effect of each sextupole on the chromaticities is computed and gathered in the chromatic matrix. The pseudo-inverse of such matrix allows the creation of the variable space of dimension $N_{sext} - 2$, where the chromaticities are kept constant. The sextupolar bounds are translated in that space. At the ring creation stage of the program, a random set is taken from that variable space, then translated back into sextupolar strengths to create a new ring, of identical linear chromaticities to the nominal lattice. This method was copied from MOGA-Bmad, and transcribed into Matlab. Figure 5.18 gathers the results for a sextupole variation of $\pm 1\%$, $\pm 5\%$ and $\pm 10\%$ from their nominal values, with 500 iterations. Logically, the higher the variation in the sextupole strength, the higher the variation in the first-order dispersion, which is promising for the foreseen minimisation.

The superimposed magnetic lattice of the HOA allows us to spot that the strongest variations in the first-order dispersion occur on the dipoles and straight sections: therefore we can expect a variation of the first-order momentum compaction factor while playing on the sextupoles, under the same conditions.

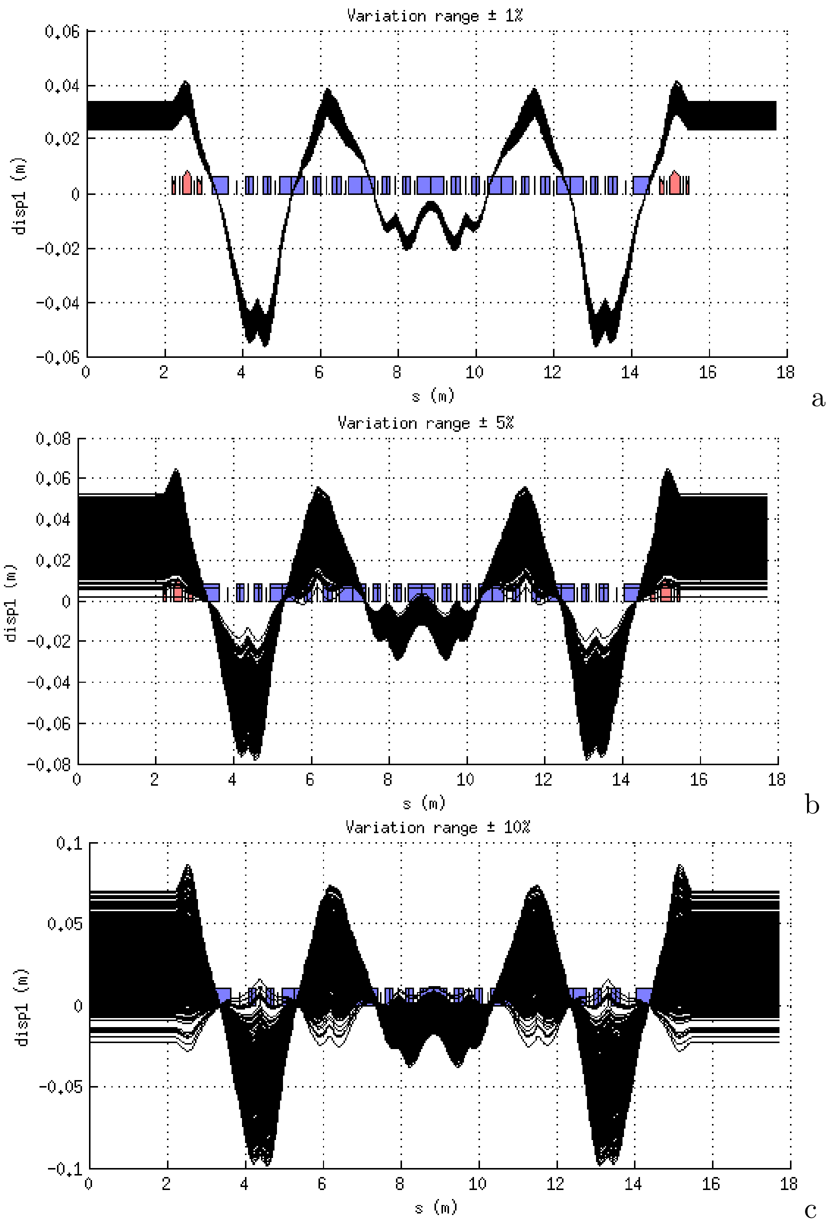

FIGURE 5.18: Variation of the first-order dispersion with N=500 new rings with sextupole strengths varying within (a) a ±1% range (b) a ±5% range and (c) a ±10% range from their nominal values, while keeping the chromaticities in both planes constant.

#### 5.4.2.2 Optimisation of the HOA 7BA lattice using A.T.

To evaluate the efficiency of the described method, the sextupole strengths are varied within a defined range to scan the first-order momentum compaction factor. The program scans the input lattice and numbers its sextupoles: the sextupoles are treated independently *i.e.* no families are taken into account, to maximise the interaction with $\alpha_1$. For comparison with the nominal lattice, the program works under constant chromaticities, using the process previously described. Once a ring is created, its first-order dispersion is calculated and printed with regards to the longitudinal position $s$. Afterwards, the first-order momentum compaction factor is calculated analytically using its integral form. The end of the program finds the minimum scanned $\alpha_1$, and saves the corresponding ring. The program has several outputs:

- Output variables: the optimised ring, the values of the sextupoles of each generated ring, and the vector 'alpha1all' gathering the values of $\alpha_1$ of all generated rings.
- Figures: a first figure is updated along the optimisation and superimposes the first-order dispersion of all generated rings. At the end of the optimisation, three additional figures are created: the variation of $\alpha_1$ during the optimisation, the relative sextupole variation of the ring of minimum $\alpha_1$ and the comparison of the first-order dispersion of the ring of minimum $\alpha_1$ with that of the nominal ring.

The whole script is available in my GitHub [136].

**Optimisation with different relative variation ranges for the sextupoles** Following the results of the first-order dispersion scan, a first optimisation was conducted using a ±10% margin. The optimisation was tested on one period of the HOA 7BA lattice, which is composed of 22 individual sextupoles. The variable space dimension is therefore 20, due to the dominant constraints of the constant vertical and horizontal chromaticities. As a reminder, the zeroth- and first-order momentum compaction factors of the HOA lattice are $\alpha_0 = 1.08 \times 10^{-4}$ and $\alpha_1 = 1.791 \times 10^{-4}$, which results in a $\frac{\alpha_0}{\alpha_1}$ ratio of $\simeq 0.6$.

Table 5.3: Achieved minimum and maximum first-order momentum compaction factors for different relative variations of the sextupole strengths in the minimisation scan conducted on the HOA 7BA lattice.

| Variation range | 10% | 25% | 50% | 100% |
|---|---|---|---|---|
| $\alpha_{1,min}$ | $1.785 \times 10^{-4}$ | $1.780 \times 10^{-4}$ | $1.774 \times 10^{-4}$ | $1.757 \times 10^{-4}$ |
| $\alpha_{1,max}$ | $1.795 \times 10^{-4}$ | $1.795 \times 10^{-4}$ | $1.804 \times 10^{-4}$ | $1.818 \times 10^{-4}$ |
| Relative variation | $-0.35/+0.2\%$ | $-0.65/+0.2\%$ | $-1/+0.7\%$ | $-2/+1.5\%$ |
| Maximum ratio $\frac{\alpha_0}{\alpha_1}$ | 0.605 | 0.607 | 0.609 | 0.615 |

The optimisation was conducted with a random generation of 1000 rings: for each ring, both the first-order dispersion and the first-order momentum compaction factor were evaluated. Figure 5.19 displays the variations of the first-order momentum compaction factor during the different optimisations conducted for different relative sextupole variations: (a) ±10%, (b) ±25%, (c) ±50% and (d) ±100%, and for each randomly generated ring. As expected, the release of the sextupole strength bounds increases the relative variations on $\alpha_1$, as displayed in Table 5.3. The strongest reduction achieved is a $-2\%$ reduction with a ±100% variation of the sextupole strengths, which remains too low to effectively influence on the longitudinal phase space, as it increases the ratio $\frac{\alpha_0}{\alpha_1}$ by only 2%.

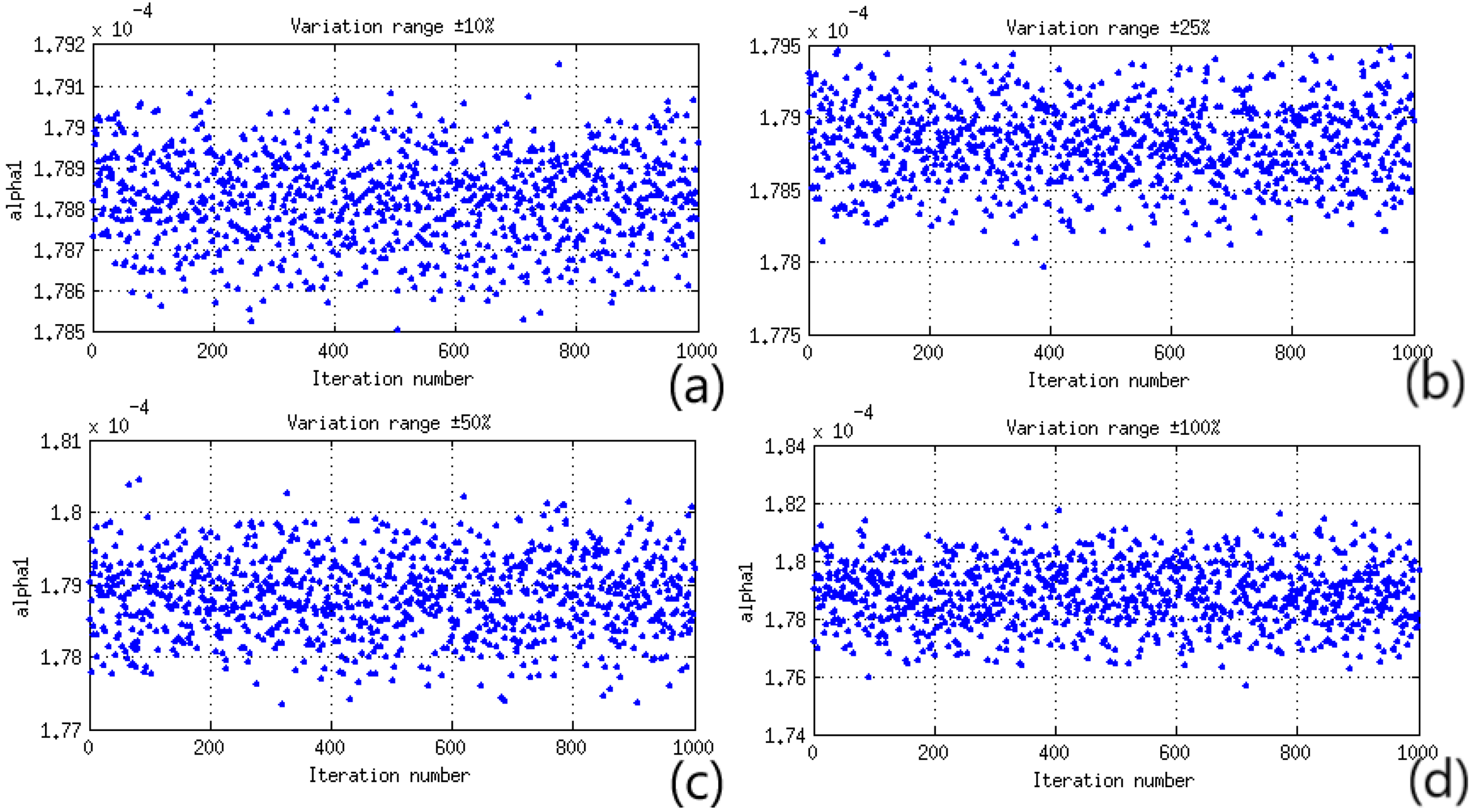

FIGURE 5.19: Variation of the first-order momentum compaction with N=1000 new HOA 7BA rings with sextupole strengths varying within a (a) ±10%, (b) ±25%, (c) ±50% and (d) ±100% range from their nominal values, while keeping the chromaticities in both planes constant.

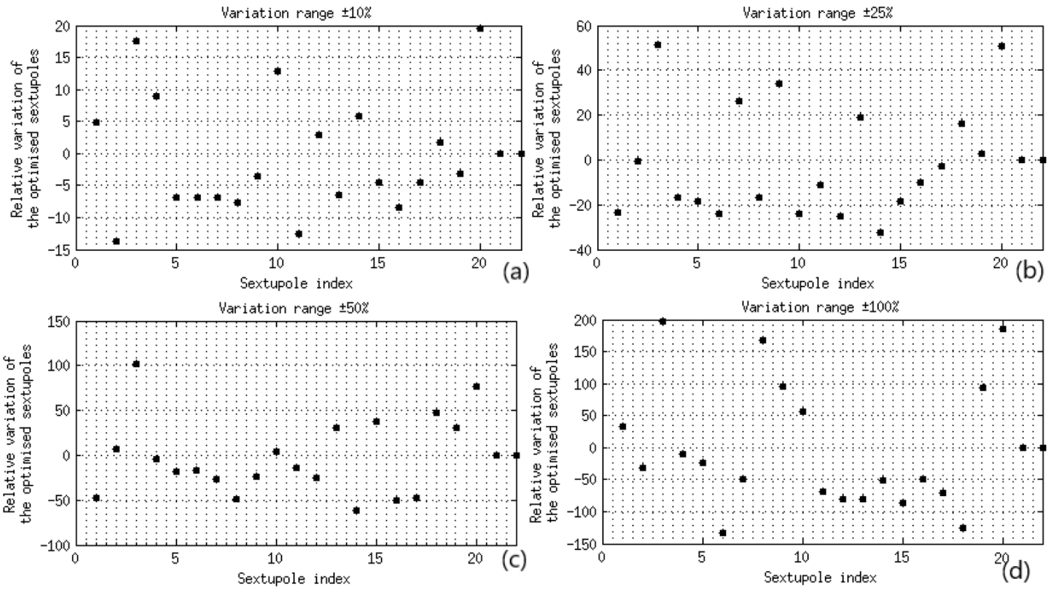

Figure 5.20: Comparison of the relative variation of the sextupole strengths of the optimised ring in the (a) ±10%, (b) ±25%, (c) ±50% and (d) ±100% optimisations.

To compare with the nominal lattice, the first-order dispersions of all optimised lattices are confronted with the nominal $D_1$ in Fig. 5.21. The nominal first-order dispersion is displayed in red in each figures. For the smallest variations of the sextupole strengths, ±10% and ±25%, the optimised first-order dispersion remains of the same order as the nominal $D_1$: the optimisation of $\alpha_1$ is there achieved with the minimisation of the integral contribution of $D_1$ in $\alpha_1$, by either an increase in $D_1$ at the antibends (Fig. 5.21 (a)), or a general reduction of the dispersion (Fig. 5.21 (b)). This process is not obvious in the larger variations of the sextupoles, where the optimised first-order dispersion is largely increased by a factor 10 to 20 in the ±50% and ±100% sextupole variation cases. The minimisation of $\alpha_1$ appears to be completed by compensating the incompressible contribution of $(D_0')^2$ in $\alpha_1$, by further increasing the first-order dispersion in the antibends, which creates a negative area.

To complete the overview of the optimisation, Fig. 5.20 compares the relative variations of the sextupoles for each ring of minimum $\alpha_1$. Despite the margin applied, some values step out of the boundary: since the translation to and from the variable space of constant chromaticity is not an invertible process, it is assumed that some sextupoles can be generated out of the defined bounds. In the case of the ±50% and ±100% variation, the sextupoles of the optimised ring strongly vary from their nominal, with Sextupole 3 and its symmetric 20 doubling and tripling their value. Such large sextupoles must perturbed the transverse dynamic of the lattice. Especially, the variations of the sextupoles not only affect the first-order dispersion but also higher orders, which play a role in the definition of the higher-order chromaticities.

**Transverse dynamic apertures of the optimised rings** The increase of the sextupole strengths has many drawbacks. The higher the sextupoles, the stronger the

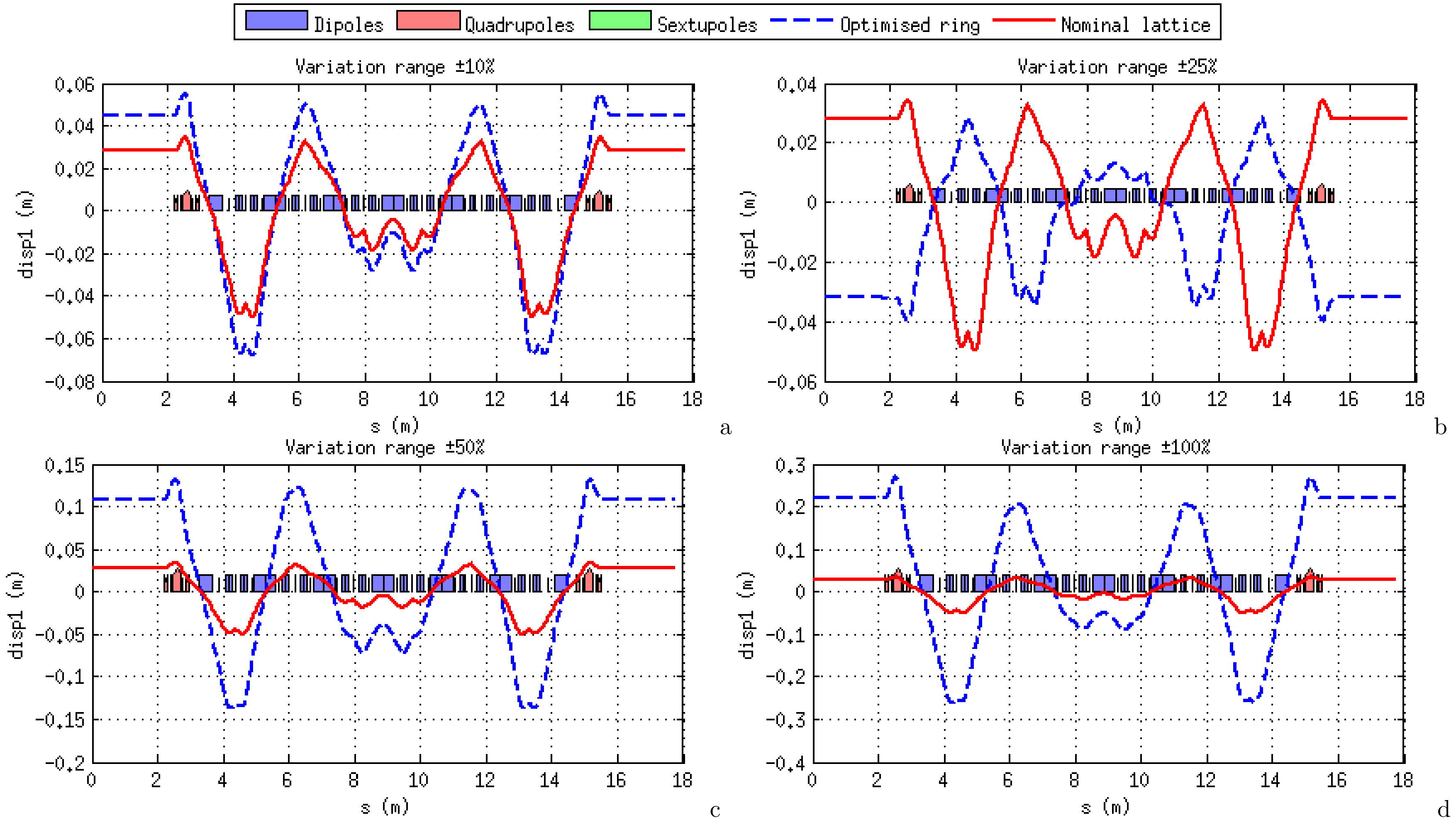

FIGURE 5.21: Comparison of the first-order dispersion of the optimised HOA 7BA ring (in blue) with the nominal HOA 7BA ring (in red), for different relative variations of the sextupole strengths: (a) ±10%, (b) ±25%, (c) ±50% and (d) ±100%.

resonances, with a potential reduction of the dynamic aperture. Furthermore, the tune-shift with energy is perturbed, thus changing the off-momentum stability. Figure 5.22 compares the on-momentum dynamic aperture of the optimised rings and the nominal lattice.

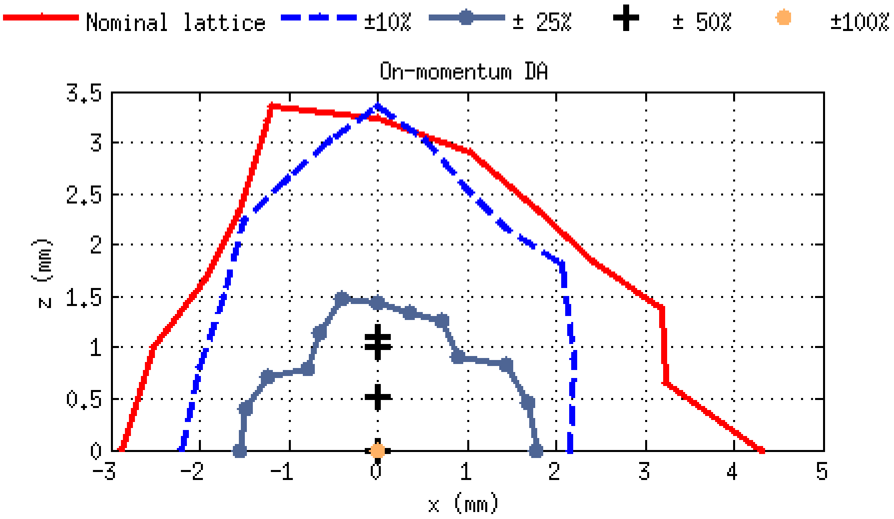

FIGURE 5.22: Comparison of the on-momentum transverse dynamic aperture of the rings optimised in $\alpha_1$ using the sextupoles.

**Tune shift with energy and nonlinear chromaticities of the optimised lattices** Although the optimisation is conducted at constant linear chromaticities, the effect of the variations of the sextupoles on the second- and third-order chromaticities is not controlled in any way, which could lead to high tune shift with energy if left unattended. Figure 5.23 compares the tune shift with energy of the four optimised lattices, with the nominal lattice performances. Small variations around the nominal strengths of the sextupoles do not perturb the tune shift with energy. While increasing the sextupole strengths, the tune shift is stronger and stronger, thus reaching the half-integer and integer values rapidly. Indeed, in the case of ±25% variations, the horizontal tune shift is dominated by the third-order chromaticities, and reaches the half-integer for an energy deviation of $\delta \simeq -10\%$. The third order also dominates the tune shift for a variation of ±50%, where the integer is reached for $\delta \simeq +6\%$. In the case of ±100% variations for which the sextupoles are the strongest, the integer resonance is reached rapidly, for $\delta \simeq -3.5\%$.

Table 5.4 gathers the values of the nonlinear chromaticities of the optimised rings for the different optimisations described in this section, and compares them to the values of the nominal lattice. As expected, the optimisation of $\alpha_1$ with the sole condition of keeping the linear lattice and the first-order chromaticities in both planes tends to increase the value of the second- and third-order chromaticities.

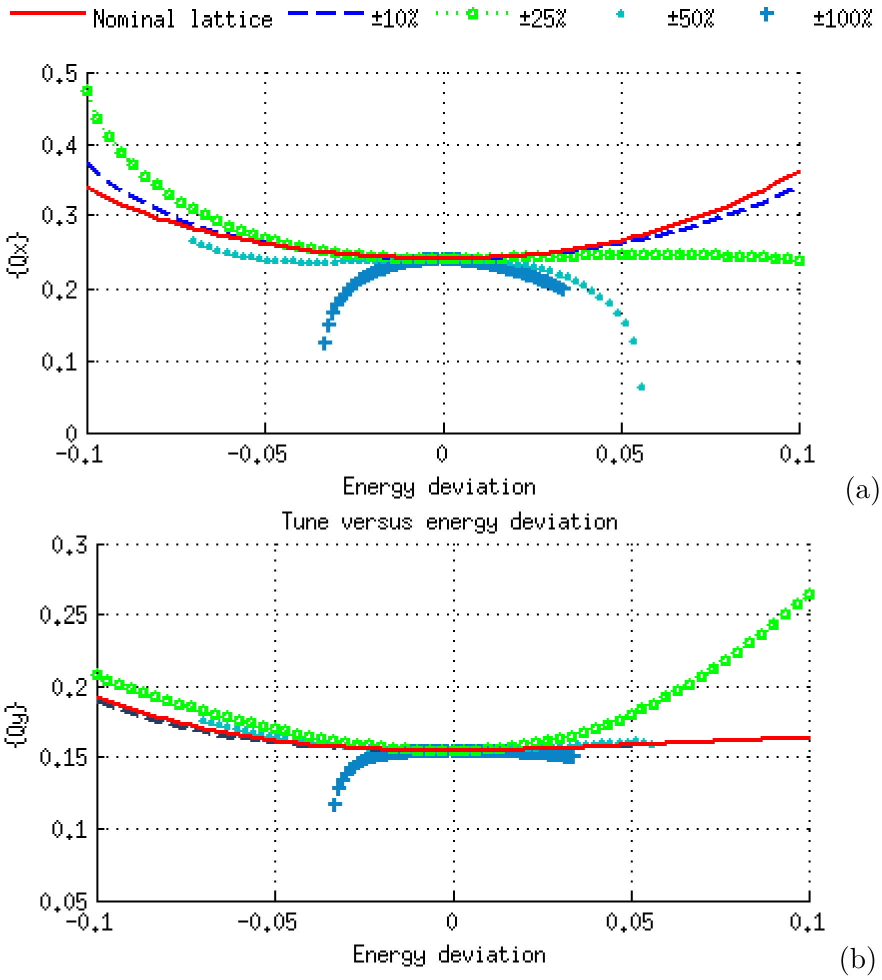

FIGURE 5.23: Comparison of tune shifts with energy of the rings optimised in $\alpha_1$ using the sextupoles: (a) in the horizontal plane and (b) in the vertical plane.

TABLE 5.4: Comparison of the nonlinear chromaticities along the four optimised periods of the HOA 7BA lattice with different relative variations of the sextupole strengths.

| Chromaticities | Nominal lattice | 10% | 25% | 50% | 100% |
|---|---|---|---|---|---|
| $\xi_x^1$ | -0.002 | -0.0018 | -0.0018 | -0.0018 | -0.0019 |
| $\xi_y^1$ | 0.006 | 0.0058 | 0.0058 | 0.0058 | 0.0057 |
| $\xi_x^2$ | 9.2 | 8.0826 | 5.9599 | -10.749 | -41.9117 |
| $\xi_y^2$ | 2.2 | 1.8990 | 7.9607 | 3.509 | -1.9668 |
| $\xi_x^3$ | 26.5 | 6.5630 | -94.2351 | -210.973 | 277.6763 |
| $\xi_y^3$ | -15.7 | -9.6762 | 40.2829 | -5.941 | 80.1506 |

#### 5.4.2.3 Optimisation of the 5BA lattice using A.T.

As this general study started with a 5BA lattice explored for the upgrade of the SOLEIL storage ring, this section is dedicated to the optimisation of its bucket area using the A.T. scan successfully tested on the HOA 7BA lattice. To do so, the 5BA lattice was translated from OPA to A.T., and the same optimisation as with the HOA lattice was conducted on one period of the ring.

**Optimisation with different relative variation ranges for the sextupoles** A 5BA period is composed of 14 sextupoles, which are considered independent. Here, the variable space is of dimension 12. Unlike the HOA 7BA lattice where the ratio $\frac{\alpha_0}{\alpha_1}$ was large enough for the destructive bucket line not to perturb the linear bucket, the linear buckets of the 5BA lattice are drastically reduced by the effect of $\alpha_1$. Indeed, its zeroth-order momentum compaction factor equals $\alpha_0 = 2.1044 \times 10^{-5}$, the first-order $\alpha_1 = 5.3435 \times 10^{-4}$, resulting in as low a ratio as $\frac{\alpha_0}{\alpha_1} \simeq 0.04$. Nevertheless, unlike the ultra-low emittance HOA 7BA lattice, the dispersion and higher-order dispersions of the 5BA lattice are higher by at least an order of magnitude: the efficiency of the minimisation on the 5BA lattice is expected to be higher.

The minimisation of $\alpha_1$ in the 5BA lattice is conducted with 1000 generated rings, for four relative variations of the sextupole strengths, ±10%, ±25%, ±50% ±100%. Table 5.5 gathers the extrema values of $\alpha_1$ for each scan. An overview of the first-order momentum compaction factor of all generated rings is available in Fig. 5.24.

Table 5.5: Achieved minimum and maximum first-order momentum compaction factors for different relative variations of the sextupole strengths in the minimisation scan conducted on the 5BA lattice.

| Variation range | 10% | 25% | 50% | 100% |
|---|---|---|---|---|
| $\alpha_{1,min}$ | $5.3942 \times 10^{-4}$ | $5.1813 \times 10^{-4}$ | $4.8915 \times 10^{-4}$ | $4.1545 \times 10^{-4}$ |
| $\alpha_{1,max}$ | $5.6488 \times 10^{-4}$ | $5.8614 \times 10^{-4}$ | $6.1754 \times 10^{-4}$ | $6.7367 \times 10^{-4}$ |
| Relative variation | $+0.9/+5\%$ | $-3/+9.7\%$ | $-8/16\%$ | $-22/+25\%$ |
| Maximum ratio $\frac{\alpha_0}{\alpha_1}$ | 0.039 | 0.040 | 0.043 | 0.05 |

As expected, the variations of $\alpha_1$ with the sextupoles are here stronger than in the HOA case: this is due to the higher first-order dispersion level: the different scans reached a maximum reduction of 22%, achieved for a relative variation of ±100%. The rings of minimum $\alpha_1$ in each case were subsequently analysed. The corresponding first-order dispersions are compared to the nominal ring parameters in Fig. 5.25. The nominal first-order dispersion of the 5BA lattice is composed of two large negative bumps, and a small positive offsets. The minimisation therefore tends to compensate the contribution of the zeroth-order dispersion derivative on $\alpha_1$ with the first-order dispersion. Indeed, the larger the bound on the sextupoles, the larger the negative bumps.

Figure 5.26 gathers the sextupole strengths variations in the rings of minimum $\alpha_1$ in each conducted scan. Similarly to the HOA case, some values are out of bounds. Nevertheless, the sextupole contribution to the minimisation appears to be better distributed than in the HOA case, as no specific sextupole stands out. Nonetheless, the minimisation of $\alpha_1$ is at the cost of the transverse dynamics, as demonstrated in the HOA case and in the following paragraphs for the 5BA lattice.

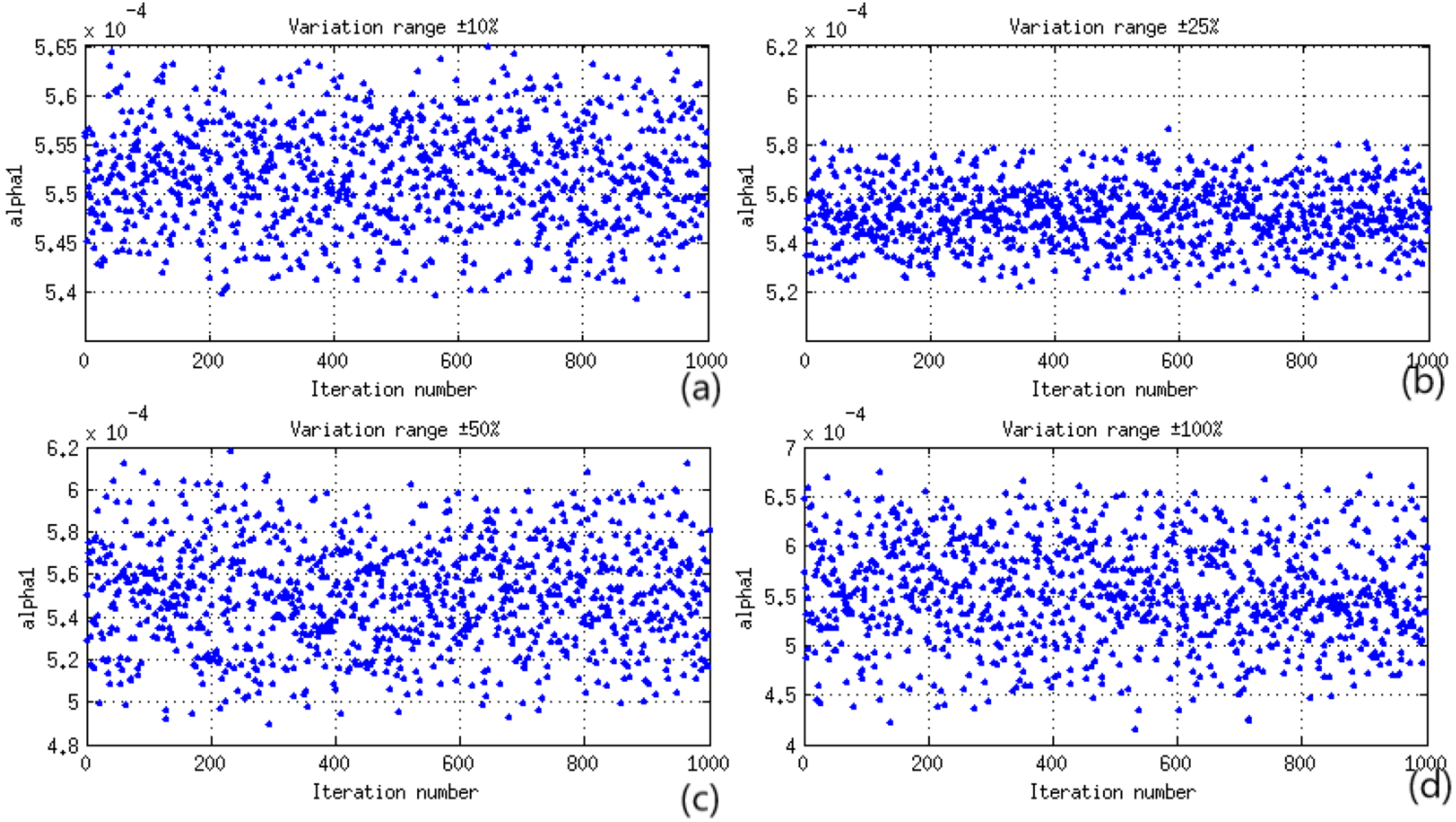

FIGURE 5.24: Variation of the first-order momentum compaction with N=1000 new 5BA rings with sextupole strengths varying within a (a) ±10%, (b) ±25%, (c) ±50% and (d) ±100% range from their nominal values, while keeping the chromaticities in both planes constant.

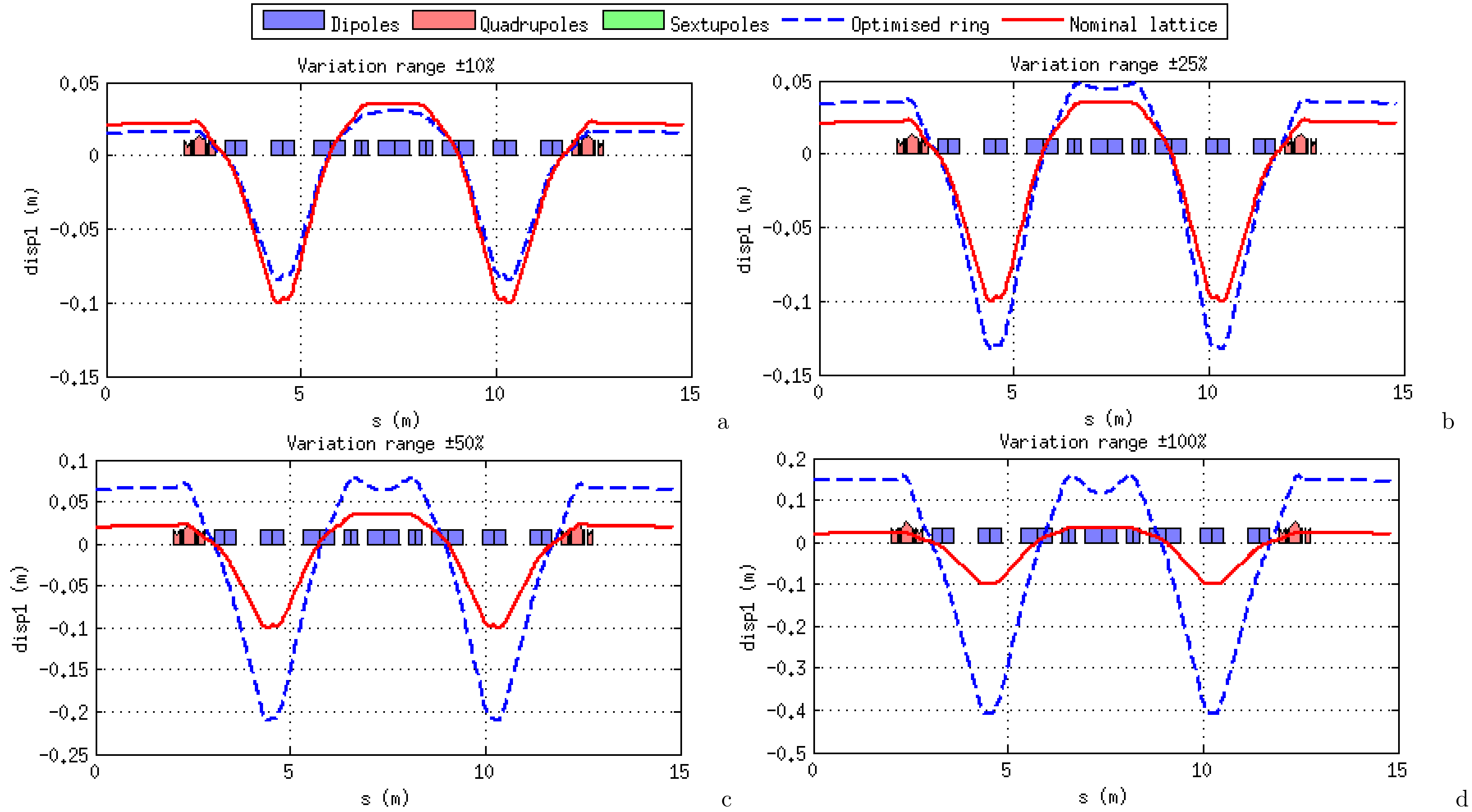

FIGURE 5.25: Comparison of the first-order dispersion of the optimised 5BA ring (in blue) with the nominal 5BA ring (in red), for different relative variations of the sextupole strengths: (a) ±10%, (b) ±25%, (c) ±50% and (d) ±100%.

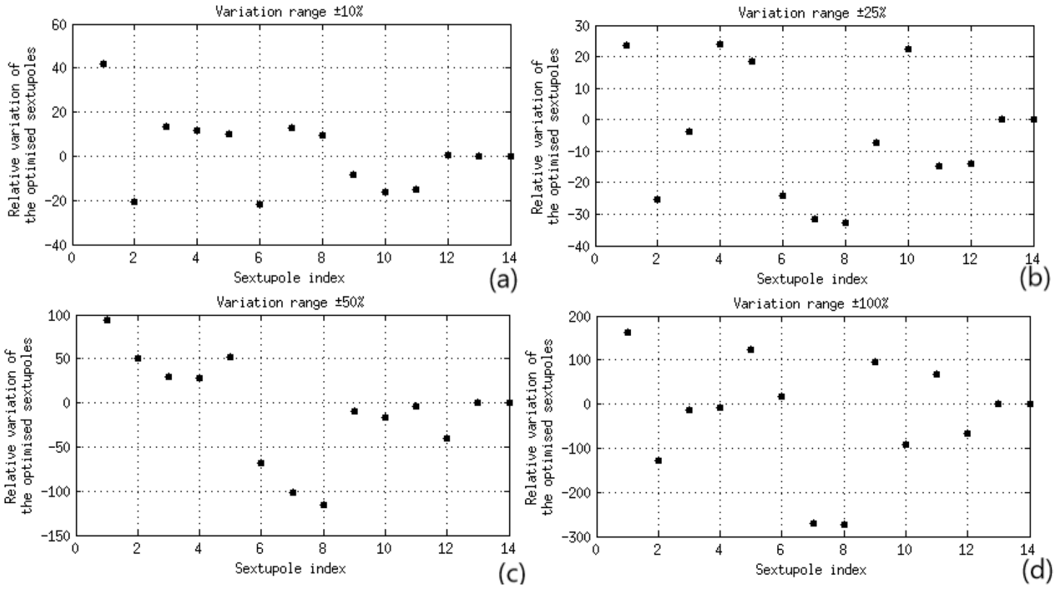

FIGURE 5.26: Comparison of the relative variation of the sextupole strengths of the optimised ring in the 5BA lattice case.

**Comparison of the longitudinal phase space** Figure 5.27 compares the longitudinal phase spaces of the obtained optimised rings with ±25%, ±50% and ±100% variations to the nominal lattice. The optimisation of ±10% variation is here ignored, as its effect on $\alpha_1$ was negligible, and no difference could be spotted in the longitudinal area.

The decrease of the first-order momentum compaction factor from (a) to (d) in Fig. 5.27 increases the ratio $\frac{\alpha_0}{\alpha_1}$ which defines the location of the first-order unstable fixed point (UFP) (*cf* section 5.2.3). Indeed, following the red point displayed on the graphs, which corresponds to the position of the first-order UFP, RF bucket size increases, up to a restored energy acceptance of $\delta \simeq -0.2$ for $\phi = 0$ in the case of the minimum achieved $\alpha_1$, in (d). This proves the feasibility of the method as a correction of the longitudinal stability.

**Tune shift with energy and nonlinear chromaticities of the optimised lattices** Nonetheless, the increase in the sextupole strengths perturb the transverse dynamics and tune shift with energy, since the optimisation do not take those parameters into account. The tune shift with energy of the different optimised lattices is displayed in Fig. 5.28. Contrary to the HOA lattice where the tune shift was clearly higher due to the increase in the sextupole strengths, the case of the 5BA lattice differs: the non-optimised lattice already had a low energy acceptance. Therefore, slight variations around the nominal sextupole strengths, of ±10%, increased the energy acceptance of the 5BA lattice, before dropping, just like the HOA lattice.

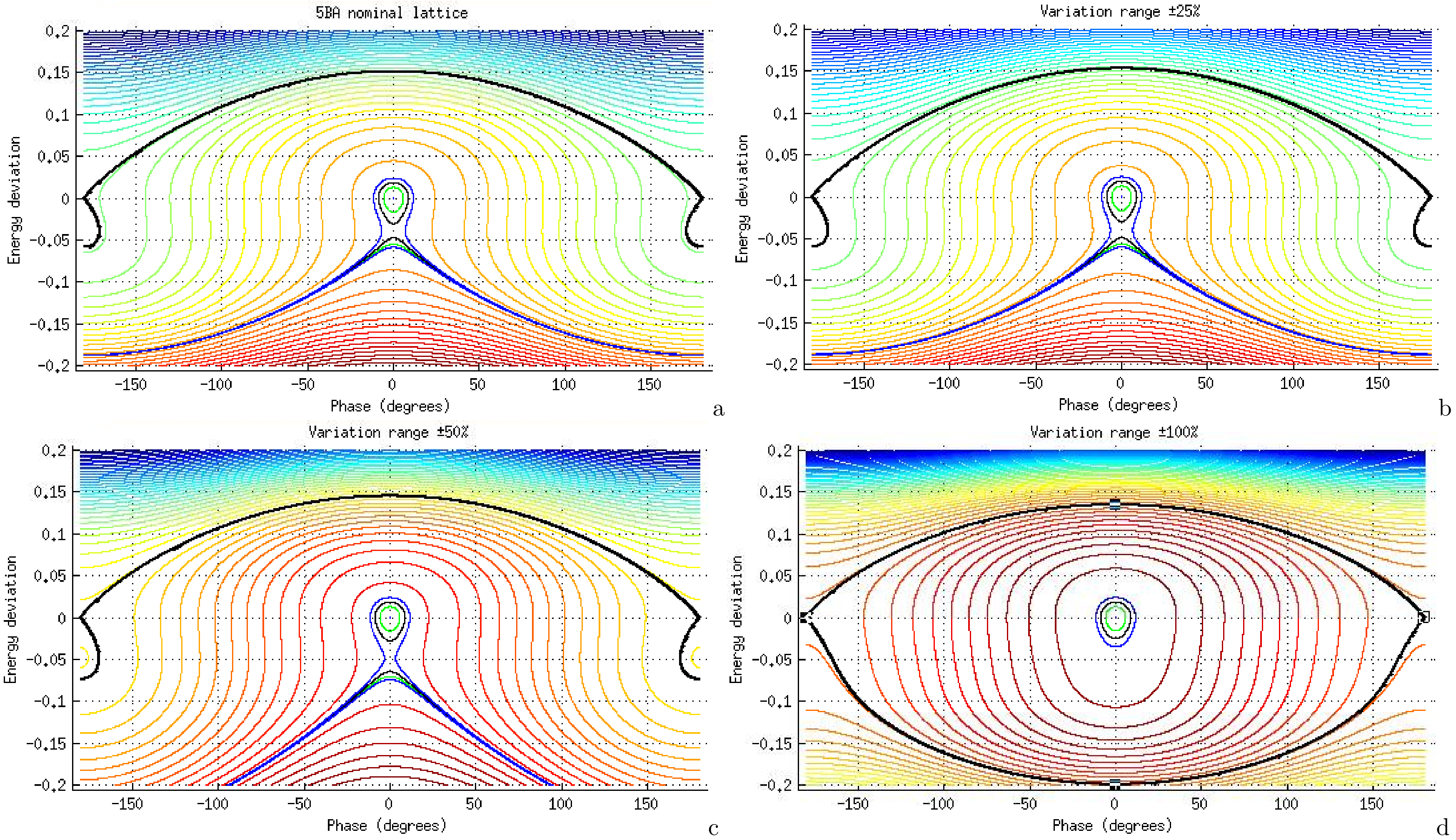

FIGURE 5.27: Comparison of the longitudinal phase spaces of the (a) nominal 5BA lattice and the optimised rings with different relative variations of the sextupole strengths (b) ±25%, (c) ±50%and (d) ±100%.

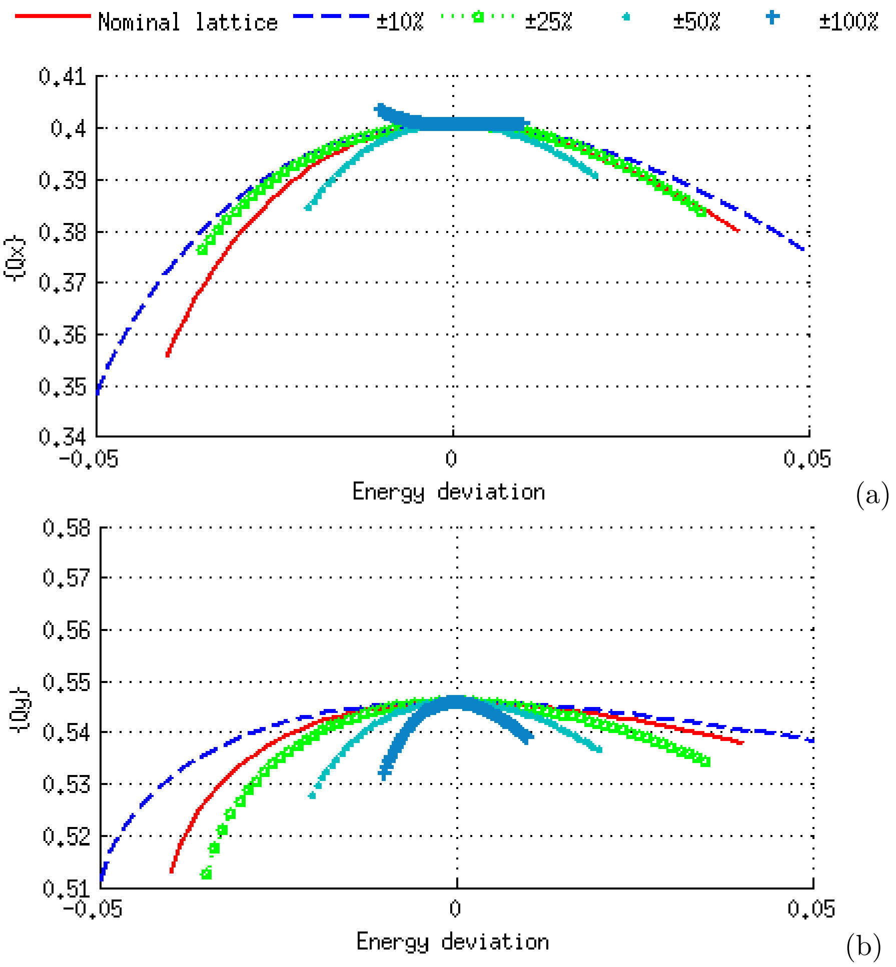

FIGURE 5.28: Comparison of tune shifts with energy of the 5BA rings optimised in $\alpha_1$ using the sextupoles: (a) in the horizontal plane and (b) in the vertical plane.

TABLE 5.6: Comparison of the nonlinear chromaticities along the fourth optimised periods of the 5BA lattice with different relative variations of the sextupole strengths.

| Chromaticities | Nominal lattice | 10% | 25% | 50% | 100% |
|---|---|---|---|---|---|
| $\xi_x^1$ | -0.00008 | -0.00008 | -0.00008 | -0.00008 | -0.0001 |
| $\xi_y^1$ | -0.00008 | -0.00008 | -0.00006 | -0.00008 | 0.008 |
| $\xi_x^2$ | -17.58 | -12.3771 | -14.4027 | -30.0621 | 12.0672 |
| $\xi_y^2$ | -7.580 | -4.9142 | -12.3745 | -27.9491 | -86.7052 |
| $\xi_x^3$ | 158.805 | 73.4288 | 37.9064 | 355.3708 | -1419.6 |
| $\xi_y^3$ | 105.926 | 55.0237 | 131.9646 | 375.1391 | 2412.8 |

### 5.4.3 Conclusion and prospects on this optimisation

This section proved the feasibility of the minimisation of $\alpha_1$ by optimising the strengths of the chromatic sextupoles. The proof of principle on the 5BA lattice showed a restoration of the longitudinal bucket and of the closed separatrix, as illustrated in Fig. 5.27 (d).

Overall, the efficiency of variation of $\alpha_1$ in such a scan remains inherently low, and depends on the lattice under scrutiny: indeed, lattices with a high number of strong magnets, such as the HOA 7BA lattice, would require a larger number of randomly generated rings to find adequate solutions. Moreover, the lack of constraints on the transverse dynamics and tune shift is problematic in high variations of the sextupoles, as the minimisation of $\alpha_1$ tends to highly increase the second- and third-order chromaticities, as well as increasing the sextupole strengths which shrinks the transverse stability areas. No other solution was envisioned at that time: as the influence of the sextupoles on the momentum compaction factor is indirect, the method of least squares could not be implemented, for instance. Moreover, the bounded generation of the sextupole strengths scans the map randomly, with no direction towards any good solution: the first-order momentum compaction factor is scanned around its nominal value, with no filter for higher values during the scan. Furthermore, the one-core calculation process of Matlab limits the number of rings to be scanned, and further optimisation processes: each scan of 1000 rings, with an analytical calculation of $D_1$ with $N = 1000$ Fourier harmonics for convergence took approximately 11 to 12h for the HOA 7BA lattice, 3 to 4h in the case of the 5BA, which dramatically reduces the accessibility of such an approach. The high calculation time is caused by the necessary slicing of the elements in each lattice, to increase the precision of the integrals for computation of the higher-order momentum compaction factor: the number of slices per element and the number of harmonics was chosen to offer a $10^{-3}$ precision on the calculation of the zeroth-order momentum compaction factor on the HOA lattice.

In order to limit the effect on the higher-order chromaticities and perhaps control both the longitudinal phase space and the transverse dynamic aperture, the already existing version of MOGA-Bmad was extended to include the minimisation of $\alpha_1$, which parallelisation and use in a cluster shall drastically decrease the calculation time as well.

## 5.5 Inclusion of the minimisation of $\alpha_1$ in MOGA-Bmad

As described in the section 4.1, MOGA-Bmad, developed by M. Ehrlichman is a multi-objective genetic algorithm which optimises the transverse on- and off-momentum dynamic aperture at a set point of electron storage ring lattices, while keeping the linear chromaticities constant. In the extended version adapted from MOGA-Bmad, the first-order momentum compaction factor should be minimised, whilst optimising the transverse dynamic apertures at three set energies.

### 5.5.1 Definition of the optimisation

To include the optimisation of $\alpha_1$ in the algorithm, it is necessary to increase the number of objective functions from 3 to 4, which needs to be carefully treated in the main file, 'moga.f90'. The longitudinal phase space can be optimised by two methods: either minimising $\alpha_1$ directly, with no other bottom limit than 0, or setting a maximum value for $\alpha_1$, which could force the optimisation into reducing $\alpha_1$ value.

**Minimisation of** $\alpha_1$ In the case of a simple minimisation, the fourth objective variable is defined as:

$$f_4(x) = \left| \frac{\alpha_1(x)}{\alpha_1^0} \right| \tag{5.47}$$

where $x$ corresponds to an individual in MOGA, *i.e.* a set of sextupole strengths, and $\alpha_1^0$ designates the first-order momentum compaction factor of the nominal ring. Contrary to the already defined objective functions in MOGA-Bmad, which are the relative variation of the dynamic aperture compared to the linear aperture, the fourth objective function introduced here can vary outside the $[0;1]$ range. Nonetheless, as the A.T. scan empirically confirms, the process of the minimisation of $\alpha_1$ will keep the objective function below 1. First steps in the MOGA extension used this minimisation objective. Nonetheless, first runs did not optimise the fourth objective, for the best solutions optimised the dynamic apertures only.

**Upper limit for** $\alpha_1$ To force the minimisation of $\alpha_1$, I introduced an upper limit, and a corresponding dominant constraint. The dominance constraint will make sure only individuals complying with the upper limit requirement will be considered feasible, forcing all results of the optimisation to have a minimised $\alpha_1$. The PISA_cfg file should be modified accordingly. The new objective function is defined according to the limit as:

$$f_4(x) = \begin{cases} \left| \frac{\alpha_1(x)}{\alpha_1^{max}} \right| & \text{if}\, \alpha_1(x) < \alpha_1^{max} \\ 1 & \text{otherwise} \end{cases} \tag{5.48}$$

with $\alpha_1^{max}$ the upper bound defined in the input file. By definition, the objective value here is comprised between 0 and 1, with 0 meaning a perfect value, where $\alpha_1 = 0$ and 1 meaning the constraint on the limit has not been satisfied.

#### 5.5.1.1 Analysis output

The analysis files that we were provided with thanks to M. Ehrlichman had to be adapted to take into account the fourth component: indeed, when the last generation is completed and evaluated, the user can manually select the individuals to be further analysed, by comparing the values of the objective functions in a python interactive figure, illustrated in Fig. 5.29.

The details of all changes and included scripts are available in the Appendix H. All scripts are available in my GitHub [136].

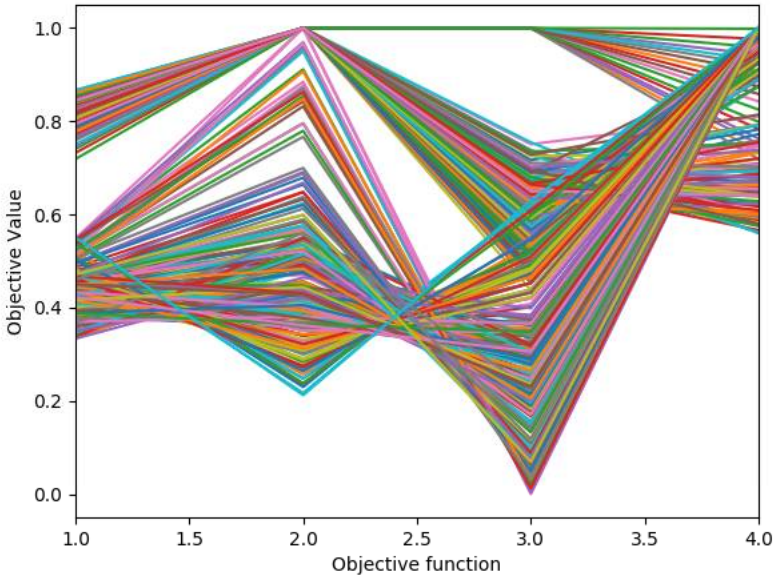

Figure 5.29: Example of the objective function values during an optimisation conducted on the 5BA lattice. The three first objective functions refer to the dynamic aperture at 0%, +1% and −1%. The fourth corresponds to the minimisation of the first-order momentum compaction factor.

### 5.5.2 Examples of the minimisation of $\alpha_1$ on an ultra-low emittance lattice

Following the tests conducted with A.T., and to compare both methods and their results, the optimisation process was tested with the 5BA lattice presented at the beginning of this chapter.

#### 5.5.2.1 Optimisation of $\alpha_1$ for the 5BA lattice

Since the 5BA lattice suffers from the effect of $\alpha_1$, the optimisation should aim at reducing its value below a certain level, which is defined with regards to $\alpha_0$ and the energy acceptance of the lattice. In the case of the 5BA lattice, the maximum stable energy deviation achieved at the synchronous phase is $\delta \simeq 0.09$. The unstable fixed points of the line $\delta = -\frac{\alpha_0}{\alpha_1}$ should therefore be located below $\delta < -0.15$ by symmetry. The corresponding value of $\alpha_1$ is $\simeq 1.4 \times 10^{-4}$, which represents a reduction of 73% compared to the nominal value. Since the results of the scan in 5.4.2.3 proved an $\alpha_1 = 4.5 \times 10^{-4}$ was enough to restore the RF bucket, this value was used in the following optimisation as an upper limit.

Adding this limit into the input file, the optimisation of the 5BA lattice was run along 20000 generations, each composed of 400 individuals. The chromaticities are kept constant at $(\xi_x, \xi_y) = (0, 0)$, to better compare with the A.T. scan. The sextupoles are inserted in the lattice as thin lenses, and are treated amongst their families, which corresponds to a total of seven variables: five chromatic families and two harmonic families. The sextupoles are treated individually within a half a period, thus each family is composed of two sextupoles, at symmetric positions in the lattice. To increase their efficiency, focusing sextupoles are inserted in between secondary dipoles, which are reverse bends, as thin lenses. The strengths of the chromatic sextupoles is varied in the range $\pm 600\,\mathrm{m}^{-2}$, the harmonics as well. Octupoles were added near the location of the sextupoles, and were set at $\pm 10000\,\mathrm{m}^{-3}$. Figure 5.30 locates the optimisation variables on the lattice.

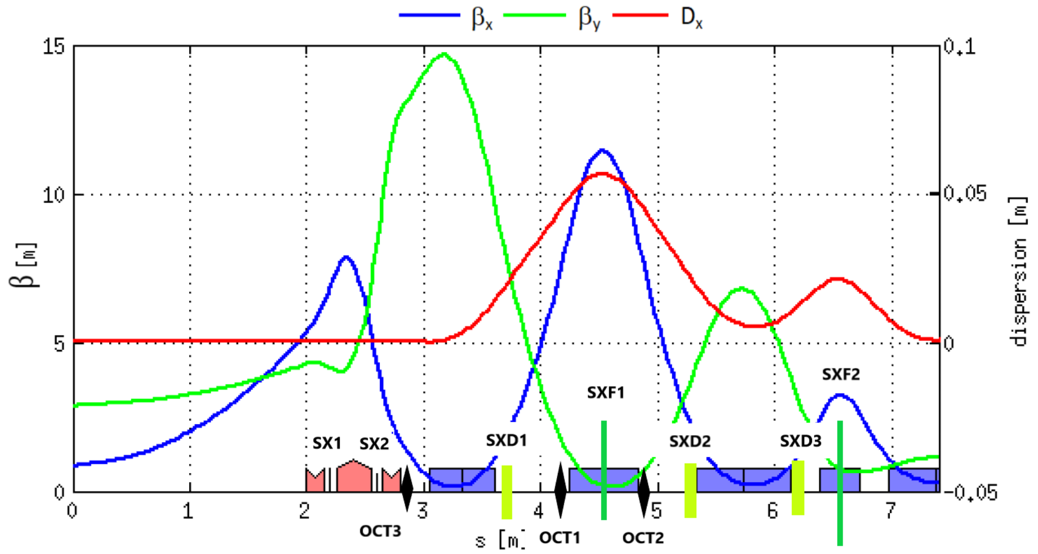

FIGURE 5.30: Variables of the $\alpha_1$ optimisation of the 5BA lattice.

### 5.5.2.2 Selection of the individuals and results

Figure 5.31 displays the values of the objective functions of the last generation. Each line corresponds to a single individual. The optimisation was conclusive, as the fourth objective function, related to $\alpha_1$, is lower than 1 in several cases. Nonetheless, the lowest DA-related objective functions correspond to a fourth objective around 1. To compare the different cases, I selected six individuals, three with a fourth objective around 1, and different dynamic aperture functions sets, and three with minimised $\alpha_1$. Their functions and names are displayed in Fig. 5.31 (b).

Table 5.7 lists the values of both the first- and second-order momentum compaction factors, for the selected individuals. The relative variation with regard to the nominal value (R.V.N.) is calculated. Out of the selected individuals, all values are below the upper limit $4.5 \times 10^{-4}$, which corresponds to a minimum reduction of $\alpha_1$ of 16%.

To ease the reading, only the frequency map analysis of two selected individuals are presented. The analysis of the other selected individuals is available in the Appendix I. The following analysis correspond to the individuals 3968943, which achieved the minimum $\alpha_1$, and 3964698, which achieved the larger dynamic apertures. Figure 5.32 compares the frequency map analysis on-momentum and at ±1% energy deviation of both individuals. They are compared to a typical result of an on-momentum and ±1% optimisation using MOGA-Bmad and the same set of sextupoles as variables.

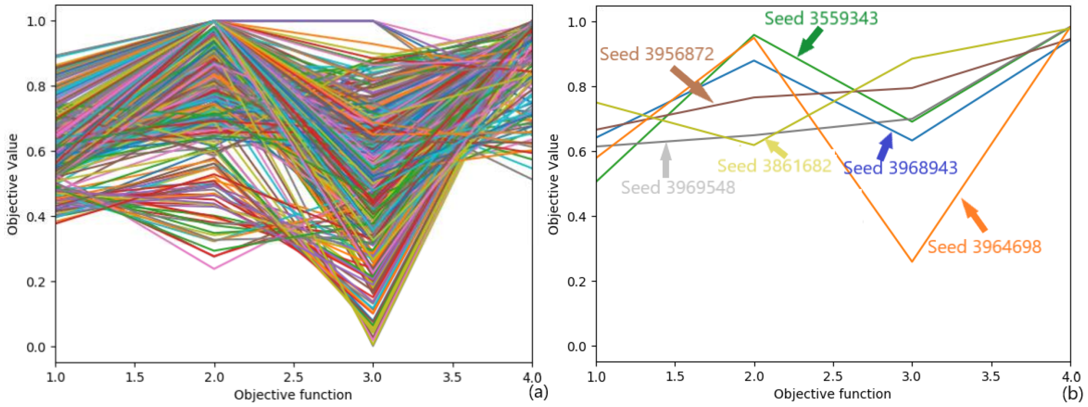

FIGURE 5.31: Variations of the objective functions (a) of the last generation and (b) if the selected individuals.

TABLE 5.7: Variation of the first- and second-order momentum compaction factors in the selected seeds of the 5BA SOLEIL lattice optimisation.

| Seed | $\alpha_1$ | R.V.N. | $\alpha_2$ |
|---|---|---|---|
| 3559343 | $4.4226 \times 10^{-4}$ | $-17.2\%$ | $4.9418 \times 10^{-3}$ |
| 3861682 | $4.4065 \times 10^{-4}$ | $-17.5\%$ | $5.4429 \times 10^{-3}$ |
| 3956872 | $4.2588 \times 10^{-4}$ | $-20.3\%$ | $6.4076 \times 10^{-3}$ |
| 3964698 | $4.4234 \times 10^{-4}$ | $-17.2\%$ | $4.9539 \times 10^{-3}$ |
| 3968943 | $4.2472 \times 10^{-4}$ | $-20.5\%$ | $6.8370 \times 10^{-3}$ |
| 3969548 | $4.4294 \times 10^{-4}$ | $-17.1\%$ | $5.5226 \times 10^{-3}$ |

The dynamic apertures of the three rings are similar, despite a limited transverse acceptance in the seed 3968943. The seed 3964698, which corresponds to the FMA at the right side of Fig. 5.32, presents a slightly lower transverse acceptance than the result of the on-momentum optimisation alone, but the results are still comparable. Table 5.8 compares the strengths of the sextupoles and octupoles of the selected seeds.

TABLE 5.8: Strengths of the 5BA optimisation variables, for the selected seeds.

| Name | Seed 3968943 | Seed 3964698 |
|---|---|---|
| sxd1 | $-64.41\,\mathrm{m}^{-2}$ | $-97.97\,\mathrm{m}^{-2}$ |
| sxf1 | $79.17\,\mathrm{m}^{-2}$ | $77.34\,\mathrm{m}^{-2}$ |
| sxd2 | $-35.62\,\mathrm{m}^{-2}$ | $-62.54\,\mathrm{m}^{-2}$ |
| sxf2 | $-95.49\,\mathrm{m}^{-2}$ | $-77.80\,\mathrm{m}^{-2}$ |
| sxd3 | $-455.77\,\mathrm{m}^{-2}$ | $-290.58\,\mathrm{m}^{-2}$ |
| sx1 | $232.73\,\mathrm{m}^{-2}$ | $162.7\,\mathrm{m}^{-2}$ |
| sx2 | $-193.69\,\mathrm{m}^{-2}$ | $-151.4\,\mathrm{m}^{-2}$ |
| oct1 | $9966\,\mathrm{m}^{-3}$ | $9831\,\mathrm{m}^{-3}$ |
| oct2 | $9968\,\mathrm{m}^{-3}$ | $9591\,\mathrm{m}^{-3}$ |

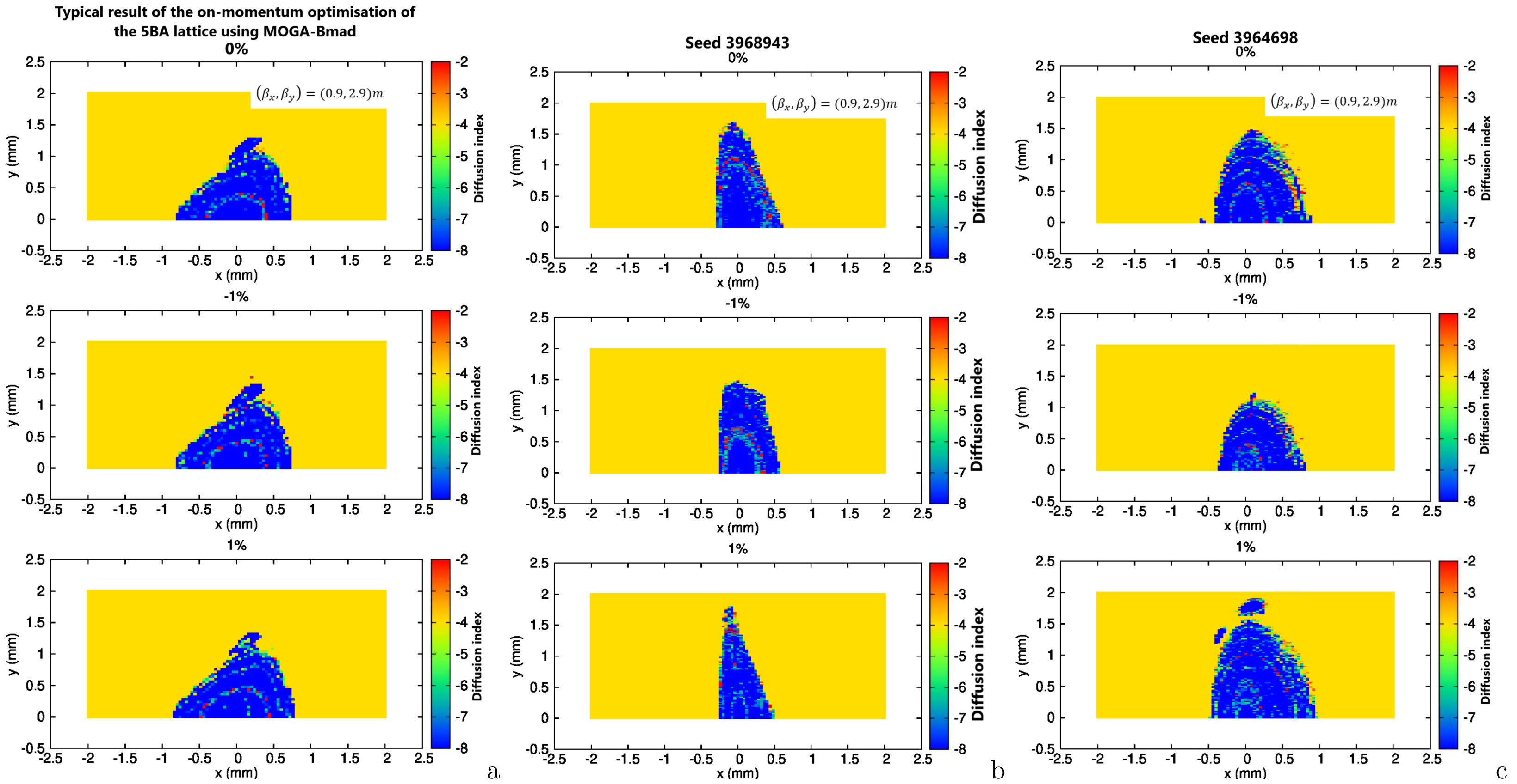

FIGURE 5.32: Frequency map analysis of (a) a typical result of an on-momentum and ±1% MOGA-Bmad optimisation of the 5BA lattice, (b) seed 3968943, of $\alpha_1 = 4.2472 \times 10^{-4}$ and (c) seed 3964698 of $\alpha_1 = 4.4234 \times 10^{-4}$.

#### 5.5.2.3 Comparison of the longitudinal phase spaces before and after the optimisation

To further analyse the results of the conducted optimisation, Fig. 5.33 compares the contours of equal Hamiltonian energy, defining the separatrix, in the longitudinal plane $(\phi, \delta)$ before and after the optimisation of the 5BA lattice. The right figure corresponds to the seed 3964698, of maximised dynamic apertures.

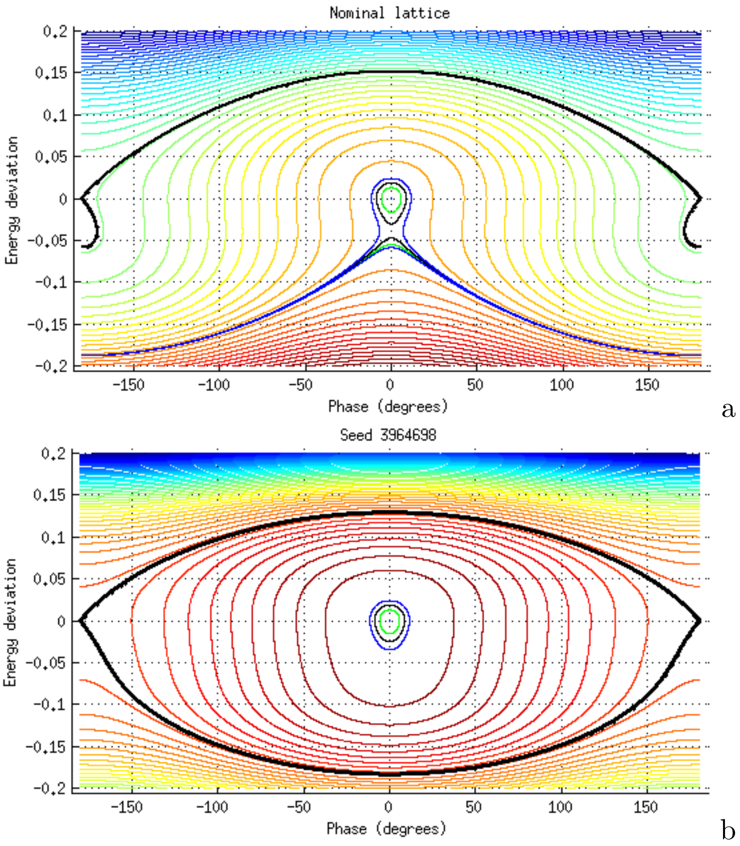

FIGURE 5.33: Comparison of the longitudinal phase spaces for the 5BA lattice (a) before and (b) after the MOGA optimisation, seed 3964698.

The RF bucket of the 5BA lattice is restored in the seed 3964698, with an energy acceptance of $-0.18/+0.13$. As expected, the use of MOGA for such an optimisation proved to be more efficient than the A.T. scan used in the previous section, both in terms of minimisation of $\alpha_1$ and the optimisation of the transverse dynamic apertures.

## 5.6 Conclusion

In this chapter, we explored different means to control the longitudinal phase space. The analytical calculation of the higher-order dispersion following [131] allowed the precise evaluation of the three lowest-orders of the momentum compaction factor and a more precise display of the longitudinal phase space. Although the extraction of the three-lowest orders from the chromatic closed orbit proved to be enough for third-generation storage ring lattices, the ultra-low emittance lattices experience a reduced energy acceptance, which can alter the results of the polynomial fit applied on the tracked pathlength.

Different methods were employed to minimise the destructive effect of $\alpha_1$ on the longitudinal area. The first, proposed by Maher Attal, aimed at increasing $\alpha_2$ with the use of the octupoles, to compensate for $\alpha_1$. Although this method worked theoretically, the required octupole strength were too high: they required long octupoles, for which ultra-low emittance lattices lack space.

To avoid the use of strong octupoles, different methods were investigated to target $\alpha_1$ in the after-design process. a script in A.T. scanned the sextupoles strengths with a defined range and with constant chromaticities, and calculates the first-order momentum compaction factor of each sextupole set. The scan proved the possibility of reducing $\alpha_1$ by changing the sextupole strengths. It lowered it by 2% in the case of the HOA 7BA lattice, at the price of strong sextupoles - one reached three times its nominal value. Furthermore, the calculations of the higher-order dispersion and the momentum compaction factor in A.T. requires to manipulate large vectors, as the ring is sliced to increase the precision of the integral summation. The time required for a 1000 scanned rings varied between 11 to 12h. The need of parallelisation motivated the translation of the scripts into Bmad, and the addition of the optimisation of $\alpha_1$ as an objective to the existing MOGA-Bmad.

The addition of a fourth objective into MOGA-Bmad allowed both the optimisation of the transverse dynamics and the restoration of the RF bucket. Two methods were implemented: a simple minimisation on the image of the A.T. scan, which was tested on the HOA lattice, and the implementation of an upper limit and corresponding dominant constraint, which was used on the 5BA lattice. First results on the 5BA lattice conserved the on-momentum dynamic aperture, while decreasing the first-order momentum compaction factor by 20%. The decrease in $\alpha_1$ was combined with an increase in $\alpha_2$, which completely restored the longitudinal stability area. Although this optimisation included octupoles for control of the tune shift, it can be done without: the constructive effect of $\alpha_2$ will less impact the shape of the longitudinal phase space.

Further methods could include the three lowest-orders of the momentum compaction factor, using the ratio $\frac{\alpha_0\alpha_2}{\alpha_1^2}$ described in section 5.2.5.1. Yet, the extraction of a condition was not trivial with the second-order Hamiltonian: no clear link between the three lowest-orders momentum compaction factor and the RF bucket size and area were found analytically. Moreover, the calculation of $\alpha_2$ could not be confirmed by the tracking or any other method. Therefore the extension focussed on reducing $\alpha_1$.

# Chapter 6

# Study of the distorted trajectory in ultra-low emittance lattices with different chromatic schemes

## 6.1 Description of the phenomenon

The correction of the two transverse chromaticities in the ultra-low emittance lattices generally requires the use of stronger sextupoles than in the third generation storage rings. The dynamic aperture of such lattices is dramatically reduced by the tight focusing schemes and the prominence of stronger resonances. Different schemes were developed in the literature to compensate the effect of the strong sextupoles in the fourth-generation lattices: two were studied in the present thesis: the hybrid scheme, first designed and implemented for the ESRF-EBS storage ring, and the HOA scheme, used in the exploration of the ALS-U and SLS-II upgrades for instance.

The hybrid lattice has all its sextupoles located under two dispersion bumps, in between which fixed betatron phase advances cancel the symmetric sextupolar kicks, or, in the case of the SOLEIL lattice, compensate them. Such a scheme maximises the on-momentum dynamic aperture, where the sextupolar kicks are cancelled. The rapid variation of the optics with the energy deviation induces a variation in the fixed phase advances: the non-interleaved principle is no longer valid. In that case, the off-momentum stability area is reduced to around a quarter of the on-momentum transverse stable area.

Fig 6.1 displays the evolution of the horizontal stability range with the energy deviation, with and without a RF cavity, for the SOLEIL 20-fold symmetry 7BA hybrid lattice [137]. In the presence of a RF cavity, on-momentum particles with a large betatron amplitude start synchro-betatron oscillations, possibly making those particles fall outside the stability area. Such a phenomenon reduces the effective on-momentum transverse dynamic aperture to the size of the off-momentum aperture. A comparison of the on-momentum transverse dynamic aperture with and without a RF cavity is displayed

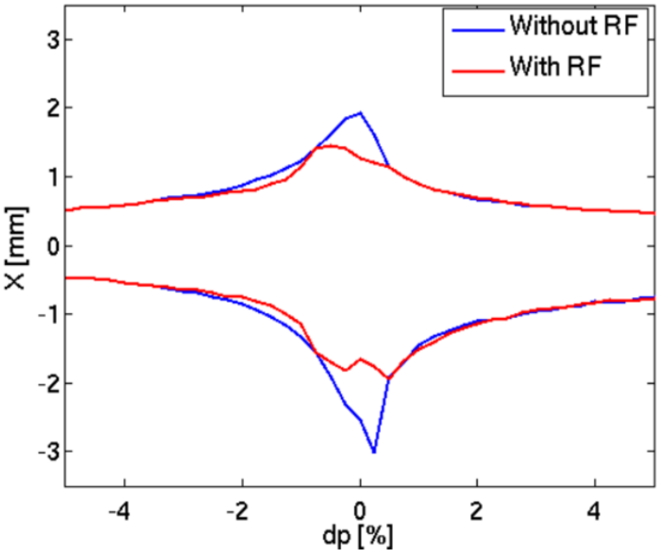

FIGURE 6.1: Variation of the horizontal dynamic aperture with the momentum deviation without (in red) and with the inclusion of RF cavities (in blue) of the SOLEIL 7BA hybrid lattice. From [137].

in Figure 6.2. The stability area is reduced by more than 50% when the RF cavity is included.

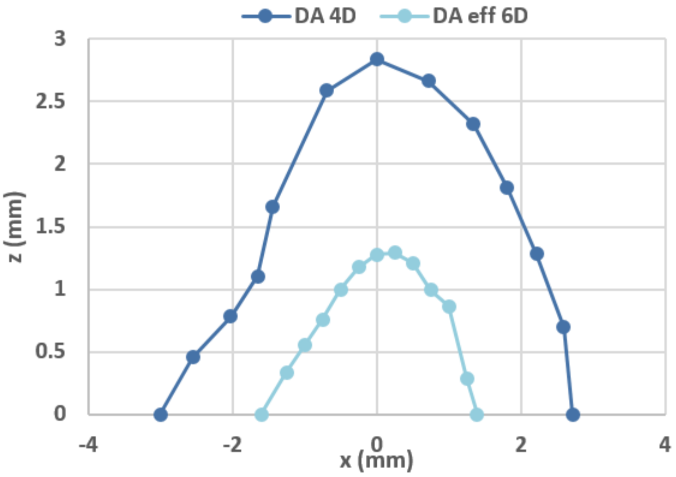

FIGURE 6.2: Transverse dynamic apertures using 4D tracking in dark blue, and 6D tracking in light blue. The strong reduction of the dynamic aperture is linked to synchro-betatron oscillations, moving the particles both in the transverse and longitudinal plane.

As a link between the transverse and the longitudinal motions, the path length of the hybrid lattice was tracked. The path length $\Delta C$ is expressed in terms of the transverse coordinates as:

$$\Delta C = \int_0^{C_0} ds \left( -hx + \frac{x'^2 + y'^2}{2} \right) \tag{6.1}$$

with $\Delta C$ the path length, $C_0$ the length of the reference particle trajectory, $-h = \frac{1}{\rho}$ the curvature of bending magnets and $(x, x', y, y')$ the coordinates of the transverse planes. Another formula links the path length $\Delta C$ to the chromaticities, and is easier to use for comparison studies:

$$\Delta C = -2\pi \left(J_x \xi_x + J_y \xi_y\right) \tag{6.2}$$

with $J_{x,y}$ the action variables, and $\xi_{x,y}$ the chromaticities. The path length is followed, after one turn, for different amplitudes. There, it is averaged over the phase to be compared to both Eq. (6.1) and Eq. (6.2). Fig. 6.3 compares the path length versus the normalised amplitude for three lattices; the SOLEIL 7BA HOA lattice (in blue), the SOLEIL hybrid lattice (in green), and the ESRF-EBS hybrid lattice (in blue stars). As a reference, the chromatic path length of Eq. (6.2) is plotted in red. All lattices were appointed to a $(1, 1)$ chromaticity, for optimum comparison.

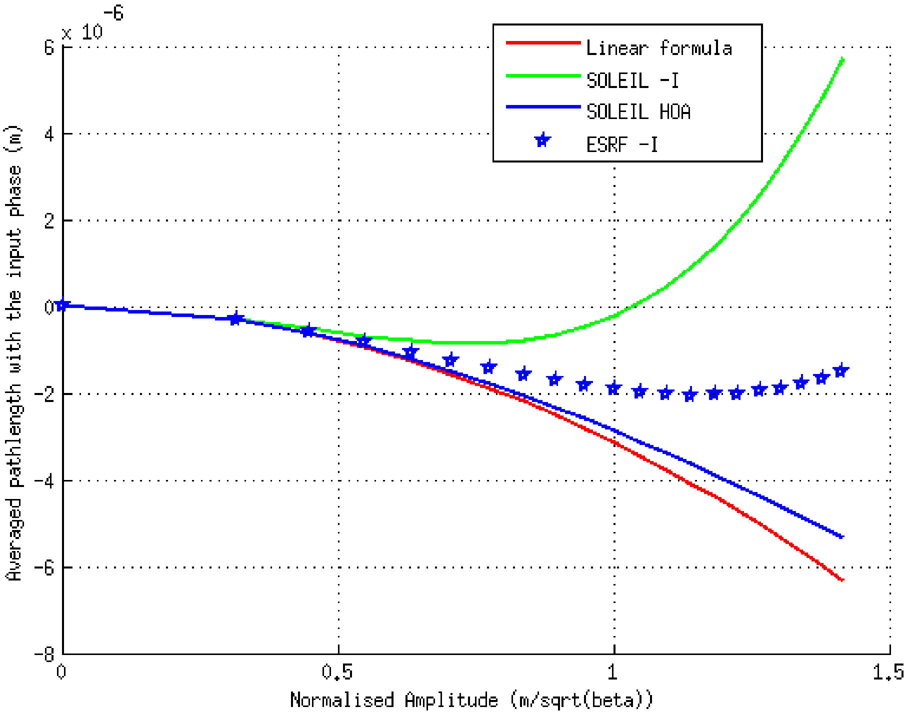

FIGURE 6.3: Comparison of the variation of path length with normalised amplitude for three lattices at a (1,1) chromaticity. The usual variation of the path length with chromaticity from Eq. (6.2) is drawn in red. The blue line is the SOLEIL 7BA HOA lattice (3.12, the green line the SOLEIL 7BA hybrid lattice (3.1), the blue stars the ESRF-EBS lattice.

While the HOA 7BA lattice remains close to the expected path length described by the chromatic expression and displayed in red in the figure, the hybrid lattices present a strong deviation of their path length from the expected curve given by Eq. (6.2), with an inversion of the expected tendency which is, in the current chromaticities, a constant decrease of the path length versus the amplitude, starting at medium amplitudes. The variations are larger and positive in the case of the SOLEIL hybrid lattice: indeed, the tighter lattice, with 20 cells in 354 m, versus (30+2) cells in 844 m in the ESRF-EBS case, and the lower nominal energy of the storage ring (2.75 versus 6 GeV) require stronger magnets and induce stronger nonlinearities in the lattice, thus creating a higher dependency of the path length on the transverse amplitude. Table 6.1 gathers the $\beta$-functions at the middle of the straight section for the three lattices under scrutiny, which allows conversion from normalised amplitude to the horizontal amplitude.

Table 6.1: $\beta$-functions at the middle of the straight sections for the three lattices compared in Fig. 6.3.

| | SOLEIL HOA 7BA | SOLEIL HYB 7BA | ESRF EBS |
|---|---|---|---|
| $\beta_x$ | 2.7 m | 1.0 m | 6.9 m |
| $\beta_y$ | 2.7 m | 1.0 m | 2.6 m |

This chapter explores the efforts made to describe and minimise this phenomenon in the SOLEIL 7BA hybrid lattice. Focusing on the path length, which links the transverse and the longitudinal motions, the dimension of the phase space under study is reduced from 6 to 2, only considering the horizontal amplitude and its derivative. The effect of the sextupoles on the path length is derived thanks to the first-order canonical perturbation theory. To recover the on-momentum dynamic aperture of the hybrid lattice, an optimisation program is written to reduce the contribution of the sextupole magnets to the perturbed trajectory.

## 6.2 Evaluation of the path length for different hybrid lattices

To understand the existence of such a phenomenon in the hybrid lattices, a perfect non-interleaved hybrid lattice is designed. It consists in removing all sextupoles which are not located under the dispersion bump, harmonic sextupoles included in the compared lattices, and only introducing two thin sextupole families under the bump, for chromaticity correction. In that case, the non-interleaved principle is strictly respected, for the focusing sextupoles only. The resulting variation of the path length with the horizontal amplitude is displayed in Fig. 6.4, and compared to the nominal lattice with and without octupoles.

The difference between the perfect non-interleaved lattice and the nominal SOLEIL 7BA lattice is anecdotal. Furthermore, the addition of octupoles in the lattice slightly changes the path length, but does not influence its general variation. In conclusion, the number of nonlinear magnets do not appear to play an important role in the variation of the path length.

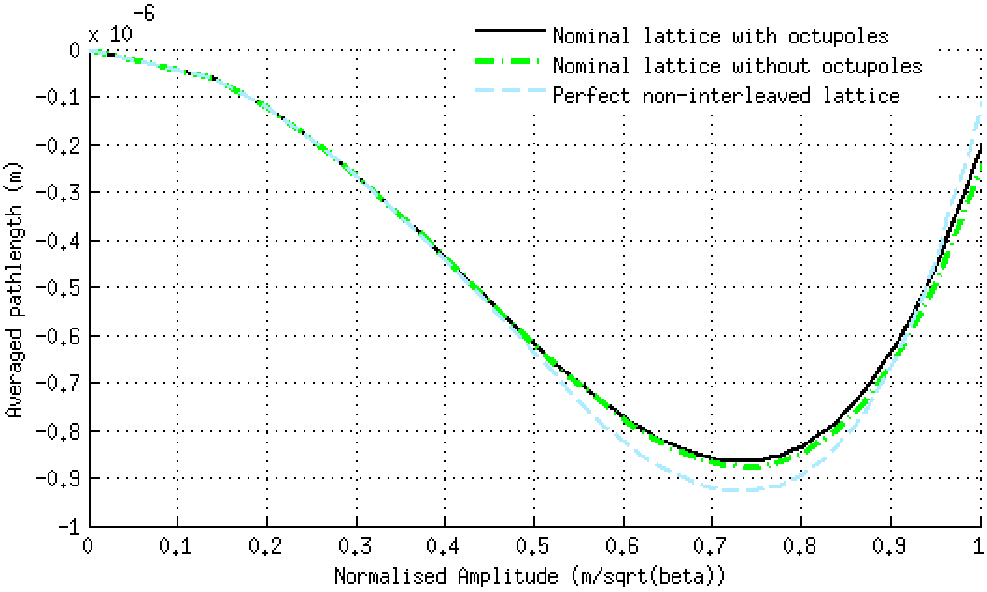

FIGURE 6.4: Comparison of the path length variation with the normalised horizontal amplitude for a perfect hybrid lattice (in dotted blue lines), the nominal hybrid lattice without (dashed green) and with the octupoles (black). All lattices were set to $(\xi_x, \xi_y) = (1, 1)$ chromaticities.

## 6.3 First-order canonical perturbation theory

The investigation of the phenomenon continued with a paper of M. Takao, [138], where he derives the effect of the perturbation of the sextupoles on the transverse motion: the averaged horizontal amplitude trajectory was derived and as such, the path length. Following this paper, the first-order canonical perturbation theory was applied to increase the order of derivation in the path length; where Takao derived the perturbed transverse amplitude, the perturbation of the horizontal deviation was expressed by the sextupoles following the same method. The aim of this section is to derive the path length below in terms of sextupole perturbation, following Takao's derivation steps. The path length $\Delta C$, averaged on the transverse phases, is expressed as:

$$\langle \Delta C \rangle_{(\phi_x, \phi_y)} = \int_0^{C_0} ds \left( k_x \langle x \rangle_{\phi_x} + \frac{\langle x'^2 \rangle_{\phi_x} + \langle y'^2 \rangle_{\phi_y}}{2} \right) \tag{6.3}$$

In [138], the derivation was completed for the horizontal amplitude only. This section attempts to derive the first-order perturbed horizontal deviation $x'$ as well. To limit the equations and long derivations, the study is conducted for a purely horizontal motion. The derivations for the vertical plane are available in the Appendix J.

### 6.3.1 Hamiltonian and canonical perturbation theory

The purely transverse Hamiltonian considered for this study is, following [138]:

$$H = \frac{p_x^2 + p_y^2}{2} + \frac{1}{2}(h^2 + k_1)x^2 - \frac{1}{2}k_1 y^2 + \frac{k_2}{3}(x^3 - 3xy^2) - \frac{1}{2}hx(p_x^2 + p_y^2) \tag{6.4}$$

with $k_1$ and $k_2$ the strengths of the quadrupoles and sextupoles respectively, and $h = -\frac{1}{\rho}$ the bending curvature. The Hamiltonian can be split into $H = H_0 + V$, where $H_0$ is the linear Hamiltonian, describing the unperturbed betatron motion as described in the section 2.1.1, and $V = \frac{k_2}{3}(x^3 - 3xy^2) + \frac{1}{2}k_x x(p_x^2 + p_y^2)$ the effect of sextupoles and bending distortion. The effect of the sextupoles on the transverse dynamics were previously described through the excitation of resonances (*cf* sec. 2.1.3). In this section, this Hamiltonian will serve to derive the effect of the sextupolar kicks on the transverse motion.

Switching the coordinates to the canonical variables $(\phi, J)$, the perturbation can be described through the sum $V(\phi, J, s) = \sum_{n>0} V_n(\phi, J, s)e^{in\phi}$. The term-to-term perturbation $V(\phi, J, s)$ is, in the case of Eq. (6.4):

$$\begin{aligned} V(\phi, J, s) = & \frac{J_x^{3/2}\beta_x^{1/2}}{\sqrt{2}}(k_2\beta_x)\cos(\phi_x) + \frac{J_x^{3/2}\beta_x^{1/2}}{3\sqrt{2}}(k_2\beta_x)\cos(3\phi_x) \\ & - \frac{J_x^{1/2}J_y\beta_x^{1/2}}{\sqrt{2}}(k_2\beta_y)\cos(\phi_x) - \frac{J_x^{1/2}J_y\beta_x^{1/2}}{2\sqrt{2}}(k_2\beta_y)\cos(\phi_x + 2\phi_y) \\ & - \frac{J_x^{1/2}J_y\beta_x^{1/2}}{2\sqrt{2}}(k_2\beta_y)\cos(\phi_x - 2\phi_y) + \frac{J_x^{3/2}\sqrt{\beta_x}}{\sqrt{2}}k_x\gamma_x\cos(\phi_x) \\ & + \frac{J_x^{1/2}J_y\sqrt{\beta_x}}{\sqrt{2}}k_x\gamma_y\cos(\phi_x) + \frac{J_x^{3/2}}{\sqrt{2\beta_x}}k_x(\alpha_x^2 - 1)\left(\cos(\phi_x) + \cos(3\phi_x)\right) \\ & + \frac{J_x^{1/2}J_y\sqrt{\beta_x}}{\sqrt{2}\beta_y}k_x(\alpha_y^2 - 1)\left(\cos(\phi_x + 2\phi_y) + \cos(\phi_x - 2\phi_y)\right) \\ & + \frac{J_x^{3/2}}{\sqrt{2\beta_x}}k_x\alpha_x\left(\sin(\phi_x) + \sin(3\phi_x)\right) \end{aligned} \tag{6.5}$$

Gathering the terms of the same harmonic, the perturbation can be split into three parts: a perturbation $V_1(\phi, J, s)$ of simple harmonic of $\phi_x$, a perturbation $V_3(\phi, J, s)$ corresponding to the third harmonic of $\phi_x$, and a perturbation $V_{1,2}(\phi, J, s)$ combining both the vertical and the horizontal planes through $\phi_x$ and $2\phi_y$:

$$\begin{aligned}
V_1(\phi, J, s) &= \frac{J_x^{3/2}\sqrt{\beta_x}}{\sqrt{2}}\left(k_2\beta_x + k_x\gamma_x\right)\cos(\phi_x) + \frac{J_x^{1/2}J_y\sqrt{\beta_x}}{\sqrt{2}}\left(-k_2\beta_y + k_x\gamma_y\right)\cos(\phi_x) \\
&+ \frac{1}{\sqrt{2\beta_x}}J_x^{3/2}k_x\alpha_x\left(\sin(\phi_x) + \alpha_x\cos(\phi_x)\right) - \frac{1}{\sqrt{2\beta_x}}J_x^{3/2}k_x\cos(\phi_x) \\
V_3(\phi, J, s) &= \frac{J_x^{3/2}\sqrt{\beta_x}}{3\sqrt{2}}k_2\beta_x\cos(3\phi_x) + \frac{1}{\sqrt{2\beta_x}}J_x^{3/2}k_x\alpha_x\left(\sin(3\phi_x) + \alpha_x\cos(3\phi_x)\right) \\
V_{1,2}(\phi, J, s) &= \frac{1}{2\sqrt{2}}J_x^{1/2}J_y\sqrt{\beta_x}\left(-k_2\beta_y + \frac{k_x}{\beta_y}(\alpha_y^2 - 1)\right)\cos(\phi_x \pm 2\phi_y)
\end{aligned} \tag{6.6}$$

Following Takao's paper on nonlinear chromaticity [139], one builds the action-angle variable $(\overline{\phi}, \overline{J})$ which verify $\frac{dJ}{ds} = \text{cst}$ in the perturbed space. For this purpose, we introduce the canonical transformation $S(\phi, \overline{J}, s) = \phi\overline{J} + S_1(\phi, \overline{J}, s)$, resulting in the Hamiltonian:

$$\overline{H}(\overline{J}, s) = H_0(\overline{J}, s) + K_1(\overline{J}, s) \tag{6.7}$$

which is independent of $\phi$ thanks to the choice of $S_1$. For space reasons and to ease the reading, the complete expression of $S_1$ is written in the Appendix J.

### 6.3.2 Perturbed averaged horizontal trajectory

The overall link between the transverse plane $(x, p_x)$ to the canonical perturbed plane is described by the following relationship:

$$(x, p_x) \longrightarrow_{G_1(x,\phi,s)} (\phi, J) \longrightarrow_{S(\phi,\overline{J},s)} (\overline{\phi}, \overline{J}), \tag{6.8}$$

where $G_1(x, \phi, s) = -\frac{x^2}{2\beta_x}\left(\tan(\phi) - \frac{\beta_x'}{2}\right)$ the generating function between $(x, p_x)$ and $(\phi, J_x)$, and $S$ the perturbed generating function, restoring a canonical system, defined in the previous section. Expressing the perturbed action angle $J_x$ using both generating functions $G_1$ and $S$, the following equality, involving $x$, $\phi_x$ and $\overline{J}$, is obtained:

$$-\frac{\partial G_1}{\partial \phi_x} = \frac{\partial S}{\partial \phi_x} \iff \frac{x^2}{2\beta_x(\cos(\phi_x))^2} = \overline{J} + \frac{\partial S_1}{\partial \phi_x} \tag{6.9}$$

The sign of the betatron amplitude is determined by the cosine of the betatron phase advance. Assuming a positive sign, one can extract the horizontal amplitude $x$ from Eq. 6.9. Its expression with the perturbed angle $\overline{J}$ is linearised to the first-order in the perturbation derivative:

$$x = \sqrt{2\overline{J}\beta}\cos(\phi)\sqrt{1 + \frac{1}{\overline{J}}\frac{\partial S_1}{\partial \phi_x}} \simeq \sqrt{2\overline{J}\beta}\cos(\phi)\left(1 + \frac{1}{2\overline{J}}\frac{\partial S_1}{\partial \phi_x} + ...\right) \tag{6.10}$$

Since the perturbation is considered small for small amplitudes, the square-root can be Taylor expanded. This section only focuses on the first-order of the perturbation.

Then, only the two first terms of the development are considered in the following derivations. The above equation is expanded by including the expression of the derivative of the perturbed generation $S$ derived with respect to the betatron phase advance $\phi_X$ in J. The perturbed horizontal trajectory $x$ to the first-order in perturbation is expressed as a sole function of $(\phi_x, \overline{J})$, according to:

$$\begin{aligned}
x = {} & \sqrt{2\overline{J}\beta}\cos(\phi) + \frac{J_x\sqrt{\beta_x}}{4\sin(\pi\nu_x)}\int_s^{s+C} ds' k_x\beta_x^{-1/2}\cos(\phi_x)\cos(\phi_x+\overline{\psi}(s',s)) \\
& - \frac{J_y\sqrt{\beta_x}}{4\sin(\pi\nu_x)}\int_s^{s+C} ds'\sqrt{\beta_x}\,(-k_2\beta_y+k_x\gamma_y)\cos(\phi_x)\cos(\phi_x+\overline{\psi}(s',s)) \\
& - \frac{J_x\sqrt{\beta_x}}{4\sin(\pi\nu_x)}\int_s^{s+C} ds'\sqrt{\beta_x}\,(k_2\beta_x+k_x\gamma_x)\cos(\phi_x)\cos(\phi_x+\overline{\psi}(s',s)) \\
& - \frac{J_x\sqrt{\beta_x}}{2\sin(\pi\nu_x)}\times \\
& \int_s^{s+C} ds' k_x\beta_x^{-1/2}\alpha_x\cos(\phi_x)\Big(\sin(\phi_x+\overline{\psi}(s',s))+\alpha_x\cos(\phi_x+\overline{\psi}(s',s))\Big) \\
& - \frac{J_x\sqrt{\beta_x}}{4\sin(3\pi\nu_x)}\int_s^{s+C} ds'\sqrt{\beta_x}k_2\beta_x\cos(\phi_x)(\cos(3\phi_x+3\overline{\psi}(s',s)) \\
& - \frac{3J_x\sqrt{\beta_x}}{2\sin(3\pi\nu_x)}\times \\
& \int_s^{s+C} ds' k_x\beta_x^{-1/2}\alpha_x\cos(\phi_x)\Big(\sin(3\phi_x+3\overline{\psi}(s',s))+\alpha_x\cos(3\phi_x+3\overline{\psi}(s',s))\Big) \\
& + \frac{3J_x\sqrt{\beta_x}}{4\sin(\pi\nu_x)}\int_s^{s+C} ds' k_x\beta_x^{-1/2}\cos(\phi_x)\cos(3\phi_x+3\overline{\psi}(s',s)) \\
& + \frac{J_xJ_y\sqrt{\beta_x}}{8\sin(\pi\nu_x)}\int_s^{s+C} ds'\sqrt{\beta_x}\left(-k_2\beta_y+\frac{k_x}{\beta_y}(\alpha_y^2-1)\right)\cos(\phi_\pm(s)+\overline{\psi_\pm}(s',s)))
\end{aligned} \tag{6.11}$$

where $\phi_\pm = \phi_x \pm 2\phi_y$ and $\psi_\pm = \psi_x \pm 2\psi_y$. Averaging on the angle variable $\phi_x$ and ignoring the coupled terms, the perturbed averaged horizontal amplitude is expressed with four integrals:

$$\begin{aligned}
\langle x(s)\rangle_{\phi_x} = & -\frac{J_x\sqrt{\beta_x}}{4\sin(\pi\nu_x)}\int_s^{s+C} ds'\sqrt{\beta_x}\,(k_2\beta_x+k_x\gamma_x)\cos(\overline{\psi}(s',s)) \\
& - \frac{J_y\sqrt{\beta_x}}{4\sin(\pi\nu_x)}\int_s^{s+C} ds'\sqrt{\beta_x}\,(-k_2\beta_y+k_x\gamma_y)\cos(\overline{\psi}(s',s)) \\
& - \frac{J_x\sqrt{\beta_x}}{2\sin(\pi\nu_x)}\int_s^{s+C} ds' k_x\beta_x^{-1/2}\alpha_x\Big(\sin(\overline{\psi}(s',s))+\alpha_x\cos(\overline{\psi}(s',s))\Big) \\
& + \frac{J_x\sqrt{\beta_x}}{4\sin(\pi\nu_x)}\int_s^{s+C} ds' k_x\beta_x^{-1/2}\cos(\overline{\psi}(s',s))
\end{aligned} \tag{6.12}$$

The hereabove equation adds a fourth term to the expression found in [138]. Fig. 6.5 compares both analytical expressions on a SOLEIL HOA period and a hybrid period in Fig. 6.6, with the tracked averaged amplitude, for $J_x = 35\,\mathrm{pm.rad}$ in both cases. The tracked amplitude is obtained by tracking a single particle through a large number of turns, thus on a large number of phases, and extracting the averaged position $\langle x(s)\rangle_{\phi_x} = \frac{1}{N}\sum_{k=1}^{N} x(s,k)$, where $x(s,k)$ is the horizontal transverse position of the particle after $k$ turns, at the longitudinal position s. Such tracking is done in Accelerator Toolbox.

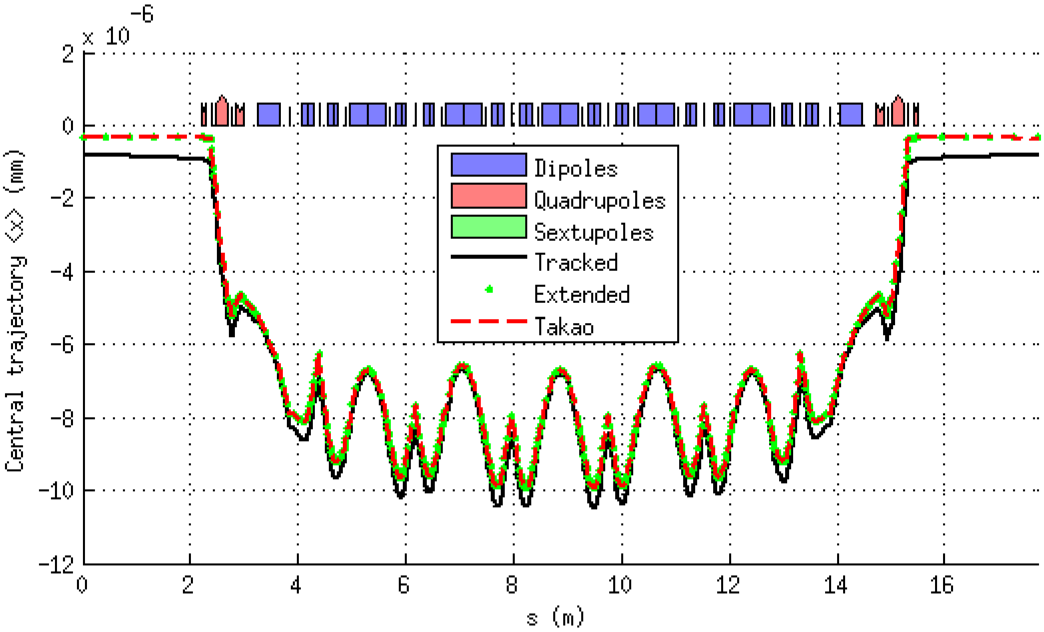

FIGURE 6.5: Averaged amplitude along a HOA 7BA cell, for $J_x = 35\,$pm.rad. The green dots are the analytical calculations of the averaged amplitude, using the equation (6.12) above.

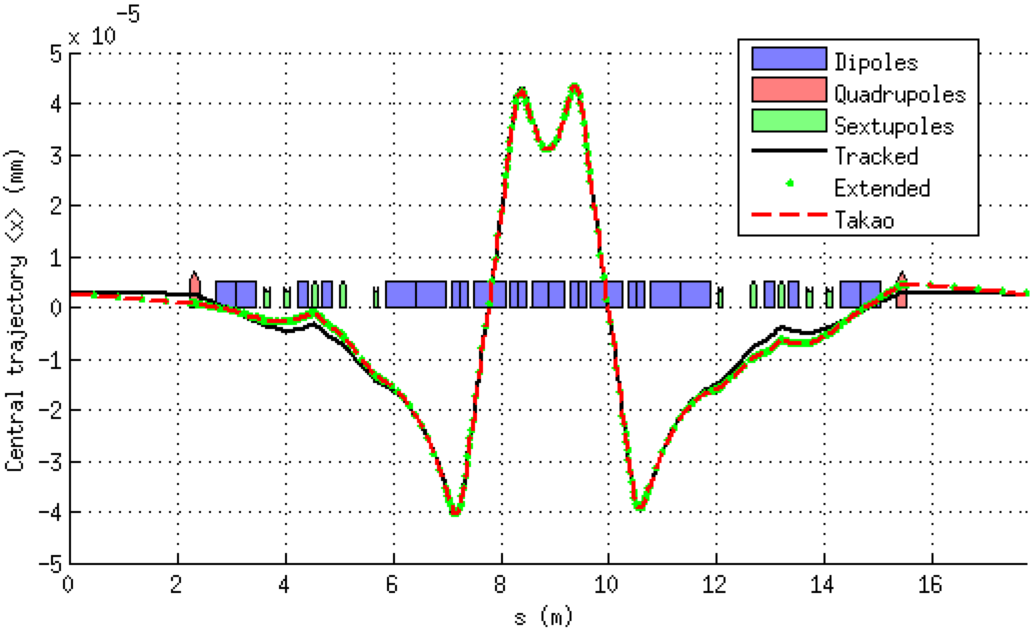

FIGURE 6.6: Averaged amplitude along a hybrid 7BA cell, for $J_x = 35\,$pm.rad. The green dots are the analytical calculations of the averaged amplitude, using the equation (6.12) above.

Comparison between the expression found in [138] and the expression in Eq. (6.12) in Fig. 6.5 and 6.6 does not identify any disagreement between the two formulae. The following section will nonetheless keep using Eq. (6.12) in their derivation and calculations. Figure 6.6 nonetheless highlights the discrepancy between the tracked averaged trajectory of the hybrid lattice and the calculated trajectory. The calculations display a discrepancy with the tracked amplitude, in both lattices. Furthermore, a slight asymmetry between the two dispersion bumps appear in the hybrid lattice, which is not expected since the lattice presents an inherent mirror symmetry. The formulae must lack precision when reaching extrema in the dispersion.

### 6.3.3 Derivation of the deviation angle term, $\langle x'^2 \rangle_{\phi_x}$

The second horizontal term in the analytical expression of the path length is related to the square of the deviation angle $x'$, averaged on the horizontal phase, $\phi_x$. Some derivation steps are detailed in the Appendix J, such as the derivative of the transverse phases with the longitudinal position, and the general derivative of the functions $f : (\phi, J, s) \longmapsto A(J, s) \int_s^{s+C} ds' B(J, s') \cos(n\phi(s) + m\psi(s') - m\psi(s) - m\pi\nu)$, with $n, m \in \mathbb{Z}$.

### 6.3.4 Expression of $\langle \left(\frac{dx}{ds}\right)^2 \rangle$

From the Hamiltonian in Eq. (6.4), the derivative of the horizontal amplitude with the longitudinal position $s$ is a function of the transverse coordinates $(x, p_x)$:

$$x' = \frac{dx}{ds} = \frac{\partial H}{\partial p_x} = p_x \left(1 + k_x x\right) \tag{6.13}$$

Since the transverse coordinates are linked to the canonical action-angle variable $(\phi_x, J_x)$ through $x = \sqrt{2J_x\beta_x}\cos(\phi_x)$ and $p_x = -\sqrt{\frac{2J_x}{\beta_x}}\left(\sin(\phi_x) + \alpha_x\cos(\phi_x)\right)$, the derivative of the horizontal amplitude with the longitudinal position is expressed, in the action-angle plane, as:

$$\begin{aligned} x'(\phi, J) = -k_x\alpha_x J_x - \sqrt{\frac{2J_x}{\beta_x}}\left(\sin(\phi_x) + \alpha_x\cos(\phi_x)\right) \\ - J_x k_x \left(\sin(2\phi_x) + \alpha_x\cos(2\phi_x)\right) \end{aligned} \tag{6.14}$$

Expanding J in the previous equation using its expression with the perturbed action-angle variables $J = \overline{J} + \frac{\partial S}{\partial \phi}$ derived in Eq. (6.9), the perturbed horizontal amplitude derivative $x'$ becomes:

$$
\begin{aligned}
x'(\phi, J) = -k_x\alpha_x J_x - \sqrt{\frac{2J_x}{\beta_x}}\left(\sin(\phi_x) + \alpha_x\cos(\phi_x)\right) - J_x k_x\left(\sin(2\phi_x) + \alpha_x\cos(2\phi_x)\right)\\
- k_x\alpha_x\frac{\partial S}{\partial\phi} - \frac{1}{\sqrt{2\beta_x}}\left(\sin(\phi_x) + \alpha_x\cos(\phi_x)\right)\frac{\partial S}{\partial\phi}\\
- k_x\left(\sin(2\phi_x) + \alpha_x\cos(2\phi_x)\right)\frac{\partial S}{\partial\phi}
\end{aligned}
\tag{6.15}
$$

The path length is proportional to the square of the transverse coordinates derivatives with the longitudinal position. By construction of the generating function $S$ (*cf* [139]), the averaged derivative of $S$ with the betatron phases is $\langle\frac{\partial S}{\partial\phi}\rangle_{\phi_x} = 0$. It only contains first and third harmonics in $\phi_x$ (*cf* Appendix J for the full derivation). Therefore:

$$
\langle\cos(2\phi_x)\frac{\partial S}{\partial\phi}\rangle_{\phi_x} = \langle\sin(2\phi_x)\frac{\partial S}{\partial\phi}\rangle_{\phi_x} = 0 \tag{6.16}
$$

At the first-order in the perturbed generation function derivative, the averaged horizontal amplitude derivative to the square $\langle x'^2\rangle$ is fully expressed with:

$$
\begin{aligned}
\langle x'^2\rangle_{\phi_x} = J_x\gamma_x k_x^2 + \alpha_x^2 J_x^2 + J_x^2 k_x^2\frac{\beta_x\gamma_x}{2}\\
+ 2k_x\alpha_x\frac{J_x}{\sqrt{2\beta_x}}\langle(\sin(\phi_x) + \alpha_x\cos(\phi_x))\frac{\partial S}{\partial\phi_x}\rangle_{\phi_x}\\
+ 2k_x\alpha_x\sqrt{\frac{2J_x}{\beta_x}}\langle(\sin(\phi_x) + \alpha_x\cos(\phi_x))\frac{\partial S}{\partial\phi_x}\rangle_{\phi_x}\\
+ k_x\sqrt{\frac{2J_x}{\beta_x}}\langle\Big((\alpha_x^2 - 1)\cos(3\phi_x) + \beta_x\gamma_x\cos(\phi_x) + 2\alpha_x\sin(3\phi_x)\Big)\frac{\partial S}{\partial\phi_x}\rangle_{\phi_x}\\
+ \frac{J_x k_x}{\sqrt{2\beta_x}}\langle\Big((\alpha_x^2 - 1)\cos(3\phi_x) + \beta_x\gamma_x\cos(\phi_x) + 2\alpha_x\sin(3\phi_x)\Big)\frac{\partial S}{\partial\phi_x}\rangle_{\phi_x}
\end{aligned}
\tag{6.17}
$$

**Comparison of the tracked $\langle x'^2\rangle_{\phi_x}$ and the calculations** Figures 6.7 and 6.8 compare the averaged horizontal amplitude deviation $x'$ tracked for a random particle at $J_x = 35\,$pm.rad, over a large number of turns, its linear formula used in [138] and its analytical calculation using Eq. (6.17), for both the HOA and the hybrid lattices. No difference can be spotted between the tracked and the calculated values.

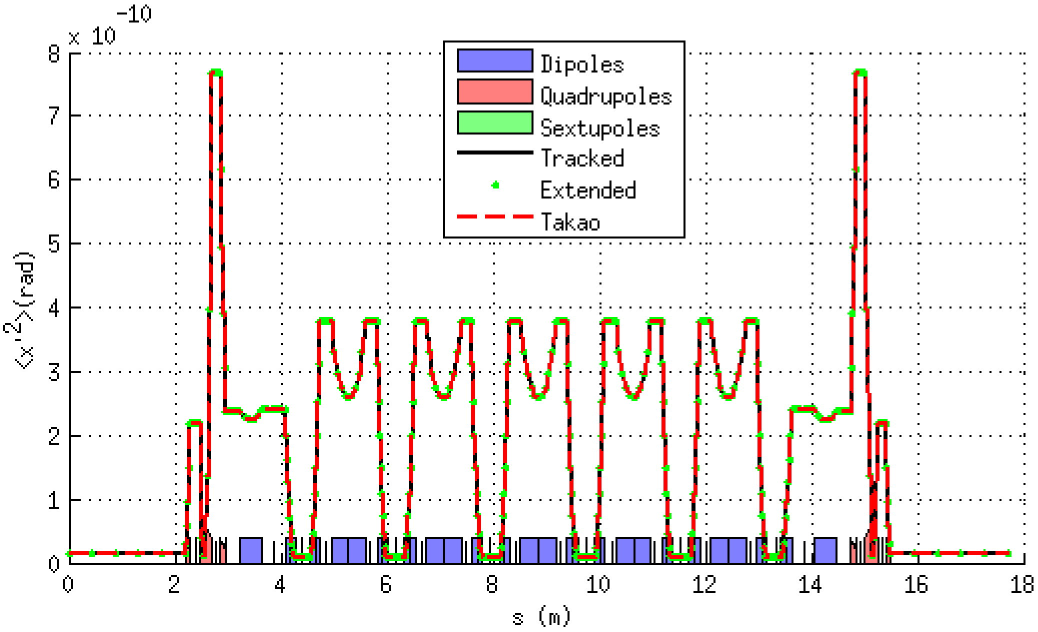

FIGURE 6.7: Comparison between the tracked variation of $\langle x'^2 \rangle$ and its first-order perturbed analytical expression for the HOA lattice.

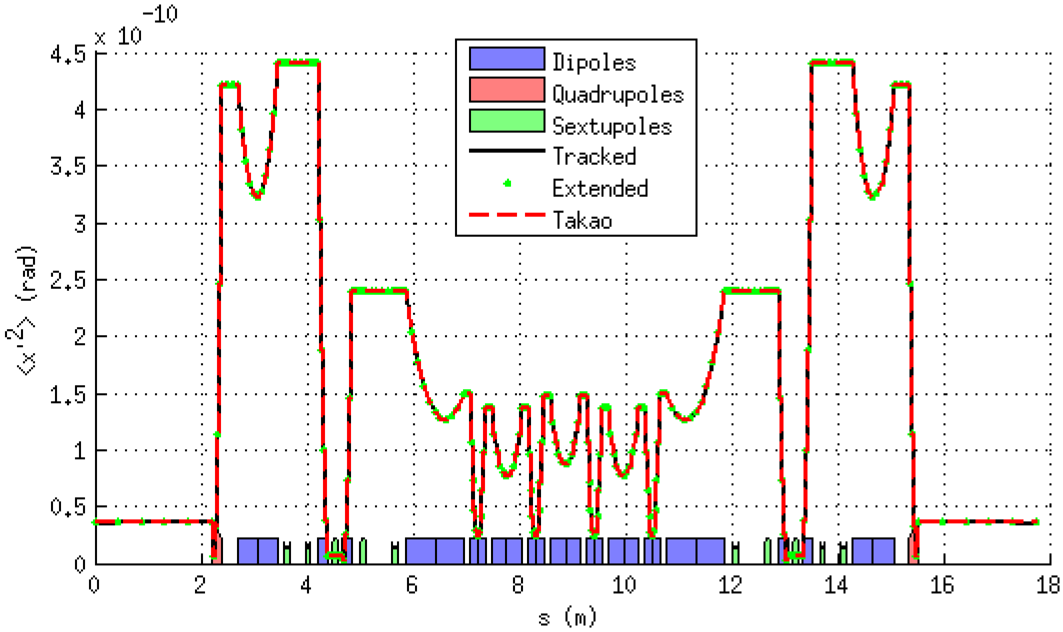

FIGURE 6.8: Comparison between the tracked variation of $\langle x'^2 \rangle$ and its first-order perturbed analytical expression for the hybrid lattice.

## 6.4 Numerical derivation

The analytical formulae of the averaged horizontal amplitude and its derivative were written in an A.T. script, available in my GitHub [136]. The total horizontal path length was calculated through the integral in Eq. (6.3). Figure 6.9 and 6.10 compares the path length versus the amplitude extracted from the linear formula at Eq. (6.2) in red, from the tracking in green and the calculated path length with amplitude using the first-order perturbation canonical theory, for both the HOA and the hybrid lattices.

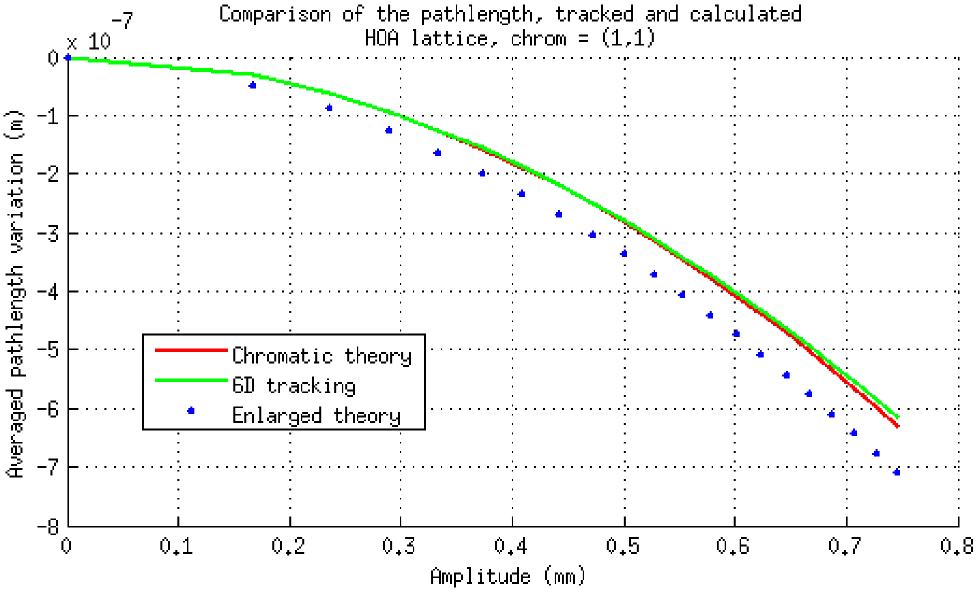

FIGURE 6.9: Comparison of the linear path length (red) with the tracked path length (green) and the calculated path length with the first-order perturbation theory (blue dots) of the HOA lattice.

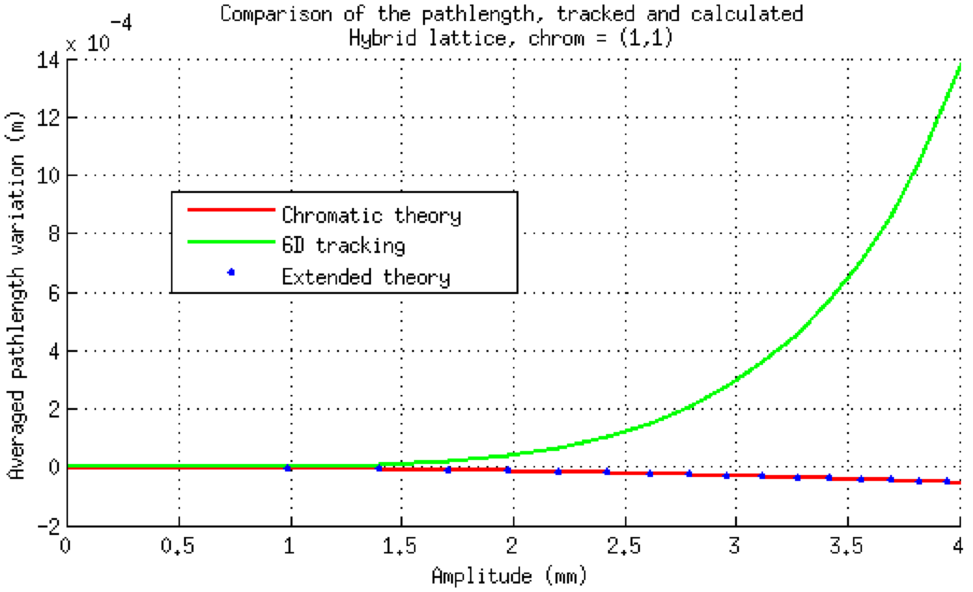

FIGURE 6.10: Comparison of the linear path length (red) with the tracked path length (green) and the calculated path length with the first-order perturbation theory (blue dots) of the hybrid lattice.

In the case of the HOA, the integral does not match the tracked path length. Nonetheless, the imprecision of the integral could explain such a discrepancy. The tendency of the calculated path length remain identical to the tracked path length of the HOA lattice. Nonetheless, the calculation do not match the hybrid path length, neither in value, nor in tendency.

## 6.5 Sextupole distribution and its effect on the path length

The first-order canonical perturbation theory was not enough to describe the variations of the path length at medium amplitudes in the case of the hybrid lattice. This section lists other small studies around the path length, such as its variation with the input phase advance, to check if there are any residual dependency, and the variations of the action variable.

### 6.5.1 Dependence of the path length with the input phase advance

The path length depends on the linear chromaticities, following Eq. (6.2). After one turn, the path length is evaluated with regard to the horizontal amplitude, for different phase advances, and compared to the linear formula. Figure 6.11 displays the corresponding path length with amplitude for both the 7BA HOA and hybrid lattices, 20-fold symmetry. They were both set to chromaticities $(\xi_x, \xi_y) = (-1, -1)$.

In the case of the HOA lattice, the path length after one turn for each input phase is close to the linear path length. A variation of ±7% occurs at the highest amplitude. In the case of the hybrid lattice, the dependence on the input phase advance starts even at low amplitudes, reaching a $\simeq \pm 80\%$ variation at $x = 1\,\mathrm{mm}$.

### 6.5.2 Averaged path length of a random particle

Theoretically, the averaged path length should not depend on this input phase. To verify that, a particle of fixed amplitude was tracked over a thousand turns. After each turn k, the difference in path length with the reference particle is extracted. The averaged path length is therefore $\langle \Delta C \rangle_{turns} = \frac{1}{N_{turns}} \sum_{k=1}^{N_{turns}} \Delta C_k$, following the method of [140]. They are compared to the linear path length of Eq. (6.2), depending on the chromaticities. The exercise was conducted on both the 7BA HOA and hybrid 20-fold symmetry lattices, and the results are displayed in Fig. 6.12.

While the path length of both lattices reach an equilibrium after 500 turns, the hybrid path length limit reaches a different value than expected. The same tracking was done for an opposite phase, which then reached again a different limit. This result is consistent with the remaining dependence in phase that was found in the previous section.

### 6.5.3 Variation of the horizontal action variable

The horizontal action variable is defined with the transverse coordinates $(x, p_x)$ and is linked to the betatron amplitude $x_\beta = \sqrt{2J_x\beta_x}$. By definition, the action variable does not depend on the phase advance $\phi_x$. Indeed, the corresponding transverse Hamiltonian in the absence of any perturbation is:

$$H_0(\phi_x, J_x) = \frac{J_x}{\beta_x} \tag{6.18}$$

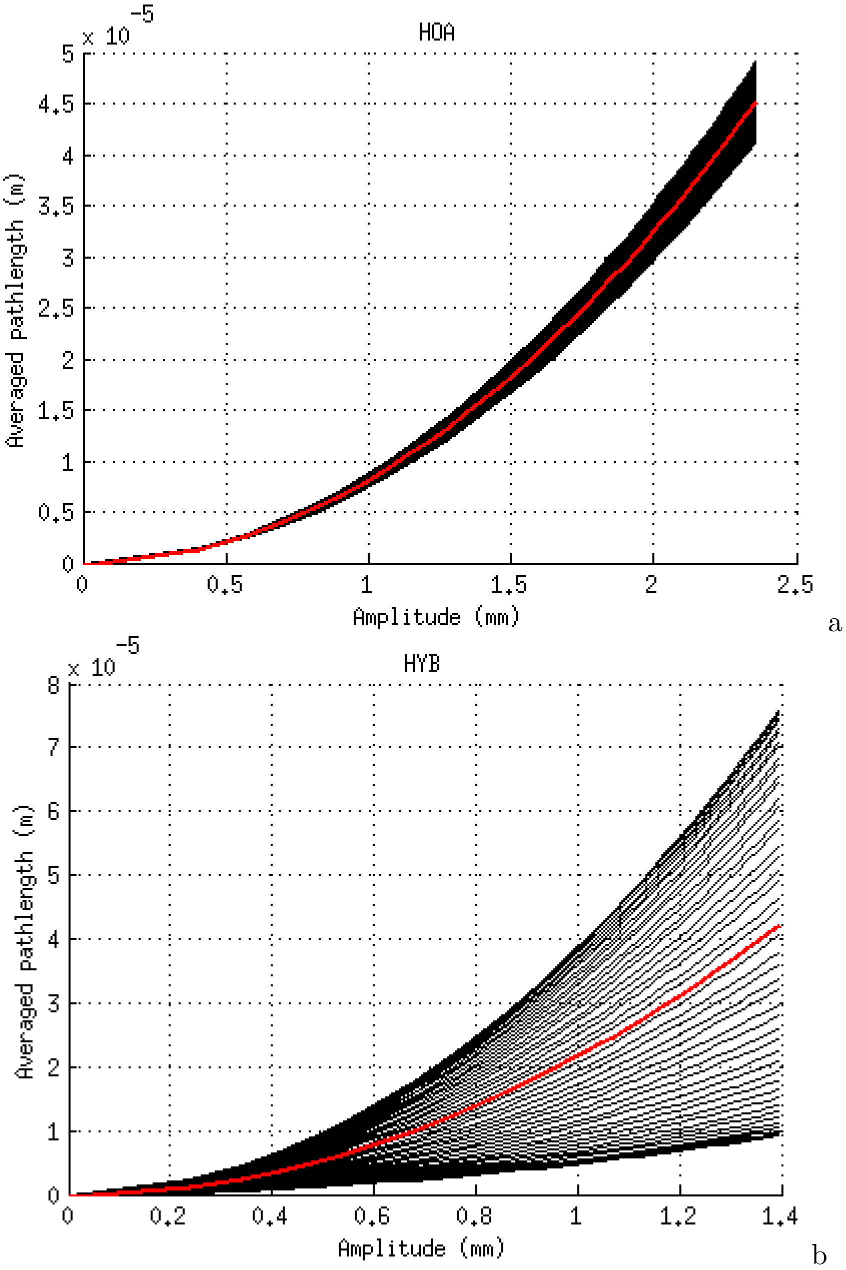

FIGURE 6.11: Comparison of the tracked path length for different input phases, with the linear path length (in red), for (a) the HOA lattice and (b) the hybrid lattice. The chromaticities of both lattices were set at $(\xi_x, \xi_y) = (-1, -1)$.

Because of the path length effect reported in 6.1 and the inadequacy of the first-order canonical perturbation theory, additional tests were conducted to understand if this regime is still applicable to both the HOA and the hybrid lattices. In both cases, a particle of set amplitude was tracked over a thousand turns. The corresponding action of each transverse position was extracted using the amplitude and the phase advance. Figure 6.13 compares the variation of $J_x$ for both lattices, and compares it to the averaged action over the thousand turns. To best appreciate its variations, the last subplot enhances the difference $(\langle J_x \rangle_{N_{turns}} - J_x)$, by multiplying it by $10^7$. The first

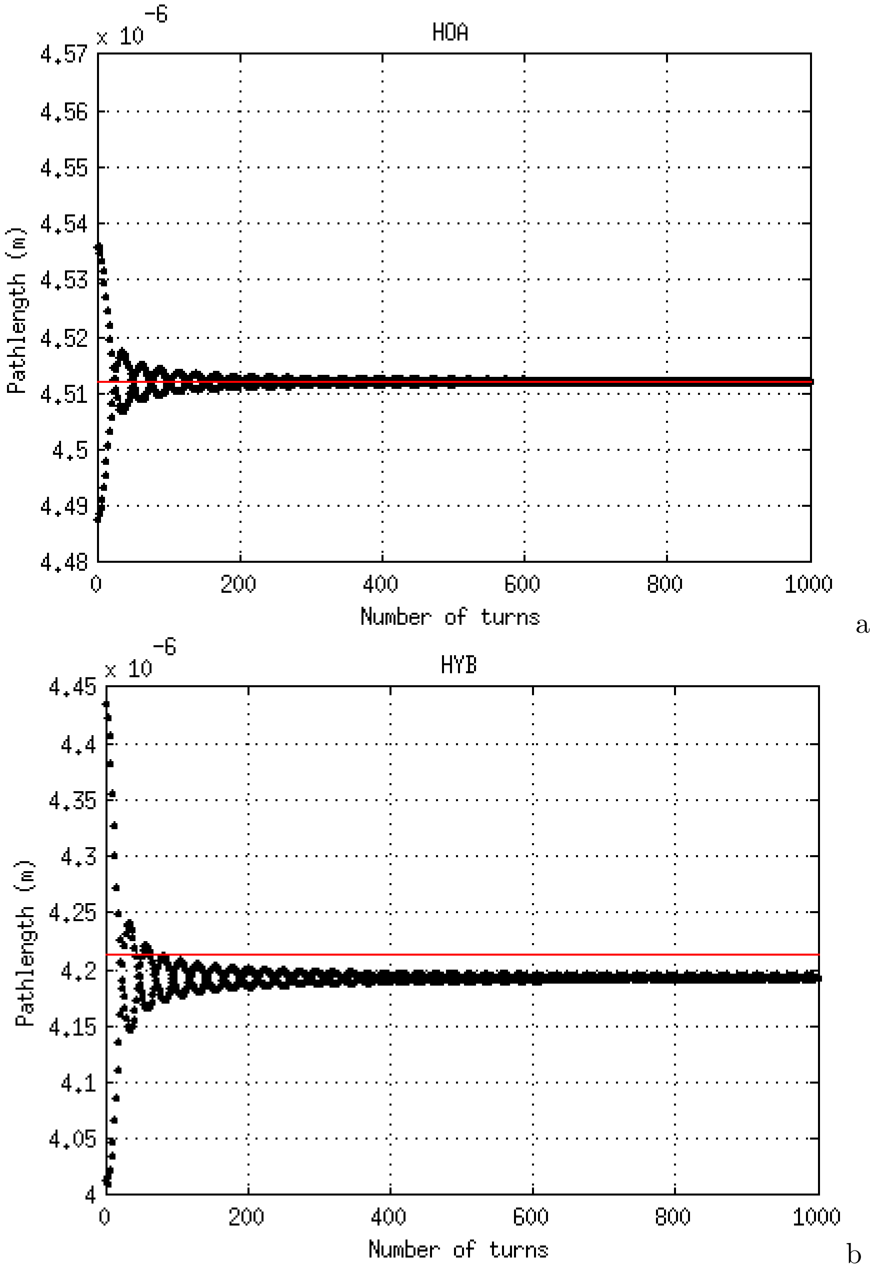

FIGURE 6.12: Variation of the path length of a fixed particle over a thousand turns for (a) the HOA lattice and (b) the hybrid lattice. The red line corresponds to the calculated path length with the linear formula. The chromaticities of both lattices are set at $(\xi_x, \xi_y) = (-1, -1)$.

plot displays the tracked path length, turn after turn, to verify the linear dependency with $J_x$.

The evolution of the path length appears normal in both cases, and slight oscillations occur around the averaged path length in red. The action variable $J_x$ in the case of the HOA lattice presents chaotic variations, of the order $10^{-20}$, around its averaged value. Since all tracking was conducted in A.T., based on Matlab, which limits its precision to $10^{-16}$, the experienced variations can therefore be considered as noise. In the case of the hybrid lattice, the action oscillates around its averaged value, with around 8/9

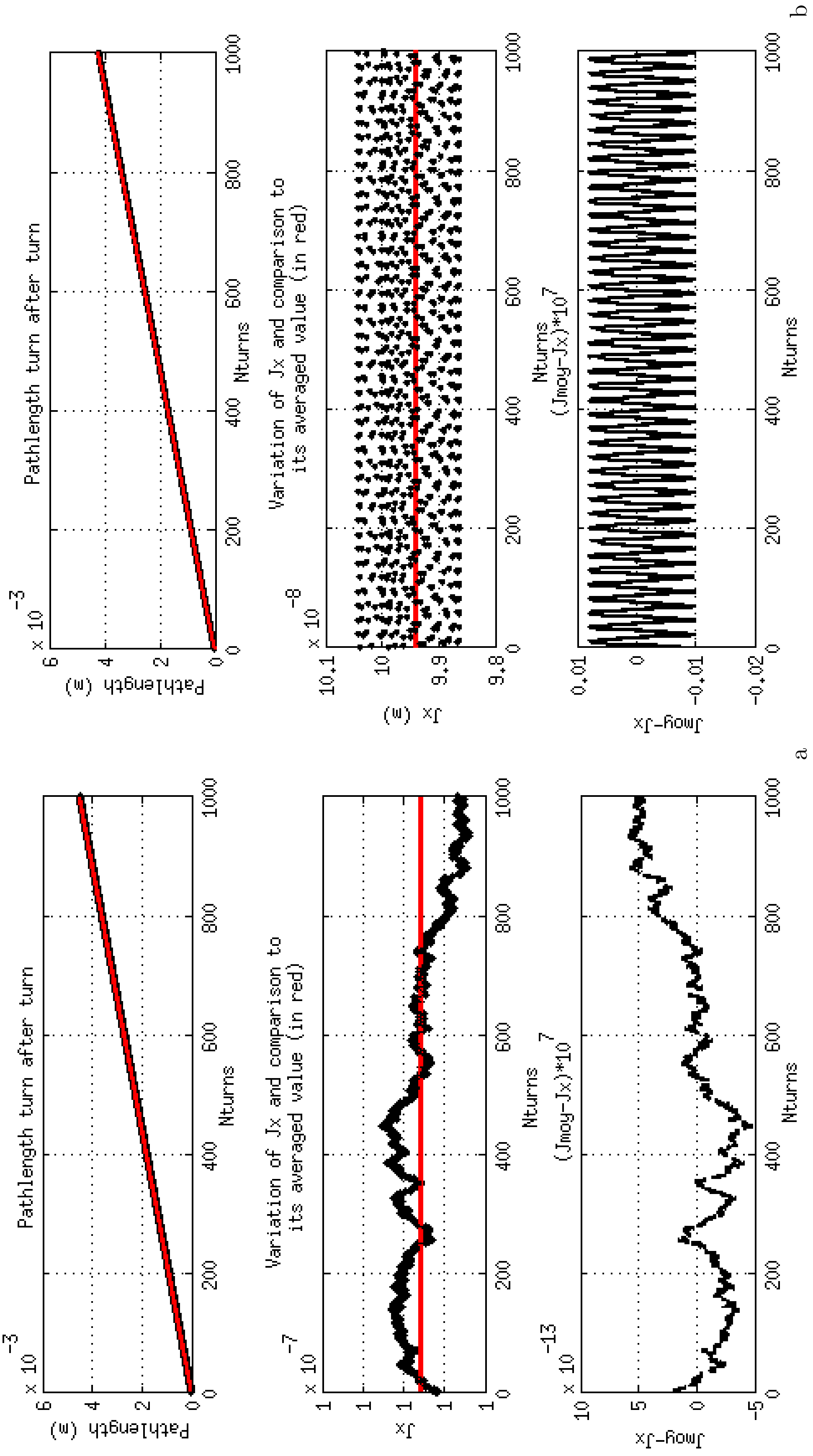

FIGURE 6.13: Variations of the horizontal action variable $J_x$ tracked over a thousand turns in (a) the HOA lattice and (b) the hybrid lattice.

periods over 200 turns. The variations have an amplitude of $\pm 10^{-9}$ around the averaged value, which corresponds to the same order as $J_x$. This could correspond to the phase dependence found in the previous sections.

## 6.6 Reduction of the path length effect

To reduce the path length variation of the hybrid lattice, a scanning script in A.T. was developed to vary the sextupole strengths of the nominal lattice in hopes of reducing the path length at a set amplitude. The script is available in my GitHub [136]. The chromaticities are kept identical to that of the nominal lattice, at $(1, 1)$, to compare with Fig. 6.3. The sextupoles are kept symmetric, to comply with the non-interleaved principle requirements. A hundred rings were generated, with relative variations of the sextupole strengths of 50% with regard to their nominal value. Figure 6.14 displays the path length with amplitude of all generated rings during the scan. The chromaticities of the rings are set at $(\xi_x, \xi_y) = (1, 1)$. The path length is evaluated for a maximum $J_x = 1 \times 10^{-7}$ m.rad.

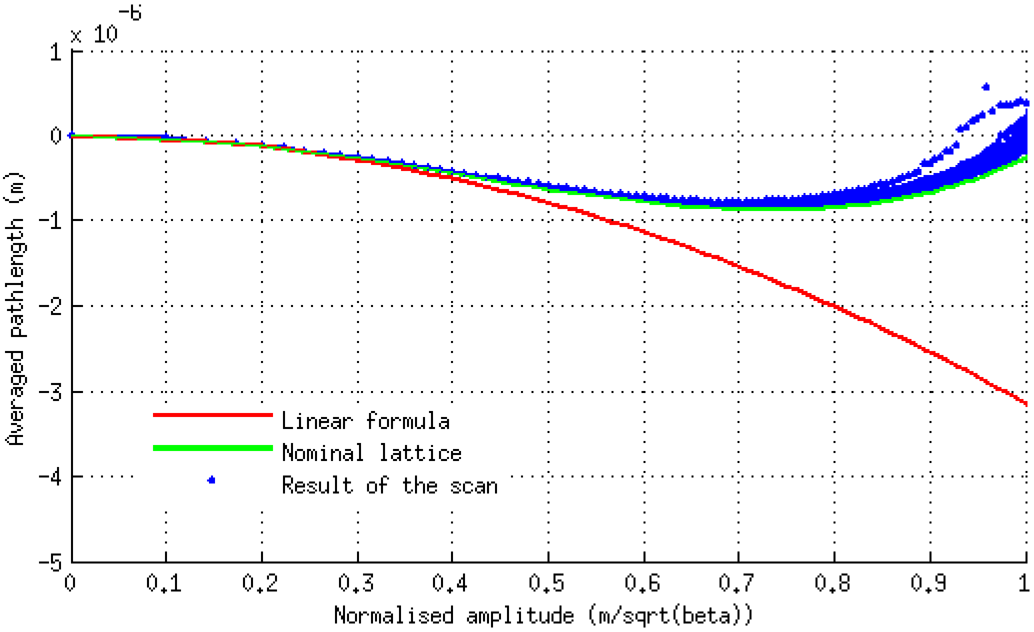

FIGURE 6.14: Path length with amplitude of the SOLEIL hybrid lattice with a hundred different sets of sextupoles. They were randomly generated within a space of constant chromaticities.

The ring of minimum path length deviation from the linear formula is selected, and further compared to the nominal lattice. Their path lengths are displayed in Fig. 6.15, and their strengths in Table 6.2.

The scan was not enough to reduce the path length variation, and the nominal setting seems to be a minimum already. A last test was conducted with the addition of the octupole magnets in the scan. The octupoles are treated individually. Their location is identical to the MOGA-Bmad case in Fig. 4.4. Figure 6.16 displays the path length

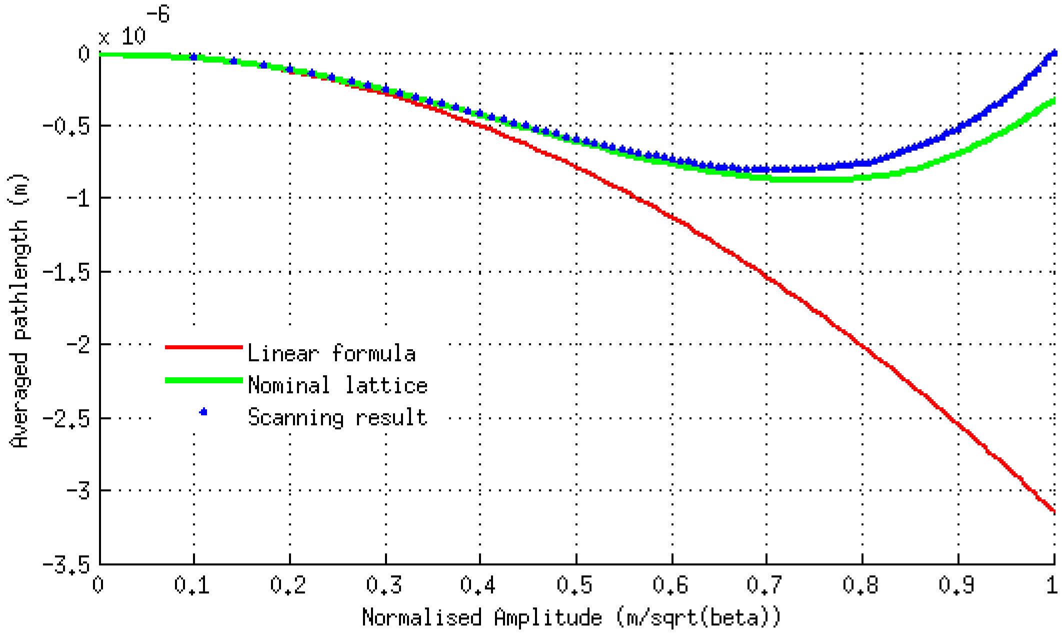

FIGURE 6.15: Path length with amplitude of the SOLEIL hybrid lattice after the scan (in blue), compared with the nominal lattice (in green) and the linear formula (in red).

TABLE 6.2: Comparison of the sextupole integrated strengths of the nominal lattice and of the result of the path length scan.

| Name | Nominal lattice | Result of the scan |
|---|---|---|
| sxd1e | $-21.50\,\mathrm{m}^{-2}$ | $-10.49\,\mathrm{m}^{-2}$ |
| sxf2e | $-10.5\,\mathrm{m}^{-2}$ | $-24.75\,\mathrm{m}^{-2}$ |
| sxf1e | $16.83\,\mathrm{m}^{-2}$ | $24.34\,\mathrm{m}^{-2}$ |
| sxf3e | $10.4\,\mathrm{m}^{-2}$ | $11.10\,\mathrm{m}^{-2}$ |
| sxd2e | $-21.5\,\mathrm{m}^{-2}$ | $-54.76\,\mathrm{m}^{-2}$ |

of all generated rings. The overall variations do not appear to drastically change from the sextupole-only scan.

The ring of minimum path length deviation from the linear formula is selected, and further compared to the nominal lattice. Their path length variations are displayed in Fig. 6.17, and their strengths in Table 6.3.

TABLE 6.3: Comparison of the sextupole strengths of the nominal lattice and of the result of the path length scan.

| Name | Nominal lattice | Result of the scan |
|---|---|---|
| sxd1e | $-21.50\,\mathrm{m}^{-2}$ | $-14.55\,\mathrm{m}^{-2}$ |
| sxf2e | $-10.5\,\mathrm{m}^{-2}$ | $-15.07\,\mathrm{m}^{-2}$ |
| sxf1e | $16.83\,\mathrm{m}^{-2}$ | $24.94\,\mathrm{m}^{-2}$ |
| sxf3e | $10.4\,\mathrm{m}^{-2}$ | $73.57\,\mathrm{m}^{-2}$ |
| sxd2e | $-21.5\,\mathrm{m}^{-2}$ | $-46.96\,\mathrm{m}^{-2}$ |
| octd1 | $-124\,\mathrm{m}^{-3}$ | $363/31.35\,\mathrm{m}^{-3}$ |
| octf1 | $55\,\mathrm{m}^{-3}$ | $77.0/76.3\,\mathrm{m}^{-3}$ |
| octd2 | $45\,\mathrm{m}^{-3}$ | $254/334\,\mathrm{m}^{-3}$ |

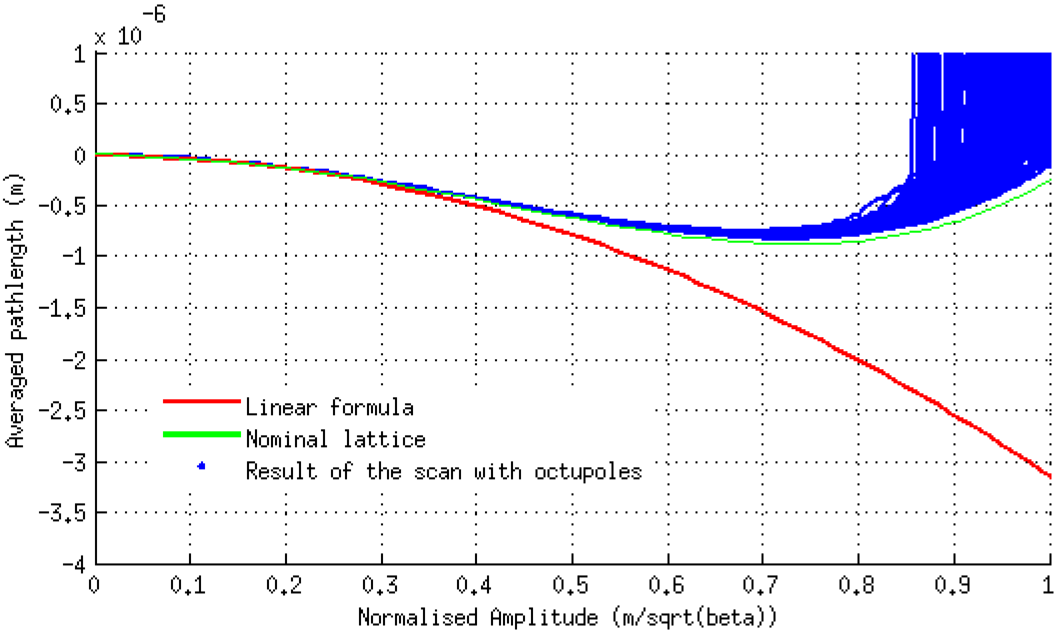

FIGURE 6.16: Path length variation with amplitude of the SOLEIL hybrid lattice with a hundred different sets of sextupoles and octupoles. They were randomly generated within a space of constant chromaticities.

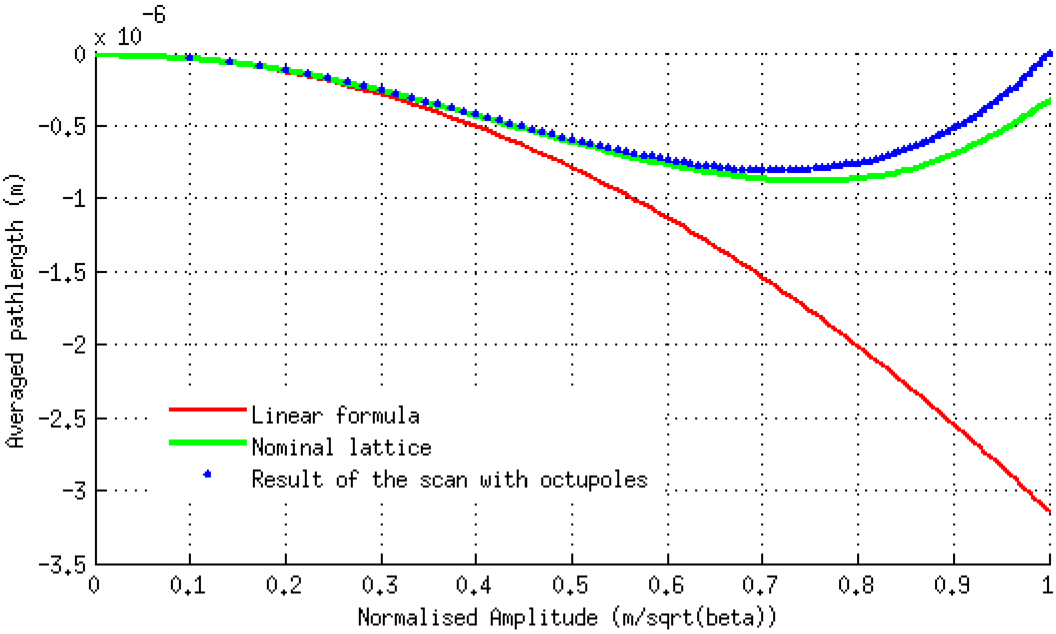

FIGURE 6.17: Path length variation with amplitude of the SOLEIL hybrid lattice after the scan which included octupoles (in blue), compared with the nominal lattice (in green) and the linear formula (in red).

## 6.7 Conclusion

The hybrid lattice presents a limiting effect which drastically reduces its on-momentum stability: once a RF cavity is inserted in the lattice, the particles with small energy deviation starts oscillating transversally, falling out of the peaked transverse acceptance. This phenomenon is coupled to a large path length deviation $\Delta C$ which starts at medium amplitudes: this quantity is further studied, as a link between the longitudinal and the transverse plane. To further understand the phenomenon, the path length of three different lattices was compared in Fig. 6.3: the SOLEIL 7A HOA and hybrid lattices, and the ESRF-EBS hybrid lattice. To do so, their chromaticities were fixed to $(\xi_x, \xi_y) = (1, 1)$. While the HOA lattice did not present any unusual variations of its path length with regard to the classical linear formula, both hybrid lattices shared the same tendency, yet slower in the case of the ESRF-EBS lattice which could be due to its larger cell length per period and higher energy.

In an attempt to theoretically describe its phenomenon and understand its origin, the path length was derived with regard to the transverse coordinates, using the first-order perturbation theory to extract the influence of the sextupoles, following [138]. The resulting calculation was not conclusive, as it did not improve the description of the nonlinear behaviour of the path length. Another method scanned the sextupoles' strengths in the SOLEIL hybrid lattice, with the hope of finding a path length closer to the linear formula, however this was in vain. The addition of octupoles did not help either. Further studies should evaluate the impact of the non-interleaved lattice on the path length and the averaged transverse trajectory, as a $-I$ transformation could make the lattice act as an anti-symmetric system.

# Chapter 7

# Conclusion and outlook

The present thesis introduced different aspects of the global effort towards fourth-generation storage ring. As part of the SOLEIL upgrade project, the presented studies took part in the early design and exploration of a suitable lattice for SOLEIL 2.75 GeV storage ring, stressing the linear and nonlinear challenges of ultra-low emittance rings. To achieve a natural horizontal emittance below 100 pm.rad, ultra-low emittance lattices are developed with an extensive use of Multi-Bend Achromats, which introduces a large number of dipoles and therefore reduces their emittance creation, following the principle of the theoretical minimum emittance. Further reduction of the natural horizontal emittance is achieved with the implementation of reverse bending magnets. Other adaptations can be implemented, such as longitudinal-gradient dipoles or a round beam. The latter could increase the Touschek lifetime of the lattice, placing the lattice in the favourable regime. To maximise the transverse dynamics of the upgrade lattices and reduce the number of systematic resonances, the developed lattices comprise a 20/24-fold symmetry, additionally to the mirror-symmetry of each period. The strong focusing required to contain the beam sizes yields to strong quadrupole magnets which create high natural chromaticities. They are corrected with sextupoles, located under a reduced dispersion and space, thus decreasing their efficiency which could affect the transverse stability. Maintaining stability and a large dynamic aperture requires that the sextupole-induced non-linearities are controlled: this can be achieved by modelling the linear lattice such as to compensate the negative sextupolar effects. For this purpose, two schemes were developed in the community.

A first scheme developed for the ESRF-EBS storage ring was adapted into a 7BA 20-fold symmetry scheme for the SOLEIL lattice. The so-called hybrid scheme applies the non-interleaved sextupole principle: the kicks of the sextupoles are compensated by their symmetric, provided that the phase advance in between fulfils $(\Delta\phi_x, \Delta\phi_y) = ((2p+1)\pi, (2q+1)\pi)$, with $p, q \in \mathbb{Z}$. This corresponds to a $-I$ transformation, where $I$ is the identity matrix. The condition in the vertical plane is enlarged to $\Delta\phi_y \equiv 0[\pi]$, for cancellation of some resonant driving terms [105]. The sextupoles are located under two symmetric dispersion bumps, which increases their efficiency in correcting the chromaticities, thus reducing their strengths and required lengths. Such a scheme, as detailed in sec. 2.3.1, maximises the transverse on-momentum dynamic aperture. A second scheme was implemented on the SOLEIL storage ring; the so-called High-Order Achromat lattice. Such lattice is based on a series of $N$ unit cells, of which a fixed phase advance allow the cancellation of all first-order resonant driving terms, over $M$ unit cells. Each HOA unit cell for SOLEIL includes two half dipoles, two reverse bends, a focusing sextupole and two defocusing sextupoles. In the literature, the phase advance suggested for 7BA lattices is $(\nu_x^c, \nu_y^c) = (\frac{3}{7}, \frac{1}{7})$, which cancels all first-order and second-order perturbative resonances over seven unit cells. Other phase advances are tested in Sec. 3.2.3. The cancellation of third-order perturbative resonances can be achieved by increasing the number of unit cells per period. Yet, the fixed length of each SOLEIL period limits the inclusion of more than seven unit cells per period. Thus, to preserve the unit cell phase advance, a dispersion-free section was created by manipulating the extrema dipole and reverse bending angles: the resulting resonant driving terms over one period were minimised compared to the traditional ”missing dipole” method. Nonetheless, the traditional method presented a higher transverse dynamic aperture and was thus conserved in the 7BA HOA lattice proposal for SOLEIL.

Both ultra-low emittance schemes were compared in Sec. 3.3. By construction, the HOA lattice is composed of a large number of magnets, increasing its cost: each HOA period is composed of a minimum of 44 magnets, resulting in $\simeq 60\%$ magnet occupation, compared to 27 magnets and 50% magnet occupation in the hybrid case. Moreover, the HOA lattice offers little space for the sextupoles, and low dispersion levels, resulting in high sextupolar strengths. The HOA dipoles are also shorter compared the hybrid case, resulting in a higher natural emittance and an increased energy loss. Nonetheless, its dynamic performances surpasses the hybrid lattice in terms of transverse stability and robustness. Indeed, the inner symmetry of the HOA lattice offers a higher resistance to quadrupole errors with a $\pm 15\%$ variation of its transverse amplitudes compared to reduction of $\simeq 30\%$ in the hybrid case, for a quadrupolar error of $\pm 1\%$. The stronger stability of the HOA lattice is also demonstrated by its frequency map analysis, with a large stable area both on- and off-momentum, where the hybrid lattice presents a dramatically reduced off-momentum transverse acceptance, with a reduced stability area. Both schemes were optimised using MOGA-Bmad, which allows fast optimisations of the on- and off-momentum dynamic apertures, while conserving the chromaticities. Although no outstanding results were found, the optimisation demonstrated the difficulties of optimising the off-momentum dynamics of the hybrid lattice, and the effectiveness of the HOA optimisation.

The inclusion of a RF cavity in both lattices highlighted a strong reduction the on-momentum dynamic aperture of the hybrid lattice, which remains a quarter of the nominal transverse dynamic aperture, while this phenomenon slightly affects the HOA lattice. As the off-momentum particles experience a different phase advance in between the sextupoles, the non-interleaved principle is not applied outside the vicinity of the on-momentum particle. The dynamic aperture versus energy deviation of such a lattice peaks when particles are on-momentum. Therefore, once a Radio-Frequency (RF) cavity is inserted in the lattice, small-energy particles oscillates transversally, and fall outside the stability area. This phenomenon is coupled to a large path length deviation which starts at medium amplitudes. The effect of the inhomogeneous sextupole distribution in the hybrid scheme was detailed in Chapter 6, and compared to the HOA and ESRF-EBS lattices. While the HOA lattice did not present any unusual variations of its path length with regard to the classical linear formula, both hybrid lattices shared the same tendency, yet slower in the case of the ESRF-EBS lattice which could be due to its larger cell length per period and higher energy. In hopes to theoretically describe the perturbed path length of the hybrid lattice, the first-order canonical perturbation theory was applied, following [138]. The transverse coordinates were derived in terms of sextupolar perturbation. An additional element was derived in the averaged distorted amplitude compared to [138], with no significant contribution. The path length was then expressed in terms of perturbed amplitude and derivative and compared to the tracking. Nonetheless, the calculations did not follow the tracked path length. Further numerical analysis exhibited a remaining perturbation of the phase space, with a perturbed action oscillating with the betatron phase. Numerical minimisation of the path length variation with amplitude was conducted on the SOLEIL hybrid lattice using sextupoles and octupoles with no success. Additional studies should evaluate the impact of the non-interleaved principle on the path length and the averaged transverse trajectory, as the $-I$ transformation could make the lattice act as an anti-symmetric system.

As it is based on independent sets of unit cells, the HOA principle can be preserved while differentiating the length of a period, and its number of dipoles. This flexibility allowed the design of several 4-superperiod lattices, which fit the tunnel and minimise the displacement of the current beamlines. Amongst them, the current SOLEIL baseline described in the Conceptual Design Report, the 7BA-4BA HOA lattice, was designed by Alexandre Loulergue. To inject beam into such ultra-low emittance lattices, where the transverse acceptance is drastically reduced compared to the current storage ring, the inclusion of special straight sections is necessary, along with the use of a Multipole-Injector Kicker (MIK). The conservation of the transverse off-axis injection, currently used in SOLEIL, requires the a high-$\beta_x$ straight section. Another scheme kicks the beam directly on-axis. To differentiate the chromatic closed orbit at the centre of the MIK, a dispersion bump is necessary. Several types of dispersion bumps were described and compared. The selected method inserts two quadrupole doublets around the centre of the straight section, to achieve a 16 cm dispersion bump at the MIK. The current specifications of the MIK place the septa close to the machine axis. Therefore, a further analysis of the nonlinear dispersion was required, and a minimisation script was developed in A.T. to decrease the value of the first-order dispersion at the location of the septa. By scanning the strengths of the nearby sextupoles, and conserving the linear chromaticity, the first-order dispersion could be decreased.

Ultra-low emittance lattices present a general reduction of their dispersion level and their zeroth-order momentum compaction factor which can be overtaken by the first-order, impacting the longitudinal stability. A 5BA SOLEIL lattice of natural horizontal emittance 80 pm.rad and presented in Chapter 5, had a reduced bucket of energy acceptance $\pm 2\%$ for a $\frac{\alpha_0}{\alpha_1} = 0.04$ ratio. The effect of the higher-order momentum compaction factor on the energy acceptance was therefore studied. Three methods were developed to restore the RF bucket. A first method, following [133], prescribed the insertion of octupoles to increase the second-order momentum compaction factor and restore the bucket's symmetry. Although inclusion of octupoles in the dispersive area did restore the linear bucket, the required strong octupoles could not be inserted in the real machine. A second method aims at minimising the first-order momentum compaction factor directly. The analytical calculations of the three lowest-orders in dispersion and in momentum compaction factor were implemented in A.T. and a script was developed to scan the sextupole strengths whilst conserving the linear chromaticities. While this method found a satisfying sextupole set with a large bucket for the 5BA lattice, the transverse dynamics could not be controlled. The large higher-order chromaticities enlarged the tune shift with energy thus limiting the transverse acceptance and the beam lifetime. To manage both planes, an extended version of MOGA-Bmad was proposed, where the first-order momentum compaction factor can be analytically calculated and minimised, while optimising the transverse dynamic apertures. Two targets were included: a simple minimisation and a minimisation with an upper bound which, conjugated with a corresponding dominant constraint, forces the optimisation to find individuals with a lower first-order momentum compaction factor. A proof of principle was conducted on the 5BA lattice, with good results. Several optimised rings were found, with a reduced first-order and increased second-order momentum compaction factor, which resulted in a large RF bucket, with maximised on-momentum dynamic apertures. Further options will be included in the extended MOGA. For instance, a lower bound on the first-order momentum compaction factor could be implemented, to limit the optimisation within a set range and focus on the transverse dynamic apertures. The inclusion of octupoles in ultra-low emittance lattices varies the second-order momentum compaction factor: while its analytical calculation has already been implemented in the presented version, an additional option could set an upper and/or lower bound on its value, to fully control the RF bucket.

*All scripts mentioned and detailed in the present thesis can be found on my GitHub.*

*Please drop me a message at lina.hoummi@gmail.com, for further information or questions.*

# Appendix A

# Acceleration of a charged particle

This appendix introduces the different types of acceleration, and the resulting accelerators, developed prior to the synchrotrons and still in use.

## A.1 Electrostatic acceleration of a charged particle

In the event of an electric field, the charged particle experiences an electric force $\mathbf{F} = q\mathbf{E}$. Using the fundamental principle of dynamics, the acceleration of such a particle is then $\frac{q}{m}\mathbf{E}$. Depending on the direction of the electric field, the force will either accelerate (if $\mathbf{E} \times \mathbf{v} = \|vE\| \mathbf{z}$) or decelerate the particle (if $\mathbf{E} \times \mathbf{v} = -\|vE\| \mathbf{z}$). First accelerators used electrostatic fields to accelerate particles. Among them, the Van de Graaf generator, invented in 1929 [141] uses a moving belt to transport electric charges: a top comb electrode collects positive charges on the top metal globe, a second at the bottom collects negative charges. Approaching both globes create an electric spark due to the charge difference. Nonetheless, an electrostatic field is limited at amplitudes of the order 10 MV.m$^{-1}$. Further acceleration is achieved with a time-varying (non-static) field.

## A.2 Acceleration of a time-varying field

Indeed, a charged particle can be accelerated by being exposed to a time-varying field. Provided the field frequency is matched with the particle's trajectory and velocity, the particle will see the same positive voltage and will be further accelerated. This process is known as the resonant acceleration, and was first described by Ising in 1924 [142]. This principle is used in all modern high-energy accelerators, and is also called the Radio-Frequency (RF) acceleration.

### A.2.1 Linear accelerator

In 1928 [144], Wideröe applied this principle on the linear accelerator pictured in Fig. A.1. To describe the principle, let us express the time-varying electric field as:

$$\tilde{E}(t) = \tilde{E}_0 \sin(\omega_{RF}(t - t_0) + \phi_s) \tag{A.1}$$

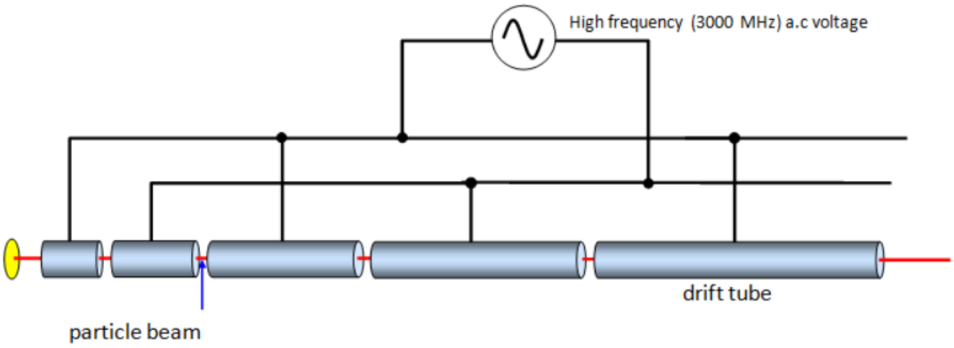

FIGURE A.1: Wideröe linear accelerator scheme, using the time-varying field acceleration. The length of each drift tube is fixed by the synchronism condition. From [143].

with $\tilde{E}_0\,[\mathrm{V.m^{-1}}]$ the amplitude, $\omega_{RF} = h\omega_0\,[\mathrm{s^{-1}}]$ the RF angular frequency, $\omega_0 = \frac{\beta_0 c}{R_0}$ the angular revolution frequency of the reference particle, $\beta_0 c$ the average speed, $R_0$ [m] the averaged radius of the reference particle, $t_0$ the time origin and $\phi_s$ the synchronous phase. The corresponding particle encounters the RF field at the same phase $\phi_s$: it is the synchronous particle. The time $t_0$ is set at the beginning of the positive field in circular accelerators. In linacs, the origin is set at the positive crest of the RF voltage.

The time-varying field is applied to each drift tube. To ensure the accelerated particles encounters the field during its positive crest and benefits from the whole accelerating span, the length of each drift tube has to be defined according to the distance a particle of velocity $v$ will travel under half a RF period. Such condition is called the synchronism condition, which fixes the length of each drift tube $L_{drift} = \frac{1}{2}T_{RF}v$, with $T_{RF}$ the RF period and $v$ the particle speed at the entrance of the drift tube. This accelerating method is rapidly limited by the total length of the linear acceleration: achieving higher energies require a circular motion.

### A.2.2 Cyclotrons

The acceleration of particles can be achieved in a circular path, with the same acceleration principle. Combining a constant magnetic-field which bends the particles and ensures the circular trajectory, and the RF acceleration principle, the cyclotron was patented by L. Slizard in 1929 in Germany [145] and built in 1931 by E.O. Lawrence and his student M. Stanley Livingston [146] at the University of California, Berkeley (USA). Figure A.2 illustrates the cyclotron principle on the right side, and images the first cyclotron on the left side, with MM. Lawrence and Livingston standing by it.

Cyclotrons are composed of two round poles of constant magnetic field, called dees: the particles circulate in a plane between the poles. Acceleration occurs in a gap between the poles, by a time-varying electric field: once the particles cross the gap between the dees, they experience the RF field, and gain energy. The energy gain for the reference

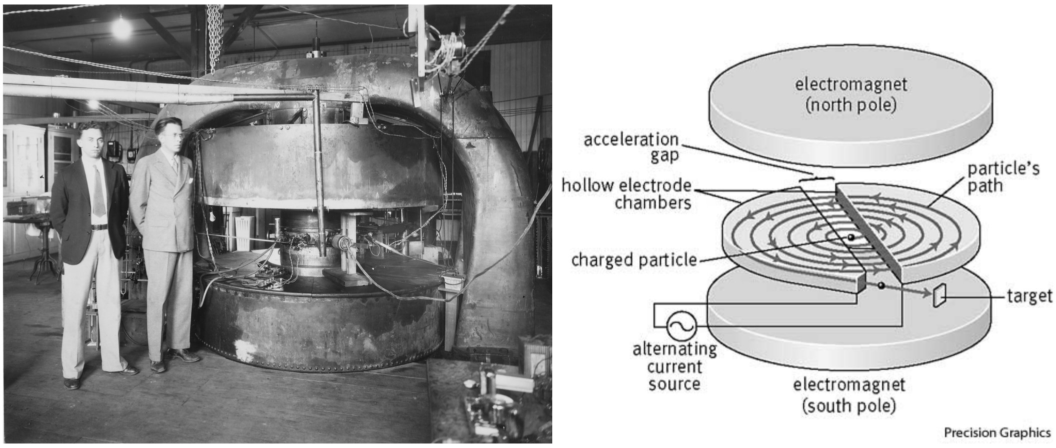

FIGURE A.2: Picture of E.O. Lawrence and M. Stanley Livingston next to the first cyclotron from [147] (left) and illustration of the cyclotron principle from [148] (right).

particle per passage is:

$$\Delta E = q\tilde{E}_0\beta_L c \int_{-\frac{g}{2\beta_0 c}}^{\frac{g}{2\beta_0 c}} \sin(h\omega_0 t + \phi_s)dt = q\tilde{E}_0 g T \sin(\phi_s) \tag{A.2}$$

with $q$ the particle charge, $\beta_L c$ the particle speed, $T = \frac{\sin(\frac{hg}{2R_0})}{\frac{hg}{2R_0}}$ the transit time factor and $\phi_s$ the synchronous phase. The first 4.5 inch cyclotron accelerated protons to 80 keV, with a RF field of 1 kV [146].

Like the Wideröe linear accelerator, efficient acceleration only occurs if the RF cavity is synchronised with the particles revolution frequency. In cyclotron, the angular revolution frequency, also called cyclotron frequency reads $\omega_{cyc} = \frac{eB_0}{\gamma_L m_0}$. This frequency is a constant for non-relativistic particles, where $\gamma_L \simeq 1$: $\omega_{cyc} \approx \frac{eB_0}{m}$. Since the acceleration occurs every half revolution, the RF frequency shall be a multiple of the revolution frequency, to satisfy the synchronism condition:

$$\omega_{RF} = h\omega_{cyc} \tag{A.3}$$

with $h$ the harmonic number, representing the maximum number of bunches in a circular accelerator.

### A.2.3 Relativistic mass effect

In the case of relativistic particles for which $\gamma_L \gg 1$, the cyclotron frequency decreases with higher energy: the synchronism condition is no longer valid, and the particles eventually cross the RF gap when the field decelerates them, limiting the maximum energy achievable by the particles: protons could only be accelerated up to 12/25 MeV. This is the relativistic mass effect.

To overcome this limitation and maintain the synchronism condition, two methods were developed. The first idea from R.H. Thomas in 1938 [149] was to increase the magnetic field with the bending radius $B = \gamma_L B_0$. The magnetic field corrects the trajectory of higher energy particles for a constant cyclotron frequency. It is the principle of the isochronous cyclotron, or azimuthal varying field (AVF) cyclotron. The second idea, by E. Mc Millan in 1945, is to synchronise the frequency of the RF system with the revolution frequency $\omega_{RF} = \gamma_L \omega_0$: with this method, the created synchrocyclotron could accelerate protons to about 1 GeV. The first synchrocyclotron was built in 1947 in Berkeley, and was the first accelerator at CERN, operating from 1958 to 1990 [150].

# Appendix B

# Electromagnetic magnets for synchrotrons

This appendix introduces the forces and use of three electromagnetic magnets implemented in third-generation storage ring-based light sources: dipoles, quadrupoles and sextupoles.

## B.1 Electromagnetic dipoles

In a storage ring, the particles are enclosed in a circular trajectory, with distributed bending forces. The constant magnetic field which defines the particles' designed orbit is provided by dipoles, or bending magnets. They bend the charged particle's trajectory with an angle $\theta$ dependent on their length and bending radius $\rho$[m], according to $\sin(\theta) = \frac{l}{\rho} \simeq_{\theta \ll 1} \theta$. The bending radius is entirely defined by the magnetic field and the energy of the machine, according to Eq. (1.3).

An electromagnetic dipole is composed of two magnetic poles, surrounded by a coil and separated by a gap $2g$[m]. The ensemble is encapsulated in a ferromagnetic material, ensuring a better return path for the magnetic field. The coils are fed by an electric current I. The created magnetic flux of such a dipoles depends on both the current I and the gap left between the coils:

$$B_{dipole} = \mu_o \frac{I}{g} \tag{B.1}$$

with $B_{dipole}$ [T] the generated constant magnetic field, $\mu_o$ [H.m$^{-1}$] the permeability of the ferromagnetic encapsulation, $I$[A] the current in the coils and $g$[m] half the gap. Figure B.1 is a picture of a dipole in the Advanced Photon Source (APS) storage ring.

## B.2 Quadrupoles

Focusing forces require an affine magnetic field, which is achieved by quadrupoles. Electric quadrupoles were invented to compensate for the defocusing forces in linacs [153].

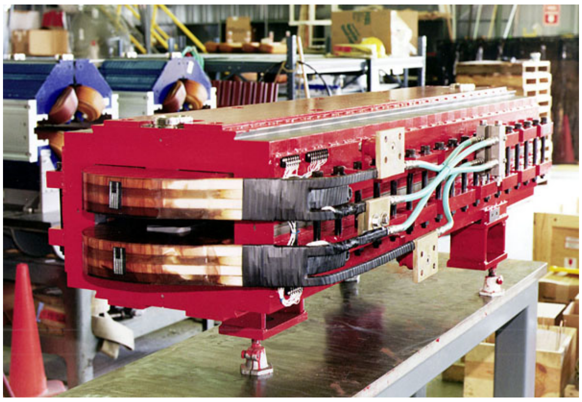

FIGURE B.1: Picture of a dipole magnet of the Advanced Photon Source (APS). From [151].

FIGURE B.2: Picture of a quadrupole magnet in the tunnel of the TRIUMF linac. From [152].

In synchrotrons, magnetic quadrupoles are implemented to focus the beam.

$$\begin{cases} B_x = g_1 y \\ B_y = g_1 x \end{cases} \Longrightarrow \begin{cases} F_x = -q v_z g_1 x \\ F_y = +q v_z g_1 y \end{cases} \tag{B.2}$$

with $g_1$[T.m$^{-1}$]= $\frac{B}{r}$ the quadrupole gradient, $\mathbf{B}$[T] the magnetic field of the poles, and $r$[m] the aperture radius of the quadrupole, $v_z$[m.s$^{-1}$] the longitudinal speed of the particle, $(x, y)$ the transverse coordinates. Figure B.2 displays a quadrupole of the TRIUMF storage ring. For an electromagnetic quadrupole, its gradient is linked to the electric current by the expression:

$$g\,[\mathrm{T.m}^{-1}] = \frac{2\mu_0 I}{r^2} \tag{B.3}$$

with $I$[A] the electric current, $\mu_0$[H.m$^{-1}$] the permittivity and $r$[m] the inner radius of the quadrupole. The linear force $F_x$ exerted by a quadrupole on the horizontal axis is, if $g > 0$, pushing the particles horizontally towards the ideal orbit: it is then called a focusing quadrupole. In this event, the force exerted in the vertical axis has the opposite sign, thus the opposite effect: it pushes the particles further away from the ideal orbit, or defocusing. To control the particles in both planes, at least one focusing and one defocusing quadrupoles are required. A basic cell controlling the beam size in both planes would include two quadrupoles per dipole, one focusing and one defocusing. Those cells are called FOcusing DefOcusing (FODO) cells. Figure B.3 illustrates the magnetic arrangement of a FODO arrangement. Quadrupoles are inserted in between dipoles, which draw the design path. The alternance of focusing and defocusing quadrupoles provoke the betatron oscillations.

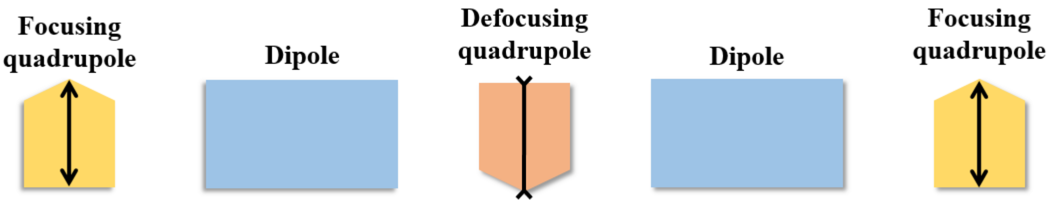

FIGURE B.3: Schematic of a typical FODO cell.

Quadrupoles are defined by their length and gradient. To be compared with the weak-focusing dipole strength $\frac{1}{\rho^2}$, the quadrupole gradient is made independent of the momentum, by dividing it with the beam rigidity. The normalised strength $k_1[\mathrm{m}^{-2}]$is defined:

$$k_1[\mathrm{m}^{-2}] = \frac{g[\mathrm{T.m}^{-1}]}{B\rho[\mathrm{T.m}]} \tag{B.4}$$

With the convention here applied, a positive strength $k_1[\mathrm{m}^{-2}]$ corresponds to a focusing quadrupole. Using the analogy with light optics, in thin lens approximation, the focal length of a quadrupole is $f_{quad} = \frac{1}{k_1 L}$, with $k_1$ its normalised focusing strength defined in Eq. (B.4) and $L$ its length.

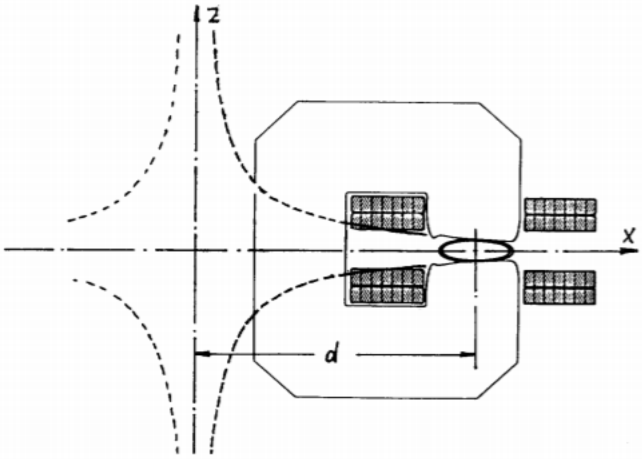

FIGURE B.4: Cross section of a synchrotron magnet: a quadrupole field is built by superimposing two extra coils on the side of a dipole magnet. Figure taken from [154].

Early strong-focusing accelerators used combined-function magnets: dipoles magnets had superimposed quadrupoles, as illustrated in Fig.B.4, which allowed focusing of the charged particles while bending their trajectory. They were called synchrotron magnets. Yet, the focusing forces available by superimposition are limited both in size and in magnetic saturation. To avoid this, nowadays most synchrotrons use separate-function magnets. The Fermilab 6.3 km Main Ring was the first to operate with separated-function magnets, increasing the strength of the focusing forces [155].

## B.3 Sextupoles

Since the chromaticity is created by a quadrupole strength variation of $-k_1\delta$, its correction requires to compensate it, with a magnet which the focusing (defocusing) strength increases (decreases) linearly with the momentum. Such compensation can be achieved using sextupoles, of magnetic flux:

$$\begin{cases} B_y = g_2(x^2 - y^2) \\ B_x = g_2 xy \end{cases} \tag{B.5}$$

with $g_2[\text{T.m}^{-2}] = \frac{1}{2}\frac{\partial^2 B}{\partial x^2}$. Figure B.5 displays the picture of a sextupole from SESAME. Sextupoles are composed of six coils of alternating polarity, encapsulated in a ferromagnetic material. The sextupole gradient is expressed in terms of electric current $I$[A] as:

$$g_2 = \frac{6\mu_0 I}{r^3} \tag{B.6}$$

with $\mu_0[\text{H.m}^{-1}]$ the permeability of the ferromagnetic encapsulation, and $r$[m] the aperture radius of the sextupole. As with quadrupole gradient, the sextupole gradient can be normalised into a momentum-independent sextupole strength $k_2[\text{m}^{-3}]= \frac{g_2[\text{T.m}^{-2}]}{B\rho[\text{T.m}]}$. They are often characterised by their integrated strength, $k_2 l[\text{m}^{-2}]$ with $l$ their length.

Only sextupoles located in a non-zero dispersion zone participate in the correction of the chromaticity. They are called the chromatic sextupoles. They create a chromaticity $\xi_{sext_u} = \frac{1}{4\pi}\int_{ring} k_2(s)D_x(s)\beta_u(s)ds$, which is corrective if its sign is positive. The total chromaticity of the ring is the sum of both the natural chromaticity and the corrective effect of the sextupoles:

$$\xi_{tot_u} = -\frac{1}{4\pi}\int_{ring} \left[k(s) - k_2(s)D_x(s)\right]\beta_u(s)ds \tag{B.7}$$

Correcting the chromaticity in both planes requires at least two sextupole families. A sextupole correcting the chromaticity in the horizontal plane is called a focusing sextupole, defocusing otherwise. Once the first-order chromaticity is corrected, the tune shift with momentum depends entirely on the second-order chromaticity, which can be significant in large rings. Additional families are then inserted in the ring to increase the degrees of freedom in minimising the tune shift.

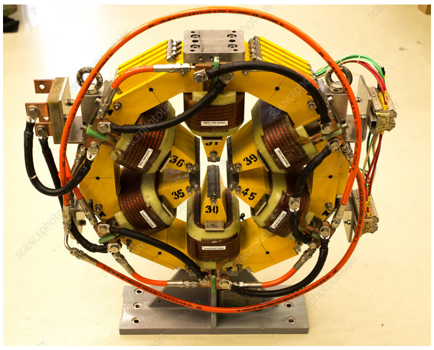

Figure B.5: Picture of a sextupole magnet of SESAME [156].

**Optimisation of the sextupole efficiency** Sextupole magnets trigger many first- and third-order resonances (*cf* section 2.1.3). To limit their negative effect on the dynamic, their strengths have to be lowered. Different placement strategies are possible as a first approach to minimise the sextupole gradients. First, a sextupole should preferably be located near focusing (resp. defocusing) quadrupoles, where the product $\beta_x D_x$ (resp. $\beta_y D_x$) is large for focusing (resp. defocusing) sextupoles. Secondly, to benefit from a large corrective effect provided by the product $(\beta_u D_x)_{u\in\{x,y\}}$, the location of the sextupole should minimise its effect on its defocusing plane. Indeed, in the case of a focusing sextupole, its effect on the vertical plane is $\beta_y D_x$, which adds constructively to the natural chromaticity, meaning it has to be compensated as well by the defocusing sextupoles. To minimise this defocusing effect, focusing (resp. defocusing) sextupoles should be located at a position $s$ where the ratio $\frac{\beta_x}{\beta_y}$ (resp. $\frac{\beta_y}{\beta_x}$) is the largest possible. Further strategies will be discussed in the section 2.3.

# Appendix C

# Properties of synchrotron radiation

## C.1 Frequency distribution of the radiated energy

The radiation emitted by highly relativistic particles comes from the instantaneous emission of quanta occurring in a bent trajectory. The radiation is emitted continuously during the bending process. For highly relativistic particles in a circular trajectory, the emission is enclosed in a cone, which direction copies the electron velocity's, as illustrated in Fig. C.1 from [157]. The cone is characterised by its opening angle $\frac{1}{\gamma_L}$.

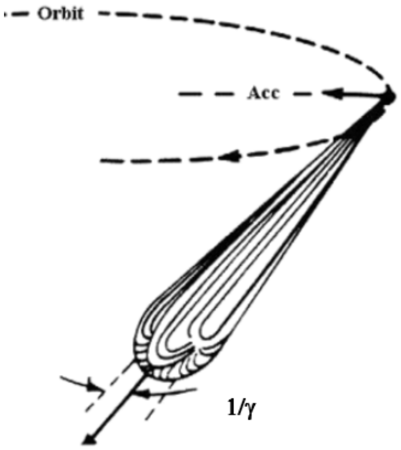

FIGURE C.1: Scheme of the cone of instantaneous mission for highly relativistic particles. From [157].

The emitted photon beam is polychromatic: the bandwidth defines the frequency range of the radiation. The wavelength can be selected in the beamline using monochromators [158]. The duration $t = \frac{2\rho}{\beta c \gamma}$ of the radiation is short: it provides a large continuous spectrum. Its most brilliant frequency is reached at half the pulse duration: it is the critical frequency $\omega_c$:

$$\omega_c = \frac{3c\gamma_L^3}{2\rho} \tag{C.1}$$

with $c$ the speed of light, $\gamma_L$ the Lorentz factor and $\rho$ the bending radius.

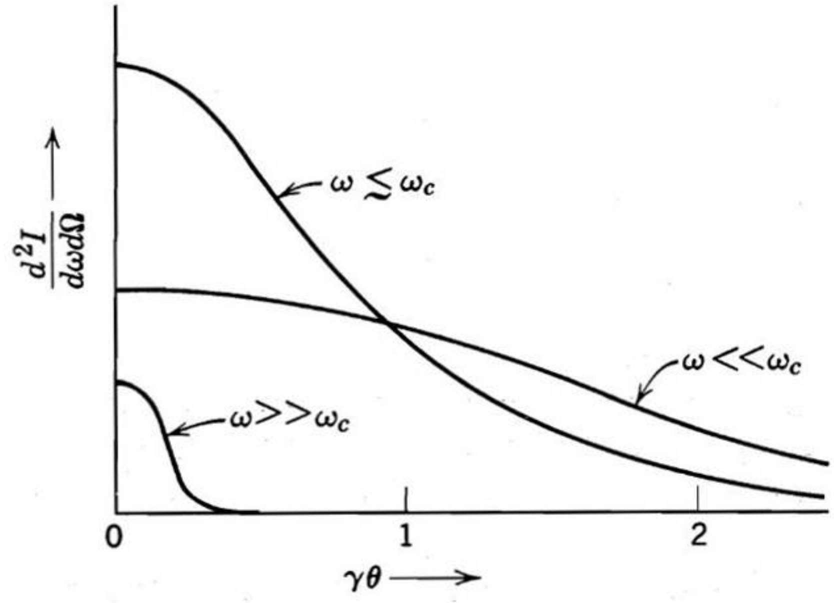

FIGURE C.2: Comparison of the radiation intensity per frequency per solid angle with the ratio of the deflecting angle $\theta$ with the cone opening angle $\frac{1}{\gamma_L}$ around the critical frequency. From [13].

Fig. C.2 illustrates the variation of the intensity per frequency and per solid angle of the radiation with the ratio of the emission angle $\theta$ with the cone opening angle $\frac{1}{\gamma_L}$, i.e. the relative position of the emitted photons in the radiation cone. Such variations depend on the photon frequency, as the radiation pikes at the critical frequency $\omega_C$, which maximum intensity is emitted at the critical angle $\theta_C \simeq \frac{1}{\gamma_L}(\frac{2\omega_C}{\omega})^{\frac{1}{3}}$. For lower frequencies emitted at the beginning of the radiation, the intensity varies slowly with the factor $\gamma_L\theta$, and can almost be considered independent of the emission angle. For higher frequencies $\omega \gg \omega_C$ and higher angles $\theta \gg \theta_C$, the radiation is negligible.

## C.2 Energy distribution of the radiated energy

The critical photon energy $E_C = \hbar\omega_c$ depends quadratically on the electron beam energy and linearly on the magnetic field according to:

$$E_c = \frac{3\hbar c}{2(mc^2)^3}\frac{E^3}{\rho} =_{e^-} 2.2183\frac{E^3[\text{GeV}]}{\rho[\text{m}]} = 0.665E^2[\text{GeV}]B[\text{T}] \tag{C.2}$$

Figure C.3 illustrates the energy distribution of the emitted radiation with the critical energy. The radiation of low-energy photon, which frequency is much lower than the critical frequency, does not depend on the critical energy. It appears that the larger the critical energy, the more photons are emitted at higher energies.

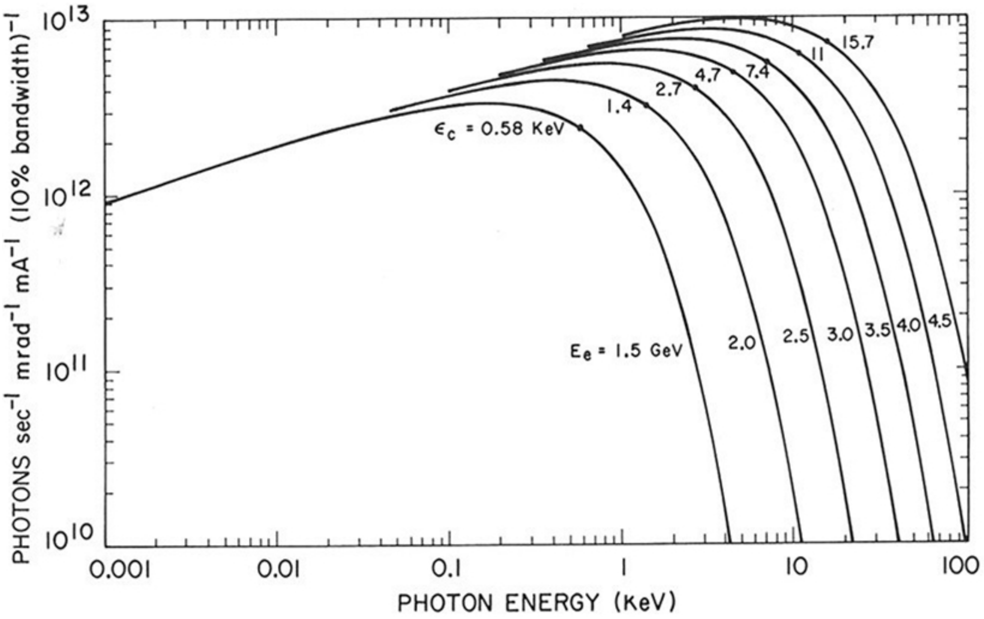

FIGURE C.3: Variation of the brilliance of the radiated photon beam with the photon energy, for different critical energies. From [13].

# Appendix D

# Radiation regime of an insertion device

Analogically to optical interferences on a network, the radiation emission occurs periodically, of period the undulator period $\lambda_u$[m]. Constructive interferences of such an optical network allow the emission of photons at the wavelengths:

$$\lambda_n = \frac{\lambda_u}{2\gamma_L^2 n}\left(1 + \frac{K_u^2}{2} + \gamma_L^2\theta^2\right) \tag{D.1}$$

where $\theta = \frac{v_x}{v_z} \approx \frac{K_u}{\gamma_L}\sin(k_u z)$ the emission angle and $K_u \equiv \frac{eB_0\lambda_u}{2\pi mc}$ is the undulator parameter. This equation is the undulator equation, characterising its radiation comb: the thickness of the pike at any harmonic $\lambda_n$ depends entirely on the number of periods $N_u$. The higher $N_u$, the more selective is the interference, and the lower the bandwidth $\left(\frac{\Delta\lambda}{\lambda}\right)_n \sim \frac{1}{nN_u}$.

Figure D.1 illustrates the radiation spectrum emitted from insertion devices. Undulators and wigglers are manipulated by the synchrotron radiation users, to match their experimental requirements: indeed, the gap of the insertion device can be mechanically modified to vary their $K_u$ factor and therefore shifts the radiation spectrum accordingly. This property is called the tunability.

The parameter $K_u$ defines in which radiation regime the undulator is. For $K_u \ll 1$, the deflecting angle $\theta = \frac{1}{\gamma_L\sqrt{N_u}}$ is lower than the cone opening angle $\frac{1}{\gamma_L}$ where $N_u$ defines the number of periods. In that case, the intensity of the radiation is proportional to $N_u^2$. A longer undulator will then produce a more brilliant photon beam. Undulators are then insertion devices of weaker field or short periods. In the case of ($K_u \gtrsim 1$), the magnetic field resembles a Dirac series of alternating sign: the radiation is emitted at angles much larger than the cone opening angle. The emission occurs on a broader wavelength range, of intensity proportional to $N_u$. Such devices are wigglers.

An insertion device is therefore characterised by four main parameters: its period $\lambda_u$, which defines the wavelength spectrum of the emitted photons, its gap $2g$, its factor $K_u$ and its length $L_u$. These parameters govern the shape of the emitted radiation.

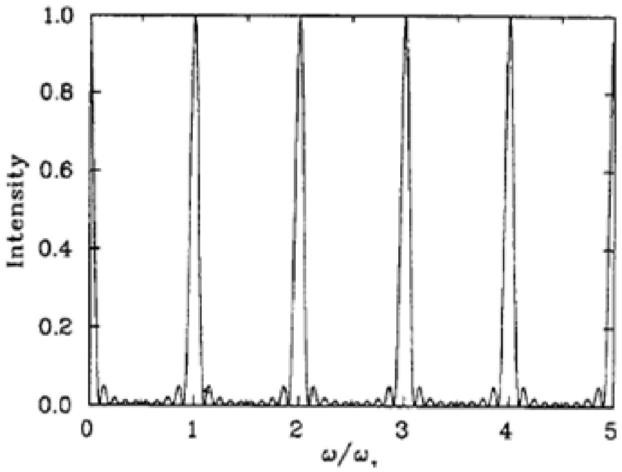

FIGURE D.1: Radiation emission of an undulator. The comb thinness depends entirely on the K factor. From [157].

Different types of insertion devices are implemented in third generation storage rings, to comply with the different requirements of synchrotron radiation users. A brief overview of some insertion devices is given in Appendix E.

# Appendix E

# Types of insertion devices

Different types of wigglers and undulators are used in third-generation storage ring.

**Types of magnets** The basic insertion device is composed of permanent magnets (PM), disposed along a planar axis. The resulting sinusoidal magnetic field, either vertical or horizontal, creates a photon beam linearly polarised. The PM are organised regarding their field integral and remaining field. Using a special software, the undulator is built piece by piece to better match its theoretical magnetic field. Small displacements of the PM are possible to correct potential magnet field imperfections.

Electromagnetic magnets Permanent magnets fix the magnetic field peak for the undulator. The use of electromagnetic magnets allows fast variation of the magnetic field, thus controlling the combs. Yet, the peak magnetic field achievable remains lower than with permanent magnets.

Superconducting magnets The use of superconducting magnets allows a higher magnetic field peak, for a shorter magnet. Their use requires cryogenic cooling to achieve temperature below 10 K, for best performances.

**Types of polarisation** As the basic undulator creates a one-dimensional magnetic field, the polarisation of its emitted radiation is linear: either vertical or horizontal depending on the direction of the magnetic field. Circular polarisation can be achieved using helical undulators. Varying the polarisation is achievable with APPLE-II-types undulators.

Helical undulators or wigglers To create a circular polarisation, the electrons should see similar oscillatory magnetic field in both the vertical and the horizontal plane. Such a magnetic field $\mathbf{B} = B_0(\mathbf{x}\cos(\frac{2\pi s}{\lambda_u}) + \mathbf{z}\sin(\frac{2\pi s}{\lambda_u}))$ is created by either superposing two planar undulators and shifting them by a period, or by introducing a magnetised ferromagnetic helix, placed along the axis [160]. The polarisation of the radiation is then circular, as illustrated in Fig. E.1, from [159].

APPLE-II undulator Choosing the polarisation of the emitted photon beam is possible using an APPLE-II undulator[161, 162]. Such an undulator is composed

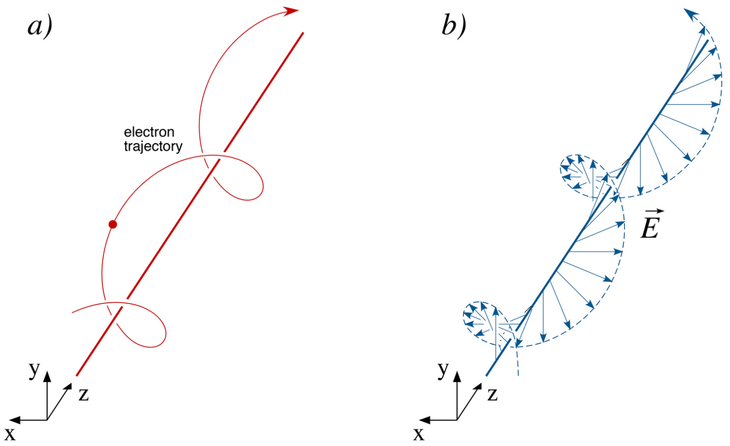

FIGURE E.1: Motion of the electrons in an helical undulator, and resulting photon beam polarisation, from [159].

of four arrays, four blocks per period. Longitudinally shifting two opposing magnetic arrays varies the magnetic field of the undulator, thus the polarisation of the radiation: the achievable polarisations are illustrated in Fig. E.2.

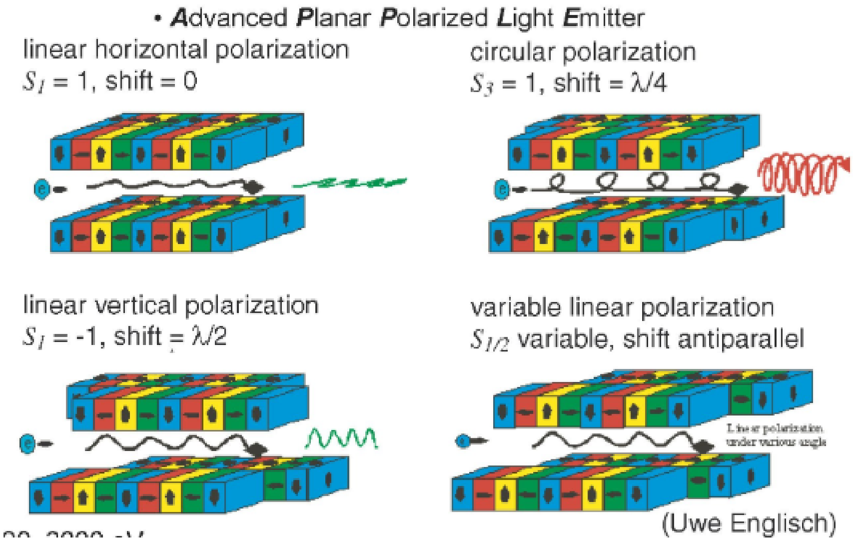

FIGURE E.2: Achievable polarisations of the emitted radiation from an APPLE-II undulator, from [161].

Revolver undulator To provide users with more flexibility in the period of planar undulators, two pairs of arrays can be placed on two rotating bras: the users then have the choice between two undulators of different periods. Revolver undulators were first developed as an out-vacuum undulator at Photon Factory, Japan, in 1989 [163] and are widely used [164, 165]. Its use is demonstrated in [166]. For instance, Fig. E.3 is a schematic of the commissioned revolver undulator for the beamline BL15XU at SPring-8 [164]: it allows the user to switch between a planar undulator and a helical undulator, therefore changing the polarisation of the photon beam.

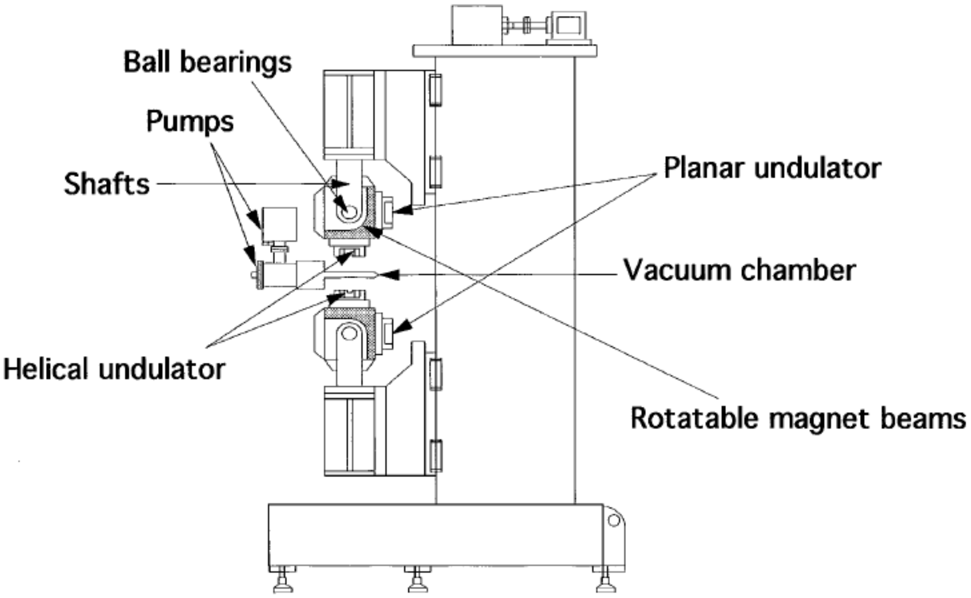

Figure E.3: Description of the SPring-8 revolver undulator for the BL15XU beamline, from [164].

**In-vacuum and cryogenic insertion devices** Further reduction of the undulator gap can be achieved by placing the undulator in-vacuum: the vacuum chamber is therefore no longer a limitation. The first undulator operating in-vacuum was designed and tested in KEK, Japan [167] They must be composed of permanent magnets which have to be coated and baked. The achievable gap can be as low as 2 mm [168]. Undulators and wigglers can be placed in a cryogenic chamber [23], to benefit from the remanent field of PM at low temperature.

# Appendix F

# Design of a 9BA HOA lattice

The design of a HOA 20-fold symmetry lattice for the SOLEIL upgrade demanded further exploration of its main characteristics. Since the HOA is based on a sequence of unit cells, both its phase advance and the number of unit cells per period are to be determined. In the main part of the present thesis, 7BA lattices were compared, with a HOA phase advance of $(\frac{3}{7}, \frac{1}{7})$. This appendix presents a 9BA lattice, with phase advances of $(\frac{3}{11}, \frac{1}{11})$. Please refer to the section 3.2.3 for a detailed explanation of this couple. Figure F.1 displays the Twiss functions and dispersion of the new unit cell. The reduction of the unit cell phase advance and the length of the half-dipole to 0.22 m reduces the dispersion level, which reaches 0.013 m maximum, compared to 0.0195 m in the case of the $(\frac{3}{7}, \frac{1}{7})$ unit cell with 0.3 m half-dipole in Fig. 3.4.

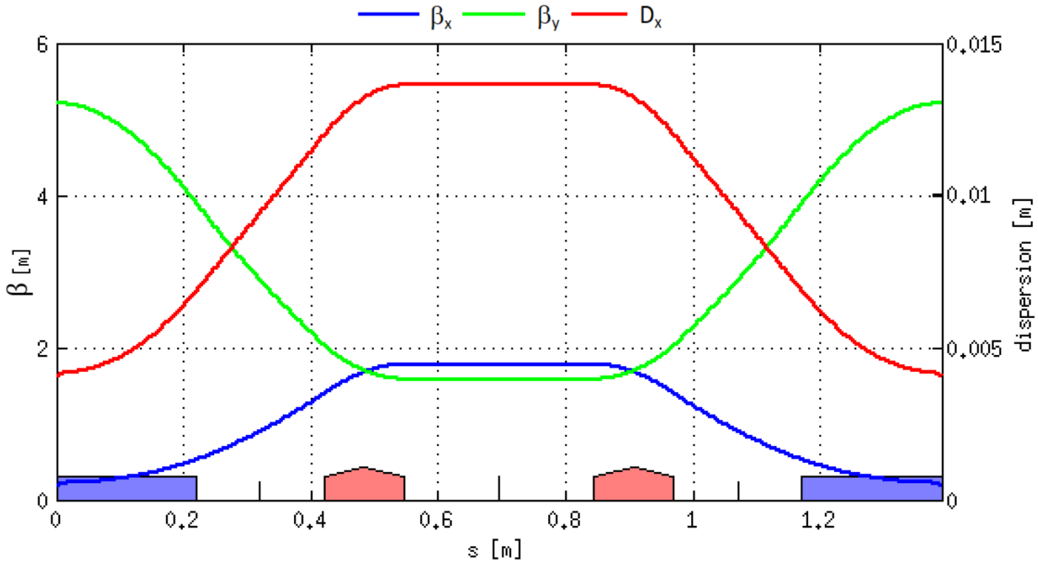

FIGURE F.1: Twiss parameters and dispersion of a HOA unit cell, which unit cell phase advances are $(\nu_x, \nu_y) = (\frac{3}{11}, \frac{1}{11})$.

The momentum compaction factor of the unit cell is $1.39 \times 10^{-4}$, and a natural emittance of 48 pm.rad, with no addition of reverse bends. These values will be modified by the addition of a dispersion-free straight section and the necessary matching section.

Figure F.2 displays the Twiss parameters and dispersion of the designed 9BA HOA period.

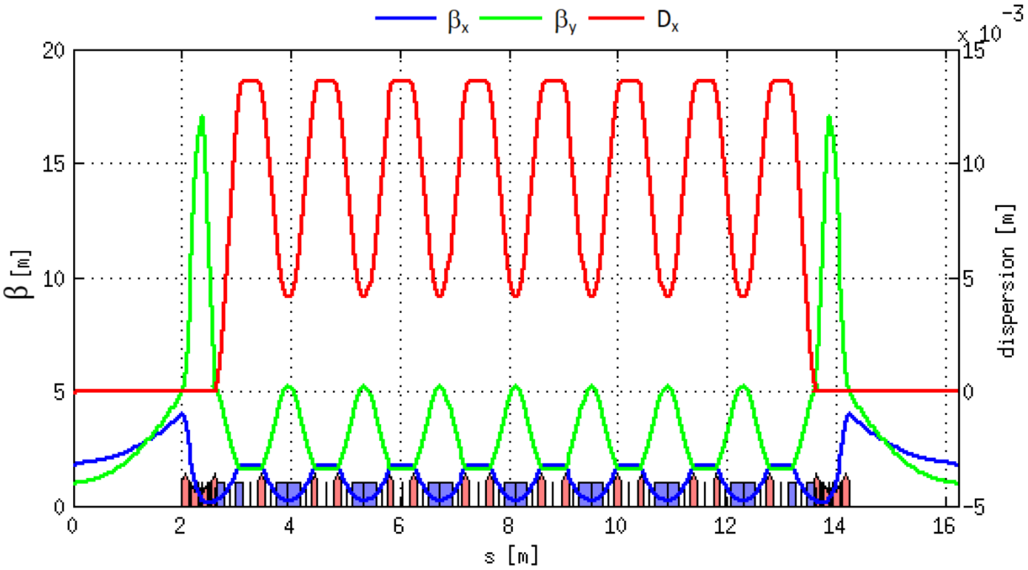

FIGURE F.2: Twiss parameters and dispersion of a 9BA HOA lattice, which unit cell phase advances are $(\nu_x, \nu_y) = (\frac{3}{11}, \frac{1}{11})$.

Table F.1 lists the main characteristics of the above lattice. The lattice achieves a natural horizontal emittance of 71 pm.rad, with no reverse bends. The angular dispersion suppressor method is applied, which requires the insertion of a reverse bending angle of -0.66 degrees. The low dispersion level along the lattice yields to a low momentum compaction factor, $6.80 \times 10^{-5}$. This value remains slightly higher than the 7BA HOA lattice, due to the absence of reverse bending angles in the core and the longer dispersive zone.

TABLE F.1: SOLEIL 2.75 GeV 9BA HOA lattice proposal, 20-fold symmetry.

| | |
|---|---|
| Emittance $\epsilon_x$ | 71 pm.rad |
| Tunes per period $(\nu_x, \nu_y)$ | (3.74, 1.10) |
| Momentum compaction factor $\alpha_0$ | $6.80 \times 10^{-5}$ |
| Reverse bending angle | 0(core)/-0.66(disp. suppressor) degrees |
| Energy loss per turn | 29 keV |
| Energy spread | $9.69 \times 10^{-4}$ |
| Natural chromaticities $(\xi_x, \xi_y)$ | (-5.23, -8.30) |
| $(\beta_x, \beta_y)$ @ID | (1.9, 1.0) m |

Figure F.3 displays the variation of the transverse dynamic aperture with the energy deviation. The scheme is typical of the encountered HOA lattices: a small acceptance but almost constant with energy deviation.

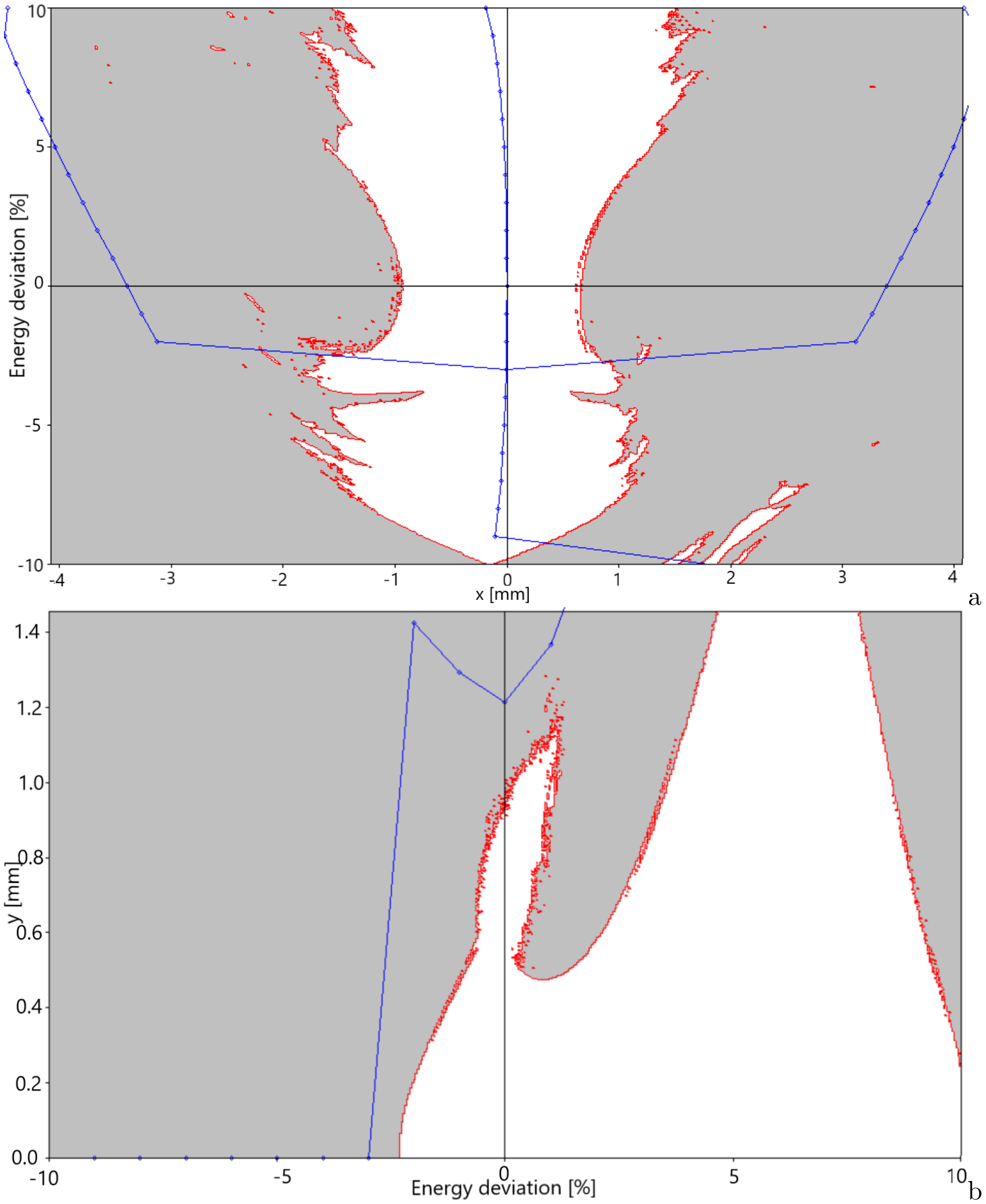

FIGURE F.3: Dynamic aperture with energy deviation for (a) the horizontal plane and (b) the vertical plane.

# Appendix G

# Variation of the function $f : (\phi, \phi_S)$ with the synchronous phase

This appendix gathers the complete variations of the defined function $f : (\phi, \phi_s) \longmapsto \cos(\phi) + \cos(\phi_s) + [\phi - (\pi - \phi_s)] \sin(\phi_s)$ where $\phi$ is the phase advance and $\phi_s$ is the synchronous phase. The function is used and defined in the Chapter 5.

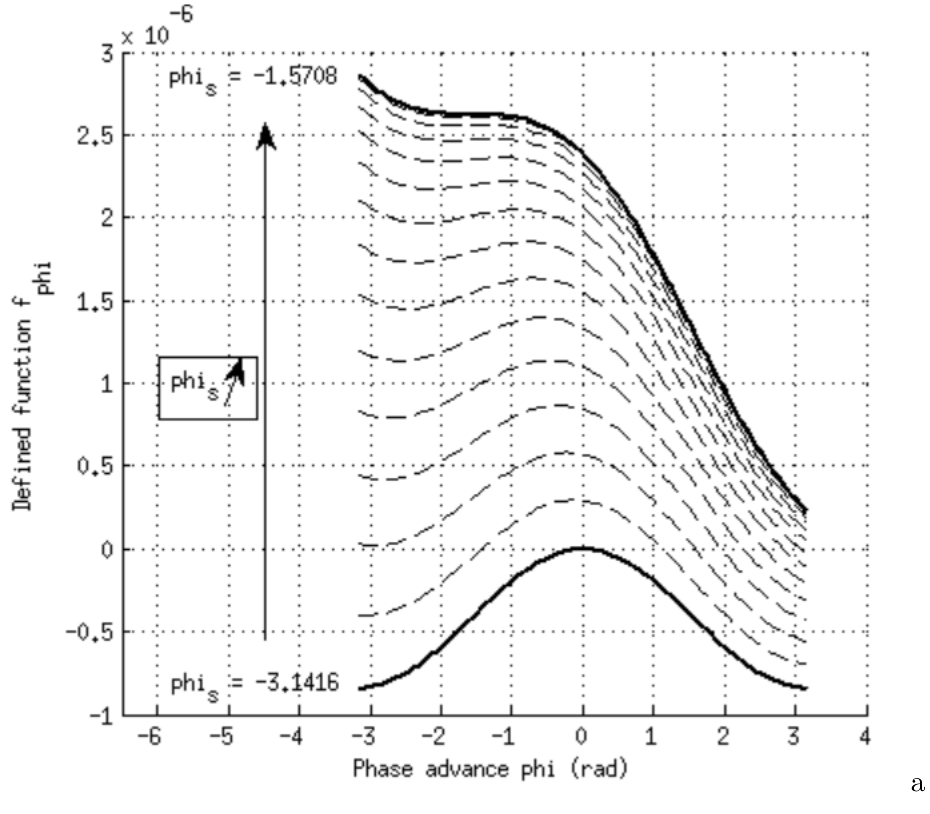

FIGURE G.1: Variation of the function $f : (\phi, \phi_s)$ over a period $[-\pi, \pi]$ for different (a) $\phi_s \in [-\pi, -\frac{\pi}{2}]$.

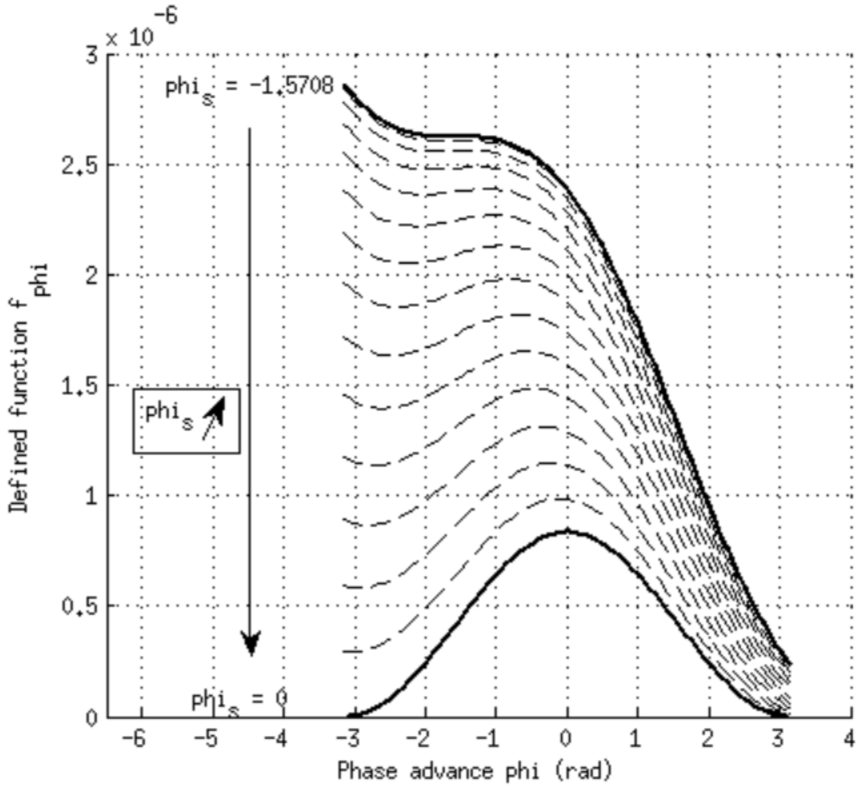

b

FIGURE G.2: Variation of the function $f : (\phi, \phi_s)$ over a period $[-\pi, \pi]$ for different (b) $\phi_s \in [-\frac{\pi}{2}, 0]$.

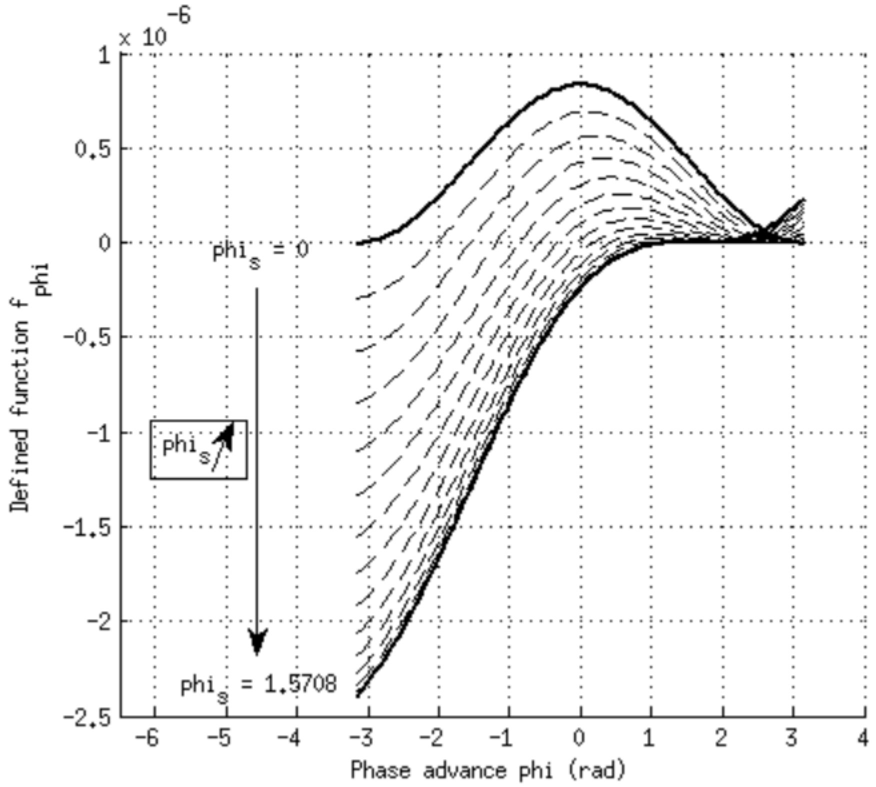

c

FIGURE G.3: Variation of the function $f : (\phi, \phi_s)$ over a period $[-\pi, \pi]$ for different (c) $\phi_s \in [0, \frac{\pi}{2}]$.

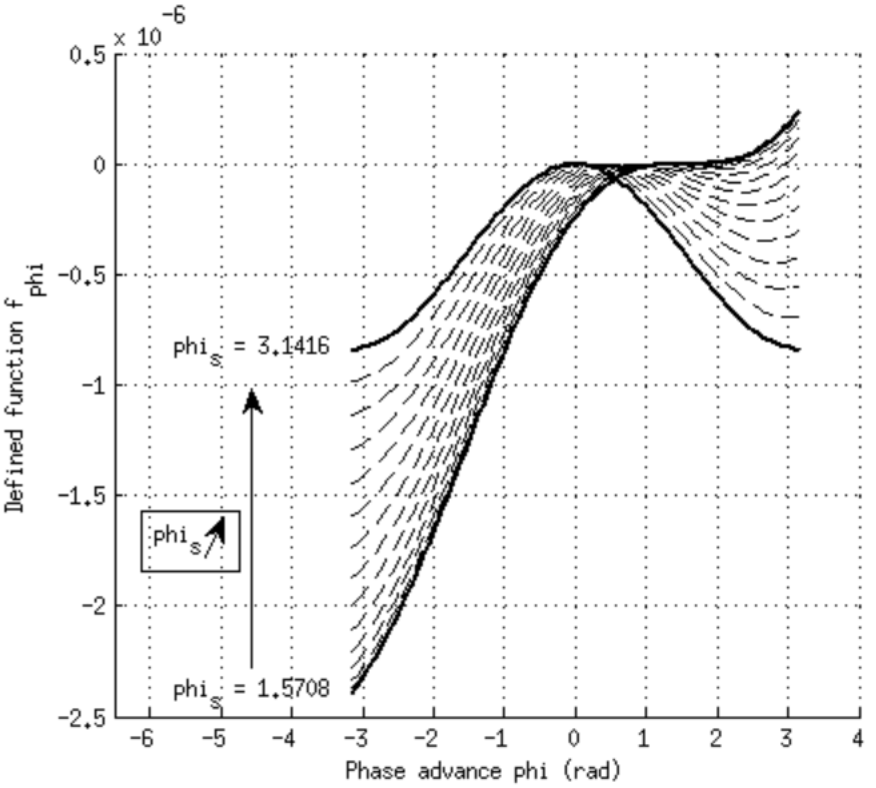

d

FIGURE G.4: Variation of the function $f : (\phi, \phi_s)$ over a period $[-\pi, \pi]$ for different (d)$\phi_s \in [\frac{\pi}{2}, \pi]$.

# Appendix H

# Extension of MOGA-Bmad: list of changes and files

To analytically calculate the first-order momentum compaction factor, I wrote a Fortran90 script to be read by Bmad, alike the script already written for A.T.. To compare both codes and ease problem solving, I also included the calculation of the zeroth-order dispersion and momentum compaction factor. The full script and all necessary files are available in my GitHub [136]. It was successfully tested on both the HOA 7BA lattice and the hybrid 7BA lattice.

## H.1 Input file: common.in

The longitudinal optimisation process can be either a simple minimisation or requires the definition of an upper limit, as described above. Therefore, it was necessary to add one line in the generic input file of MOGA-Bmad, 'common.in'. In the section &nl_moga, the variable 'alpha1max' has been created. Subsequently, the module held in 'namelist_moga_alpha.f90' has been adapted to read the new 'common.in' file. If the value of 'alpha1max' is negative, the program uses the minimisation process and the objective function is defined by Eq. (5.47). If positive, the given value is used as an upper bound on $\alpha_1$, and the objective value is defined by Eq. (5.48).

## H.2 List of the added files and their location

- alpha_modules.f90: The necessary functions are gathered there to analytically calculate the three first orders of the momentum compaction factor. Contrary to A.T. where each Fourier harmonic and higher-order components of both the dispersion and the momentum compaction factor had their own independent function, I decided to define only two functions: one deriving all the Fourier harmonics, named $F_{0n}$, $F_{1n}$ and $F_{2n}$, and a second function deriving the contribution of the different dispersion components to the higher-order MCF integrals of Eq. (5.34). The outputs of the second function are directly the zeroth-, first- and second-order momentum compaction factors.

- alpha_program.f90: To test and debug the latter functions, I wrote a little program, linked to the environmental variable *alpha_opt*, which gathers the Twiss functions of a lattice and calculate its three lowest-orders in momentum compaction factors.
- namelist_moga_alpha.f90: reads the new 'common.in' &nl_moga section.
- moga_alpha.f90: Main file of the extended version of MOGA, including the fourth objective function. Its use is identical to the basic moga file. It is linked to the environmental variable *moga_alpha* for later use.
- cmake.alpha_opt: Creation of an environmental variable to calculate the higher orders of the momentum compaction factor externally to MOGA.
- cmake.moga_alpha: Creation of an environmental variable linked to the extended MOGA main file.
- Location of the above files:

| File name | Location |
|---|---|
| alpha_modules.f90 | DIST_BASE\DIR\util_program\modules\ |
| alpha_program.f90 | DIST_BASE\DIR\util_program\alpha_opt\ |
| namelist_moga_alpha.f90 | DIST_BASE\DIR\util_program\modules\ |
| moga_alpha.f90 | DIST_BASE\DIR\util_program\moga\ |
| cmake.alpha_opt | DIST_BASE\DIR\util_program\ |
| cmake.moga_alpha | DIST_BASE\DIR\util_program\ |

## H.3 Running the extended version

Once the files are downloaded and included in their specified location, the program can be run similarly to the transverse MOGA version, using the command: $BBIN\moga_alpha common.in PISA_ 1.0 &, with $BBIN the path to the util_program bin folder. No change in the environment should be needed.

## H.4 Output files

Following the organisation of the current MOGA-Bmad version, I included a fourth column in the objective section of the output file 'moga_results.out'. This allows the user to check the progress of this particular value during the optimisation process.

The analysis files that we were provided with thanks to M. Ehrlichman had to be adapted to take into account the fourth component: indeed, when the last generation is completed and evaluated, the user can manually select the individuals to be further

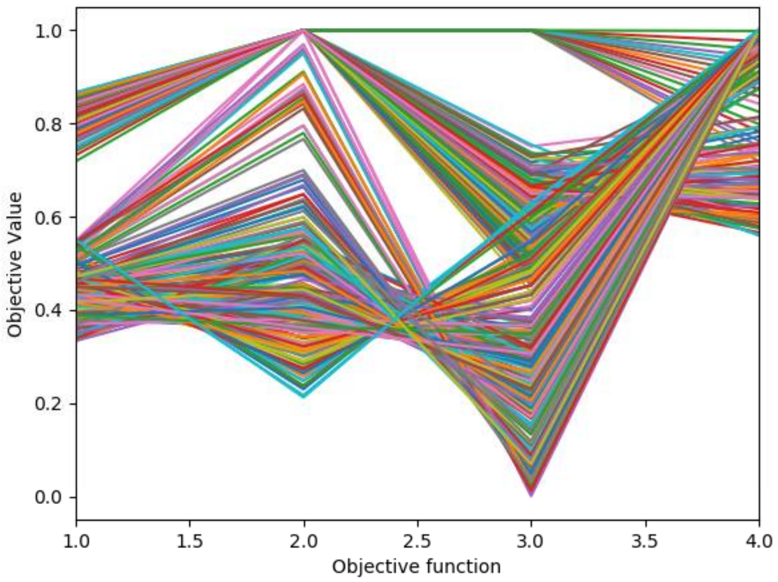

FIGURE H.1: Example of the objective function values during an optimisation conducted on the 5BA lattice. The three first objective functions refer to the dynamic aperture at 0%, +1% and −1%. The fourth corresponds to the minimisation of the first-order momentum compaction factor.

analysed, by comparing the values of the objective functions in a python interactive figure, illustrated in Fig. H.1.

The fourth objective is located at the number 4 on the horizontal axis. Its value among the last generation varies from $\simeq 0.58$ to $\simeq 1$ in this example, which proves the optimisation managed to minimise $\alpha_1$ at a higher level than the A.T. scan.

# Appendix I

# 6D optimisation of an ultra-low emittance lattices - evaluation of the selected solutions

This appendix presents some steps of the analysis of the selected solutions of the optimisation of the 5BA 24-fold symmetry lattice. The optimisation parameters were presented in 5.5.2.1.

## I.1 Optimisation of the 5BA lattice - Frequency map analysis

Figure I.1 displays the frequency map analysis of the remaining individuals of Fig. 5.31.

## I.2 Optimisation of the 5BA lattice - Sextupole strengths

Table I.1 lists the strengths of the sextupoles and octupoles of the seeds above.

TABLE I.1: Strengths of the 5BA optimisation variables.

| Name | Seed 3559343 | Seed 3861682 | Seed 3956872 | Seed 3969548 |
|---|---|---|---|---|
| sxd1 | $-81.45\mathrm{m}^{-2}$ | $-129.7\mathrm{m}^{-2}$ | $-99.09\mathrm{m}^{-2}$ | $-76.47\mathrm{m}^{-2}$ |
| sxf1 | $77.35\mathrm{m}^{-2}$ | $76.76\mathrm{m}^{-2}$ | $79.84\mathrm{m}^{-2}$ | $75.55\mathrm{m}^{-2}$ |
| sxd2 | $-71.49\mathrm{m}^{-2}$ | $-9.50\mathrm{m}^{-2}$ | $-53.33\mathrm{m}^{-2}$ | $-2.897\mathrm{m}^{-2}$ |
| sxf2 | $-72.20\mathrm{m}^{-2}$ | $-91.99\mathrm{m}^{-2}$ | $-105.1\mathrm{m}^{-2}$ | $-70.26\mathrm{m}^{-2}$ |
| sxd3 | $-332.6\mathrm{m}^{-2}$ | $-281.0\mathrm{m}^{-2}$ | $-294.8\mathrm{m}^{-2}$ | $-489.2\mathrm{m}^{-2}$ |
| sx1 | $158.0\mathrm{m}^{-2}$ | $47.80\mathrm{m}^{-2}$ | $118.1\mathrm{m}^{-2}$ | $193.6\mathrm{m}^{-2}$ |
| sx2 | $-175.\mathrm{m}^{-2}$ | $-194.6\mathrm{m}^{-2}$ | $-19.6\mathrm{m}^{-2}$ | $-195.5\mathrm{m}^{-2}$ |
| oct1 | $9951\mathrm{m}^{-3}$ | $9896\mathrm{m}^{-3}$ | $9979\mathrm{m}^{-3}$ | $9978\mathrm{m}^{-3}$ |
| oct2 | $9923\mathrm{m}^{-3}$ | $9895\mathrm{m}^{-3}$ | $9876\mathrm{m}^{-3}$ | $9892\mathrm{m}^{-3}$ |

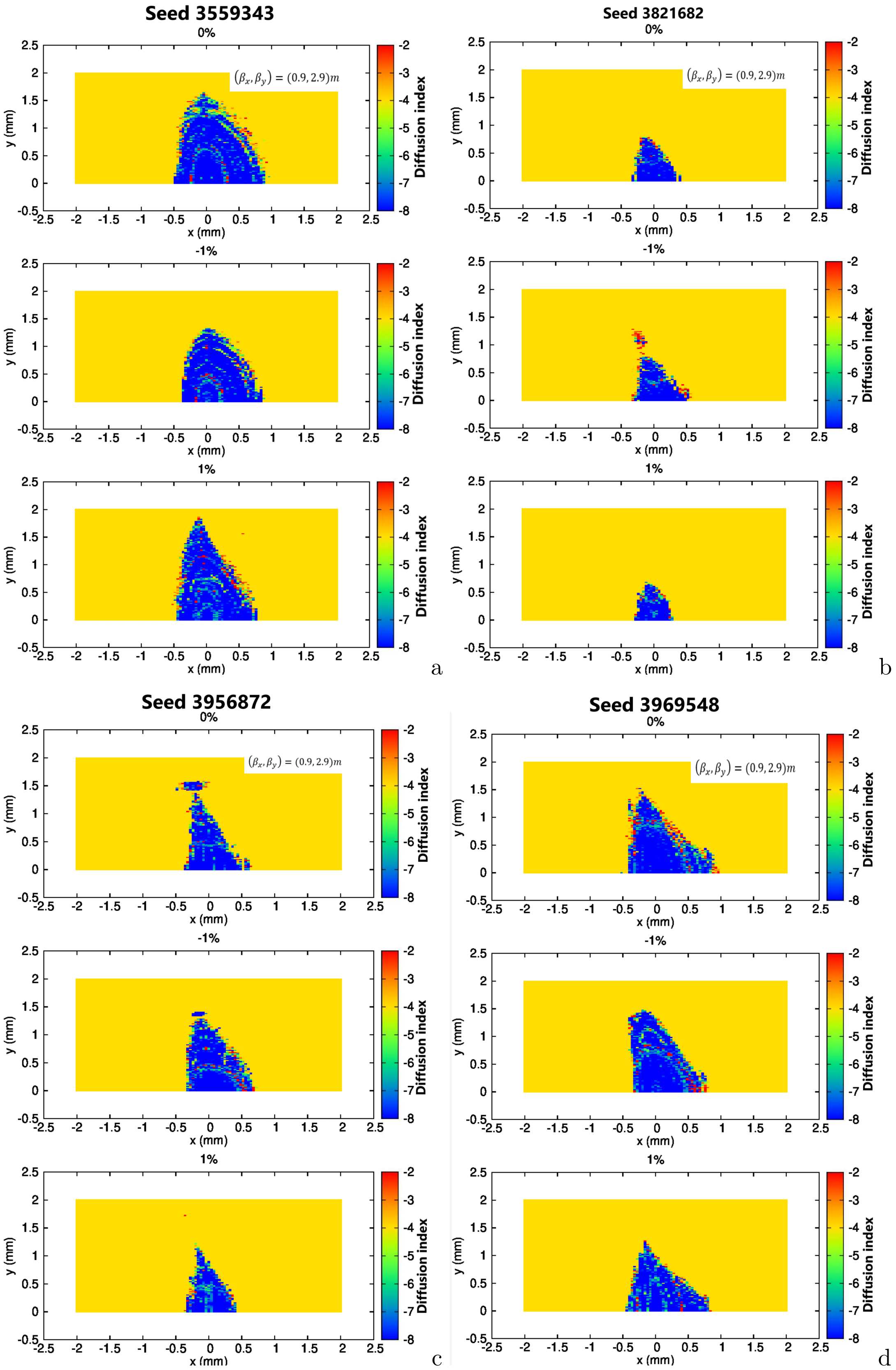

FIGURE I.1: Frequency map analysis of the remaining selected seeds of a 5BA optimisation, using the extended version of MOGA: (a) seed 3559343, (b) seed 3861682, (c) seed 3956872 and (d) seed 3969548.

# Appendix J

# First-order canonical perturbation theory

## J.1 Generating function

Following Takao's paper on nonlinear chromaticity [139], one builds the action-angle variable $(\overline{\phi}, \overline{J})$ which verify $\frac{dJ}{ds} = cst$ in the perturbed space. For this purpose, we introduce the canonical transformation $S(\phi, \overline{J}, s) = \phi \overline{J} + S_1(\phi, \overline{J}, s)$, resulting in the Hamiltonian:

$$\overline{H}(\overline{J}, s) = H_0(\overline{J}, s) + K_1(\overline{J}, s) \tag{J.1}$$

which is independent of $\phi$ thanks to the choice of $S_1$ [139]:

$$S_1(\phi, \overline{J}, s) = \sum_m \frac{i}{2\sin(m\pi\nu)} \int_s^{s+C} ds' e^{im(\phi+\psi(s')-\psi(s)-\pi\nu)} F_1(m, \overline{J}, s) \tag{J.2}$$

Alike the perturbation, $S_1$ can be split into three parts depending on the phase dependency:

$$\begin{aligned}
S_{1,1}(\phi, J, s) &= \frac{J_x^{3/2}}{2\sqrt{2}\sin(\pi\nu_x)} \int_s^{s+C} ds' \sqrt{\beta_x}\,(g_1\beta_x + k_x\gamma_x)\,(-\sin(\phi_x + \overline{\psi}(s', s)) \\
&+ \frac{J_x^{1/2}J_y}{2\sqrt{2}\sin(\pi\nu_x)} \int_s^{s+C} ds' \sqrt{\beta_x}\,(-g_1\beta_y + k_x\gamma_y)\,(-\sin(\phi_x + \overline{\psi}(s', s)) \\
&+ \frac{J_x^{3/2}}{\sqrt{2}\sin(\pi\nu_x)} \int_s^{s+C} ds' k_x\beta_x^{-1/2}\alpha_x \Big(\cos(\phi_x + \overline{\psi}(s', s)) - \alpha_x \sin(\phi_x + \overline{\psi}(s', s))\Big) \\
&+ \frac{J_x^{3/2}}{2\sqrt{2}\sin(\pi\nu_x)} \int_s^{s+C} ds' k_x\beta_x^{-1/2} \sin(\phi_x + \overline{\psi}(s', s)),
\end{aligned} \tag{J.3}$$

$$\begin{aligned}
S_{1,3}(\phi, J, s) &= \frac{J_x^{3/2}}{6\sqrt{2}\sin(3\pi\nu_x)} \int_s^{s+C} ds' \sqrt{\beta_x} g_1 \beta_x (-\sin(3\phi_x + 3\overline{\psi}(s', s))) \\
&+ \frac{J_x^{3/2}}{\sqrt{2}\sin(3\pi\nu_x)} \int_s^{s+C} ds' k_x \beta_x^{-1/2} \alpha_x \Big(\cos(3\phi_x + 3\overline{\psi}(s', s)) - \alpha_x \sin(3\phi_x + 3\overline{\psi}(s', s))\Big) \\
&+ \frac{J_x^{3/2}}{2\sqrt{2}\sin(\pi\nu_x)} \int_s^{s+C} ds' k_x \beta_x^{-1/2} \sin(3\phi_x + 3\overline{\psi}(s', s)),
\end{aligned} \tag{J.4}$$

and

$$\begin{aligned}
S_{1,2}(\phi, J, s) = -&\frac{J_x^{1/2} J_y}{4\sqrt{2}\sin(\pi\nu_x)} \times \\
&\int_s^{s+C} ds' \sqrt{\beta_x} \left(-g_1\beta_y + \frac{k_x}{\beta_y}(\alpha_y^2 - 1)\right) \sin(\phi + \overline{\psi_x}(s', s) \pm 2\phi_y)
\end{aligned} \tag{J.5}$$

## J.2 Derivative of the phase $\phi_{x,y}$ with regard to the longitudinal position $s$

As defined, the derivative of the unperturbed phase advance is :

$$\frac{d\psi}{ds} = \frac{1}{\beta} \tag{J.6}$$

The derivative of the angle from the action-angle coordinates is, by definition:

$$\frac{d\phi}{ds} = \frac{\partial H}{\partial J} = \frac{H_0}{J} + \frac{\partial V}{\partial J} \tag{J.7}$$

The derivative of the horizontal angle therefore is:

$$\begin{aligned}
\frac{d\phi_x}{ds} = \frac{\partial H}{\partial J_x} &= \frac{\partial H_0}{\partial J_x} + \frac{\partial V}{\partial J_x} \\
&= \frac{1}{\beta_x} + \frac{3J_x^{1/2}\sqrt{\beta_x}}{2\sqrt{2}}(g_1\beta_x + k_x\gamma_x)\cos(\phi_x) \\
&\quad + \frac{J_y\sqrt{\beta_x}}{2\sqrt{2}J_x^{1/2}}(-g_1\beta_y + k_x\gamma_y)\cos(\phi_x) \\
&\quad + \frac{3J_x^{1/2}}{2\sqrt{2\beta_x}} k_x\alpha_x \left(\sin(\phi_x) + \alpha_x\cos(\phi_x)\right) \\
&\quad - \frac{3J_x^{1/2}}{2\sqrt{2\beta_x}} k_x\cos(\phi_x) + \frac{J_x^{1/2}\sqrt{\beta_x}}{2\sqrt{2}}(g_1\beta_x)\cos(3\phi_x) \\
&\quad + \frac{3J_x^{1/2}}{2\sqrt{2\beta_x}} k_x\alpha_x \left(\sin(3\phi_x) + \alpha_x\cos(3\phi_x)\right) \\
&\quad + \frac{J_x^{-1/2} J_y\sqrt{\beta_x}}{4\sqrt{2}} \left(-g_1\beta_y + \frac{k_x}{\beta_y}(\alpha_y^2 - 1)\right)\cos(\phi_x \pm 2\phi_y)
\end{aligned} \tag{J.8}$$

and as for the vertical angle:

$$\begin{aligned}\frac{d\phi_y}{ds} &= \frac{\partial H}{\partial J_y} = \frac{\partial H_0}{\partial J_y} + \frac{\partial V}{\partial J_y} \\ &= \frac{1}{\beta_y} + \frac{J_x^{1/2}\sqrt{\beta_x}}{\sqrt{2}}\left(-g_1\beta_y + k_x\gamma_y\right)\cos(\phi_x) \\ &\quad + \frac{1}{2\sqrt{2}}J_x^{1/2}\sqrt{\beta_x}\left(-g_1\beta_y + \frac{k_x}{\beta_y}(\alpha_y^2 - 1)\right)\cos(\phi_x \pm 2\phi_y)\end{aligned} \tag{J.9}$$

#### J.2.0.1 Differentiation model

The amplitude is a sum of terms of form:

$$f : (\phi, J, s) \longmapsto A(J, s)\int_s^{s+C} ds' B(J, s')\cos(n\phi(s) + m\psi(s') - m\psi(s) - m\pi\nu) \tag{J.10}$$

where $A(J, :)$ and $B(J, :)$ are C-periodic. Therefore, the derivative of the function $f$ regarding the longitudinal position $s$ writes:

$$\frac{\partial f}{\partial s}(\phi, J, s) = \frac{\partial A}{\partial s}(J, s)I(\phi, J, s) + A(J, s)\frac{\partial I}{\partial s}(\phi, J, s), \tag{J.11}$$

where $I(\phi, J, s) = \int_s^{s+C} ds' B(J, s')\cos(n\phi(s) + m\psi(s') - m\psi(s) - m\pi\nu)$. To ease the differentiation, let us isolate the phase term which only depends on $s$ from the integral:

$$\begin{aligned}I(\phi, J, s) = \cos(n\phi(s) - m\psi(s))\int_s^{s+C} ds' B(J, s')\cos(m\psi(s') - m\pi\nu) \\ - \sin(n\phi(s) - m\psi(s))\int_s^{s+C} ds' B(J, s')\sin(m\psi(s') - m\pi\nu)\end{aligned} \tag{J.12}$$

Since $B(J, :)$ is C-periodic, the derivative of $I$ can be expressed as:

$$\begin{aligned}\frac{\partial I}{\partial s}(\phi, J, s) = &-\left(n\frac{d\phi}{ds} - m\frac{d\psi}{ds}\right)\sin(n\phi(s) - m\psi(s))\times \\ &\int_s^{s+C} ds' B(J, s')\cos(m\psi(s') - m\pi\nu) \\ &-\left(n\frac{d\phi}{ds} - m\frac{d\psi}{ds}\right)\cos(n\phi(s) - m\psi(s))\times \\ &\int_s^{s+C} ds' B(J, s')\sin(m\psi(s') - m\pi\nu) \\ &- 2B(s)\cos(n\phi(s) - m\psi(s))\sin(m\psi)\sin(m\pi\nu) \\ &- 2B(s)\sin(n\phi(s) - m\psi(s))\cos(m\psi)\sin(m\pi\nu)\end{aligned} \tag{J.13}$$

Gathering the cosinus and sinus terms:

$$\begin{aligned}\frac{\partial I_{sin}}{\partial s}(\phi, J, s) = & -2B(s)\sin(n\phi)\sin(m\pi\nu) \\ & -\left(n\frac{d\phi}{ds} - m\frac{d\psi}{ds}\right)\int_s^{s+C} ds' B(J, s')\sin(n\phi(s) + m\overline{\psi}(s', s))\end{aligned} \tag{J.14}$$

and

$$\begin{aligned}\frac{\partial I_{cos}}{\partial s}(\phi, J, s) = & \, 2B(s)\sin(n\phi)\cos(m\pi\nu) \\ & +\left(n\frac{d\phi}{ds} - m\frac{d\psi}{ds}\right)\int_s^{s+C} ds' B(J, s')\cos(n\phi(s) + m\overline{\psi}(s', s))\end{aligned} \tag{J.15}$$

### J.2.1 Intermediate calculations

The perturbative terms of $S_1^2$ are to be multiplied with cosinus and sinus functions. The following equations derive the resulting harmonics for $(\cos(n\phi), \sin(n\phi)) \times \frac{\partial S}{\partial \phi}$:

#### J.2.1.1 Mono-terms

$$\begin{aligned}\langle\sin(\phi_x)\frac{\partial S}{\partial \phi}\rangle_{\phi_x} = & \frac{J_x^{3/2}}{4\sqrt{2}\sin(\pi\nu_x)}\int_s^{s+C} ds'\sqrt{\beta_x}\left(g_1\beta_x + k_x\gamma_x\right)\sin(\overline{\psi}(s', s)) \\ & + \frac{J_x^{1/2}J_y}{4\sqrt{2}\sin(\pi\nu_x)}\int_s^{s+C} ds'\sqrt{\beta_x}\left(-g_1\beta_y + k_x\gamma_y\right)\sin(\overline{\psi}(s', s)) \\ & - \frac{J_x^{3/2}}{2\sqrt{2}\sin(\pi\nu_x)}\int_s^{s+C} ds' k_x\beta_x^{-1/2}\alpha_x\left(\cos(\overline{\psi_x}(s', s)) - \alpha_x\sin(\overline{\psi_x}(s', s))\right) \\ & - \frac{J_x^{3/2}}{4\sqrt{2}\sin(\pi\nu_x)}\int_s^{s+C} ds' k_x\beta_x^{-1/2}\sin(\overline{\psi}(s', s)) \\ & + \frac{J_x^{1/2}J_y}{8\sqrt{2}\sin(\pi\nu_x)}\times \\ & \int_s^{s+C} ds'\sqrt{\beta_x}\left(-g_1\beta_y + \frac{k_x}{\beta_y}(\alpha_y^2 - 1)\right)\sin(\overline{\psi_x}(s', s) + 2(\phi_y + \overline{\psi_y})) \\ & + \frac{J_x^{1/2}J_y}{8\sqrt{2}\sin(\pi\nu_x)}\times \\ & \int_s^{s+C} ds'\sqrt{\beta_x}\left(-g_1\beta_y + \frac{k_x}{\beta_y}(\alpha_y^2 - 1)\right)\sin(\overline{\psi_x}(s', s) - 2(\phi_y + \overline{\psi_y}))\end{aligned} \tag{J.16}$$

$$
\begin{aligned}
&\langle \cos(\phi_x)\frac{\partial S}{\partial \phi}\rangle_{\phi_x} = -\frac{J_x^{3/2}}{4\sqrt{2}\sin(\pi\nu_x)}\int_s^{s+C} ds'\sqrt{\beta_x}\,(g_1\beta_x + k_x\gamma_x)\cos(\overline{\psi}(s',s))\\
&-\frac{J_x^{1/2}J_y}{4\sqrt{2}\sin(\pi\nu_x)}\int_s^{s+C} ds'\sqrt{\beta_x}\,(-g_1\beta_y + k_x\gamma_y)\cos(\overline{\psi}(s',s))\\
&-\frac{J_x^{3/2}}{2\sqrt{2}\sin(\pi\nu_x)}\int_s^{s+C} ds' k_x\beta_x^{-1/2}\alpha_x\left(\sin(\overline{\psi_x}(s',s)) + \alpha_x\cos(\overline{\psi_x}(s',s))\right)\\
&+\frac{J_x^{3/2}}{4\sqrt{2}\sin(\pi\nu_x)}\int_s^{s+C} ds' k_x\beta_x^{-1/2}\cos(\overline{\psi}(s',s))\\
&-\frac{J_x^{1/2}J_y}{8\sqrt{2}\sin(\pi\nu_x + 2\pi\nu_y)}\times\\
&\int_s^{s+C} ds'\sqrt{\beta_x}\left(-g_1\beta_y + \frac{k_x}{\beta_y}(\alpha_y^2 - 1)\right)(\cos(\overline{\psi_x}(s',s) + 2(\phi_y + \overline{\psi_y}))\\
&-\frac{J_x^{1/2}J_y}{8\sqrt{2}\sin(\pi\nu_x - 2\pi\nu_y)}\times\\
&\int_s^{s+C} ds'\sqrt{\beta_x}\left(-g_1\beta_y + \frac{k_x}{\beta_y}(\alpha_y^2 - 1)\right)\cos(\overline{\psi_x}(s',s) - 2(\phi_y + \overline{\psi_y}))
\end{aligned}
\tag{J.17}
$$

$$
\begin{aligned}
&\langle \cos(3\phi_x)\frac{\partial S}{\partial \phi}\rangle_{\phi_x} = -\frac{J_x^{3/2}}{4\sqrt{2}\sin(3\pi\nu_x)}\int_s^{s+C} ds'\sqrt{\beta_x}g_1\beta_x(\cos(3\overline{\psi}(s',s))\\
&-\frac{3J_x^{3/2}}{2\sqrt{2}\sin(3\pi\nu_x)}\int_s^{s+C} ds' k_x\beta_x^{-1/2}\alpha_x\left(\sin(3\overline{\psi}(s',s)) + \alpha_x\cos(3\overline{\psi}(s',s))\right)\\
&+\frac{3J_x^{3/2}}{4\sqrt{2}\sin(3\pi\nu_x)}\int_s^{s+C} ds' k_x\beta_x^{-1/2}\cos(3\overline{\psi}(s',s))
\end{aligned}
\tag{J.18}
$$

$$
\begin{aligned}
&\langle \sin(3\phi_x)\frac{\partial S}{\partial \phi}\rangle_{\phi_x} = \frac{J_x^{3/2}}{4\sqrt{2}\sin(3\pi\nu_x)}\int_s^{s+C} ds'\sqrt{\beta_x}g_1\beta_x(\sin(3\overline{\psi}(s',s))\\
&-\frac{3J_x^{3/2}}{2\sqrt{2}\sin(3\pi\nu_x)}\int_s^{s+C} ds' k_x\beta_x^{-1/2}\alpha_x\left(\cos(3\overline{\psi}(s',s)) - \alpha_x\sin(3\overline{\psi}(s',s))\right)\\
&-\frac{3J_x^{3/2}}{4\sqrt{2}\sin(3\pi\nu_x)}\int_s^{s+C} ds' k_x\beta_x^{-1/2}\sin(3\overline{\psi}(s',s))
\end{aligned}
\tag{J.19}
$$

#### J.2.1.2 Square terms

The table below gathers the resulting harmonics of the perturbation generating function $S_1$ to the square:

Therefore,

TABLE J.1: Residual harmonics in the derivative of $S_1^2$.

| | |
|---|---|
| $\left(\frac{\partial S}{\partial \phi}\right)^2 = \left(\frac{\partial S_{1,0}}{\partial \phi_x}\right)^2$ | Harmonics 0, 2 |
| $+\left(\frac{\partial S_{3,0}}{\partial \phi_x}\right)^2$ | Harmonics 0, 6 |
| $+\left(\frac{\partial S_{1,2}}{\partial \phi_x}\right)^2$ | Harmonics 0, 2 |
| $+2\frac{\partial S_{1,0}}{\partial \phi_x} \times \frac{\partial S_{3,0}}{\partial \phi_x}$ | Harmonics 2, 4 |
| $+2\frac{\partial S_{1,0}}{\partial \phi_x} \times \frac{\partial S_{1,2}}{\partial \phi_x}$ | Harmonics 0, 2 |
| $+2\frac{\partial S_{3,0}}{\partial \phi_x} \times \frac{\partial S_{1,2}}{\partial \phi_x}$ | Harmonics 2, 4 |

$$\begin{aligned}\langle\left(\frac{\partial S}{\partial \phi}\right)^2\rangle_{\phi_x} &= \langle\left(\frac{\partial S_{1,0}}{\partial \phi_x}\right)^2\rangle_{\phi_x} \\ &+ \langle\left(\frac{\partial S_{3,0}}{\partial \phi_x}\right)^2\rangle_{\phi_x} \\ &+ \langle\left(\frac{\partial S_{1,2}}{\partial \phi_x}\right)^2\rangle_{\phi_x} \\ &+ 2 * \langle\left(\frac{\partial S_{1,0}}{\partial \phi_x}\right) * \left(\frac{\partial S_{1,2}}{\partial \phi_x}\right)\rangle_{\phi_x}\end{aligned} \tag{J.20}$$

$$\begin{aligned}&\langle(\sin(2\phi_x) + \alpha_x \cos(2\phi_x))\left(\frac{\partial S}{\partial \phi_x}\right)^2\rangle_{\phi_x} = \langle(\sin(2\phi_x) + \alpha_x \cos(2\phi_x))\left(\frac{\partial S_{1,0}}{\partial \phi_x}\right)^2\rangle_{\phi_x} \\ &+ \langle(\sin(2\phi_x) + \alpha_x \cos(2\phi_x))\left(\frac{\partial S_{3,0}}{\partial \phi_x}\right)^2\rangle_{\phi_x} \\ &+ \langle(\sin(2\phi_x) + \alpha_x \cos(2\phi_x))\left(\frac{\partial S_{1,2}}{\partial \phi_x}\right)^2\rangle_{\phi_x} \\ &+ 2 * \langle(\sin(2\phi_x) + \alpha_x \cos(2\phi_x))\left(\frac{\partial S_{1,0}}{\partial \phi_x}\right) * \left(\frac{\partial S_{1,2}}{\partial \phi_x}\right)\rangle_{\phi_x} \\ &+ 2 * \langle(\sin(2\phi_x) + \alpha_x \cos(2\phi_x))\left(\frac{\partial S_{3,0}}{\partial \phi_x}\right) * \left(\frac{\partial S_{1,2}}{\partial \phi_x}\right)\rangle_{\phi_x}\end{aligned} \tag{J.21}$$

$$\begin{aligned}\langle\cos(4\phi_x)\left(\frac{\partial S}{\partial \phi_x}\right)^2\rangle_{\phi_x} &= 2 * \langle\cos(4\phi_x)\left(\frac{\partial S_{1,0}}{\partial \phi_x}\right) * \left(\frac{\partial S_{3,0}}{\partial \phi_x}\right)\rangle_{\phi_x} \\ &+ 2 * \langle\cos(4\phi_x)\left(\frac{\partial S_{1,2}}{\partial \phi_x}\right) * \left(\frac{\partial S_{3,0}}{\partial \phi_x}\right)\rangle_{\phi_x}\end{aligned} \tag{J.22}$$

$$\begin{aligned}\langle\sin(4\phi_x)\left((\frac{\partial S}{\partial \phi_x}\right)^2\rangle_{\phi_x} &= 2 * \langle\sin(4\phi_x)\left((\frac{\partial S_{1,0}}{\partial \phi_x}\right) * \left(\frac{\partial S_{3,0}}{\partial \phi_x}\right)\rangle_{\phi_x} \\ &+ 2 * \langle\sin(4\phi_x)\left(\frac{\partial S_{1,2}}{\partial \phi_x}\right) * \left(\frac{\partial S_{3,0}}{\partial \phi_x}\right)\rangle_{\phi_x}\end{aligned} \tag{J.23}$$

Using:

$$\begin{aligned}&\langle\int_s^{s+C} ds' \int_s^{s+C} dt\, f(s')g(t) \cos(\phi(s) + \overline{\psi}(s', s)) \times \cos(\phi(s) + \overline{\psi}(t, s))\rangle_\phi = \\ &\frac{1}{2}\int_s^{s+C} ds' \int_s^{s+C} dt\, f(s')g(t) \cos(\psi(s') - \psi(t))\end{aligned} \tag{J.24}$$

$$\begin{aligned}&\langle\int_s^{s+C} ds' \int_s^{s+C} dt\, f(s')g(t)\sin(\phi(s)+\overline{\psi}(s',s))\times\sin(\phi(s)+\overline{\psi}(t,s))\rangle_\phi = \\ &\frac{1}{2}\int_s^{s+C} ds' \int_s^{s+C} dt\, f(s')g(t)\cos(\psi(s')-\psi(t))\end{aligned} \tag{J.25}$$

$$\begin{aligned}&\langle\int_s^{s+C} ds' \int_s^{s+C} dt\, f(s')g(t)\sin(\phi(s)+\overline{\psi}(s',s))\times\cos(\phi(s)+\overline{\psi}(t,s))\rangle_\phi = \\ &\frac{1}{2}\int_s^{s+C} ds' \int_s^{s+C} dt\, f(s')g(t)\sin(\psi(s')-\psi(t))\end{aligned} \tag{J.26}$$

Therefore, noting $\Delta\phi(s',t) = \psi(s') - \psi(t)$ to ease the calculations, one can derive:

$$
\begin{aligned}
&\langle\left(\frac{\partial S_{1,0}}{\partial \phi_x}\right)^2\rangle_{\phi_x} = \frac{J_x^3}{16\sin(\pi\nu_x)^2}\times \\
&\int_s^{s+C} ds' \int_s^{s+C} dt \sqrt{\beta_x(s')\beta_x(t)} g_x(s') g_x(t) \cos(\Delta\phi(s',t)) \\
&+ \frac{J_x^2 J_y}{8\sin(\pi\nu_x)^2}\times \\
&\int_s^{s+C} ds' \times \\
&\int_s^{s+C} dt \sqrt{\beta_x(s')\beta_x(t)} g_x(s') g_y(t) \cos(\Delta\phi(s',t)) \\
&+ \frac{J_x J_y^2}{16\sin(\pi\nu_x)^2}\times \\
&\int_s^{s+C} ds' \int_s^{s+C} dt \sqrt{\beta_x(s')\beta_x(t)} g_y(s') g_y(t) \cos(\Delta\phi(s',t)) \\
&+ \frac{J_x^3}{4\sin(\pi\nu_x)^2}\times \\
&\int_s^{s+C} ds' \int_s^{s+C} dt \sqrt{\frac{\beta_x(s')}{\beta_x(t)}} g_x(s') k_x \alpha_x(t) C_{-a}(s',t) \\
&+ \frac{J_x^2 J_y}{4\sin(\pi\nu_x)^2}\times \\
&\int_s^{s+C} ds' \int_s^{s+C} dt \sqrt{\frac{\beta_x(s')}{\beta_x(t)}} g_y(s') k_x \alpha_x(t) C_{-a}(s',t) \\
&+ \frac{J_x^3}{4\sin(\pi\nu_x)^2} \int_s^{s+C} ds' \int_s^{s+C} dt \beta_x(s')^{-1/2} \beta_x(t)^{-1/2} k_x(s') \alpha_x(s') k_x(t) \alpha_x(t) \\
&\times \left((1+\alpha_x(s')\alpha_x(t)) \cos(\Delta\phi(s',t)) - \sin(\Delta\phi(s',t))(\alpha_x(s') - \alpha_x(t))\right) \\
&- \frac{J_x^3}{8\sin(\pi\nu_x)^2} \int_s^{s+C} ds' \int_s^{s+C} dt \sqrt{\frac{\beta_x(s')}{\beta_x(t)}} g_x(s') k_x(t) \cos(\Delta\phi(s',t)) \\
&- \frac{J_x^2 J_y}{8\sin(\pi\nu_x)^2} \int_s^{s+C} ds' \int_s^{s+C} dt \sqrt{\frac{\beta_x(s')}{\beta_x(t)}} g_y(s') k_x(t) \cos(\Delta\phi(s',t)) \\
&- \frac{J_x^3}{4\sin(\pi\nu_x)^2}\times \\
&\int_s^{s+C} ds' \int_s^{s+C} dt k_x(s') \alpha_x(s') \beta_x(s')^{-1/2} k_x(t) \beta_x(t)^{-1/2} C_a(s',t) \\
&+ \frac{J_x^3}{16\sin(\pi\nu_x)^2} \int_s^{s+C} ds' \int_s^{s+C} dt k_x(s') \beta_x(s')^{-1/2} k_x(t) \beta_x(t)^{-1/2} \cos(\Delta\phi(s',t))
\end{aligned}
\tag{J.27}
$$

with $g_x : s' \longmapsto (g_1\beta_x + k_x\gamma_x)(s')$, $g_y : s' \longmapsto (-g_1\beta_y + k_x\gamma_y)(s')$, and:

$$
\begin{aligned}
C_a : (s',t) &\longmapsto \left(\sin(\Delta\phi(s',t)) + \alpha_x(t')\cos(\Delta\phi(s',t))\right) \\
C_{-a} : (s',t) &\longmapsto \left(-\sin(\Delta\phi(s',t)) + \alpha_x(t')\cos(\Delta\phi(s',t))\right)
\end{aligned}
\tag{J.28}
$$

$$
\begin{aligned}
\langle\left(\frac{\partial S_{3,0}}{\partial \phi_x}\right)^2\rangle_{\phi_x} = \frac{J_x^3}{8\sin(3\pi\nu_x)^2}\int_s^{s+C} ds' \times \\
\int_s^{s+C} dt\sqrt{\beta_x(s')\beta_x(t)}(g_1\beta_x)(s')(g_1\beta_x)(t)\cos(\Delta\phi(s',t))
\end{aligned}
\tag{J.29}
$$

$$
\begin{aligned}
& S_{1,3}(\phi, J, s) = \frac{J_x^{3/2}}{6\sqrt{2}\sin(3\pi\nu_x)}\int_s^{s+C} ds'\sqrt{\beta_x}g_1\beta_x(-\sin(3\phi_x + 3\overline{\psi}(s',s)) \\
& + \frac{J_x^{3/2}}{\sqrt{2}\sin(3\pi\nu_x)}\times \\
& \int_s^{s+C} ds' k_x\beta_x^{-1/2}\alpha_x\left(\cos(3\phi_x + 3\overline{\psi}(s',s)) - \alpha_x\sin(3\phi_x + 3\overline{\psi}(s',s))\right) \\
& + \frac{J_x^{3/2}}{2\sqrt{2}\sin(\pi\nu_x)}\int_s^{s+C} ds' k_x\beta_x^{-1/2}\sin(3\phi_x + 3\overline{\psi}(s',s))
\end{aligned}
\tag{J.30}
$$

#### J.2.1.3 Useful terms

$$
\begin{aligned}
& \langle\,(\sin(\phi_x) + \alpha_x\cos(\phi_x))\,\frac{\partial S}{\partial \phi_x}\rangle_{\phi_x} = \frac{J_x^{3/2}}{4\sqrt{2}\sin(\pi\nu_x)}\times \\
& \int_s^{s+C} ds'\sqrt{\beta_x}\,(g_1\beta_x + k_x\gamma_x)\,(\sin(\overline{\psi}(s',s) - \alpha_x(s)\cos(\overline{\psi}(s',s))) \\
& + \frac{J_x^{1/2}J_y}{4\sqrt{2}\sin(\pi\nu_x)}\times \\
& \int_s^{s+C} ds'\sqrt{\beta_x}\,(-g_1\beta_y + k_x\gamma_y)\,(\sin(\overline{\psi}(s',s) - \alpha_x(s)\cos(\overline{\psi}(s',s))) \\
& - \frac{J_x^{3/2}}{2\sqrt{2}\sin(\pi\nu_x)}\int_s^{s+C} ds' k_x\sqrt{\beta_x}\gamma_x\alpha_x(\cos(\overline{\psi_x}(s',s)) - \alpha_x\sin(\overline{\psi}(s',s)) \\
& - \frac{J_x^{3/2}}{2\sqrt{2}\sin(\pi\nu_x)}\int_s^{s+C} ds' k_x\sqrt{\beta_x}\gamma_x\alpha_x\alpha(s)(\sin(\overline{\psi_x}(s',s)) + \alpha_x\cos(\overline{\psi}(s',s)) \\
& - \frac{J_x^{3/2}}{4\sqrt{2}\sin(\pi\nu_x)}\int_s^{s+C} ds' k_x\beta_x^{-1/2}(\sin(\overline{\psi}(s',s) - \alpha_x(s)\cos(\overline{\psi}(s',s))) \\
& + \frac{J_x^{1/2}J_y}{8\sqrt{2}\sin(\pi\nu_x)}\times \\
& \int_s^{s+C} ds'\sqrt{\beta_x}\left(-g_1\beta_y + \frac{k_x}{\beta_y}(\alpha_y^2 - 1)\right)\times \\
& \left(\sin(\overline{\psi_x}(s',s) + 2(\phi_y + \overline{\psi_y})) - \alpha_x\cos(\overline{\psi_x}(s',s) + 2(\phi_y + \overline{\psi_y}))\right) \\
& + \frac{J_x^{1/2}J_y}{8\sqrt{2}\sin(\pi\nu_x)}\times \\
& \int_s^{s+C} ds'\sqrt{\beta_x}\left(-g_1\beta_y + \frac{k_x}{\beta_y}(\alpha_y^2 - 1)\right)\times \\
& \left(\sin(\overline{\psi_x}(s',s) - 2(\phi_y + \overline{\psi_y})) - \alpha_x\cos(\overline{\psi_x}(s',s) - 2(\phi_y + \overline{\psi_y}))\right)
\end{aligned}
\tag{J.31}
$$

$$
\begin{aligned}
&\Big((\alpha_x^2-1)\cos(3\phi_x)+\beta_x\gamma_x\cos(\phi_x)+2\alpha_x\sin(3\phi_x)\Big)\,\frac{\partial S}{\partial \phi_x}\rangle_{\phi_x} = \\
&-\frac{J_x^{3/2}}{4\sqrt{2}\sin(\pi\nu_x)}\int_s^{s+C} ds'\sqrt{\beta_x}\,(g_1\beta_x+k_x\gamma_x)\cos(\overline{\psi}(s',s)) \\
&-\frac{J_x^{1/2}J_y}{4\sqrt{2}\sin(\pi\nu_x)}\int_s^{s+C} ds'\sqrt{\beta_x}\,(-g_1\beta_y+k_x\gamma_y)\cos(\overline{\psi}(s',s)) \\
&-\frac{J_x^{3/2}}{2\sqrt{2}\sin(\pi\nu_x)}\int_s^{s+C} ds' k_x\beta_x^{-1/2}\alpha_x\,\Big(\sin(\overline{\psi_x}(s',s))+\alpha_x\cos(\overline{\psi_x}(s',s))\Big) \\
&+\frac{J_x^{3/2}}{4\sqrt{2}\sin(\pi\nu_x)}\int_s^{s+C} ds' k_x\beta_x^{-1/2}\cos(\overline{\psi}(s',s))
\end{aligned}
\tag{J.32}
$$

# Bibliography

[1] E. M. McMillan. The Synchrotron—A Proposed High Energy Particle Accelerator. *Phys. Rev.*, 68:143–144, Sep 1945. doi: 10.1103/PhysRev.68.143.

[2] V. I. Veksler. A new method of acceleration of relativistic particles. *J. Phys.*, 9: 153–158, 1945.

[3] S. R. Mane, Y. M. Shatunov, and K. Yokoya. Spin-polarized charged particle beams in high-energy accelerators. *Reports on Progress in Physics*, 68(9):1997–2265, aug 2005. doi: 10.1088/0034-4885/68/9/r01.

[4] H. Wiedemann. *Particle Accelerator Physics, 116-117*. Springer International, 2007. doi: https://doi.org/10.1007/978-3-319-18317-6.

[5] O. Chamberlain, E. Segre, C. Wiegand, and T. Ypsilantis. Observation of antiprotons. 10 1955. doi: 10.2172/915069.

[6] E. D. Courant, M. S. Livingston, and H. S. Snyder. The Strong-Focusing Synchroton—Anew high energy accelerator. *Phys. Rev.*, 88:1190–1196, Dec 1952. doi: 10.1103/PhysRev.88.1190.

[7] B. McDaniel and A. Silverman. Robert Rathbun Wilson, 4 March 1914 · 16 January 2000. *Proceedings of the American Philosophical Society*, 146(2):230–234, 2002. ISSN 0003049X.

[8] R. A. Beth and C. Lasky. The Brookhaven Alternating Gradient Synchrotron. *Science*, 128(3336):1393–1401, 1958. ISSN 0036-8075. doi: 10.1126/science.128.3336.1393.

[9] F.R. Elder et. al. *Physical Review*, 71, 1947. doi: https://doi.org/10.1103/PhysRev.71.829.5.

[10] F. R. Elder, A. M. Gurewitsch, R. V. Langmuir, and H. C. Pollock. Radiation from Electrons in a Synchrotron. *Phys. Rev.*, 71:829–830, Jun 1947. doi: 10.1103/PhysRev.71.829.5.

[11] D. H. Tomboulian and P. L. Hartman. Spectral and Angular Distribution of Ultraviolet Radiation from the 300-Mev Cornell Synchrotron. *Phys. Rev.*, 102: 1423–1447, Jun 1956. doi: 10.1103/PhysRev.102.1423.

[12] STFC. Accelerator Modeling with MATLAB Accelerator Toolbox. Particle Accelerator Conference, 2001, 2001.

[13] J.D. Jackson. *Classical Electrodynamics*. John Wiley & Sons, 1999. ISBN 0-471-30932-X.

[14] A. Liénard. *Champ électrique et magnétique produit par une charge électrique concentrée en un point et animée d'un mouvement quelconque.* Paris : G. Carré et C. Naud, 1898.

[15] `https://lightsources.org/about-2/`.

[16] H. Motz. Applications of the Radiation from Fast Electron Beams. *Journal of Applied Physics*, 22(5):527–535, 1951. doi: 10.1063/1.1700002.

[17] H. Motz, W. Thon, and R. N. Whitehurst. Experiments on radiation by fast electron beams. *Journal of Applied Physics*, 24(7):826–833, 1953. doi: 10.1063/1.1721389.

[18] F. Mateeau and et al. Development and installation of insertion devices at SOLEIL. *Proceedings of PAC2009, Vancouver, BC, Canada*, 2009.

[19] I. M. Kapchinskii and V. A. Teplyakov. Linear ion accelerator with spatially homogeneous strong focusing. *Instrum. Exp. Tech. (USSR) (Engl. Transl.) No. 2, 322-6(Mar-Apr 1970).*, 1 1970.

[20] `https://www.synchrotron-soleil.fr/fr/qui-sommes-nous/quest-ce-que-soleil/soleil-en-3-questions#1`.

[21] M. Borland, G. Decker, L. Emery, V. Sajaev, Y. Sun, and A. Xiao. Lattice design challenges for fourth-generation storage-ring light sources. *Journal of Synchrotron Radiation*, 21(5):912–936, Sep 2014. doi: 10.1107/S1600577514015203.

[22] H. Wiedemann. *Particle Accelerator Physics, 783-784*. Springer International, 3 edition, 2007. doi: https://doi.org/10.1007/978-3-319-18317-6.

[23] J.-C. Huang, H. Kitamura, C. Yang, Cheng-Hsing Chang, Cheng-Hsiang Chang, and C.-S. Hwang. Challenges of in-vacuum and cryogenic permanent magnet undulator technologies. *PHYSICAL REVIEW ACCELERATORS AND BEAMS*, 20:064801, 06 2017. doi: 10.1103/PhysRevAccelBeams.20.064801.

[24] CNRS. Quelques défis scientifique des synchrotrons de 4éme génération, septembre 2019.

[25] SACLA XFEL. `http://xfel.riken.jp/eng/sacla/index00.html`, .

[26] LCLS. `https://lcls.slac.stanford.edu/overview`, .

[27] European XFEL. `http://xfel.riken.jp/eng/sacla/index00.html`, .

[28] R. Bartolini. Pres. at the Low Emittance Rings workshop (LER), Frascati , Italy, September 2014.

[29] R. Hettel. DLSR design and plans: an international overview. *Journal of Synchrotron Radiation*, 21(5):843–855, Sep 2014. doi: 10.1107/S1600577514011515.

[30] J. Collins, Z. Liu, J. Nudell, C. Preissner, and H. Cease. *Proceedings of MEDSI2016, Barcelona, Spain*, 2016.

[31] M. Borland, G. Decker, L. Emery, V. Sajaev, Y. Sun, and A. Xiao. Lattice design challenges for fourth-generation storage-ring light sources. *Journal of Synchrotron Radiation*, 21(5):912–936, Sep 2014. doi: 10.1107/S1600577514015203.

[32] M. Johansson, B. Anderberg, and L.-J. Lindgren. Magnet design for a low-emittance storage ring. *Journal of Synchrotron Radiation*, 21(5):884–903, Sep 2014. doi: 10.1107/S160057751401666X.

[33] G. Le Bec, J. Chavanne, C. Benabderrahmane, L. Farvacque, L. Goirand, S. Liuzzo, P. Raimondi, and F. Villar. High gradient quadrupoles for low emittance storage rings. *Physical Review Accelerators and Beams*, 19, 05 2016. doi: 10.1103/PhysRevAccelBeams.19.052401.

[34] J. Chavanne and G. Le Bec. *Proceedings of IPAC2014, Dresden, Germany*, 2014.

[35] C. Herbeaux, N. Béchu, and J.-M. Filhol. Vacuum conditioning of the SOLEIL storage ring with extensive use of NEG coating. *Proceedings of EPAC2008,Genoa, Italy*, 2008.

[36] E. Al-Dmour, J. Ahlback, D. Einfeld, P. Fernandes Tavares, and M. Grabski. Diffraction-limited storage-ring vacuum technology. *Journal of Synchrotron Radiation*, 21(5):878–883, Sep 2014. doi: 10.1107/S1600577514010480.

[37] S. Calatroni, P. Chiggiato, P. Costa Pinto, M. Taborelli, M. Grabski, J. Ahlbäck, E. Al-Dmour, and P. Fernandes Tavares. NEG thin film coating development for the MAX IV vacuum system. *Proceedings of IPAC2013, Shangai, China*, 2013.

[38] T.F. Günzel, T. Perron, L. Farvacque, and J.L. Revol. Evolution of the machine impedance following the ESRF upgrade to low gap NEG coated aluminium chambers. *Proceedings of IPAC2005, Knoxville, Texas*, 2005.

[39] M. Aiba, M. Böge, F. Marcellini, Á. Saá Hernández, and A. Streun. Longitudinal injection scheme using short pulse kicker for small aperture electron storage rings. *Phys. Rev. ST Accel. Beams*, 18:020701, Feb 2015. doi: 10.1103/PhysRevSTAB.18.020701.

[40] ALS-Uswap out explanatory video. `https://als.lbl.gov/debut-of-als-u-swap-out-injection-video/`, April 2020.

[41] ESRF-EBS Orange book. `http://www.esrf.eu/files/live/sites/www/files/about/upgrade/documentation/Design%20Report-reduced-jan19.pdf`, Septembre 2018.

[42] A. et al. Hofler. Innovative applications of genetic algorithms to problems in accelerator physics. *Phys. Rev. ST Accel. Beams*, 16:010101, Jan 2013. doi: 10.1103/PhysRevSTAB.16.010101.

[43] M. P. Ehrlichman. Genetic algorithm for chromaticity correction in diffraction limited storage rings. *Physical Review Accelerators and Beams*, 19(4), Apr 2016. ISSN 2469-9888. doi: 10.1103/physrevaccelbeams.19.044001.

[44] Y. Li, W. Cheng, L. H. Yu, and R. Rainer. Genetic algorithm enhanced by machine learning in dynamic aperture optimization. *Phys. Rev. Accel. Beams*, 21:054601, May 2018. doi: 10.1103/PhysRevAccelBeams.21.054601.

[45] `https://www.synchrotron-soleil.fr/en/research/sources-and-accelerators/parameters-accelerators-storage-ring`, .

[46] `https://www.synchrotron-soleil.fr/fr/lignes-de-lumiere/localisation-des-lignes`, .

[47] `https://www.synchrotron-soleil.fr/fr/recherche/sources-et-accelerateurs/caracteristiques-du-faisceau-delectrons/fonctions-optiques-du`.

[48] J. Bengtsson and A. Streun. Robust Design Strategy for SLS-2. *Tech. Rep.*, pages SLS2–BJ84–001, June 2007.

[49] S.C. Leemann et al. A novel 7BA lattice for a 196-m circumference diffraction. *Physical Review E*, 47(3), March 1993.

[50] H. Wiedemann. pages 249–252. Springer International, 2007. doi: https://doi.org/10.1007/978-3-319-18317-6.

[51] H. Wiedemann. *Particle Accelerator Physics, 158-161.* Springer International, 3 edition, 2007. doi: https://doi.org/10.1007/978-3-319-18317-6.

[52] H. Wiedemann. *Particle Accelerator Physics, 172-174.* Springer International, 3 edition, 2007. doi: https://doi.org/10.1007/978-3-319-18317-6.

[53] H. Wiedemann. *Particle Accelerator Physics, 158.* Springer International, 3 edition, 2007. doi: https://doi.org/10.1007/978-3-319-18317-6.

[54] H. Wiedemann. *Particle Accelerator Physics, 175-178.* Springer International, 3 edition, 2007. doi: https://doi.org/10.1007/978-3-319-18317-6.

[55] H. Wiedemann. *Particle Accelerator Physics, 293-300.* Springer International, 3 edition, 2007. doi: https://doi.org/10.1007/978-3-319-18317-6.

[56] S.Y. Lee. *Accelerator Physics, 437-445*. World Scientific, 2011. ISBN 978-981-4374-94-1. doi: https://doi.org/10.1142/8335.

[57] A. Streun. Opa, Lattice Design Code. `https://ados.web.psi.ch/opa/`, 2012.

[58] K.L. Brown. A Second Order Magnetic Optical Achromat. *IEEE Trans. Nucl. Sci.*, 26:3490–3492, 1979. doi: 10.1109/TNS.1979.4330076.

[59] W. Wan and M. Berz. Analytical theory of arbitrary-order achromats. 54(3): 2870–2883, September 1996. doi: 10.1103/PhysRevE.54.2870.

[60] R. Chasman and G. K. Green. Design of a national dedicated synchrotron radiation facility. 1 1976.

[61] R. Chasman, G. K. Green, and E. M. Rowe. Preliminary Design of a Dedicated Synchrotron Radiation Facility. *IEEE Transactions on Nuclear Science*, 22(3): 1765–1767, 1975.

[62] R. Bartolini. Lecture on Sunchrotron Radiation, part III. *JUAS 2017*, 2017.

[63] A. Jackson. A comparison of the Chasman-Green and triple bend achromat lattices. *Particle Accelerators*, 22:111–128, 3 1987.

[64] S.L. Kramer, E.A. Crosbie, and Cho. Y. *Proc. Europ. Particle Accelerator Conf.*, pages 749–751, 1988.

[65] H. Tanaka and A. Ando. Minimum effective emittance in synchrotron radiation sources composed of modified Chasman-Green lattice. *Nuclear Instruments and Methods in Physics Research Section A: Accelerators, Spectrometers, Detectors and Associated Equipment*, 369(1):312 – 321, 1996. ISSN 0168-9002. doi: https://doi.org/10.1016/0168-9002(95)00773-3.

[66] H. Tanaka, L. Farvacque, J. L. Laclare, P. Nghiem, J. Payet, A. Ropert, and A. Tkatchenko. Emittance reduction in electron storage rings. *AIP Conference Proceedings*, 356(1):151–162, 1996. doi: 10.1063/1.49604.

[67] J.-M. Lefebvre. *Proc. Europ. Particle Accelerator Conf., Barcelona, Spain*, 1996.

[68] P. Brunelle, M.-P. Level, A. Nadji, M. Sommer, H. Zyngier, P. Nghiem, J. Payet, and A. Tkatchenko. *Proc. Europ. Particle Accelerator Conf., London, UK*, pages 615–617, 1994.

[69] L. Farvaque, J.L. Laclare, P. Nghiem, J. Payet, A. Ropert, H. Tanaka, and A. Tkatchenko. *Proc. Europ. Particle Accelerator Conf., London, UK*, pages 612–614, 1994.

[70] A Andersson, M. Eriksson, L.-J. Lindgren, P. Röjsel, and S. Werin. *Proc. Europ. Particle Accelerator Conf., London, UK*, pages 588–590, 1994.

[71] R. Nagaoka. *Proc. Europ. Particle Accelerator Conf., Barcelona, Spain*, 1996.

[72] D. Einfeld and M. Plesko. A modified QBA optics for low emittance storage rings. *Nuclear Instruments and Methods in Physics Research Section A: Accelerators, Spectrometers, Detectors and Associated Equipment*, 335(3):402–416, 1993. ISSN 0168-9002. doi: https://doi.org/10.1016/0168-9002(93)91224-B.

[73] D. Einfeld, M. Plesko, and J. Schaper. First multi-bend achromat lattice consideration. *Journal of Synchrotron Radiation*, 21(5):856–861, Sep 2014. doi: 10.1107/S160057751401193X.

[74] D. Einfeld. Multi-bend achromat lattices for storage ring light sources. *Synchrotron Radiation News*, 27(6):4–7, 2014. doi: 10.1080/08940886.2014.970929.

[75] P. F. Tavares, S. C. Leemann, M. Sjöström, and A. Andersson. The MAX IV storage ring project. *Journal of Synchrotron Radiation*, 21(5):862–877, Sep 2014. doi: 10.1107/S1600577514011503.

[76] M. Eriksson, L.-J. Lindgren, M. Sjöström, E. Wallén, L. Rivkin, and A. Streun. Some small-emittance light-source lattices with multi-bend achromats. *Nuclear Instruments and Methods in Physics Research Section A: Accelerators, Spectrometers, Detectors and Associated Equipment*, 587(2):221 – 226, 2008. ISSN 0168-9002. doi: https://doi.org/10.1016/j.nima.2008.01.068.

[77] Detailed design report on the MAX IV facility. `https://www.maxiv.lu.se/accelerators-beamlines/accelerators/accelerator-documentation/max-iv-ddr/`, August 2010.

[78] Lattice file of MAX IV 3GeV storage ring. `https://www.maxiv.lu.se/accelerators-beamlines/accelerators/accelerator-documentation/public-archive/`.

[79] Stanford Synchrotron Radiation Lightsource (SSRL). PEP-X Light Source Status Report. `www-ssrl.slac.stanford.edu/pep-x/pdf/acceleratorPhysics.pdf`.

[80] Conceptual design report of spring-8-ii. `http://rsc.riken.jp/pdf/SPring-8-II.pdf`, November 2014.

[81] S. Henderson, M. Billing, R. Holtzapple, R. Littauer, B. McDaniel, D. Rice, D. Rubin, D. Sagan, R. Talman, and A. Temnykh. Investigation of the Mobius accelerator at CESR. volume 1, pages 410 – 412 vol.1, 02 1999. ISBN 0-7803-5573-3. doi: 10.1109/PAC.1999.795719.

[82] Mini-workshop on round beam, soleil, france. `https://www.synchrotron-soleil.fr/fr/evenements/mini-workshop-round-beams`, June 2017.

[83] R. Talman. *Phys. Rev. Lett.*, 74:1590, 1995.

[84] R. Talman. The Möbius Accelerator. *Cornell CBN*, pages 94–1, 1994.

[85] M. Aiba, M. Erhlichman, and A. Streun. Round beam operation in electron storage rings and generalisation of Mobius accelerator. *Proceedings of IPAC2015, Richmond, VA, USA*, 2015. doi: 10.18429/JACoW-IPAC2015-TUPJE045.

[86] V.V. Danilov, P.M. Ivanov, I.A. Koop, I. Nesterenko, E.A. Perevedentsev, D.N. Shatilov, Yu.M. Shatunov, and A.N. Skrinsky. The concept of round colliding beams. 01 1996.

[87] H. L. Mcdaniel, S. Henderson, R. Littauer, B. Mcdaniel, T. Pelaia, R. Talman, and E. Young. Investigation Of Chromaticity Sharing At The Cornell Electron Storage Ring, 1997.

[88] P. Kuske. Review of methods to produce round beams. Pres. at Mini-Workshop on Round Beam, SOLEIL, France, June 2017.

[89] A. Chao and P. Raimondi. Emittance adapter for a diffraction limited synchrotron radiation source. SLAC-PUB-14808.

[90] T. Moreno, H. Westfahl, R. de Oliveira Freitas, Y. Petroff, and P. Dumas. Optical layouts for large infrared beamline opening angles. *Journal of Physics: Conference Series*, 425(14):142003, mar 2013. doi: 10.1088/1742-6596/425/14/142003.

[91] T. Moreno. Synchrotron beamline designs. Pres. at Mini-Workshop on Round Beam, SOLEIL, France, June 2017.

[92] P. Brunelle, K. Klementiev, J.-M. Luque-Raigon, O. Marcouille, T. Moreno, and R. Nagaoka. Application of an emittance adapter to increase photon flux density on a synchrotron radiation beam line. 22(6), 06 2019. ISSN 2469-9888. doi: 10.1103/PhysRevAccelBeams.22.060702.

[93] P. Brunelle, K. Klementiev, J.-M. Luque-Raigon, O. Marcouille, T. Moreno, and R. Nagaoka. Application of an emittance adapter to increase photon flux density on a synchrotron radiation beam line. *Phys. Rev. Accel. Beams*, 22:060702, Jun 2019. doi: 10.1103/PhysRevAccelBeams.22.060702.

[94] P. Kuske. Round beam related challenges in storage ring light sources. Pres. at FLS2018, Shanghai, China, March 2018.

[95] H. Wiedemann. *Particle Accelerator Physics, 625-629.* Springer International, 3 edition, 2007. doi: https://doi.org/10.1007/978-3-319-18317-6.

[96] C. et al. Swenson. *Proceedings of IPAC2016, Busan, Korea*, 2016.

[97] Advanced Photon Source Upgrade Project. *Final Design Report.*

[98] A. Streun. The anti-bend cell for ultra-low emittance storage ring lattices. *Nuclear Instruments and Methods in Physics Research A*, 737:148–154, 2014.

[99] B. Riemann and A. Streun. Low emittance lattice design from first principles: reverse bending and longitudinal gradient bends. *Phys. Rev. Accel. Beams*, 22: 021601, Feb 2019. doi: 10.1103/PhysRevAccelBeams.22.021601.

[100] R. Nagaoka and A. Wrulich. Emittance minimisation with longitudinal dipole field variation. *Nuclear Instruments and Methods in Physics Research Section A: Accelerators, Spectrometers, Detectors and Associated Equipment*, 575:292–304, 06 2007. doi: 10.1016/j.nima.2007.02.086.

[101] A. Streun and A. Wrulich. Compact low emittance light sources based on longitudinal gradient bending magnets. *Nuclear Instruments and Methods in Physics Research Section A Accelerators Spectrometers Detectors and Associated Equipment*, 770, 01 2015. doi: 10.1016/j.nima.2014.10.002.

[102] M. Aiba, M. Böge, M. Ehrlichman, and A. Streun. Magnetic field of longitudinal gradient bend. *Nuclear Instruments and Methods in Physics Research Section A: Accelerators, Spectrometers, Detectors and Associated Equipment*, 892:41 – 47, 2018. ISSN 0168-9002. doi: https://doi.org/10.1016/j.nima.2018.02.111.

[103] ESRF-EBS. `http://www.esrf.eu/home/news/general/content-news/general/first-accumulation-and-world-record-horizontal-emittance-of-308-pm.html`, December 2019.

[104] R. Servranckx and K. Browm. Chromatic corrections for large storage rings. *Nuclear Science, IEEE Transactions on*, 26:3598 – 3600, 07 1979. doi: 10.1109/TNS.1979.4330113.

[105] A. Franchi. *A new lattice for the ESRF upgrade, November 19-20, 2012.*

[106] K. Oide and H. Koiso. Dynamic aperture of electron storage rings with non-interleaved sextupoles. *Physical Review E*, 47(3), March 1993.

[107] C. Steier, A. Allézy, A. Anders, K. Baptiste, E. Buice, K. Chow, G. Cutler, R. Donahue, D. Filippetto, J. Harkins, T. Hellert, M. Johnson, J.-Y. Jung, S. Leemann, D. Leitner, M. Leitner, T. Luo, H. Nishimura, T. Oliver, O. Omolayo, J. Osborn, C. Pappas, S. Persichelli, M. Placidi, G. Portmann, S. Reyes, D. Robin, F. Sannibale, S. De Santis, C. Sun, C. Swenson, M. Venturini, S. Virostek, W. Waldron, and E. Wallén. Status of the conceptual design of ALS-U. *Proceedings of IPAC2018, Vancouver, BC, Canada*, 2018. doi: https://doi.org/: 10.18429/JACoW-IPAC2018-THPMF036.

[108] A. Loulergue. *Proceedings of IPAC2018, Vancouver, Canada*, 2018.

[109] A. Terebilo. The social and economic impact of the Daresbury Synchrotron Radiation Source. `https://stfc.ukri.org/files/impact-publications/new-light-on-science/`, 2010.

[110] M. Takao. Formulation of nonlinear chromaticity in circular accelerators by canonical perturbation method. *Physical Review. E, Statistical Physics, Plasmas, Fluids, and Related Interdisciplinary Topics*, 72(4), 10 2005. ISSN 1063-651X. doi: 10.1103/PhysRevE.72.046502.

[111] C. Bernardini, G. F. Corazza, G. Di Giugno, G. Ghigo, J. Haissinski, P. Marin, R. Querzoli, and B. Touschek. Lifetime and Beam Size in a Storage Ring. *Phys. Rev. Lett.*, 10:407–409, May 1963. doi: 10.1103/PhysRevLett.10.407.

[112] A. Piwinski. Proceedings of the 9th international conference on high energy accelerators, stanford, ca, 1974.

[113] J. Bjorken and S. Mtingwa. Intrabeam Scattering. *Particle Accelerator*, 13, May 1983.

[114] K. Tsumaki and N. Kumagai. Very low emittance light source storage ring. *Nuclear Instruments and Methods in Physics Research Section A: Accelerators, Spectrometers, Detectors and Associated Equipment*, 565(2):394 – 405, 2006. ISSN 0168-9002. doi: https://doi.org/10.1016/j.nima.2006.06.030.

[115] A. Xiao, L. Emery, V. Sajaev, and Bingxin Yang. Experience with round beam operation at the Advanced Photon Source. 1 2015.

[116] J. Breunlin, S.C. Leemann, and A. Andersson. Improving Touschek lifetime in ultra-low emittance lattices through systematic application of successive closed vertical dispersion bumps. *Physical Review Accelerators and Beams*, 19, 06 2016. doi: 10.1103/PhysRevAccelBeams.19.060701.

[117] A. Piwinski. The Touschek Effect in Strong Focusing Storage Rings, 1999.

[118] M.S. Zisman. ZAP and its application to the optimization of synchrotron light source parameters. `https://escholarship.org/uc/item/48w0v03h`, 1987.

[119] G. Skriptka et al. *Proceedings of IPAC2016, Busan, Korea*, 2016.

[120] J. Byrd, S. De Santis, G. Stover, J. Teytelman, D.and Fox, J. Jacob, V. Serriere, and M. Georggson. Harmonic cavities and longitudinal beam stability in electron storage rings. 1:380 – 384 vol.1, 02 2001. doi: 10.1109/PAC.2001.987520.

[121] J.M. Byrd, K. Baptiste, S. De Santis, S. Kosta, C.C. Lo, D. Plate, R.A. Rimmer, and M. Franks. Design of a higher harmonic RF system for the Advanced Light Source. *Nuclear Instruments and Methods in Physics Research Section A: Accelerators, Spectrometers, Detectors and Associated Equipment*, 439(1):15 – 25, 2000. ISSN 0168-9002. doi: https://doi.org/10.1016/S0168-9002(99)00892-X.

[122] H. Wiedemann. *Particle Accelerator Physics, 458-463*. Springer International, 2007. doi: https://doi.org/10.1007/978-3-319-18317-6.

[123] R. Nagaoka, K. Yoshida, and M. Hara. Nonlinear dynamics with sextupoles in low-emittance light source storage rings. *Nuclear Instruments and Methods in Physics Research Section A: Accelerators, Spectrometers, Detectors and Associated Equipment*, 302(1):9 – 26, 1991. ISSN 0168-9002. doi: https://doi.org/10.1016/0168-9002(91)90487-B.

[124] `https://www.classe.cornell.edu/bmad/`.

[125] `http://www-hpc.cea.fr/fr/complexe/tgcc.htm`.

[126] J. Da Silva Castro, P. Alexandre, R. Ben El Fekih, and S. Thoraud. Multipole Injection Kicker (MIK), a Cooperative Project SOLEIL and MAX IV. *10th Mechanical Engineering Design of Synchrotron Radiation Equipment and Instrumentation, Paris, France*, 2018. doi: 10.18429/JACoW-MEDSI2018-TUPH12.

[127] P. Alexandre, R. Ben El Fekih, A. Letrésor, S. Thoraud, J. da Silva Castro, F. Bouvet, J. Breunlin, A. Andersson, and P. Fernandes Tavares. Transparent top-up injection into a fourth-generation storage ring. *Nuclear Instruments and Methods in Physics Research Section A: Accelerators, Spectrometers, Detectors and Associated Equipment*, 986:164739, 2021. ISSN 0168-9002. doi: https://doi.org/10.1016/j.nima.2020.164739.

[128] L. Nadolski on behalf of P. Alexandre. SOLEIL Multipole Injector Kicker (Nonlinear Kicker), ESLS, Krakow, Poland, 2018. `https://synchrotron.uj.edu.pl/documents/1457771/141441388/24_2018_ESLS_MIKnadolski.pdf/52e34f6a-ddc1-4e46-97d9-34ec2f711b54`.

[129] R. Nagaoka. Soleil upgrade. `https://agenda.infn.it/event/20813/contributions/110195/attachments/76445/98315/SOLEILupgrade_LER2020.pdf`, October 2020.

[130] A. Loulergue. Projet d'upgrade majeur pour SOLEIL. `https://indico.ijclab.in2p3.fr/event/5423/contributions/18238/attachments/14435/17808/SOLEIL-Upgrade-status-SFP2019.pdf`, October 2019.

[131] H Wiedemann. Chromaticity correction in large storage rings. 9 1976.

[132] X. Nuel Gavaldà, L. Nadolski, and A Ortiz. Multi-objective optimization of the non-linear beam dynamics of synchrotron SOLEIL. *Proceedings of IPAC 2014*, 06 2014.

[133] M. Attal. PhD Thesis, Paris-Sud XI University. 2009.

[134] A. Riabko, M. Bai, B. Brabson, C. M. Chu, X. Kang, D. Jeon, S. Y. Lee, and X. Zhao. Particle dynamics in quasi-isochronous storage rings. *Phys. Rev. E*, 54: 815–829, Jul 1996. doi: 10.1103/PhysRevE.54.815.

[135] M. H. R. Donald, P. L. Morton, and H. Wiedemann. Chromaticity correction in large storage rings. *IEEE Trans. Nucl. Sci*, pages 1200–1202, 1977.

[136] `https://github.com/linahv/Thesis`.

[137] A. et al. Loulergue. Baseline Lattice for the Upgrade of SOLEIL. *Proc. IPAC'18, Van- couver, Canada,*, pages 4762–4769, Apr-May 2018. doi: 10.18429/JACoW-IPAC2018-THPML034.

[138] M. Takao. Impact of betatron motion on path lengthening and momentum aperture in a storage ring. *Proceedings of EPAC08, Genoa, Italy*, 2008.

[139] M. Takao. Formulation of nonlinear chromaticity in circular accelerators by canonical perturbation method. *Phys. Rev. E*, 72:046502, Oct 2005. doi: 10.1103/PhysRevE.72.046502.

[140] Y. Shoji. Dependence of average path length betatron motion in a storage ring. *Physical Review Special Topics-accelerators and Beams - PHYS REV SPEC TOP-AC*, 8, 09 2005. doi: 10.1103/PhysRevSTAB.8.094001.

[141] R. J. Van de Graaff, K. T. Compton, and L. C. Van Atta. The Electrostatic Production of High Voltage for Nuclear Investigation. *Phys. Rev.*, 43:149–157, Feb 1933. doi: 10.1103/PhysRev.43.149.

[142] A. Nassiri, B. Chase, P. Craievich, A. Fabris, H. Frischholz, J. Jacob, E. Jensen, M. Jensen, R. Kustom, and R. Pasquinelli. History and Technology Developments of Radio Frequency (RF) Systems for Particle Accelerators. *IEEE Transactions on Nuclear Science*, 63:1–1, 11 2015. doi: 10.1109/TNS.2015.2485164.

[143] `http://www.schoolphysics.co.uk/age16-19/Nuclear%20physics/Accelerators/text/Linear_accelerator/index.html`.

[144] R. Wideröe. Über ein neues prinzip zur herstellung hoher spannungen. *Archiv f. Elektrotechnik*, pages 387–406, 1928. doi: 10.1007/BF01656341.

[145] H. Slizard. `https://library.ucsd.edu/dc/object/bb82951280/_1.pdf`, 1929.

[146] E. O. Lawrence and M. S. Livingston. The Production of high speed light ions without the use of high voltages. *Phys. Rev.*, 40:19–35, Apr 1932. doi: 10.1103/PhysRev.40.19.

[147] `https://catalog.archives.gov/id/558593`.

[148] `https://sites.google.com/site/puenggphysics/home/unit-iii/cyclotron`.

[149] L. H. Thomas. The Paths of Ions in the Cyclotron I. Orbits in the Magnetic Field. *Phys. Rev.*, 54:580–588, Oct 1938. doi: 10.1103/PhysRev.54.580.

[150] CERN synchro-cylcotron corking at full energy. `http://cds.cern.ch/record/839880/files/CM-P00053829.pdf`, 1958.

[151] `https://en.wikipedia.org/wiki/Dipole_magnet`.

[152] `https://www.triumf.ca/experimental-result/baartman-scores-touchdown-magnet-desig`

[153] J. P. Blewett. Radial Focusing in the Linear Accelerator. *Phys. Rev.*, 88:1197–1199, Dec 1952. doi: 10.1103/PhysRev.88.1197.

[154] K. Steffen. Basic Course on Accelerator Optics. *Proceedings of the 1984 CERN Accelerator School*, 85-19, 1984.

[155] L. Hoddeson, A. Kolb, and C. Westfall. Fermilab: Physics, the Frontier, and Megascience. *Bibliovault OAI Repository, the University of Chicago Press*, 77, 01 2011. doi: 10.1119/1.3098334.

[156] `https://www.sesame.org.jo/`.

[157] R. Bartolini. Synchrotron radiation lecture, JUAS, January 2017.

[158] R. D. Deslattes. X-ray monochromator development for synchrotron radiation facilities. *Nuclear Instruments and Methods*, 172(1):201 – 208, 1980. ISSN 0029-554X. doi: https://doi.org/10.1016/0029-554X(80)90635-7.

[159] E. B. Szarmes. Helical undulators. In *Classical Theory of Free-Electron Lasers*, 2053-2571, pages 13–1 to 13–7. Morgan and Claypool Publishers, 2014. ISBN 978-1-6270-5573-4. doi: 10.1088/978-1-6270-5573-4ch13.

[160] N. Balal, V.L. Bratman, and E. Magory. New varieties of helical undulators. *Nuclear Instruments and Methods in Physics Research Section A: Accelerators, Spectrometers, Detectors and Associated Equipment*, 971:163895, 2020. ISSN 0168-9002. doi: https://doi.org/10.1016/j.nima.2020.163895.

[161] S. Sasaki, K. Kakuno, T. Takada, T. Shimada, K. Yanagida, and Y. Miyahara. Design of a new type of planar undulator for generating variably polarized radiation. *Nuclear Instruments and Methods in Physics Research Section A: Accelerators, Spectrometers, Detectors and Associated Equipment*, 331:763–767, 07 1993. doi: 10.1016/0168-9002(93)90153-9.

[162] S. Sasaki. Analyses for a planar variably-polarizing undulator. *Nuclear Instruments and Methods in Physics Research Section A: Accelerators, Spectrometers, Detectors and Associated Equipment*, 347(1):83 – 86, 1994. ISSN 0168-9002. doi: https://doi.org/10.1016/0168-9002(94)91859-7.

[163] G. Isoyama, S. Yamamoto, T. Shioya, H. Ohkuma, S. Sasaki, T. Mitsuhashi, T. Yamakawa, and H. Kitamura. Construction of a multi-undulator, Revolver No. 19, at the Photon Factory. *Review of Scientific Instruments*, 60(7):1863–1866, 1989. doi: 10.1063/1.1140924. cited By 24.

[164] T. Hara, T. Tanaka, T. Seike, T. Bizen, X.-M. Maréchal, A. Nisawa, S. Fukushima, H. Yoshikawa, and H. Kitamura. Revolver undulator for BL15XU at SPring-8. *Nuclear Instruments and Methods in Physics Research Section A: Accelerators, Spectrometers, Detectors and Associated Equipment*, 467-468:161 – 164, 2001. ISSN 0168-9002. doi: https://doi.org/10.1016/S0168-9002(01)00264-9. 7th Int.Conf. on Synchrotron Radiation Instrumentation.

[165] B. Stilwell et al. *Proceedings of IPAC2012, New Orleans, Louisiane, USA*, 2012.

[166] APS revolver undulator. `https://youtu.be/RiUscAQHnxs`.

[167] S. Yamamoto, T. Shioya, M. Hara, H. Kitamura, X. W. Zhang, T. Mochizuki, H. Sugiyama, and M. Ando. Construction of an in-vacuum type undulator for production of undulator X-rays in the 5–25 keV region. *Review of Scientific Instruments*, 63(1):400–403, 1992. doi: 10.1063/1.1142768.

[168] T. Tanaka, T. Hara, R. Tsuru, D. Iwaki, X.-M. Maréchal, T. Bizen, T Seike, and H. Kitamura. In-Vacuum Undulators. *Proceedings of the 27th International Free Electron Laser Conference*, 01 2005.

# Acronyms

**A.T.** Accelerator Toolbox. 67, 71, 136, 157–159, 169, 170, 195, 208, 233

**AdA** Anello di Accumulazione. 92

**AGS** Alternating Gradient Synchrotron. 20

**ALS** Advanced Light Source. 26, 58

**ALS-U** Advanced Light Source - Upgrade. 38, 64, 65, 105, 184

**APS** Advanced Photon Source. 23, 26, 52, 53, 56, 58, 214, 215, 276

**AS** Australian Synchrotron at ANSTO. 26

**ASN** Agence de Sûreté Nucléaire. 119

**BNL** Brookhaven National Laboratory. 19

**CCRT** Centre de Calcul Recherche et Technologie. 100

**CDR** Conceptual Design Report. 128

**CEA** Commissariat à l'Énergie atomique et aux Énergies Alternatives. 33, 100

**CERN** Centre Européen pour la Recherche Nucléaire. 20

**CESR** Cornell Electron Storage Ring. 56

**CLS** Canadian Light Source. 26

**CNRS** Centre National de la Recherche Scientifique. 33

**DA** Dynamic Apertures. 100, 130

**DBA** Double Bend Achromat. 43, 52, 54, 55, 59, 62, 63, 267

**DLSR** Diffraction Limited Storage Ring. 27

**ESRF** European Synchrotron Radiation Facility. 23, 26, 53, 61, 71

**ESRF-EBS** ESRF-Extremely Brilliant Source. 8, 38, 54, 61, 105, 184, 205

**FEL** Free Electron Laser. 26

**FMA** Frequency Map Analysis. 90, 91, 111, 115

**FODO** FOcusing DefOcusing. 20, 30, 71, 216

**HMBA** Hybrid Multi-Bend Achromat. 62

**HOA** High-Order Achromat. 8, 38, 61, 63, 65, 66, 71, 105, 113, 184

**IBS** Intra-Beam Scattering. 93, 95, 96, 278

**ID** Insertion Device. 34, 35

**LBNL** Lawrence Berkeley National Laboratory. 19

**LGB** Longitudinal-Gradient Bend. 59

**linac** LINear ACcelerator. 25, 33

**LNLS** Brazilian Synchrotron Light Laboratory. 26

**m-DBA** Modified Double Bend Achromat. 33

**MBA** Multi-Bend Achromat. 54, 55, 59, 64–66

**MIK** Multipole-Injector Kicker. 123, 124, 131, 132, 136

**MOGA** Multi-Objective Genetic Algorithm. 8, 100–102, 104, 176

**PLS** Pohang Light Source. 26

**PS** Proton Synchrotron. 20

**QBA** Quadrupole-Bend Achromat. 54, 58

**RDT** Resonant Driving Terms. 49, 50, 80

**RF** Radio-Frequency. 16, 22, 25, 34, 58, 91, 140, 184, 203, 207

**RMS** Root-Mean Square. 46

**SESAME** Synchrotron-light for Experimental Science and Applications in the Middle East. 26

**SFP** Stable Fixed Point. 141

**SLS** Swiss Light Source. 23, 26

**SLS-II** Swiss Light Source II. 38, 64, 65, 105, 184

**SOLEIL** Source Optimisée de Lumiére à Énergie Intermédiaire de Lure. 26, 33, 38, 53, 66

**SRS** Synchrotron Radiation Source. 20

**SSRF** Shanghai Synchrotron Radiation Facility. 26

**TBA** Triple Bend Achromat. 52, 54, 63

**TLS** Taiwan Light Source. 26

**TME** Theoretical Minimum Emittance. 46, 50–52, 54, 55, 58–60, 268

**UFP** Unstable Fixed Point. 141

# Glossary

$B_0\rho[\mathbf{T.m}]$ Beam rigidity. 16

$C_0$ Path length of the reference particle. 18, 22, 39

$D_0'$ Zeroth-order horizontal dispersion derivative. 153

$D_1'$ First-order horizontal dispersion derivative. 155, 158

$D_0$ Zeroth-order horizontal dispersion. 151

$D_1$ First-order horizontal dispersion. 133, 155, 158, 162

$D_2$ Second-order horizontal dispersion. 155

$D_x$ Horizontal dispersion. 45

$E[\mathbf{eV}]$ Particle energy. 16, 51

$I[\mathbf{A}]$ Current. 214, 215, 217

$I$ Identity matrix. 51

$J$ Action variable. 43

$K_u$ Undulator parameter. 222

$Q$ Betatron tune. 42

$Q_s$ Synchrotron tune. 141

$T_0[\mathbf{s}]$ Revolution period of the reference particle. 22, 140

$V_{RF}[\mathbf{V}]$ RF voltage. 140

$\Delta C$ Path length. 47, 92, 150, 185, 186, 188, 203

$\Delta\nu$ Tune shift. 47, 87

$\alpha_0$ Zeroth-order momentum compaction factor. 137

$\alpha_1$ First-order momentum compaction factor. 137, 138, 144, 158

$\alpha_2$ Second-order momentum compaction factor. 137, 146

$\alpha_C$ Momentum compaction factor. 3, 22, 46, 47, 72, 137, 140, 150

$\beta_L$ Relative speed. 140

$\delta$ Momentum deviation. 44, 47, 87, 140, 151

$\epsilon$ Geometric emittance. 44

$\epsilon_x$ Natural horizontal emittance. 46, 72

$\epsilon_{DBA}$ Minimum emittance of a Double Bend Achromat. 52

$\epsilon_{TME}$ Theoretical minimum emittance. 50

$\epsilon_{ph}$ Diffraction-limited photon emittance. 28

$\eta_p$ Slip factor. 140

$\gamma_L[\mathbf{n.d.}]$ Lorentz factor. 16, 45, 51

$\lambda[\mathbf{m}]$ Wavelength. 28

$\lambda_u[\mathbf{m}]$ Period of an undulator. 222

$\mathcal{D}$ Damping partition. 46

$\mathcal{J}_{u\in\{x,y,E\}}$ Damping partition number. 46

$\mu_0[\mathbf{H.m^{-1}}]$ permittivity. 215, 217

$\nu$ Betatron phase advance over one turn. 40, 41

$\omega_0$ Revolution angle frequency. 19, 140

$\omega_s$ Synchrotron angle frequency. 22

$\phi$ Betatron phase advance. 41

$\phi_s$ Synchronous phase. 17

$\rho[\mathbf{m}]$ Bending radius. 16, 39, 45, 214

$\mathbf{B}[\mathbf{T}]$ Magnetic field. 16, 215

$\mathbf{E}[\mathbf{V.m^{-1}}]$ Electric field. 16

$\mathbf{p}[\mathbf{eV/c}]$ Particle Momentum. 16, 140

$\mathbf{p}_0[\mathbf{eV/c}]$ Momentum of the reference particle. 44, 140

$\theta$ Bending angle. 51, 214

$\xi$ Chromaticity. 47

$\xi_{nat}$ Natural chromaticity. 47

$c[\mathbf{m.s^{-1}}]$ Speed of light. 16

$e[\mathbf{C}]$ Charge of an electron. 140

$g[\mathbf{m}]$ Half of the gap between the poles. 214

$g_1[\mathbf{T.m^{-1}}]$ Quadrupole gradient. 215

$g_2[\mathbf{T.m^{-2}}]$ Sextupole gradient. 217

$k_1[\mathbf{m^{-2}}]$ Quadrupolar strength. 39, 45, 59, 86, 216

$k_2[\mathbf{m^{-3}}]$ Sextupole strength. 217

$k_2l[\mathbf{m^{-2}}]$ Integrated sextupole strength. 86

$m_0[\mathbf{kg}]$ Particle rest mass. 16

$n$ Field index. 19, 20

$q[\mathbf{C}]$ Charge of the particle. 16

$r[\mathbf{m}]$ Aperture radius. 215, 217

$s[\mathbf{m}]$ Longitudinal coordinate. 18, 39

$v$ Relative velocity. 16

$v_z[\mathbf{m.s^{-1}}]$ Longitudinal speed of the particle. 215

$x_\beta$ Horizontal betatron amplitude. 45, 151

# Illustrations

## Illustrations

### List of Figures

## List of Tables